



UNIVERSIDAD NACIONAL AUTÓNOMA DE MÉXICO

PROGRAMA DE MAESTRÍA Y DOCTORADO EN INGENIERÍA

INGENIERÍA CIVIL – ESTRUCTURAS

**EVALUATION OF STRONG-MOTION DURATION AS
DESIGN PARAMETER IN EARTHQUAKE ENGINEERING**

TESIS

QUE PARA OPTAR POR EL GRADO DE:

DOCTOR EN INGENIERÍA

PRESENTA:

ALHELÍ SILVESTRE LÓPEZ CASTAÑEDA

TUTOR:

DR. EDUARDO REINOSO ANGULO, INSTITUTO DE INGENIERÍA

CIUDAD DE MÉXICO, SEPTIEMBRE DE 2022



Universidad Nacional
Autónoma de México



UNAM – Dirección General de Bibliotecas
Tesis Digitales
Restricciones de uso

DERECHOS RESERVADOS ©
PROHIBIDA SU REPRODUCCIÓN TOTAL O PARCIAL

Todo el material contenido en esta tesis esta protegido por la Ley Federal del Derecho de Autor (LFDA) de los Estados Unidos Mexicanos (México).

El uso de imágenes, fragmentos de videos, y demás material que sea objeto de protección de los derechos de autor, será exclusivamente para fines educativos e informativos y deberá citar la fuente donde la obtuvo mencionando el autor o autores. Cualquier uso distinto como el lucro, reproducción, edición o modificación, será perseguido y sancionado por el respectivo titular de los Derechos de Autor.

JURADO ASIGNADO:

Presidente: Dr. Luis Esteva Maraboto

Secretario: Dr. José Alberto Escobar Sánchez

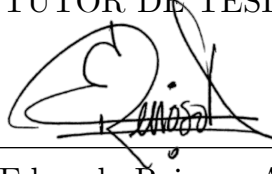
1er. Vocal: Dr. Eduardo Reinoso Angulo

2do. Vocal: Dr. Miguel Ángel Jaimes Téllez

3er. Vocal: Dr. Leonardo Alcántara Nolasco

Lugar donde se realizó la tesis: Instituto de Ingeniería, UNAM.

TUTOR DE TESIS:

A handwritten signature in black ink, appearing to read 'Eduardo Reinoso Angulo', written over a horizontal line.

Dr. Eduardo Reinoso Angulo

[This page intentionally left blank]

Dedication

To my parents, J. Isabel and Ma. del Rosario, and to my brother, José Isabel.

I will reach you in Atolinga.

To Osvaldo, who willingly helped me in all things great and small.

[This page intentionally left blank]

Acknowledgements

I feel fortunate to have completed my Ph.D. studies at the National Autonomous University of Mexico (UNAM, acronym in Spanish). I want to express my gratitude to the people and institutions that made it possible to achieve this cherished academic aspiration.

First and foremost, I am sincerely grateful to my adviser, Dr. Eduardo Reinoso Angulo, for his dedicated efforts for over three years guiding me as I worked through this dissertation. Thank you for giving me the opportunity to be a scholar at the UNAM Institute of Engineering (II-UNAM, acronym in Spanish).

Secondly, I want to thank the members of my advisory committee. It was a pleasure to learn from their expertise. In particular, I am honored with the participation of Professor Luis Esteva Maraboto as the chairman of the advisory committee. His contributions to earthquake risk engineering are the basis of this dissertation and many worldwide research projects. Let me say that he is a visionary researcher of great human qualities.

I thank Dr. Alberto Escobar Sánchez for his recommendations on engineering-related matters and, needless to say, for my personal life. They helped me to keep my feet on the ground.

I received a great deal of assistance from Dr. Leonardo Alcántara Nolasco while I wrote this dissertation. I appreciate the time he devoted to advising me on the local site conditions of the Valley of Mexico. I also cherish the fascinating conversations about cultural interests.

I want to thank Dr. Miguel Angel Jaimes Tellez for allowing me to participate in one of his research projects that led to the publication of a co-authored article in the Journal of Earthquake Engineering. Thanks for the trust.

I want to acknowledge the work team of the Instrumentation and Seismic Record Center (CIRES, acronym in Spanish) and II-UNAM that make it possible for the Mexican strong-motion databases to be available to researchers, students, and the public at large.

In addition, I want to thank the National Council for Science and Technology (CONACYT, acronym in Spanish) through the Graduate Scholarship Program for the grant provided.

Finally, I want to thank all my teachers, classmates, and friends at UNAM who gave me their support when I faced difficulties. Every word of encouragement kept me going.

Abstract

The emphasis of the new seismic design regulations on the application of nonlinear dynamic analyses to determine the response of unconventional structures (such as high-rise buildings) promotes the selection of accelerograms that truly characterize site-specific ground motions. Several parameters have been proposed throughout time to describe the ground motions. On this point, this dissertation focuses on studying the duration that characterizes the most intense part of the ground movement, i.e., the strong-motion duration.

In particular, the study implies establishing criteria to measure the strong-motion duration and developing predictive equations for its estimation. The research extends to the development of hazard curves that allow estimating the annual probability of exceedance of said parameter, either marginally or jointly with amplitude-based ground-motion parameters. It is important to mention that this thesis is limited to studying the strong-motion duration associated with interplate earthquakes occurring in the Middle America Trench. The geographic area of interest is Mexico City, where the effects of soil-dynamic amplification are manifested considerably, especially in areas characterized by lacustrine deposits.

With the tools developed in this study, the accelerograms used in nonlinear dynamic analyses and, even more so, in risk analysis can be selected more objectively. For instance, this dissertation presents examples where the estimates of the strong-motion duration obtained through the proposed predictive equations were used to generate synthetic accelerograms. Successively, such accelerograms were used to evaluate the performance of a steel frame, which was assumed to be located at different sites within Mexico City.

The example results suggest that the strong-motion duration has a significant influence on the seismic response of structures, specifically when they incur inelastic deformations. Such an influence is more noticeable if the analyzed structure is located at a site whose dominant period coincides with its natural period. Therefore, the strong-motion duration must be judiciously included as one of the principal design parameters in current earthquake engineering regulations. At least the author recommends considering it to solve problems related to cycles of fatigue, soil liquefaction, and soil settlement, as well as in the analysis of the inelastic response

of unconventional structures. In this way, structural reliability is expected to be improved.

Resumen

El énfasis de las nuevas normativas de diseño sísmico en la aplicación de análisis dinámicos no-lineales para la determinación de la respuesta de estructuras poco convencionales (como edificios de gran altura) plantea la necesidad de usar acelerogramas que realmente caractericen los movimientos del suelo en sitios específicos. Diversos parámetros se han propuesto para describir el movimiento del suelo, de los cuales esta tesis se enfoca en el estudio de la duración de la fase más intensa del movimiento del suelo.

Particularmente, el estudio implica establecer criterios para la medición de la duración del movimiento fuerte del suelo y ecuaciones predictoras que permitan su estimación. Adicionalmente, el estudio se extiende al desarrollo de curvas de peligro que posibilitan estimar la probabilidad anual de excedencia de dicho parámetro, tanto de manera marginal como junto con parámetros basados en amplitud que describen el movimiento del suelo. Es importante mencionar que esta tesis se limita al estudio de la duración del movimiento fuerte del suelo asociada a sismos interplaca ocurridos en la fosa Mesoamericana. El área geográfica de interés es la Ciudad de México, en donde los efectos de amplificación dinámica se manifiestan de manera considerable, especialmente en las zonas caracterizadas por depósitos lacustres.

Con las herramientas desarrolladas se pueden seleccionar de manera más objetiva los acelerogramas a utilizar en análisis dinámicos no-lineales, los cuales son necesarios para llevar a cabo, p. ej., análisis de riesgo sísmico. Como una pauta, en esta tesis se presenta una serie de ejemplos de aplicación de las ecuaciones predictoras de la duración del movimiento fuerte del suelo para la generación de acelerogramas sintéticos. Dichos acelerogramas fueron utilizados en la evaluación del desempeño de un sistema estructural dúctil, el cual se supone desplantado en sitios con distintas condiciones locales.

Los resultados de los ejemplos sugieren que la influencia de la duración del movimiento fuerte del suelo es significativa en la respuesta sísmica de estructuras cuando éstas incurren en el comportamiento inelástico. La influencia es más notoria si la estructura de interés se encuentra localizada en un sitio cuyo periodo dominante coincide con su periodo natural. Por lo anterior, dicho parámetro del movimiento del suelo debe de ser incluido de manera juiciosa como uno de los parámetros

principales de diseño en ingeniería sísmica. Al menos, la autora recomienda tenerlo en consideración cuando se estudien problemas relacionados con ciclos de fatiga, licuefacción y/o asentamientos del suelo, o con la respuesta inelástica de estructuras. De esta manera, se espera una mejora de la confiabilidad estructural.

Contents

List of Symbols.....	xvii
Roman Alphabet.....	xvii
Greek Alphabet.....	xxii
List of Figures	xxv
List of Tables	xxxiii
CHAPTER 1 Introduction	1
1.1 Problem Statement.....	1
1.2 Objectives and Scope of the Dissertation.....	6
1.3 Overview of the Dissertation	7
1.3.1 Computer Software	8
1.3.2 Units.....	8
1.3.3 Declaration of Co-authorship	8
CHAPTER 2 Strong-motion Duration in Earthquake Engineering.....	9
2.1 Introduction.....	9
2.2 Defining Strong-motion Duration	9
2.3 Worldwide Predictive Equations for Strong-motion Duration.....	14
2.4 Correlation Between Strong-motion Duration and Other Ground-motion Parameters.....	22
2.5 Influence of Strong-motion Duration on Structural Response	24
2.6 Discussion	26
CHAPTER 3 Strong-motion Duration Predictive Equations.....	29
3.1 Introduction.....	29

3.2	Seismological Parameters.....	31
3.2.1	Earthquake Source Parameters	31
3.2.2	Local Site Conditions	33
3.2.3	Source-to-site Distance	38
3.3	Estimation of Strong-motion Duration	39
3.3.1	Observed Trends Between Strong-motion Duration and Different Seismological Parameters	45
3.3.2	Predictive Equations for Strong-motion Duration.....	50
3.3.2.1	Residual Analysis	54
3.4	Discussion	57
CHAPTER 4 Strong-motion Duration Hazard.....		61
4.1	Introduction.....	61
4.2	Identification and Characterization of Earthquake Sources.....	63
4.2.1	Earthquake Occurrence Models and Magnitude Distribution.....	65
4.2.1.1	Estimation of Seismic Activity Parameters.....	67
4.2.2	Source-to-site Distribution.....	72
4.3	Strong-motion Duration Hazard Curves	76
4.3.1	Disaggregation of Strong-motion Hazard.....	80
4.4	Discussion	82
CHAPTER 5 Multivariate Probabilistic Seismic Hazard Analysis.....		87
5.1	Introduction.....	87
5.2	Measuring Dependence Between Strong-motion Duration and Other Ground-Motion Parameters	90
5.3	Multivariate Probabilistic Seismic Hazard Analyses for Sites Located in the Hill Zone of Mexico City.....	97
5.3.1	Predictive Equation for Peak Ground Acceleration and Acceleration Response-spectral Ordinates.....	97
5.3.2	Multivariate Seismic Hazard Curves	99

5.4	Discussion	103
CHAPTER 6 Strong-motion Duration and Structural Performance		107
6.1	Introduction.....	107
6.2	Equivalent Single Degree of Freedom System Modeling.....	108
6.3	Effects of Strong-motion Duration as Recorded in Mexico City on Structural Response	110
6.4	Relating Strong-motion Duration and Structural Damage	116
6.4.1	Incremental Dynamic Analyses	117
6.4.2	Fragility Functions.....	121
6.4.3	Translating Seismic Hazard into Risk	126
6.5	Discussion	129
CHAPTER 7 Conclusions		133
7.1	Synthesis of Results.....	133
7.1.1	Strong-motion Database Compilation	133
7.1.2	Defining Strong-motion Duration.....	134
7.1.3	Development of Strong-motion Duration Predictive Equations	134
7.1.4	Generation of Strong-motion Duration Hazard Curves.....	136
7.1.5	Evaluating the Effects of Strong-motion Duration on Structural Performance	137
7.2	The Challenges Ahead.....	139
7.3	Peer Reviewed Publications.....	140
APPENDIX A Studies on the Influence of Strong-motion Duration in Structural Response		143
APPENDIX B Earthquake Catalog.....		149
APPENDIX C Earthquake Source Parameters.....		153
APPENDIX D Accelerograph Network Catalog		155

APPENDIX E Exceedance Probabilities and Return Periods for Probabilistic Seismic Hazard Analyses..... 161

APPENDIX F Acceleration Response Spectra Determined from Accelerograms Recorded in the Hill Zone of Mexico City..... 163

APPENDIX G Predictive Equation for Peak Ground Acceleration and Acceleration Response-spectral Ordinates 165

References..... 169

List of Symbols

The symbols used in this dissertation are listed below in alphabetical order. Symbols denoted by letters of the Roman alphabet are listed first and are followed by those denoted by letters of the Greek alphabet. The author tried to adhere to the nomenclature commonly used in related literature but given the vastness of symbols, some may differ.

Roman Alphabet

Symbol	Description
a	Coefficient (intersection) in the standard Gutenberg and Richter relation.
a_0, a_1, a_2	Threshold levels of acceleration.
b	Coefficient in the standard Gutenberg and Richter relation.
\mathbf{b}	Vector of random effects assumed normally distributed with mean of $\mathbf{0}$ and variance-covariance matrix σ_b^2 .
c_e	Viscous damping coefficient.
C	Covariance between clusters in a linear mixed effects model.
CAD	Cumulative absolute displacement.
d_5, d_{95}	Values placed at the 5th and 95th percentile for $F_{D_{Sr}}$.
D_e	Structural-response duration, as defined by Esteva and Rosenblueth. ¹
D_g	Ground-motion duration.
D_B	Bracketed duration.
D_E	Effective duration.
D_S	Significant duration.
D_{Sr}	Relative significant duration.

D_U	Uniform duration.
DI_{EC}	Damage index proposed by Diaz et al. ²
e	Euler's number, approximately equal to 2.7183.
\mathbf{e}	Error vector assumed normally distributed with mean of $\mathbf{0}$ and variance matrix $\boldsymbol{\sigma}_w^2$.
$\hat{\mathbf{e}}$	Vector of marginal residuals.
E_h	Hysteretic energy.
$E_{h_{max}}$	Maximum hysteretic energy.
E_i	Input energy.
f	Ordinary frequency.
f_c	High-pass cutoff frequency.
$f_{\ln(D_{Sr})}$	Density function of the natural logarithm of D_{Sr} .
f_{max}	Frequency associated with either of the maximum spectral ratios $F_1(\omega)/F_V(\omega)$ or $F_2(\omega)/F_V(\omega)$.
$f_{D_{Sr}}$	Density function of D_{Sr} .
$f_{H/V}$	Frequency equal to the square root of the sum of the squares of the maximum frequencies of the ratios $F_1(\omega)/F_V(\omega)$ or $F_2(\omega)/F_V(\omega)$ divided by two, and equal to the inverse of T_s .
f_M	Density function of M .
f_R	Density function of the source of R .
F	Categorical variable used to characterize the focal mechanism of an earthquake.
F_k	Force associated to stiffness.
$F_{\ln(D_{Sr})}$	Distribution function of the natural logarithm of D_{Sr} .
F_u	Maximum strength of a structure.
F_y	Yield strength of a structure.
$F_{D_{Sr}}$	Distribution function of D_{Sr} .
F_R	Distribution function of the source of R .

$F_1(\omega), F_2(\omega), F_V(\omega)$	Fourier amplitude spectra of the components $\ddot{u}_{g_1}(t)$, $\ddot{u}_{g_2}(t)$, and $\ddot{u}_{g_V}(t)$, respectively, from a ground-motion recording.
g	Gravitational acceleration near Earth's surface, approximately equal to 9.8067 m/s ² .
$g(\bullet)$	Function of something.
$h(t)$	Normalized $I_A(t)$.
$H(\bullet)$	Heaviside step function.
H_h	Focal depth.
H_s	Altitude of a site.
H_{top}	Depth to the top of the fault plane.
\mathbf{I}	Identity matrix.
$I_A(t)$	Arias intensity as function of t .
$I_{A_{max}}$	Maximum Arias intensity.
I_{CM}	Factor to measure the strong-motion duration proposed by Cosenza and Manfredi. ³
k_e	Lateral stiffness (mechanical property of a structure).
L	Length of a fault plane idealized either as a line or rectangular shape.
m	Magnitude level.
\bar{m}	Arithmetic mean of earthquake magnitudes in a given catalog.
m_e	Mass of a structure.
m_u	Upper magnitude limit.
m_0	Lower magnitude limit.
M	Magnitude.
M_o	Scale-seismic moment.
M_s	Surface wave magnitude.
M_w	Moment magnitude.
n_b	Order of a Butterworth filter.

N	Poisson-distributed random variable denoting number of events occurring in a fixed time interval.
N_{conc}	Number of concordant pairs in a random sample of observations from a vector (Y_1, Y_2) of continuous random variables.
N_{disc}	number of discordant pairs in a random sample of observations from a vector (Y_1, Y_2) of continuous random variables.
N_C	Number of clusters considered in a linear mixed effects model, or number of sub-catalogs.
N_E	Number of earthquakes per sub-catalog.
N_M	Number of elements in a finite set of earthquake magnitudes.
N_R	Number of elements in a finite set of source-to-site distances.
N_S	Number of earthquake sources.
N_{SC}	Number of uniform shear stress cycles.
N_T	Number of earthquakes in a catalog.
P_F	Mean annual probability of failure.
$P_{F a}$	Probabiltily of failure given level a of PGA .
PGA	Peak ground acceleration.
PGV	Peak ground velocity.
PGD	Peak ground displacement.
r	Source-to-site distance level.
r_{min}	Lower source-to-site distance limit.
r_{max}	Upper source-to-site distance limit.
r_0	Closest distance to a shallow fault modeled as a linear source.
r_1, r_2	Levels at which the distribution function F_R of R equals 0.05 and 0.95, respectively.
R	Source-to-site distance.
R_{epi}	Epicentral distance.
R_{hypo}	Hypocentral distance.
R_{rup}	Closest distance to the fault rupture plane.

s	Standardized variable in a Generalized Extreme Value distribution.
S	Categorical variable used to characterize the local site conditions at a site.
$S_a(T_e)$	Acceleration response-spectral ordinate.
t	Time.
t_f	Total duration of an accelerogram.
t_{min}, t_{max}	Time instants associated with the occurrence of two specific values of \ddot{u}_g .
T	Time interval or exposure time.
T_e	Natural period of an oscillator or structure during free vibration.
T_s	Dominant period of the soil.
T_r	Return period.
(u, v, w)	Global coordinate system.
u_e	Relative displacement of a structure with respect to the ground.
\ddot{u}_e	Relative acceleration of a structure with respect to the ground.
u_g	Ground-motion displacement.
\dot{u}_g	Ground-motion velocity.
\ddot{u}_g	Ground-motion acceleration.
$\ddot{u}_{g_1}(t), \ddot{u}_{g_2}(t), \ddot{u}_{g_V}(t)$	Accelerograms in three orthogonal components of a ground-motion record.
u_{max}	Peak displacement.
u_u	Maximum deformation at the roof of a structure.
u_t	Relative displacement.
\ddot{u}_t	Absolute acceleration.
u_y	Yield deformation at the roof of a structure.
$\overline{v_{s30}}$	Average shear wave velocity over the uppermost 30 m of the soil at a site.
V	Variance of a linear mixed effects model.

W	Width of a fault plane idealized as a rectangular shape.
X_1, \dots, X_p	Set of explanatory variables.
\mathbf{X}	Fixed-effects design matrix.
y	Ground-motion level.
\mathbf{y}	Response vector of a specific Y .
$\hat{\mathbf{y}}$	Fitted vector of a specific Y .
Y	Response variable. Specifically, a ground-motion parameter.
\mathbf{Y}	Vector of random variables.
Y_1, Y_2	Continuous random variables.
\mathbf{Z}	Random-effects design matrix.

Greek Alphabet

Symbol	Description
α	A fixed effect (also known as model coefficient). Also, the intercept coefficient the exponential Gutenberg and Richter relation.
α_e	Factor that defines the secondary stiffness of a constitutive model.
$\boldsymbol{\alpha}$	Vector of fixed effects.
β	The slope coefficient in the exponential Gutenberg and Richter relation.
$\hat{\boldsymbol{\delta}}$	Vector of normalized residuals.
$\Delta_{P_{F \alpha}}$	Subtraction between two conditional probabilities of failure $P_{F \alpha}$.
ϵ	Composite model error.
(ζ, η)	Local coordinate system.
(ζ_0, η_0)	Local coordinates of the hypocenter.
ζ_e	Fraction of critical damping of a structure.
η_E	Factor used to estimate DI_{CE} .

θ	Fault strike.
ϑ	Vector of parameters found in Υ .
ι	Fault rake.
κ	Generalized Extreme Value parameter.
λ	Mean rate of occurrence of events.
λ_a	Mean rate of exceedance of a given level a of PGA .
λ_d	Mean rate of exceedance of a given level d of D_{Sr} .
$\lambda_{d,a}$	Joint mean annual rate of exceedance of a given level d of D_{Sr} and a given level a of either PGA and $S_a(T_e)$.
λ_y	Mean rate of exceedance of a certain ground-motion level y .
λ_m	Mean rate of exceedance of an earthquake magnitude value m .
λ_{m_0}	Mean rate of exceedance of the lower-bound magnitude m_o .
λ_F	Mean annual rate of failure.
μ	Parameter of the generalized extreme value distribution, lognormal distribution, normal distribution, and Poisson distribution.
$\boldsymbol{\mu}$	Mean vector (multivariate normal distribution parameter).
μ_1, μ_2	Parameters of the bivariate normal distribution.
μ_e	Ductility ratio (mechanical property of a structure).
ξ	Conditional errors.
$\hat{\xi}$	Conditional residuals.
σ	Parameter of the generalized extreme value distribution, lognormal distribution, and normal distribution.
σ^2	Variance of each component of the error vector \mathbf{e} .
$\boldsymbol{\sigma}_b^2$	Variance-covariance matrix of the random-effects vector \mathbf{c} .
$\boldsymbol{\sigma}_w^2$	Variance matrix of the error vector \mathbf{e} .
σ_1, σ_2	Parameters of the bivariate normal distribution.
π	Mathematical constant, approximately equal to 3.1416.
ρ	Pearson correlation coefficient.

ρ_S	Spearman's rho.
ρ	Intraclass correlation.
τ_K	Kendall's tau.
Σ	Variance-covariance matrix (multivariate normal distribution parameter).
Υ	Positive semi-definite matrix.
φ	Fault dip.
ϕ	Density function of the standard normal distribution, i.e., a normal distribution with $\mu = 0$ and $\sigma = 1$.
Φ	Distribution function of the standard normal distribution, i.e., a normal distribution with $\mu = 0$ and $\sigma = 1$.
ψ	Azimuth.
ω	Angular frequency.

List of Figures

In total, 57 figures are presented in this dissertation. Their titles are listed below, along with the page where they are displayed.

Figure 1.1	Total collapse of a 15-story reinforced concrete building located in Tlatelolco, Mexico City due to the September 19, 1985 earthquake. The photograph was taken from the El Universal newspaper archive ²¹	3
Figure 2.1	Generic definition of D_B of an accelerogram	10
Figure 2.2	Generic definition of D_U of an accelerogram	11
Figure 2.3	Generic definitions of D_S of an accelerogram	11
Figure 2.4	Accelerograms recorded at the stations CH84 and JA43 during the January 22, 2003 earthquake that occurred in Colima, Mexico. These stations are located at two different sites in Mexico City, each with T_s equal to approximately 1.4 s and 3.0 s. On the right of each accelerogram is shown its correspondent FAS	28
Figure 3.1	Plates, mid-oceanic ridges, and trenches encompassing the Mexican territory. The acronym TMVB stands for Trans-Mexican Volcanic Belt	32
Figure 3.2	Map of Mexico City (shaded in gray) showing the location of the free-field ground-motion recording stations (triangles). Data from crossed-out stations was disregarded for the development of the strong-motion duration GMPEs. From north to south these are ESTS, CT64, CP28, CE18, and TH35. Stations marked with yellow circles are related to the examples shown in Table 3.1 and Figure 3.6. These are Station DX37 located in GZII, and stations IB22, SP51, BA49, and AE02 located in GZIIIa, GZIIIb, GZIIIc, and GZIIId, respectively	35
Figure 3.3	Schematic of the global and local coordinate systems used to compute R_{hypo} and R_{rup}	39

Figure 3.4	Estimation of the absolute D_B from an accelerogram recorded at station CU01 during the September 19, 1985 earthquake, with $M_w = 8.0$	40
Figure 3.5	Estimation of D_{Sr} from two accelerograms recorded at stations CUP1 and CUP4 during the September 14, 1995 earthquake, with $M_w = 7.4$. The black lines stand for the computation of D_{Sr} using the raw accelerograms, whereas the blue lines stand for its computation using the portion of the accelerograms bounded by $a_0 = 2 \text{ cm/s}^2$	42
Figure 3.6	Collection of six accelerograms recorded at different sites in Mexico City during the March 20, 2012 earthquake, which had $M_w = 7.4$. The accelerograms are bounded by $a_0 = 2 \text{ cm/s}^2$. Shaded areas stand for the strong-motion duration lapse of each accelerogram.....	44
Figure 3.7	Estimation of D_{Sr} from an accelerogram recorded at station BA49 during the March 20, 2012 earthquake, with $M_w = 7.4$	45
Figure 3.8	Distribution of D_{Sr} in M_w , grouped by earthquake event	46
Figure 3.9	Distribution of D_{Sr} in R_{hypo} grouped by earthquake event	48
Figure 3.10	Distribution of D_{Sr} in R_{rup} grouped by earthquake event	48
Figure 3.11	Distribution of R_{hypo} and R_{rup} in M_w , grouped by earthquake event. The measures for R_{hypo} are denoted by a dot and the measures for R_{rup} by a square	49
Figure 3.12	Distribution of D_{Sr} in R_{rup} , grouped by geotechnical zone, for data from the earthquakes that occurred on July 15, 1996 (yellow box), April 18, 2018 (burgundy box), and June 30, 2010 (blue box)	49
Figure 3.13	Distribution of D_{Sr} in T_s , grouped by earthquake event	50
Figure 3.14	Distribution of μ and $\mu \pm \sigma$ of the natural logarithm of D_{Sr} , with respect to R_{hypo} and T_s , computed using GMPE C for three values of M_w . A 3D view of the plots is shown on the right, whereas their lateral view is shown on the left. Scatter plots of the data considered in the regression analysis that match the selected values of M_w are superimposed. Data points marked in red are outliers	54
Figure 3.15	Estimated BLUPs for GMPEs A and C, respectively	56

- Figure 3.16** Residual analyses for GMPE A. At the top there are illustrated a scatter plot of the standardized e versus y , a frequency histogram of e , and box plots of e grouped by earthquake event. At the bottom there are illustrated scatter plots of ξ versus M_w and R_{hypo} , respectively 56
- Figure 3.17** Residual analyses for GMPE C. At the top there are illustrated a scatter plot of the standardized e versus y , a frequency histogram of e , and box plots of e grouped by earthquake event. At the bottom there are illustrated scatter plots of ξ versus M_w , R_{hypo} , and T_s , respectively 57
- Figure 4.1** Map depicting the four source zones identified in this study for interplate earthquakes occurring along the MAT. The abbreviation RP means Rivera Plate. The epicenters of earthquakes that occurred between 1900 and 2021 and were considered to estimate the seismicity of each source zone are marked with circles. The blue triangle stands for an observational site located in Mexico City with geographic coordinates 19.35°N, 99.15°W 64
- Figure 4.2** Scatter plots of earthquake occurrences over time. For each source zone, the shaded areas represent the grouping of earthquakes into sub-catalogs 69
- Figure 4.3** Annual exceedance rates of magnitude λ_m computed from the “shifted and truncated” Gutenberg-Richter law and data given in Table 4.2..... 71
- Figure 4.4** Schematic of the variations of R for a short fault that can be modeled as a point source and shallow fault modeled as a linear source 73
- Figure 4.5** Graphical tests of goodness-of-fit used to determine the probability distribution of R_{hypo} . Density histograms of the data together with plots of density functions of samples coming from various probability distributions are shown on the left. Respective cumulative probability plots are shown on the right. The GEV distribution is shown in blue solid lines 75
- Figure 4.6** Hazard curves of D_{Sr} for sites located in GZI. The dashed lines stand for the contribution of the individual source zones identified for interplate earthquakes occurring at the MAT and the solid black line stands for the summation of all contributions 77

- Figure 4.7** Hazard curves of D_{Sr} for sites located in Mexico City that have values of T_s that vary from 1 s to 5 s in steps of 1 s 78
- Figure 4.8** Expected D_{Sr} with an exceedance probability of 2%, 5%, 10%, and 20% over various exposure times for sites located in GZI..... 79
- Figure 4.9** Expected D_{Sr} with an exceedance probability of 10% over various exposure times for sites with T_s varying from 1 s to 5 s, in steps of 1 s 79
- Figure 4.10** Joint mass distribution of M_w and R_{hypo} conditional on exceeding $D_{Sr} = 125$ s ($T_r = 250$ years) at a site located in GZI. A contour plot of the density is also displayed in the figure..... 81
- Figure 4.11** Joint mass distribution of M_w and R_{hypo} conditional on exceeding $D_{Sr} = 237$ s ($T_r = 250$ years) in a site with $T_s = 4.0$ s. A contour plot of the density is also displayed in the figure..... 81
- Figure 4.12** Comparison between the rate of exceedance of magnitude computed from the Ordaz and Reyes¹⁵⁶ data (dashed red line) and the one developed in this study (solid black line). The curves consider the contribution of all source zones, i.e., four in the present study and 14 in the work of Ordaz and Reyes.¹⁵⁶ 83
- Figure 5.1** Estimates of ρ (solid black line), ρ_S (dashed red line), and τ_K (dotted yellow line) between D_{Sr} and $S_a(T_e)$ considering data from sites located in GZI. The dash-dotted gray line stands for the estimates of ρ between the natural logarithms of D_{Sr} and $S_a(T_e)$ 94
- Figure 5.2** Scatter plots between the observations of D_{Sr} and $S_a(T_e)$, with values of T_e equal to 1.0 s, 2.0 s, 3.0 s, and 4.0 s, respectively, considering data from sites located in GZI 94
- Figure 5.3** Estimates of ρ , ρ_S , and τ_K (from top to bottom) between D_{Sr} and $S_a(T_e)$ considering data from sites located in GZII or GZIII 96
- Figure 5.4** Distribution of μ and $\mu \pm \sigma$ of the natural logarithm of PGA and $S_a(T_e)$, with values of T_e varying from 1.0 s to 5.0 s, in steps of 1.0 s, with respect to R_{hypo} and M_w . A 3D view of the plots is shown on the right, whereas their lateral view is shown on the left. Scatter plots of the strong-motion data considered in the regression are superimposed..... 98

- Figure 5.5** Hazard curves of PGA for sites located in GZI. The dashed lines stand for the contribution of the individual source zones identified for interplate earthquakes occurring at the MAT and the solid black line stands for the summation of all contributions..... 100
- Figure 5.6** Hazard curves of $S_a(T_e)$, with values of T_e varying from 1 s to 5 s, in steps of 1 s, for sites located in GZI 100
- Figure 5.7** Joint annual rate of exceedance of D_{Sr} and PGA for sites located in GZI 101
- Figure 5.8** Contour plots of the joint annual rate of exceedance of D_{Sr} and either PGA or $S_a(T_e)$ for values of T_e varying from 1 s to 5 s, in steps of 1 s, for sites located in GZI..... 102
- Figure 5.9** Comparison between the UHS for sites located in GZI developed in this study (solid black line) and the one given in the NTC-2020²⁷ (dashed red line) 105
- Figure 6.1** At the left is shown a schematic of the moment-resisting steel frame model and at the right is shown the collapse mechanism developed by the steel frame when subjected to a pushover analysis considering a first-mode distribution pattern 109
- Figure 6.2** Pushover curve for the steel frame and capacity curve of the equivalent SDOF system..... 110
- Figure 6.3** Schematics of the equivalent SDOF system and constitutive model considered for its development..... 110
- Figure 6.4** Map of Central Mexico showing the epicenters of the earthquakes that occurred on January 22, 2003, March 20, 2013, April 18, 2014, and June 18, 2020, in the Mexican subduction zone. Listed in chronological order, the first earthquake had $M_w = 7.5$, the second and fourth earthquakes had $M_w = 7.4$, and the third earthquake had $M_w = 7.3$. The map overlay shows the territorial delimitation of Mexico City and the geographical location of the stations CUP5, UC44, BO39, and AU11. The sites where these stations are located exhibit values of T_s equal to 0.5 s, 1.3 s, 2.5 s, and 4.0 s, respectively, in accordance with the NTC-2020²⁷ 111
- Figure 6.5** On the left, there are shown accelerograms (bounded by $a_0 = 2 \text{ cm/s}^2$) recorded in stations CUP5, UC44, BO39, and AU11 during four earthquakes that occurred in the Mexican subduction zone (see

- Figure 6.4). The shaded areas represent the time windows in which the ground motions may be considered strong according to the definition of D_{Sr} . On the right, there are shown the displacement histories $u_e(t)$ of the equivalent SDOF system when subjected to the accelerograms shown on the left side. The structural displacement measured considering the accelerograms (bounded by $a_0 = 2 \text{ cm/s}^2$) is depicted by the black lines and the structural displacement measured considering only the strong phase of the ground motions is depicted by the colored lines 113
- Figure 6.6** Input energy imparted to the equivalent SDOF system when subjected to accelerograms recorded at station UC44 during E2 and E4. The black line represents the energy disclosed by the accelerograms (bounded by $a_0 = 2 \text{ cm/s}^2$), whereas the red line represents the energy disclosed by the strong phase of the ground motions 115
- Figure 6.7** On the left, there are shown the design spectra given in the NTC-2020²⁷ (UHSs for $T_r = 250$ years) for the sites where stations UC44, BO39, and AU11 are located. The response spectra of three aleatory groups (one per site) of 40 synthetic accelerograms each (with $PGA = 0.3g$) overlap the design spectra. On the right, there are shown a sample of eight synthetic accelerograms with $PGA = 0.3g$ from two aleatory groups generated for the site where station BO39 is located. Each sample consists of four synthetic accelerograms with equal duration 118
- Figure 6.8** Incremental dynamic analysis results for the equivalent SDOF system, which was assumed to be located at three different sites in Mexico City. The results that considered synthetic accelerograms with a duration equal to d_5 are shown in green and those results that considered synthetic accelerograms with a duration equal to d_{95} are shown in orange. At the top are shown the results for u_{max} , while at the bottom for E_{hmax} 120
- Figure 6.9** Schematic for the determination of $E_s(u_d)$ and $E_h(u_d)$ for $u_d = u_u$ using the capacity curve of the equivalent SDOF system 122
- Figure 6.10** At the top are shown the displacement-based fragility curves developed for the operational (dashed lines), life safety (long-short lines), and collapse (solid lines) performance levels of the equivalent SDOF system located in sites with T_s of 1.3 s, 2.5 s, and 4.0 s when

subjected to sets of synthetic accelerograms with duration equal to d_5 (blue lines) and d_{95} (red lines). At the bottom are shown the differences in fragility $\Delta P_{F|a}$ between the results obtained from synthetic accelerograms with a duration equal to d_5 and those from synthetic accelerograms with a duration equal to d_{95} 124

- Figure 6.11** At the top are shown the energy-based fragility curves developed for life safety (long-short lines) and collapse (solid lines) performance levels of the equivalent SDOF system located in sites with T_s of 1.3 s, 2.5 s, and 4.0 s, when subjected to sets of synthetic accelerograms with duration equal to d_5 (blue lines) and d_{95} (red lines). At the bottom are shown the differences in fragility $\Delta P_{F|a}$ between the results obtained from synthetic accelerograms with a duration equal to d_5 and those from synthetic accelerograms with a duration equal to d_{95} 125
- Figure 6.12** Hazard curves of PGA for sites with T_s equal to 1.3 s, 2.5 s, and 4.0 s 128
- Figure 6.13** Results of three NDAs when subjecting the equivalent SDOF system to three synthetic accelerograms with $PGA = 0.4g$ and duration equal to 183 s. The duration is equal to $\mu_{D_{rs}} + \sigma_{D_{rs}}$ and was computed for the site with $T_s = 4.0$ s (see Table 6.1). At the top are the synthetic accelerograms. In the middle are the displacement histories $u_e(t)$ of the equivalent SDOF system when subjected to the accelerograms. At the bottom are the hysteresis loops resulting from each NDA 131
- Figure F.1** Acceleration response spectra determined from accelerograms recorded in GZI. They are grouped by earthquake event. The legends show the code of stations where the accelerograms were recorded. To avoid saturation, only four acceleration response spectra are referenced..... 163

[This page intentionally left blank]

List of Tables

In total, 25 tables are presented in this dissertation. Their titles are listed below, along with the page where they are displayed.

Table 2.1	Estimated functions $g(\mathbf{X}, \hat{\boldsymbol{\alpha}})$ of nine GMPEs reported in the literature from 2006 to 2021 for the natural logarithm of D_{Sr} , with $a_1 = 0.05$ and $a_2 = 0.95$. The strong-motion data used for the development of the GMPEs is summarized below each $g(\mathbf{X}, \hat{\boldsymbol{\alpha}})$. 18
Table 3.1	Estimation of T_s from a set of ground motions recorded at five stations located in different geotechnical zones..... 37
Table 3.2	Estimates of the elements of $\boldsymbol{\alpha}$ for the strong-motion duration GMPEs developed for sites located in GZI. Results shown in columns titled GMPE A correspond to those considering R_{hypo} as the measure defining the R , whereas the results shown in the columns titled GMPE B correspond to those considering R_{rup} 52
Table 3.3	Estimates of the elements of $\boldsymbol{\alpha}$ for the strong-motion duration GMPEs developed for sites located in GZII or GZIII. Results shown in columns titled GMPE C correspond to those considering R_{hypo} as the measure defining R , whereas the results shown in the columns titled GMPE D correspond to those considering R_{rup} 52
Table 3.4	Estimates of σ_b and σ_w and their corresponding 95% confidence intervals (lower, upper)..... 52
Table 4.1	Statistics used to estimate the β -values and seismicity rates λ_{m_0} 70
Table 4.2	Estimates of the β -values and seismicity rates λ_{m_0} , and magnitude thresholds m_0 and m_u 72
Table 4.3	Minimum and maximum values of R_{hypo} , i.e., r_{min} and r_{max} , respectively, observed for each source zone..... 73
Table 4.4	Probability of observing a test statistic at least as extreme as the observed value under the null hypothesis that the point-source

	distances came from a population with a specific distribution function.....	74
Table 4.5	Estimates of the GEV distribution parameters μ , σ , and κ , and distance thresholds r_1 and r_2 corresponding to the levels at which $F_{R_{hypo}}$ equals 0.05 and 0.95, respectively	76
Table 5.1	Estimates of ρ , ρ_S , and τ_K between D_{Sr} and t_f , PGA , PGV , and PGD considering data from sites located in GZI	93
Table 5.2	Estimates of ρ , ρ_S , and τ_K between D_{Sr} and t_f , PGA , PGV , and PGD considering data from sites located in GZII or GZIII	95
Table 6.1	Estimates of μ of the natural logarithm of D_{Sr} , $\mu_{D_{Sr}}$, and $\sigma_{D_{Sr}}$ obtained from a DSHA that considers a scenario earthquake with $M_w = 7.5$ occurred at $R_{hypo} = 250$ km from three sites with T_s equal to 1.3 s, 2.5 s, and 4.0 s. The last two columns summarize the values placed at the 5th and 95th percentile for $F_{D_{Sr}}$	118
Table 6.2	Estimates of μ and σ for the displacement-based fragility functions developed for the operational, life safety, and collapse performance levels of the equivalent SDOF system located in sites with T_s of 1.3 s, 2.5 s, and 4.0 s.....	124
Table 6.3	Estimates of μ and σ for the energy-based fragility functions developed for the life safety and collapse performance levels of the equivalent SDOF system located in sites with T_s of 1.3 s, 2.5 s, and 4.0 s	125
Table 6.4	Estimates of the elements of α , σ_b , and σ_w for the GMPE for PGA developed for sites located in GZII or GZIII.....	127
Table 6.5	Annual probabilities of exceeding displacement- and energy-based damage states related to the collapse performance level of the equivalent SDOF system, which is assumed to be located at sites with T_s of 1.3 s, 2.5 s, and 4.0 s.....	129
Table A.1	List of 16 studies carried out from 2006 to 2021 on the influence of the strong-motion duration in the structural response using NDAs	143
Table B.1	List of interplate earthquakes with $M_w \geq 6$ that occurred in the Mexican subduction zone from 1900 to 2021	149

Table C.1	List of interplate earthquakes and corresponding finite-source rupture model parameters used for the development of the GMPEs	153
Table D.1	List of free-field ground-motion recording stations considered for the development of the strong-motion duration GMPEs	155
Table D.2	List of free-field ground-motion recording stations disregarded for the development of the strong-motion duration GMPEs	158
Table D.3	Number of ground-motion recordings per earthquake and per geotechnical zone used for the development of the strong-motion duration GMPEs.....	159
Table E.1	Relationships among typical values of exceedance probabilities of ground-motion levels y and T_r	161
Table G.1	Estimates of the elements of α , σ_b , and σ_w of the GMPE for PGA and $S_a(T_e)$ reported in Subsection 5.3.1	165

[This page intentionally left blank]

CHAPTER 1

Introduction

1.1 Problem Statement

“Today, hundreds of millions of people through the world live with a significant risk to their lives and property from earthquakes. Billions of dollars of public infrastructure are continuously at risk of earthquake damage. The health of many local, regional, and even national economies are [*sic*] also at risk from earthquakes. These risks are not unique to the United States, Japan, or any other country. Earthquakes are a global phenomenon and a global problem”.⁴

The above quote was written by Kramer⁴ more than 25 years ago. To a large extent, these words will continue to be reflected in the future. Nevertheless, while humans do not have the power to stop earthquakes, we do have the ability to reduce the probability of incurring some socio-economic consequences caused by them, which include casualties and monetary loss.

The probability of loss due to earthquakes is precisely the definition of *seismic risk*.⁵ From an engineering point of view, a loss can be associated with a decrease in the functionality of a structure, which is directly related to structural damage. Structural damage is often quantified by discrete *damage states*, which can vary from none, slight, moderate, extensive, to complete.^{6,7} Therefore, the damage states are tied in with *structural performance levels*, which define, e.g., the operational, immediate occupancy, life safety, and collapse capacity of the structure.⁸

Hence, a *seismic risk analysis* (SRA) aims to estimate the probability of exceeding a specific damage state (at least once) during a time period, T . Based on probability theory, the most common expression used to estimate the exceedance probability of a damage state is⁷:

$$\begin{aligned} & P(\text{structural response} > \text{damage state}) \\ &= \int P(\text{structural response} > \text{damage state} | Y = y) f_Y(y) dy \end{aligned} \quad (1.1)$$

where $P(\text{structural response} > \text{damage state} | Y = y)$ is the probability that the structural response exceeds a damage state given that a ground-motion parameter, denoted as Y , takes a value equal to y , and f_Y denotes the density function of Y .

Identification of earthquake hazards is essential to conducting an SRA. An *earthquake hazard* can be ground shaking (hereafter called ground motion), ground failure, surface faulting, tectonic deformation, flooding, fire, or any other physical phenomenon associated with an earthquake that may produce adverse effects on human activities. Of these, ground motion is the most widespread and damaging earthquake-related hazard.⁹ The quantitative estimation of the expected ground motion at a site is commonly determined by a *seismic hazard analysis* (SHA). Specifically, the ground-motion characterization at a site of interest during any future T should be carried out through a *probabilistic seismic hazard analysis* (PSHA). Broadly speaking, a PSHA integrates information from ground motions caused by the full range of earthquakes that can occur at each fault or source zone that might affect the site to estimate the exceedance probability of each y .^{4,9} Commonly, the ground-motion levels y are estimated from *ground-motion prediction equations* (GMPEs), formerly known as *attenuation relationships*. Note that a GMPE relates a specific Y to one or more parameters that quantitatively characterize a seismological property of the source, propagation path, or site-response characteristics of an earthquake.¹⁰

Over the years, most SRAs have been performed using amplitude-based parameters to characterize the ground motion at a site. Yet, it has been long recognized that not only the amplitude of ground motions can greatly influence the structural response, but also their frequency content and duration.^{11–15} As the reader must know, the *peak ground acceleration*, *PGA*, and a *response-spectral parameter* have been used by convention as amplitude-based ground-motion parameters. The former is defined as the maximum ground acceleration that occurred at the site of interest during an earthquake and the latter can be specified from a *response spectrum*, which is the maximum response of a set of single-degree-of-freedom (SDOF) systems with a chosen level of (viscous) damping ratio, ζ_e , when subjected to a particular ground-motion input at its base, plotted as a function of the undamped natural period, T_e , of the SDOF systems. In engineering seismology, the ground-motion input is generally an *accelerogram*, which is a record of the ground acceleration, \ddot{u}_g , as a function of time, t , at a given site during an earthquake. On the other hand, the *frequency content* is a parameter used to characterize the way \ddot{u}_g contains energy at different ordinary frequencies, f , and it can be measured by the well-known Fourier amplitude spectrum (FAS).^{14,16} The *ground-motion duration* is defined as the total time of ground motion, from the arrival of the seismic waves until the return to ambient conditions.¹⁷

An example of a (catastrophic) combination of the aforementioned ground-motion parameters happened in Mexico City during the great Michoacán earthquake that occurred on September 19, 1985. That earthquake caused ground motions that reached quite high amplitudes, had very narrow-banded frequency content at low f , and were long-lasting. As a consequence of these ground motions, 412 buildings collapsed and 3,124 were badly damaged,¹⁸ leading to losses that likely reached 4 billion U.S. dollars in physical and economic damage.¹⁹ Specifically, buildings of 10- to 20-story located at sites with a dominant period, T_s , equal to approximately 2 s were the most affected because of resonance.^{8,20} Conversely, many stiff-short buildings were able to follow such long-period ground motions without significant damage. As a case in point, Figure 1.1 shows a photograph of a collapsed reinforced concrete building due to the September 19, 1985 earthquake. The building was part of a residential complex named Nonoalco, which was located in Tlatelolco, Mexico City, and was formed of three sections of 15-storey each. While two of the building sections collapsed during the September 19, 1985 earthquake, the third was so damaged that it had to be demolished at once.



Figure 1.1 Total collapse of a 15-story reinforced concrete building located in Tlatelolco, Mexico City due to the September 19, 1985 earthquake. The photograph was taken from the El Universal newspaper archive²¹

The possible effects of the frequency content on the response of structures can indirectly be considered in the SRAs by ensuring that all ground motions used in the PSHAs are generated by earthquakes with similar focal mechanism, originated in the same tectonic environment, and recorded in sites with similar local site conditions. The *focal mechanism* describes the orientation and sense of slip on the causative fault plane. It is typically classified into two or more categories which typically include strike-slip (horizontal slip), reverse (dip-slip with the hanging-wall side up), thrust (same as reverse but with shallow dip), and normal (dip-slip with the hanging-wall side down).¹⁰ The *tectonic environment* describes the regions where the earthquakes occur, e.g., *shallow-crustal earthquakes* commonly occur in active or stable tectonic regions, intermediate-depth earthquakes (also known as *intraslab earthquakes*) within a subducting plate, and *interplate earthquakes* in the interface of two plates, such as in a subduction zone where one plate (usually oceanic crust) subducts beneath another (usually continental crust) or on a transform fault.¹⁰ Finally, the *local site conditions* are a qualitative or quantitative description of the topography, geology, and soil profile at a site of interest.

By contrast, the ground-motion duration has rarely been used in SRAs because of the following reasons:

1. There are few GMPEs for the ground-motion duration published in the literature.²² The very first GMPEs were developed with limited strong-motion databases, hence the ground-motion duration estimates tend to be biased. Moreover, recent GMPEs are only regionally applicable.
2. It has been argued that the joint probability distribution of the ground-motion duration and at least one amplitude-based parameter must be considered for its inclusion in a PSHA and, therefore, in Eq. (1.1).
3. It has been preferred to use the *strong-motion duration*, which represents the fraction considered intense of the ground motion at a site of interest, instead of the total duration of the ground motion. Although the estimation of the strong-motion duration seems simple, a great number of methods can be found in the literature for its measurement,²³ none of which has been fully accepted by the structural engineering community.

Regarding the structural response, the probability of damage suffered by a structural system needed to carry out an SRA is typically evaluated using *fragility functions*. Specifically, a fragility function describes the conditional probability of exceeding a damage state, for different ground-motion levels y .⁶ That is, they define

the first term of the integral given in Eq. (1.1). Developing a fragility function commonly involves an *incremental dynamic analysis* (IDA), which requires performing multiple *nonlinear dynamic analyses* (NDAs).²⁴ First of all, an NDA is a step-by-step analysis of the dynamic response of a structural system to a specified loading that may vary with time, which is generally an accelerogram. Then, an IDA involves scaling the set of accelerograms used in the NDAs to different ground-motion levels y . Commonly, the ground-motion levels y are selected to force the analyzed structural system through the full range of behavior, that is, from elastic to inelastic and finally to global dynamic instability, where the structural system essentially collapses.

Beyond the SRAs, the ground-motion duration has not been formerly considered as a design ground-motion parameter in earthquake engineering regulations. The author attributes the latter to a lack of agreement between the members of the regulatory committees. This may be related to the reasons listed on page 4 and to the insufficiency of specific regional studies on the effects of ground-motion duration on the response of structures that allow obtaining reference values. In this matter, current earthquake engineering regulations, such as those established by the ASCE,²⁵ Eurocode 8-1,²⁶ and NTC-2020,²⁷ require NDAs to design certain critical facilities. Therefore, the proper definition of the ground-motion duration is necessary either for the selection of real accelerograms or the generation of synthetic accelerograms to be used in an NDA. However, it happens to be a ground-motion parameter whose importance in earthquake engineering is often overlooked. For instance, the Eurocode 8-1²⁶ ambiguously establishes the following:

“When site-specific data are not available, the minimum duration of the stationary part of the accelerograms should be equal to 10 s.”

On the other side of the world, the NTC-2020²⁷ presents a simple mathematical expression for estimating the ground-motion duration caused by either interplate or intraslab earthquakes. Nevertheless, as no details of the variance defining such mathematical expression are provided, structural practitioners cannot properly account for the randomness of the ground-motion duration when generating synthetic accelerograms. Moreover, the NTC-2020²⁷ indicates that the synthetic accelerograms to be used in NDAs to evaluate the response of a structure located at a specified site must have the same response spectrum as a given *design spectrum*. The latter specifies the required strength or capacity of the structure plotted as a function of T_e and ζ_e . For the site of interest, the proposed design spectrum equals a *uniform hazard spectrum* (UHS), which is a response spectrum with ordinates having an equal probability of being exceeded within a pre-determined *return period*, T_r . Note that T_r can be defined as the average time between exceedance of a specified

y at the site of interest. In the case of the NTC-2020,²⁷ $T_r = 250$ years. Thus, a reasonable question is if the estimated values of the ground-motion duration obtained from the mathematical expression given in the NTC-2020²⁷ correspond to ground motions with said T_r .

The preceding remarks clearly illustrate that there is a knowledge gap in the estimation of the ground-motion duration for both the seismic design and risk assessment of structures. Thus, this dissertation aims to contribute to disseminating the appropriate criterion for the characterization of that ground-motion parameter in order to improve the design of structures under earthquake action. The extent of the dissertation is given in the following section. An overview of it is given then in Section 1.3.

1.2 Objectives and Scope of the Dissertation

The goal of this dissertation is to provide the necessary mechanisms to facilitate the solution of earthquake engineering problems that require site-specific estimates of the strong-motion duration and its exceeding probabilities. Therefore, the objectives of this dissertation consist of:

- i. Gather a complete database of accelerograms and study their strong-motion duration from an adopted definition.
- ii. Select a set of seismological parameters to develop GMPEs for the strong-motion duration.
- iii. Probabilistically characterize a set of seismological parameters to develop curves of the expected exceedance rates of strong-motion duration.
- iv. Measure the dependence between the strong-motion duration and other ground-motion parameters to assess the viability of multivariate PSHAs.
- v. Evaluate the influence of the strong-motion duration on structural performance via fragility functions and SRAs.
- vi. Explore the inclusion of the strong-motion duration as a primary parameter for the structural design.

The scope of the dissertation includes the following:

- Ground motions caused by interplate earthquakes and recorded in Mexico City will be analyzed.

- Regarding the multivariate PSHAs, this dissertation extends to the modeling of the dependence structure between the strong-motion duration and both *PGA* and acceleration response spectral ordinates.
- For the evaluation of the influence of the strong-motion duration on the seismic response of structures, this dissertation is limited to the analysis of an equivalent SDOF system whose properties were estimated from the dynamic characteristics of a four-story one-bay steel moment frame designed by the plastic method.

1.3 Overview of the Dissertation

This dissertation consists of seven chapters. These include the present one, which contextualizes the reader on the role of the strong-motion duration in earthquake engineering and gives a concise description of the issues being addressed in the dissertation. The content of the remaining six chapters is briefly described below.

Chapter 2 presents the state-of-the-art methods used to measure the strong-motion duration, a list of the GMPEs developed worldwide for its estimation, and a summary of the observed trends between the strong-motion duration and other ground-motion parameters reported in three recent research works. Additionally, a summary of the findings reported by various researchers who have studied the influence of the strong-motion duration on the response of structures is given at the end of the chapter.

To get into the subject, Chapter 3 presents four GMPEs for the strong-motion duration applicable to sites located in Mexico City. The statistical method used for the development of the GMPEs is described in detail and the criteria considered to measure the strong-motion duration and seismological parameters are justified through the text.

Based on the probabilistic characterization of each earthquake source capable of inducing ground motions of engineering significance in sites located in Mexico City, Chapter 4 deals with the strong-motion duration hazard. The PSHAs are addressed using the GMPEs developed in Chapter 3.

Chapter 5 is an introduction to multivariate PSHAs. The first part of the chapter is concerned with the measurement of the dependency between the strong-motion duration and seven ground-motion parameters, which include *PGA* and acceleration response-spectral ordinates. The dependence structure between the mentioned amplitude-based ground-motion parameters and the strong-motion duration is modeled and used to perform multivariate PSHAs.

Chapter 6 presents a series of studies on the effects of the strong-motion duration on the response of an equivalent SDOF system, which is assumed to be located at different sites in Mexico City. The studies include the development of fragility functions, for which site-specific synthetic accelerograms were generated using the GMPEs developed in Chapter 3. Also, SRAs are performed in this chapter.

Chapter 7 concludes the dissertation. Specifically, a breakdown is made of how the proposed objectives were achieved under the established scope and some recommendations are given for future work on topics related to ground-motion duration. Articles derived from this study are listed at the end of this chapter.

1.3.1 Computer Software

Most of the programming and numeric computing were carried out in MATLAB. Also, SIMQKE-I was used to generate synthetic accelerograms to perform IDAs, for which ANSYS was used. Being a student enrolled, UNAM sponsors the licenses of the mentioned software for educational purposes.

1.3.2 Units

This dissertation uses the International System of Units (SI, acronym in French).

1.3.3 Declaration of Co-authorship

This dissertation includes information from articles that have been published and manuscripts sent for possible publication in peer-reviewed journals. Specifically, Chapter 3 includes data and results from two articles published in co-authorship with Dr. Eduardo Reinoso Angulo. Results in Chapters 4 and 5 are part of a manuscript that will be submitted for possible peer review. Chapter 6 includes data and results from a manuscript under review that was co-authored by the author, Dr. Eduardo Reinoso Angulo, and Ph.D. candidate J. Osvaldo Martín del Campo Preciado.

CHAPTER 2

Strong-motion Duration in Earthquake Engineering

2.1 Introduction

The ground motions produced during an earthquake are complex. As expressed by Sen⁸ in his book, there are many areas of “known unknowns”, and the knowledge base is updated with each additional piece of new information. This new information includes an increasingly adequate characterization of ground-motion parameters.

Of all of the parameters that have been proposed to characterize the amplitude, frequency content, and duration of the ground motions, this dissertation focuses (as specified in Section 1.2) on the assessment of the strong-motion duration. Then, this chapter aims to contextualize the reader about the current knowledge that surrounds said parameter from a structural engineering approach. Specifically, the methods found in the literature for the measurement of the strong-motion duration, as well as the GMPEs developed from worldwide data that allow its estimation, are presented in Sections 2.2 and 2.3. A summary of the findings reported by various researchers on the correlation between the strong-motion duration and other ground-motion parameters and its influence on the structural response is carried out in Sections 2.4 and 2.5, respectively. Some comments on the reviewed literature are given at the end of the chapter.

2.2 Defining Strong-motion Duration

Bommer and Martínez-Pereira²³ carried out extensive work that summarizes the methods used by different researchers to estimate the strong-motion duration for engineering purposes. The authors noted that nearly all of the methods, which were more than 30, allowed to estimate how long the strong shaking phase of the ground motion lasts from an accelerogram. Depending on the criteria used for the measurement of the strong-motion duration from an accelerogram, Bommer and Martínez-Pereira²³ grouped each method into three generic categories, namely, bracketed durations, uniform durations, and significant durations.

Let's consider an accelerogram $\ddot{u}_g(t)$, with total duration t_f . The *bracketed duration*, D_B , is defined as the time elapsed between the first and last excursions of a specified level a_0 of ground acceleration. The *uniform duration*, D_U , is also constrained by a threshold level of acceleration a_0 . But it is defined as the sum of the time intervals during which the ground acceleration exceeds such level. On the other hand, the *significant duration*, D_S , is based on the accumulation of energy in an accelerogram. The energy is commonly represented as a measure of the *Arias intensity*, I_A , which can be defined as a function of t as follows²⁸:

$$I_A(t) = \frac{\pi}{2g} \int \ddot{u}_g(t)^2 dt \quad (2.1)$$

Therefore, D_S can be defined as the time elapsed between the instants when I_A reaches two specified threshold values, a_1 and a_2 . Figure 2.1, Figure 2.2, and Figure 2.3 illustrate a schematic of the estimation of D_B , D_U , and D_S , respectively, from $\ddot{u}_g(t)$.

Each generic category of the strong-motion duration presented above can be further subclassified depending on whether relative or absolute values of either a_0 or a_1 and a_2 are used. Therefore, the absolute D_B can be computed as²⁹:

$$D_B = t_{max} - t_{min} \quad (2.2)$$

where t_{max} and t_{min} are the time instants associated with the first and last value of \ddot{u}_g , respectively, that meet the following solution:

$$H(|\ddot{u}_g(t)| - a_0) = 1 \quad (2.3)$$

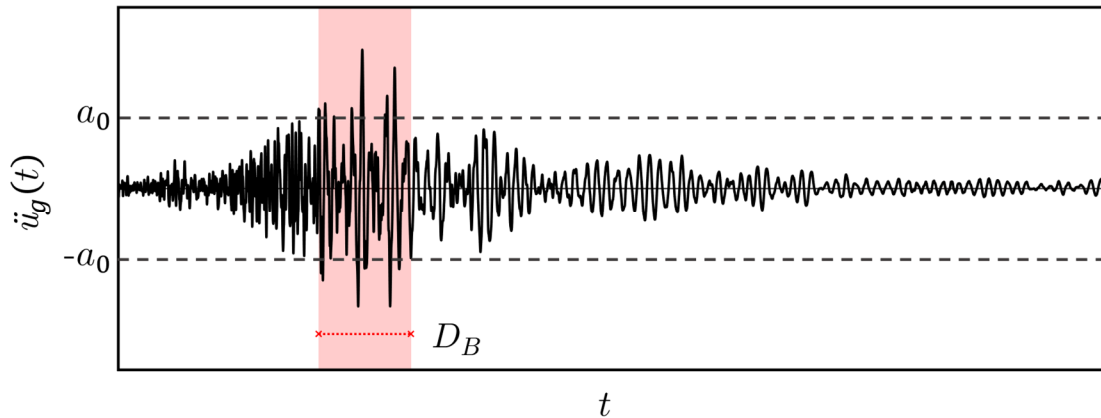


Figure 2.1 Generic definition of D_B of an accelerogram

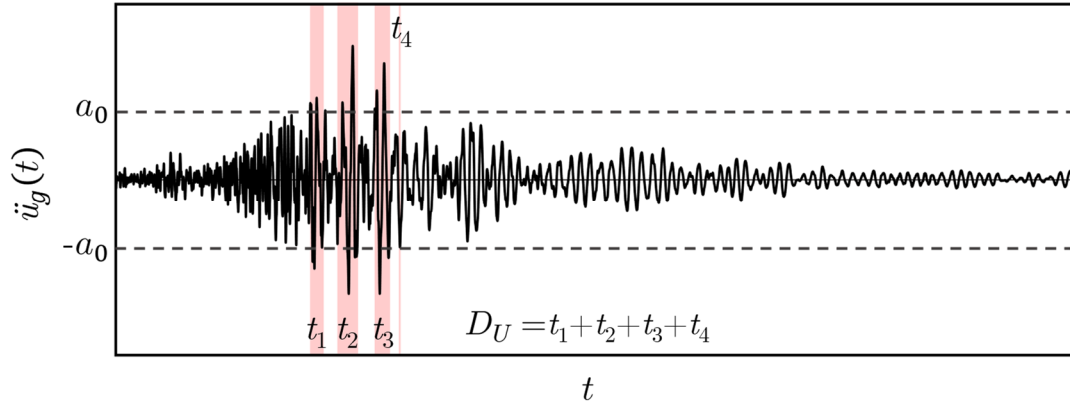


Figure 2.2 Generic definition of D_U of an accelerogram

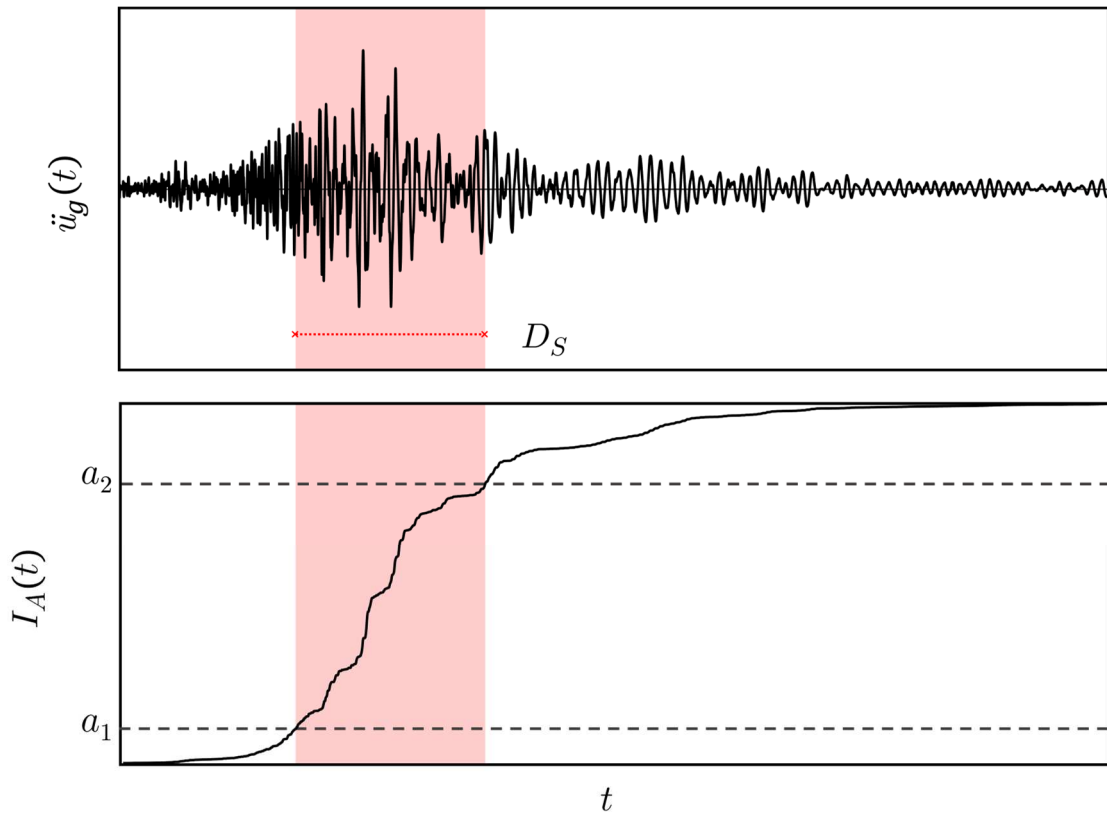


Figure 2.3 Generic definitions of D_S of an accelerogram

where $H(\bullet)$ is the Heaviside step function. Generally, a_0 ranges from $0.03g$ to $0.20g$. For instance, Ambraseys and Sarna³⁰ were the first that explicitly proposed a definition to measure the portion of an accelerogram considered to be strong. They used the concept of absolute D_B considering a_0 equal to $0.03g$. Page et al.³¹ also

used the concept, but considered a_0 equal to $0.05g$. Later, McGuire and Barnhard³² undertook an extensive study on the definitions of strong-motion duration, which included D_B . They considered a_0 equal to $0.05g$, $0.10g$, $0.15g$, and $0.20g$. Notice that g is the gravitational acceleration and is approximately 9.8067 m/s^2 near Earth's surface.

The relative D_B can also be computed using Eq. (2.2), but considering:

$$H(|\ddot{u}_g(t)| - a_0 PGA) = 1 \quad (2.4)$$

where in this case a_0 is a fraction of the peak ground acceleration, PGA .^{32,33} For instance, McGuire and Barnhard³² considered a_0 equal to 0.5 . They referred to the relative D_B as *fractional duration*.

The absolute D_U can be computed as follows²⁹:

$$D_U = \int H(|\ddot{u}_g(t)| - a_0) dt \quad (2.5)$$

and the relative D_U as:

$$D_U = \int H(|\ddot{u}_g(t)| - a_0 PGA) dt \quad (2.6)$$

The values of a_0 in Eqs. (2.5) and (2.6) can be taken as those for absolute and relative D_B , respectively. Note that Bolt³⁴ formally introduced the concept and name of (absolute) D_B and D_U . He considered a_0 equal to $0.05g$ and $0.10g$ for both definitions.

The absolute D_S can be computed as²⁹:

$$D_S = \int [H(I_A(t) - a_1) - H(I_A(t) - a_2)] dt \quad (2.7)$$

After analyzing several accelerograms, Bommer and Martínez-Pereira²³ found that a_1 and a_2 equal to 0.01 m/s and 0.125 m/s , respectively, are good indicators of the strong-motion duration from an engineering perspective. Note that they called the absolute D_S as *effective duration*, D_E , which is a name that was previously used by Zaharah and Hall.³⁵

The relative D_S (hereafter denoted as D_{Sr}) can be computed as follows²⁹:

$$D_{Sr} = \int [H(h(t) - a_1) - H(h(t) - a_2)] dt \quad (2.8)$$

where $h(t)$ stands for the normalized $I_A(t)$ and can be computed as:

$$h(t) = \frac{I_A(t)}{I_{A_{max}}} \quad (2.9)$$

where $I_{A_{max}}$ is the maximum I_A estimated from the accelerogram of interest. The graphical representation of $h(t)$ versus t is known as a *Husid plot*.³⁶ In Eq. (2.8) a_1 and a_2 are fractions that are usually taken as 0.05 and 0.95, respectively, i.e., the time interval in which 90% of the total I_A is attained.^{13,37} The limits 0.05 and 0.75 have also been taken.³⁸

Note that D_S can also be measured using the integral of the ground velocity or displacement, denoted respectively as \dot{u}_g and u_g , as function of t . For instance, Taflamplis et al.³⁹ proposed a method to estimate D_S based on the cumulative absolute displacement, *CAD*, which is defined as:

$$CAD = \int |\dot{u}_g(t)| dt \quad (2.10)$$

In the literature, there are methods to measure the strong-motion duration based on the response of structural systems subjected to ground motions. Bommer and Martínez-Pereira²³ classified these methods into a fourth generic category named *structural response durations*, but they can also be classified in one of the three categories described above. For instance, the very first study to propose a definition of strong-motion duration was by Rosenblueth and Bustamante.⁴⁰ Their method consisted in measuring the duration of uniform motion needed to produce a constant ratio between the maximum spectral displacement response of an SDOF system with and without a specified ζ_e . According to Bommer and Martínez-Pereira,²³ the method proposed by Rosenblueth and Bustamante⁴⁰ can be classified in the category of D_B .

Other methods do not fall into one of the four categories proposed by Bommer and Martínez-Pereira.²³ For instance, Cosenza and Manfredi³ proposed the following factor to measure the strong-motion duration:

$$I_{C\&M} = \frac{\int \ddot{u}_g(t)^2 dt}{PGA \cdot PGV} \quad (2.11)$$

where *PGV* is the peak ground velocity, which is defined as the maximum ground velocity occurred (or expected) at a site of interest during an earthquake.

2.3 Worldwide Predictive Equations for Strong-motion Duration

As mentioned in Section 1.1, GMPEs are commonly used to characterize the ground motion at a site of interest. Specifically, a GMPE can be obtained from a mathematical process of data fitting known as *regression analysis*,¹⁰ which is a set of statistical processes for estimating the relationships between a response (or dependent) variable, Y , and a set of explanatory (or independent) variables, X_1, \dots, X_p . Most *regression models* can be expressed in matrix form as follows⁴¹:

$$\mathbf{y} = \mathbf{g}(\mathbf{X}, \boldsymbol{\alpha}) + \mathbf{e} \quad (2.12)$$

where \mathbf{y} is a known vector of responses of Y , $\mathbf{g}(\mathbf{X}, \boldsymbol{\alpha})$ is a function of a design matrix \mathbf{X} and an unknown vector of model coefficients $\boldsymbol{\alpha}$, and \mathbf{e} is an unknown vector of errors. Note that, in the literature, a *linear regression model* is denoted in matrix form as $\mathbf{y} = \mathbf{X}\boldsymbol{\alpha} + \mathbf{e}$, where the form of the function $\mathbf{X}\boldsymbol{\alpha}$ could be of any form including nonlinear functions or polynomials as long as the linearity between Y and the terms of $\boldsymbol{\alpha}$ is maintained.

In practice, the form of $\mathbf{g}(\mathbf{X}, \boldsymbol{\alpha})$ is first specified and then a regression method is chosen to estimate the terms of $\boldsymbol{\alpha}$. The goal is to determine the form of $\mathbf{g}(\mathbf{X}, \boldsymbol{\alpha})$ that most closely fits the data. Note that the estimated value of \mathbf{y} is $\hat{\mathbf{y}} = \mathbf{g}(\mathbf{X}, \hat{\boldsymbol{\alpha}})$. The estimated function $\mathbf{g}(\mathbf{X}, \hat{\boldsymbol{\alpha}})$ can be used to assess the accuracy of the regression model in explaining the data.

Among others, two usual assumptions for regression models are that: (i) the terms of \mathbf{e} are uncorrelated with one another, and (ii) they have independent and identical normal distributions, with mean zero and variance σ^2 . Also, under certain considerations, the conditional expectation of Y when X_1, \dots, X_p take on a given set of values x_1, \dots, x_p can be approximated by $\mathbf{g}(\mathbf{X}, \hat{\boldsymbol{\alpha}})$. Note that, in probability theory, the *expected value* of a random variable is the average value that the random variable takes on.⁴² Thus, it is also known as the *mean*.

In this manner, for earthquake engineering purposes, various researchers have developed GMPEs taking as Y a specific ground-motion parameter and as part of the set X_1, \dots, X_p one or various seismological parameters, which can be¹⁰:

- The *magnitude*, M , which is a quantity intended to measure the size of an earthquake. The preferred magnitude scale used to develop GMPEs is the *moment magnitude*, M_w . Such magnitude scale was introduced by Kanamori⁴³

and can be computed from the following equation given by Hanks and Kanamori⁴⁴:

$$\log(M_0) = 1.5M_w + 16.05 \quad (2.13)$$

where M_0 is the *scalar-seismic moment*, which is defined as the magnitude of the component couple of the double couple that is the point-force system equivalent to a fault slip in an isotropic elastic body.⁴⁵

- The *source-to-site distance*, R , which is the shortest distance between an observational site and the earthquake source, which is commonly represented as either a point or finite fault plane. Point-source distance measures include the *hypocentral distance*, R_{hypo} , and *epicentral distance*, R_{epi} . The first is the distance from the site to the *hypocenter*, which is the point within the Earth where the earthquake rupture initiates. The second is the distance from the site to the *epicenter*, which is the distance from the site to the point on the Earth's surface directly above the hypocenter. On the other hand, the most common finite-source distance measure used nowadays is the closest distance from the site to the fault plane, R_{rup} .
- Either T_s or the average shear wave velocity at the uppermost 30 m of the soil, $\overline{v_{s30}}$. They describe quantitatively the local site conditions at the site of interest.

The above seismological parameters can be viewed as *numerical-valued variables* (also known as *quantitative variables*). That is, they describe a measurable quantity as a number.⁴⁶ In addition to these, GMPE developers often use categorical variables to account for the effects of ground motions recorded in sites with different local site conditions or caused by different tectonic environments. Note that a *categorical variable* (also called a *qualitative variable*) has a measurement scale consisting of a set of groups or categories defining qualitative property.⁴⁶

In the case at hand, one can find in the literature various GMPEs for the strong-motion duration. For instance, the very first GMPE was developed by Professors Luis Esteva Maraboto and Emilio Rosenblueth Deutsch.¹ The estimated function $\mathcal{g}(\mathbf{X}, \hat{\alpha})$ reported by the professors was⁴⁷:

$$\widehat{D}_e = 0.15 \exp(0.74)M + 0.3R_{hypo} \quad (2.14)$$

where D_e stands for a strong-motion duration definition that falls in the category of structural-response durations.

In general, early GMPEs were developed using the *method of least squares* (which finds the estimates of $\boldsymbol{\alpha}$ that minimize the sum of squared terms of \mathbf{e}) and a limited strong-motion database. Although the researchers recognized the effects of the local site conditions, tectonic environment, or focal mechanism in the estimates of the strong-motion duration, related seismological parameters were generally disregarded in the development of early GMPEs. An exception may be made for the GMPEs developed by Guerrero⁴⁷ and Reinoso and Ordaz,⁴⁸ who introduced T_s in the form of $\mathcal{g}(\mathbf{X}, \boldsymbol{\alpha})$. For instance, the following $\mathcal{g}(\mathbf{X}, \hat{\boldsymbol{\alpha}})$ was reported by Reinoso and Ordaz⁴⁸:

$$\widehat{D}_{Sr} = 0.01 \exp(M) + (0.036M - 0.07)R + (4.8M - 16)(T_s - 0.5) \quad (2.15)$$

where $T_s = 0.5$ s for rock or firm soil sites.

It should be mentioned that the GMPEs proposed by Guerrero⁴⁷ and Reinoso and Ordaz⁴⁸ were developed considering ground motions recorded in various states of Mexico, which include Mexico City. The selected ground motions were caused by intraplate and intraslab earthquakes with M ranging from 5.2 to 8.1, and that occurred until 1995. As noted from Eq. (2.15), the researchers considered D_{Sr} , but with $a_1 = 0.025$ and $a_2 = 0.975$, for the development of the GMPEs. They argued that such values of a_1 and a_2 hold the part of the ground motions that is useful for engineering purposes.

A summary of other early GMPEs can be found in the research works of Guerrero⁴⁷ and Douglas.²² The work of Guerrero⁴⁷ (his master's thesis) must be especially recognized. It can be considered the basis for the development of the GMPE proposed by Reinoso and Ordaz⁴⁸ and, to some extent, a guideline for understanding the level of development reached 25 years ago on the ground-motion duration in Mexico City.

On another note, recent GMPEs have been often developed with robust strong-motion databases and, when necessary, they contemplate as part of the set X_1, \dots, X_p one or various seismological parameters to consider the effects of ground motions recorded in sites with different local site conditions and caused by earthquakes with different tectonic environments or characterized by different focal mechanisms. The vast majority of recent GMPEs have been developed using *mixed-effects models*, which constitute a class of regression models for data that are collected and summarized in groups.⁴⁹ In general, as long as a limited strong-motion dataset is used to develop a GMPE, the estimates of Y will be quite similar either if the method of least squares or a mixed-effects model is used. However, with more robust strong-motion datasets, the estimates of Y obtained from a GMPE developed

using a mixed-effects model tend to be more accurate than those estimated from a GMPE developed using the method of least squares.^{50,51}

Particularly, approximately 15 studies can be found in the literature in the last 20 years that address the development of GMPEs for the strong-motion duration.²² The relative significant duration D_{Sr} has been preferred over D_B or D_U because the definition of a_1 and a_2 is more stable than the definition of a_0 .⁵² Clearly, an accelerogram with amplitudes smaller than a_0 would lead to values of D_B or D_U equal to zero. Such zero strong-motion durations can be problematic when developing GMPEs and, therefore, in their use for earthquake engineering purposes. Nevertheless, GMPEs have also been developed for such definitions.^{53,54} For instance, to avoid problems, Bommer et al.⁵³ disregarded those accelerograms that lead to D_B or D_U values equal to zero for the development of the GMPEs.

Table 2.1 lists the estimated functions $\mathcal{g}(\mathbf{X}, \hat{\boldsymbol{\alpha}})$ of nine GMPEs reported in the literature between 2006 and 2021 that allow estimating the strong-motion duration. The GMPEs were developed using mixed-effects models and considering the natural logarithm of D_{Sr} , with $a_1 = 0.05$ and $a_2 = 0.95$. The strong-motion data used for their development is also summarized in Table 2.1. Note that the GMPEs developed by the author are not reported in Table 2.1. They will be addressed in Chapter 3.

Note that the recordings supplied in accelerograph network catalogs, such as those provided by the CIRES and II-UNAM, commonly contain accelerograms in two or three orthogonal components of the ground motion. That is, each ground-motion recording could include two orthogonal horizontal accelerograms, $\ddot{u}_{g_1}(t)$ and $\ddot{u}_{g_2}(t)$, and one vertical, $\ddot{u}_{g_V}(t)$. Then, to develop the GMPEs, most of the researchers cited in Table 2.1 considered the geometric mean of the values of D_{Sr} obtained for each pair of horizontal accelerograms of a ground-motion recording. This is done to match with the current practice that several researchers incur for the measuring of other ground-motion parameters from accelerograms.⁵⁵

It can be said from the estimated functions $\mathcal{g}(\mathbf{X}, \hat{\boldsymbol{\alpha}})$ reported in Table 2.1 that D_{Sr} increases as either the earthquake magnitude or the source-to-site distance increase and as $\overline{v_{s30}}$ decreases. Note that the interpretation of (nonlinear) functions $\mathcal{g}(\mathbf{X}, \boldsymbol{\alpha})$ is not straightforward. If $\mathcal{g}(\mathbf{X}, \boldsymbol{\alpha})$ were $\alpha_0 + \alpha_1 X_1 + \dots + \alpha_p X_p$ the sign of each α_i , with $i = 1, \dots, p$, would indicate whether Y is positively or negatively correlated with each X_i . Then, to interpret the estimated functions $\mathcal{g}(\mathbf{X}, \hat{\boldsymbol{\alpha}})$ given in Table 2.1, it is quite good to rely on graphical tools such as scatter plots of the observed strong-motion data or inspect the estimated values of Y using a given GMPE and holding all but one X fixed.

Table 2.1 Estimated functions $\mathcal{g}(\mathbf{X}, \hat{\alpha})$ of nine GMPEs reported in the literature from 2006 to 2021 for the natural logarithm of D_{Sr} , with $a_1 = 0.05$ and $a_2 = 0.95$. The strong-motion data used for the development of the GMPEs is summarized below each $\mathcal{g}(\mathbf{X}, \hat{\alpha})$

Author(s)	$\mathcal{g}(\mathbf{X}, \hat{\alpha})$
1. Kempton and Stewart ⁵²	$\ln \left(\frac{\left\{ \frac{\exp[2.79 + 0.82(M - 6)]}{10^{1.5M + 16.05}} \right\}^{-\frac{1}{3}}}{15.68 \cdot 10^6} + 0.15R + (3.00 - 0.0041\overline{v_{s30}}) \right)$ <p>Strong-motion data: 1,559 ground-motion recordings from 73 worldwide shallow-crustal earthquakes with M ranging from 5.0 to 7.6. Here, R varies from 0 km to 200 km. The strong-motion recordings were obtained from the Next Generation of Ground-Motion Attenuation Models (NGA) project operated by the Pacific Earthquake Engineering Research Center (PEER).⁵⁶</p>
2. Bommer et al. ⁵³	$-2.2393 + 0.9368M_w + (1.5686 - 0.1953M_w) \ln \left(\sqrt{R_{rup}^2 + 2.5^2} \right) - 0.3478 \ln(\overline{v_{s30}}) - 0.0365H_{top},$ <p>where H_{top} is the depth to the top of the fault plane.</p> <p>Strong-motion data: 2,406 ground-motion recordings (each with two horizontal accelerograms) from 114 worldwide earthquakes (56 strike-slip, 35 reverse or reverse oblique, and 23 normal or normal oblique) with M_w ranging from 4.8 to 7.9. All ground motions were recorded at $R_{rup} \leq 100$ km. The sites had $\overline{v_{s30}}$ ranging from 100 m/s to 2,000 m/s. Individual values of D_{Sr} were considered to develop the GMPE. The strong-motion data was obtained from the PEER NGA database.⁵⁶</p>
3. Ghanat ⁵⁷	$[1.54241 + 0.61466(M_w - 6)] + [-0.33216 + 0.011385R_{rup}] + -0.00048\overline{v_{s30}}$ <p>Strong-motion data: 2,690 ground-motion recordings (each with two horizontal components) from 129 shallow-crustal earthquakes (62 strike-slip, 42 reverse or reverse oblique, and 25 normal or normal oblique) with M_w ranging from 4.8 to 7.9 and R up to 200 km. The sites had $\overline{v_{s30}}$ ranging from 120 m/s up to 2,250 m/s. The geometric mean of the values of D_{Sr} computed from the horizontal accelerograms of each ground-motion recording was considered to develop the GMPE. The ground-motion recordings were obtained from the PEER NGA database.⁵⁶</p>

Table 2.1 Estimated functions $\mathcal{g}(\mathbf{X}, \hat{\boldsymbol{\alpha}})$ of nine GMPEs reported in the literature from 2006 to 2021 for the natural logarithm of D_{Sr} , with $a_1 = 0.05$ and $a_2 = 0.95$. The strong-motion data used for the development of the GMPEs is summarized below each $\mathcal{g}(\mathbf{X}, \hat{\boldsymbol{\alpha}})$

Author(s)	$\mathcal{g}(\mathbf{X}, \hat{\boldsymbol{\alpha}})$
4. Yaghmaei et al. ⁵⁸	$0.21 + [-0.473 + 0.31 \log(R)]^{1.24} + 0.097M_w^{1.2} - 0.052S,$ <p>where S is equal to 3, 2, 1, or 0 depending on whether the site is categorized as Class B, C, D, or E, respectively, following the FEMA 450.⁵⁹ The logarithm base 10 of D_{Sr} was used rather than the natural logarithm of D_{Sr}.</p> <p>Strong-motion data: 286 ground-motion recordings (each with two horizontal accelerograms) from shallow-crustal earthquakes occurred in Iran up to the year 2007, with M_w ranging from 3.7 to 7.7 and R ranging from 0.6 km to 294 km. The geometric mean of the values of D_{Sr} computed from the horizontal accelerograms of each ground-motion recording was considered to develop the GMPE. The ground-motion recordings were obtained from the Building and Housing National Research Center (HBRC) database operated by the Iranian Ministry of Housing Utilities and Urban Development.⁶⁰</p>
5. Lee and Green ⁶¹	$\ln\{2.5 + 4.21 \exp(M_w - 6) + 0.14R_{rup} + [-0.98 - 0.45(M_w - 6) - 0.0071R_{rup}]S\}$ <p>and</p> $\ln\{1.5 + 3.22 \exp(M_w - 6) + 0.11R_{rup} + [2.01 + 0.80(M_w - 6) - 0.0097R_{rup}]S\},$ <p>where S is a binary number equal to zero for “rock” sites and equal to 1 for “soil” sites. The first $\mathcal{g}(\mathbf{X}, \hat{\boldsymbol{\alpha}})$ is for shallow-crustal earthquakes in stable continental regions, whereas the second is for shallow-crustal earthquakes in active tectonic regions.</p> <p>Strong-motion data: For the first GMPE, 324 ground-motion recordings (each with three accelerograms) from 49 shallow-crustal earthquakes in active tectonic regions with M_w ranging from 5.0 to 7.6. For the second GMPE, 28 accelerograms from shallow-crustal earthquakes in stable continental tectonic regions and 592 scaled accelerograms from shallow-crustal earthquakes in active tectonic regions with M_w varying from 4.5 to 7.6 and R_{rup} varying from 0.1 km to 199.1 km. The D_{Sr} values from the horizontal accelerograms were considered to develop the GMPEs.</p>

Table 2.1 Estimated functions $\mathcal{g}(\mathbf{X}, \hat{\alpha})$ of nine GMPEs reported in the literature from 2006 to 2021 for the natural logarithm of D_{Sr} , with $a_1 = 0.05$ and $a_2 = 0.95$. The strong-motion data used for the development of the GMPEs is summarized below each $\mathcal{g}(\mathbf{X}, \hat{\alpha})$

Author(s)	$\mathcal{g}(\mathbf{X}, \hat{\alpha})$
6. Afshari and Stewart ⁶²	$\ln[g(M_w) + \mathcal{g}(R_{rup})] + \mathcal{g}(\overline{v_{s30}}),$ <p>where $\mathcal{g}(M_w)$ and $\mathcal{g}(R_{rup})$ are functions of source and path durations, respectively, and $\mathcal{g}(\overline{v_{s30}})$ is a site term.</p> <p>Strong-motion data: 11,195 ground-motion recordings (each with two horizontal accelerograms) from worldwide shallow-crustal earthquakes in active tectonic regions with M_w ranging from 3.0 to 7.9. The ground motions were recorded at R_{rup} up to 500 km. The geometric mean of the values of D_{Sr} obtained from the horizontal accelerograms of each ground-motion recording was considered to develop the GMPE. The ground-motion recordings were obtained from the PEER NGA-West2 database.⁵⁶</p>
7. Du and Wang ⁶³	$1.736 + \mathcal{g}(M_w, R_{rup}) - 0.242 \ln(\overline{v_{s30}}) + 0.007 H_{top},$ <p>where $\mathcal{g}(M_w, R_{rup})$ is a function of M_w and R_{rup}.</p> <p>Strong-motion dataset: 13,958 ground-motion recordings (each having three horizontal accelerograms) from 311 shallow-crustal earthquakes in active tectonic regions with M_w between 3.05 and 7.9. The ground motions were recorded at R_{rup} from 0.1 km to 499.54 km. The ground-motion recordings were obtained from the PEER NGA-West2 database.⁵⁶</p>
8. Meimandi-Parizi et al. ⁶⁴	$2.846 + \mathcal{g}(M_w, R_{rup}) - 0.179 \ln(\overline{v_{s30}}) + 0.027 F,$ <p>where $\mathcal{g}(M_w, R_{rup})$ is a function of M_w and R_{rup}, and F categorizes the earthquakes based on the fault rake, ι. Thus, F is equal to 1 if $-30 \leq \iota \leq 30$, to 2 if $-150 \leq \iota \leq -30$, and to 3 if $30 \leq \iota \leq 150$.</p> <p>Strong-motion dataset: 2,228 ground-motion recordings (each having three horizontal accelerograms) from 749 earthquakes with M_w varying between 4.5 and 7.6. The ground motions were recorded at various sites located in Iran at R_{rup} up to 200 km. The sites had values of $\overline{v_{s30}}$ from 100 m/s to 2500 m/s. The method proposed by Boore et al.⁶⁵ was used to compute the maximum D_{Sr} from the horizontal accelerograms. The ground-motion recordings were obtained from the HBRC database.⁶⁰</p>

Table 2.1 Estimated functions $\mathcal{g}(\mathbf{X}, \hat{\boldsymbol{\alpha}})$ of nine GMPEs reported in the literature from 2006 to 2021 for the natural logarithm of D_{Sr} , with $a_1 = 0.05$ and $a_2 = 0.95$. The strong-motion data used for the development of the GMPEs is summarized below each $\mathcal{g}(\mathbf{X}, \hat{\boldsymbol{\alpha}})$

Author(s)	$\mathcal{g}(\mathbf{X}, \hat{\boldsymbol{\alpha}})$
9. Jaimes and García-Soto ⁶⁶	$-1.4768 + 0.0147M_w + 0.9258 \ln(\sqrt{R^2 + 0.0075 \cdot 10^{0.507M_w}})$ and $-1.9163 + 0.0979M_w + 0.9219 \ln(\sqrt{R^2 + 0.0075 \cdot 10^{0.507M_w}}) - 0.0070[\min(H_h, 75) - 50],$
	<p>where H_h is the focal depth. Here, $R = R_{rup}$ for earthquakes with $M_w > 6.5$ and $R = R_{hypo}$ for other earthquakes. The first $\mathcal{g}(\mathbf{X}, \hat{\boldsymbol{\alpha}})$ is for intraplate earthquakes, and the second is for intraslab earthquakes.</p> <p>Strong-motion dataset: For the first GMPE, 209 ground-motion recordings (each with two horizontal accelerograms) from 40 interplate earthquakes with M_w ranging from 5.0 to 8.0 and at R varying from 17 km to 400 km. For the second GMPE, 183 ground-motion recordings (each with two horizontal accelerograms) from 23 intraslab earthquakes with M_w ranging from 5.2 to 8.2. All ground motions were recorded at free-field ground-motion recording stations located in states of Mexico called Chiapas, Guerrero, Oaxaca, and Michoacán at R varying from 22 km to 400 km. The sites were categorized as Class B following the FEMA 450.⁵⁹ The quadratic mean of the values of D_{Sr} from the horizontal accelerograms of each ground-motion recording was considered to develop the GMPE. The ground-motion recordings were obtained from the database provided by the II-UNAM accelerograph network.⁶⁷</p>

Finally, the work of Alcántara et al.⁶⁸ was also found in the literature. Similar to the authors cited in Table 2.2, they developed a GMPE for the natural logarithm of D_{Sr} , with $a_1 = 0.05$ and $a_2 = 0.95$, but they used *artificial neural networks* (ANNs) rather than mixed-effects models for this purpose. In broad terms, an ANN is an adaptive system that learns by using interconnected nodes (also called neurons) in a layered structure that resembles a human brain. It can be trained to recognize patterns, classify data, and forecast future events.⁶⁹ Then, from the learning of strong-motion data, any form of $\mathcal{g}(\mathbf{X}, \boldsymbol{\alpha})$, such as those given in Table 2.1, can be approximated. The estimated function $\mathcal{g}(\mathbf{X}, \hat{\boldsymbol{\alpha}})$ developed by Alcántara et al.⁶⁸ was not reported in their work. Nevertheless, they presented scatter plots of the estimated values of D_{Sr} versus the empirical data. The accelerograms used by Alcántara et al.⁶⁸ came from ground motions caused by interplate and intraslab

earthquakes with M_w varying between 4.1 and 8.1 that occurred at $R_{epi} \geq 300$ km and were recorded in sites mainly characterized by rock located in Puebla and Oaxaca, which are states of Mexico.

2.4 Correlation Between Strong-motion Duration and Other Ground-motion Parameters

Many researchers have measured the dependence between ground-motion parameters.⁷⁰⁻⁷⁴ The *Pearson correlation coefficient*, ρ , which measures the linear correlation between two random variables, has been used by the cited for this purpose. Note that the sample version of ρ can be defined as:

$$\hat{\rho} = \frac{\sum_{j=1}^n (y_{1j} - \bar{Y}_1)(y_{2j} - \bar{Y}_2)}{\sqrt{\sum_{j=1}^n (y_{1j} - \bar{Y}_1)^2 \sum_{j=1}^n (y_{2j} - \bar{Y}_2)^2}} \quad (2.16)$$

where $\{(y_{1_1}, y_{2_1}), \dots, (y_{1_n}, y_{2_n})\}$ is a sample of n observations from a vector of continuous random variables (Y_1, Y_2) , which in this instance are two ground-motion parameters, $\bar{Y}_1 = \frac{1}{n} \sum_{j=1}^n y_{1j}$ and $\bar{Y}_2 = \frac{1}{n} \sum_{j=1}^n y_{2j}$ are the sample means of Y_1 and Y_2 , respectively. As per Eq. (2.16), $\hat{\rho}$ is the ratio between the covariance of two random variables and the product of their standard deviations; thus, it is essentially a normalized measurement of the covariance, such that the result always has a value between -1 and 1.⁴²

It has become common practice to obtain the estimates of ρ between the (normalized) residuals computed as part of the development of the GMPEs for the pair of ground-motion parameters of interest rather than directly from the observations of such ground-motion parameters. Notice that, for each ground-motion parameter, the *normalized residuals* are defined as

$$\hat{\delta} = \frac{\hat{e}}{\hat{\sigma}} \quad (2.17)$$

where $\hat{e} = \mathbf{y} - \hat{\mathbf{y}}$ is the vector of residuals that predict \mathbf{e} and $\hat{\sigma}$ is the estimate of σ computed from the regression analysis. The aforementioned procedure for estimating ρ was first introduced in the research work of Baker and Cornell,⁷⁵ who focused on measuring the dependence between pairs of acceleration response-spectral ordinates. Among other things (and in general terms), they argued that the estimated value of ρ between Y_1 and Y_2 is equal to the estimated value of ρ between the normalized

residuals, δ_1 and δ_2 , computed as part of the development of the GMPEs for Y_1 and Y_2 because they are related simply by a linear function —see Eq.(2.17)—.

Thus, of all the reviewed literature, the research works of Bradley,⁷⁶ Baker and Bradley,⁷⁷ and Harati et al.⁷³ are the only ones that focused the attention on measuring the dependence between the strong-motion duration and other ground-motion parameters. The first researchers used the procedure proposed by Baker and Cornell.⁷⁵ In particular, Bradley⁷⁶ reported the estimates of ρ between the natural logarithm of D_{Sr} , considering $a_1 = 0.05$ and a_2 equal to 0.75 and 0.95, and the natural logarithm of seven ground-motion parameters that include PGA , PGV , amplitudes of a response spectrum at various values of T_e , and the cumulative absolute velocity, CAV . The latter is defined as:

$$CAD = \int |\dot{u}_g(t)| dt \quad (2.18)$$

Bradley⁷⁶ obtained the observations of the ground-motion parameters from 1842 ground-motion recordings from active shallow-crustal earthquakes that occurred at source-to-site distances up to 200 km (obtained from the PEER NGA database⁵⁶). and to estimate the elements of $\hat{\delta}$ they used GMPEs proposed by various researchers applicable to said tectonic environment. In the case of D_{Sr} , the GMPE developed by Bommer et al.⁵³ (given in Table 2.1) was used. The estimates of ρ reported by Bradley⁷⁶ indicated that the natural logarithm of D_{Sr} is negatively correlated with the natural logarithm of PGA and PGV . He rereported negative estimates of ρ between the natural logarithms of D_{Sr} and the acceleration response-spectral ordinates for values of T_e up to approximately 1 s, but positive estimates of ρ for values of T_e varying from approximately 1 s to 10 s. For this case, the estimated values of ρ varied from approximately -0.5 to 0.4. Regarding the estimates of ρ between the natural logarithms of D_{Sr} and CAV , they were positive and up to approximately 0.15.

For their part, Baker and Bradley⁷⁷ reported estimates of ρ between D_{Sr} (considering $a_1 = 0.05$ and a_2 equal to 0.75 and 0.95) and acceleration response spectral-ordinates. They obtained the observations of the ground-motion parameters from ground-motion recordings provided in the PEER NGA-West2 database⁵⁶ and associated with shallow crustal earthquakes with $M > 5$ that occurred at $R < 100$ km. Baker and Bradley⁷⁷ obtained the elements of $\hat{\delta}$ using GMPEs proposed by various researchers, within which the GMPE for D_{Sr} developed by Afshari and Stewart⁶² (given in Table 2.1) was selected. Similar to Bradley,⁷⁶ they reported

negative estimates of ρ between D_{Sr} and acceleration response-spectral ordinates, except for values of T_e varying from approximately 1 s to 10 s.

Finally, Harati et al.⁷³ measure the dependence between D_{Sr} , with $a_1 = 0.05$ and $a_2 = 0.75$, and PGA , PGV , acceleration response spectral-ordinates, and CAV using Eq. (2.16). In absence of a robust strong-motion database, $\{(y_{1_1}, y_{2_1}), \dots, (y_{1_n}, y_{2_n})\}$ was obtained using a Monte Carlo simulation. Note that an unknown quantity can be approximately computed using a Monte Carlo simulation, whereby independent replications of a random experiment (usually on a computer) are averaged to estimate the quantity.⁴² Thus, Harati et al.⁷³ carried out Monte Carlo simulations considering different possible earthquake scenarios. Broadly speaking, one case consisted in simulating ground motions caused by earthquakes having different miscellaneous characteristics (e.g., having distinct focal mechanisms and occurring at a different source-to-site distance). A second case consisted in simulating ground motions at a specific site caused by earthquakes with distinct M_w , but caused by the same tectonic environment. A third case consisted in simulating the ground motions at different sites caused by the same earthquake. It should be mentioned that the ground-motion parameters were computed by existing GMPEs, within which the GMPE for D_{Sr} proposed by Afshari and Stewart⁶² (given in Table 2.1) was considered. Depending on the simulation case, the values of M_w were sampled between 4 and 8, the values of R_{rup} between 5 km and 100 km, and the values of $\overline{v_{s30}}$ between 100 m/s and 1000 m/s. For the first two simulation cases, the results reported by Harati et al.⁷³ indicated that D_{Sr} is positively correlated with either PGA , PGV , the acceleration response-spectral ordinates, or CAV . For the third simulation case, the estimates of ρ between D_{Sr} and the acceleration response-spectral ordinates resulted in negative values.

2.5 Influence of Strong-motion Duration on Structural Response

Over the last decades, several researchers have studied the influence of the strong-motion duration on the seismic response of soils and civil structures. On the one hand, the effects of the strong-motion duration on soil behavior have been fairly well identified, causing some methodologies to consider this ground-motion parameter for the solution of multiple geotechnical engineering problems.^{78–81} For instance, the seismic demand on potentially liquefiable soils can be approximated by a series of uniform shear stress cycles, N_{SC} . The number of N_{SC} can be estimated by GMPEs.⁸⁰ By contrast, the effects of the strong-motion duration on structural response remain a matter of discussion. The latter arises from the fact that structural response is demarked not only by the inherent characteristics of the seismic loads but by many

diverse parameters that typify the elements of each structural system. In other words, the effects of strong-motion duration will (obviously) differ for different civil structures. In general, it can be said that the effects of the strong-motion duration on structural response may be more evident in masonry or reinforced concrete buildings (whose stiffness and strength degrade under the action of seismic loadings) than in steel buildings.⁵³ Regardless of the structural system analyzed, it can be said that the significance attributed to the strong-motion duration relies mainly on the damage measure used to evaluate their performance. For instance, Hancock and Bommer⁸² reviewed a large number of studies on this matter. They concluded that while the strong-motion duration has a negligible effect on the estimates of maximum-response damage measures, it has a significant effect on the estimates of energy-based damage measures.

Many researchers have studied the effects of the strong-motion duration caused by distinct tectonic environments in structural response. In the literature, those ground motions generated by subduction (either interplate or intraslab) earthquakes have been referred to as long-lasting, whereas those generated by shallow-crustal earthquakes have been denominated as short-lasting. Appendix A summarizes the strong-motion data used by various researchers that have studied the influence of the strong-motion duration on structural response. The structural systems analyzed are also reported in Appendix A. They comprise mostly buildings or idealizations of them through SDOF or multiple-degree-of-freedom (MDOF) systems. All the researchers evaluated the structural response through NDAs, and some of them developed fragility functions. Those researchers cited in Appendix A that compared the effects of short-lasting ground motions against long-lasting ground motions in the structural response concluded that long-lasting ground motions tended to produce larger estimates of energy-based damage measures and some of them reported an increase in the estimates of certain maximum-response damage measures when large spectral ordinates were involved.

As can be noticed from the information given in Appendix A, the local site conditions, as well as other seismological parameters, were disregarded in the majority of the cited studies. Specifically, except for the studies carried out by Chandramohan et al.⁸³ and Ruíz-García,⁸⁴ no attention was paid to ensure that the selected accelerograms used to perform the NDAs were recorded in sites with similar local site conditions as those where the analyzed structural systems were located. It should be recognized that this omission was somehow avoided in some of these studies as the accelerograms employed were scaled in such a way that their response spectra matched a site-specific target spectrum.

2.6 Discussion

Several methods to estimate the strong-motion duration are found in the literature, which in turn lead to many definitions. Of these, D_{Sr} has been preferred for engineering purposes because it preserves all the information of an accelerogram without excluding any interval.⁶⁶

Not many strong-motion duration GMPEs have been reported in the literature. The most recent have been developed using strong-motion data from shallow-crustal earthquakes, which are out of the scope of this dissertation. Alcántara et al.,⁶⁸ Jaimes and García-Soto,⁶⁶ and Reinoso and Ordaz⁴⁸ are the only researchers who have proposed GMPEs considering accelerograms of ground motions caused by interplate earthquakes and recorded at $R_{rup} \geq 250$ km. Nevertheless, the GMPEs proposed by Alcántara et al.⁶⁸ and Jaimes and García-Soto⁶⁶ were generated using ground-motion recordings from sites characterized mostly by rock or firm soil sites located in various states of Mexico, of which Mexico City was omitted. Therefore, discretion is advised in using such GMPEs to estimate the strong-motion duration in sites located in Mexico City. Likewise, discretion is advised when using the GMPE proposed by Reinoso and Ordaz⁴⁸ because, although they used (not many) accelerograms recorded in Mexico City, no distinction between focal mechanisms and no correlation between ground motions caused by the same earthquake were considered for the development of the GMPE. Furthermore, fellow researchers have commented about the overestimation of the strong-motion duration in sites located in Mexico City when employing the GMPE proposed by Reinoso and Ordaz.⁴⁸ For instance, when computing response spectra with random vibration theory, Jaimes et al.⁸⁵ applied a factor of 0.5 to the estimated values, arguing that “they were too long”.

From the estimated functions $(\mathbf{X}, \hat{\alpha})$ reported by various researchers that have developed GMPEs for the strong-motion duration (such as those given in Table 2.1), it can be concluded that such ground-motion parameter increases as both the earthquake magnitude and source-to-site distance increase when is defined as D_{Sr} , but when is defined as either D_B or D_U it has been demonstrated that it decreases as the source-to-site distance increases.^{53,54}

Three research works were found in the literature on the measurement of the dependence between the strong-motion duration and other ground motion parameters. In all of them, the dependence was measured by means of ρ . At the end, with the reported estimates of ρ , it is not possible to give a clear idea of what might be expected in Mexico City because they were obtained from strong-motion data associated with shallow-crustal earthquakes.

As mentioned in Section 2.4, nowadays (many) researchers obtain the estimates of ρ between the vectors $\hat{\delta}$ of normalized residuals computed as part of the development of GMPEs for pairs of ground-motion parameters of interest, such as D_{Sr} and another ground-motion parameter (e.g., PGA , PGV , CAV , or acceleration response-spectral ordinates) rather than from the vectors \mathbf{y} of observations of such ground-motion parameters. Although the author has followed such procedure to measure the dependence between ground-motion parameters,⁷⁴ she has reasoned that the argument that has been made since the research work of Baker and Cornell⁷⁵ (see page 22) is not entirely true. As Lebrun and Dutfoy⁸⁶ have stated, the estimated value of ρ between two random variables, Y_1 and Y_2 , is not equal to the estimated value of ρ between another two random variables, Z_1 and Z_2 , that are in function of Y_1 and Y_2 , i.e., $Z_1 = \mathcal{g}(Y_1)$ and $Z_2 = \mathcal{g}(Y_2)$, if the functions are strictly increasing.

Concerning the influence of the strong-motion duration on structural response, attention was focused on summarizing the number and characteristics of the accelerograms used by various researchers to perform NDAs (see Appendix A) rather than making a report on the measured values of the structural response. In the humble opinion of the author, such values could not be representative of the seismic response of structures located in Mexico City because they were estimated from accelerograms of ground motions that do not match those observed in the geographical region of interest.

Moreover, although comparing the seismic response of a structural system subjected to ground motions of different durations is quite beneficial, the comparisons carried out by several researchers (such as those cited in Appendix A) lose sense due to the criteria considered to group the ground motions into short- and long-lasting. For instance, based on the work of Chandramohan et al.,⁸⁷ Barbosa et al.,⁸⁸ Belejo et al.,⁸⁹ Bravo-Haro and Elghazouli,⁹⁰ and many other researchers had classified as long-lasting those ground-motion recordings having at least one accelerogram with $D_{Sr} > 25$ s. Doing this kind of classification is highly subjective. Indeed, the ground-motion duration caused by a single earthquake can be so different at different sites as to classify it as short or long. For instance, Figure 2.4 shows a glimpse of the seismic response of the soil in Mexico City. It shows two accelerograms recorded during the same earthquake at two sites located in Mexico City within a radius of less than approximately 5 km. As can be appreciated from Figure 2.4, the accelerograms had t_f equal to approximately 150 s and 300 s. Then, it could be said that while one ground motion was short-lasting, the other was long-lasting. Therefore, care must be taken when selecting and grouping the accelerograms for the evaluation of the structural response.

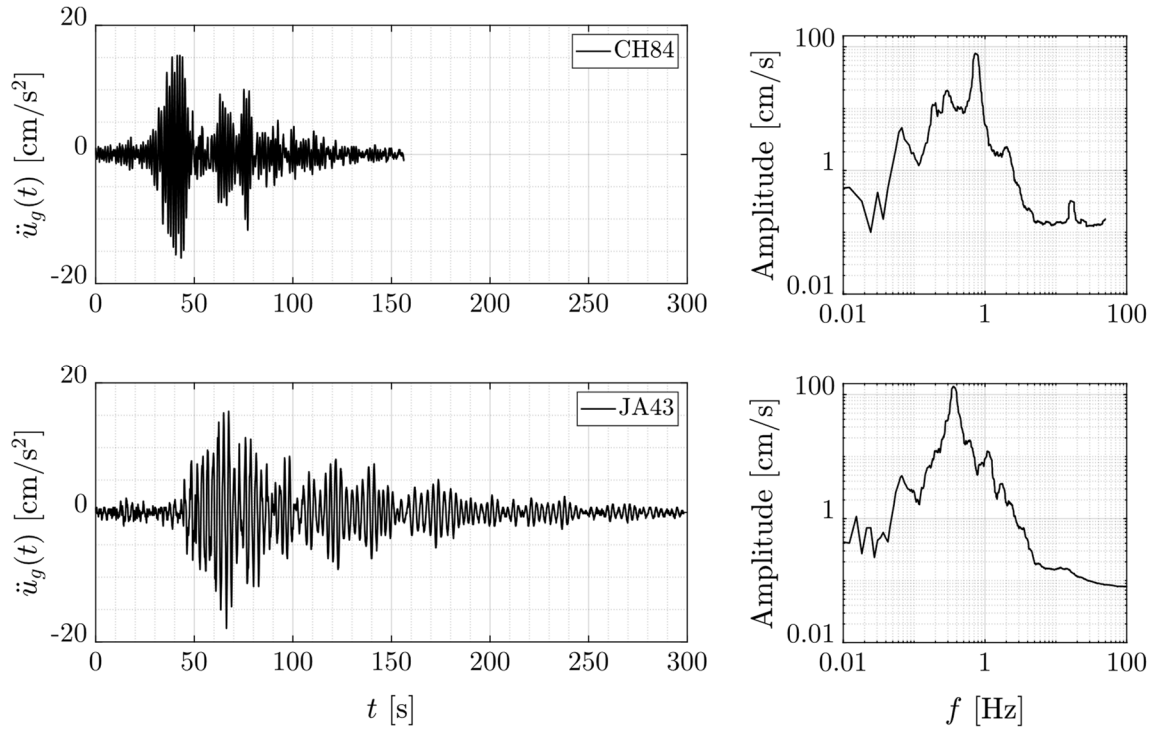


Figure 2.4 Accelerograms recorded at the stations CH84 and JA43 during the January 22, 2003 earthquake that occurred in Colima, Mexico. These stations are located at two different sites in Mexico City, each with T_s equal to approximately 1.4 s and 3.0 s. On the right of each accelerogram is shown its correspondent FAS

CHAPTER 3

Strong-motion Duration Predictive Equations

3.1 Introduction

As mentioned in Section 1.1, GMPEs play an important role in SHAs as they allow to estimate the ground-motion levels y that can occur at a site of interest and, therefore, to which an earthquake-resistant structure will be subjected. In this study, the GMPEs were developed using *linear mixed-effects (LME) models*, which are a class of statistical models containing both *fixed effects* and *random effects*. The former are parameters associated with an entire population or with certain repeatable levels of experimental factors and the latter are parameters associated with individual experimental units drawn at random from a population.⁴⁹ In the LME models both fixed and random effects occur linearly in the model function.

In principle, an LME model allows for describing the relationship between a response variable and some covariates in data that are grouped according to one or more classification factors.⁴⁹ For a single level of grouping, the LME model can be expressed in matrix notation as follows⁹¹:

$$\mathbf{y}_i = \mathbf{X}_i \boldsymbol{\alpha} + \mathbf{Z}_i \mathbf{b}_i + \mathbf{e}_i \quad i = 1, \dots, N_C \quad (3.1)$$

where \mathbf{y}_i is an $n_i \times 1$ vector of responses of the i th cluster, $\boldsymbol{\alpha}$ is a $p \times 1$ vector of fixed effects, \mathbf{b}_i is a $q \times 1$ vector of random effects, \mathbf{X}_i is an $n_i \times p$ design matrix of fixed effects, \mathbf{Z}_i is an $n_i \times q$ design matrix of random effects, and \mathbf{e}_i is an $n_i \times 1$ error vector with independent components, each of them having zero mean and variance σ^2 .

It is assumed that \mathbf{b}_i and \mathbf{e}_i are normally distributed with a mean of $\mathbf{0}$ and variance-covariance and variance matrices $\boldsymbol{\sigma}_b^2 = \sigma^2 \boldsymbol{\Upsilon}$ and $\boldsymbol{\sigma}_w^2 = \sigma^2 \mathbf{I}$, respectively, where $\boldsymbol{\Upsilon}$ is a symmetric and positive semi-definite matrix parameterized by a variance component vector $\boldsymbol{\vartheta}$ and \mathbf{I} is an identity matrix. Also, the random effects vectors \mathbf{b}_i are assumed to be independent of each other and of the error vectors \mathbf{e}_i .^{49,92} Note that, as \mathbf{b}_i are defined to have a mean of $\mathbf{0}$, any nonzero mean for a term in the random effects must be expressed as part of the fixed-effects terms. Thus, the columns of \mathbf{Z}_i are usually a subset of the columns of \mathbf{X}_i .

By combining vectors \mathbf{y}_i into a $\sum n_i$ vector, matrices \mathbf{X}_i into a $\sum n_i \times p$ matrix, letting $\mathbf{Z} = \text{diag}(\mathbf{Z}_1, \dots, \mathbf{Z}_{N_c})$, Eq. (3.1) can be compressed into one equation as $\mathbf{y} = \mathbf{X}\boldsymbol{\alpha} + \mathbf{Z}\mathbf{b} + \mathbf{e}$. Notice that $\sum n_i$ is the total number of observations, with $j = 1, \dots, n_i$ observations per cluster i . Also note that, if the random effects were disregarded, the compressed form of the regression model given in Eq. (3.1) would be $\mathbf{y} = \mathbf{X}\boldsymbol{\alpha} + \mathbf{e}$, which is equivalent to the generic regression model given in Eq. (2.12) considering that the form of $\mathcal{g}(\mathbf{X}, \boldsymbol{\alpha})$ is linear. Recall that the linearity in mixed-effects models refers to the linearity of the terms of $\boldsymbol{\alpha}$.

Although the LME model given in Eq. (3.1) looks like a linear model, the fact that the variance parameters are unknown makes it a nonlinear statistical model with an elaborated estimation methodology. Under the assumption that \mathbf{b}_i and \mathbf{e}_i are normally distributed random variables, Eq. (3.1) can be written more compactly as⁹²:

$$\mathbf{y}_i \sim \mathcal{N}(\mathbf{X}_i\boldsymbol{\alpha}, \sigma^2 \mathbf{Z}_i \mathbf{D} \mathbf{Z}_i') \quad i = 1, \dots, N_c \quad (3.2)$$

meaning that \mathbf{y}_i has a multivariate normal distribution with mean $\mathbf{X}_i\boldsymbol{\alpha}$ and covariance matrix $\sigma^2(\mathbf{Z}_i \mathbf{D} \mathbf{Z}_i')$, where \mathbf{Z}_i' is the transpose of the design matrix \mathbf{Z}_i . Note that a multivariate normal distribution is a probability distribution for random vectors of correlated variables where each vector element has a univariate normal distribution.⁹³

Inference of an LME model can be based on least squares and maximum likelihood methods, or empirical Bayes methodology.⁹¹ For instance, if \mathbf{D} were known, as follows from the Gauss-Markov theorem, the following generalized least squares estimator would be efficient:

$$\hat{\boldsymbol{\alpha}} = \left[\sum_{i=1}^{N_c} \mathbf{X}_i' (\mathbf{I} + \mathbf{Z}_i \mathbf{D} \mathbf{Z}_i')^{-1} \mathbf{X}_i \right]^{-1} \sum_{i=1}^{N_c} \mathbf{X}_i' (\mathbf{I} + \mathbf{Z}_i \mathbf{D} \mathbf{Z}_i')^{-1} \mathbf{y}_i \quad (3.3)$$

However, \mathbf{D} is unknown, thus its estimation becomes a central issue in the framework of the LME models. In this study, the maximum likelihood estimation (MLE) method was used to estimate both fixed-effects coefficients $\boldsymbol{\alpha}$ and variance components σ^2 and $\boldsymbol{\vartheta}$. A detailed description of the procedure can be found in the work of Pinheiro and Bates.⁴⁹

Thus, the next section describes the seismological parameters used to define \mathbf{X} and \mathbf{Z} for the development of the strong-motion duration GMPEs for Mexico City. The criteria used to compute the strong-motion duration vector of responses \mathbf{y} are given then in Section 3.3. In this section, four of the GMPEs developed in this

study are presented. The observed trends between strong-motion duration and the seismological parameters are also given in this section. Some comments about the proposed GMPEs are given in Section 3.4.

3.2 Seismological Parameters

As mentioned in Section 1.1, seismological parameters are those that characterize the earthquake source, the soil and geological profile beneath a site of interest, and the wave propagation path between the source and the site.¹⁰ The more accurate their estimation, the greater the potential of reducing the level of uncertainty in the expected level of ground motion at the site.

The seismological parameters used to define \mathbf{X} and \mathbf{Z} for the development of the strong-motion duration GMPEs are presented next.

3.2.1 Earthquake Source Parameters

Mexico is located at the intersection of five plates, which are: (a) the North American and Pacific major plates, (b) the Caribbean and Cocos minor plates, and (c) the Rivera microplate.⁹⁴ Figure 3.1 illustrates these plates, along with the mid-oceanic ridges, and trenches that span Mexican territory. In Figure 3.1, the East Pacific Rise is a divergent plate boundary that separates the oceanic Pacific Plate from the continental North American Plate and the oceanic Rivera and Cocos plates. The Middle America Trench (MAT) is the boundary between the Rivera and Cocos plates on one side and the North American and Caribbean plates on the other. It extends as far as northern Costa Rica, in Central America. The Trans-Mexican Volcanic Belt (TMVB) is an active continental volcanic arc that spans across south-central Mexico from the Pacific Ocean to the Gulf of Mexico. It was formed due to the subduction of the Rivera and Cocos plates beneath the North American Plate along the northern part of the MAT.^{95,96} While the Rivera Plate moves to the northeast with respect to the Rivera and North American plate boundary, the motion of the Cocos Plate relative to the North American Plate is also to the northeast, slightly counterclockwise from the normal to the MAT.⁹⁷

Figure 3.1 also shows the geographical localization of Mexico City, which is the capital of Mexico. One of the largest metropolises in North America is located there. Mexico City is principally exposed to the seismic hazard caused by very frequent interplate earthquakes occurring at the MAT and intraslab earthquakes occurring within the subducted Cocos Plate, as well as infrequent shallow-crustal earthquakes occurring in the TMVB.⁹⁸ In general, large thrust faulting interplate

earthquakes occur at shallow depths, whereas intraslab normal faulting earthquakes in the subducted Cocos Plate generally occur down-dip at some distance from the strongly coupled interplate interface.⁹⁹ This dipping planar (flat) zone of earthquakes is known as the *Wadati-Benioff zone*.⁹⁴

As mentioned in Section 2.3, GMPE developers commonly introduce as part of the set X_1, \dots, X_p a seismological parameter to define either the earthquake tectonic environment or focal mechanism. This is very important (at least for Mexico City) because the seismic response of various sites, and consequently of structures, can differ greatly depending on the tectonic setting that originates the ground motions.^{84,100,101} For instance, intraslab earthquakes tend to affect low-rise structures because they are shown to have larger energy content at higher frequencies.^{100,102} On the contrary, interplate earthquakes commonly affect long-period structures as they have lower-frequency contents.^{103,104} Shallow-crustal earthquakes that occur within the TMVB are not known to produce significant damage in Mexico City.¹⁰⁴ Nevertheless, as this study extends up to the evaluation of the strong-motion duration hazard caused only by interplate earthquakes, there is no need to define any source parameters for the development of the GMPEs.

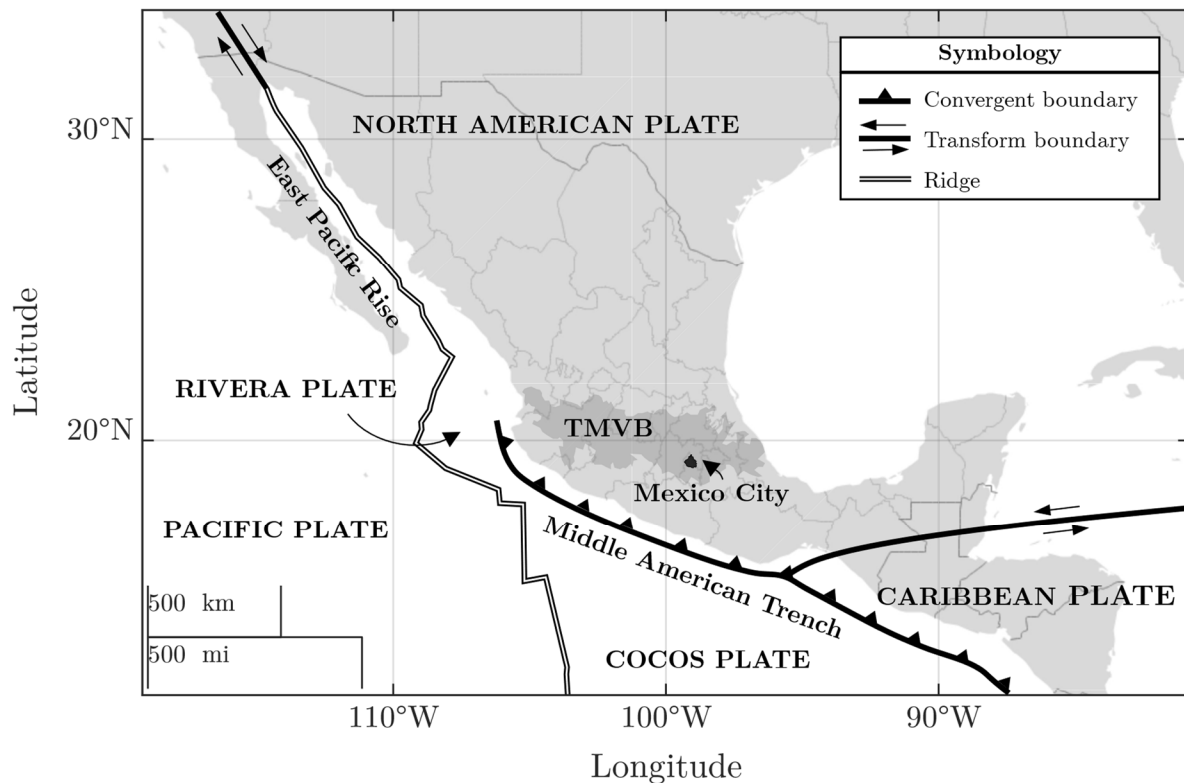


Figure 3.1 Plates, mid-oceanic ridges, and trenches encompassing the Mexican territory. The acronym TMVB stands for Trans-Mexican Volcanic Belt

The identification of interplate earthquakes that have occurred along the MAT was possible due to the catalogs provided by the Global Centroid Moment Tensor (CMT) Project,^{105,106} the International Seismological Centre (ISC),¹⁰⁷ and the National Earthquake Information Center (NEIC) from the U.S. Geological Survey.¹⁰⁸ The research works of Singh et al.¹⁰⁹ and Zúñiga et al.¹¹⁰ were also consulted. The search was focused on moderate and large earthquakes. To evaluate their size, M_w was chosen among other conventional magnitude scales because it does not “saturate” for large earthquakes.¹¹¹ Note that saturation occurs when the fault dimension greatly exceeds the wavelength of the seismic waves to which a particular scale is keyed. In the end, all earthquakes in the compiled catalog have $M_w \leq 6$. This level of M_w was chosen to consider all those earthquakes that can cause damage, however minimal, in Mexico City.¹¹² The compiled earthquake catalog is presented in Appendix B.

It is to be noted that many ground motions from historical earthquakes that occurred at the MAT were not recorded in Mexico City. In fact, early accelerograms were too short to accurately measure the strong-motion duration. Therefore, several of the interplate earthquakes presented in Appendix B were disregarded in the development of the strong-motion duration GMPEs. Those that were used are listed in Appendix C. These issues are discussed in more detail in Section 3.3.

3.2.2 Local Site Conditions

Most of the present-day Mexico City metropolitan area is contained in the Valley of Mexico, which is located on a volcanic high plateau in the central part of the TMVB. The valley is settled on very soft lacustrine deposits, which are the remnant of the ancient Zumpango, Xaltocan, San Cristóbal, Texcoco, Xochimilco, and Chalco lakes.¹¹³ Of these, only portions of the Zumpango, Xochimilco, and Texcoco lakes remain today.

Several efforts have been made over the years to gain information about the local site conditions in Mexico City, which are extremely heterogeneous.^{112,113} Traditionally, the city has been divided into three zones, each encompassing sites with similar geotechnical characteristics, namely, the *hill zone*, *transition zone*, and *lake zone*.^{27,113,114} On the west side of Mexico City, the hill zone is characterized by deposits of granular soil and volcanic tuffs, with interspersed sandy deposits in the loose or relatively soft cohesive state. The Pedregal area is located in southern Mexico City and is typified by basalt deposits with a maximum thickness of 20 m. Similarly, basalt deposits are found on the east side of Mexico City. On the other hand, the lake zone is characterized by highly compressible clay deposits separated

by sandy layers containing silt, clay, and volcano ash, and covered by alluvial soils, dried materials, and debris. The total thickness of these deposits can exceed 50 m in depth. The transition zone separates the hill zone from the lake zone. It is characterized by intercalated sandy layers on clay deposits, but with a thickness that varies from centimeters to a few meters. Hereafter, the hill, transition, and lake zones are referred to as GZI, GZII, and GZIII, respectively.

According to Singh et al.,⁹⁸ $\overline{v_{s30}}$ is approximately equal to 750 m/s and 250 m/s for sites located in GZI and GZII, respectively, and varies from 50 m/s to 100 m/s for sites located in GZIII.

Although the geotechnical classification described above depicts in practical terms the materials that lie directly beneath Mexico City, for the development of the GMPEs it is desirable to measure, rather than categorize, the local site conditions. For this, T_s was used.

Eighty-four reference sites in which free-field ground-motion recording stations are (or were) located were selected for the measurement of T_s . Specifically, 16 stations are located in GZI, 12 in GZII, and 56 in GZIII. Note that the stations are part of the accelerograph networks operated by the CIRES and II-UNAM.^{67,115} A list of them is given in Appendix D and a map showing their geographical localization is presented in Figure 3.2. As per Figure 3.2, the sites located in GZIII have been grouped into four subzones, namely, a, b, c, and d.

Following the NTC-2020,²⁷ T_s in sites located in GZI could be up to approximately 0.5 s. Yet, several regional studies of the Valley of Mexico have reported that ground motions recorded at the southwestern and northern hill zone stations, as well as at stations located at the outcrops of two mountains (named Cerro de la Estrella and Cerro del Peñón) are anomalous with respect to other sites located in the hill zone.^{104,116,117} The differences are attributed to local geologic and topographic conditions at the recording sites. Based on these statements, the ground motions recorded at stations CE18, CP28, CT64, and ESTS were disregarded for the development of the GMPEs. Figure 3.2. shows their geographical localization. A list of the stations disregarded in this study is presented in Appendix D.

For each site located in GZII or GZIII, the values of T_s were estimated as the inverse of the frequency $f_{H/V}$, which is defined as follows:

$$f_{H/V} = \sqrt{\frac{\left[\max \left(\frac{F_1(\omega)}{F_V(\omega)} \right) \right]^2 + \left[\max \left(\frac{F_2(\omega)}{F_V(\omega)} \right) \right]^2}{2}} \quad (3.4)$$

where $\max(\bullet)$ are the frequencies, f_{max} , associated with the maximum spectral ratios $F_1(\omega)/F_V(\omega)$ and $F_2(\omega)/F_V(\omega)$, with $F_1(\omega)$, $F_2(\omega)$, and $F_V(\omega)$, being the FAS of the orthogonal components $\ddot{u}_{g_1}(t)$, $\ddot{u}_{g_2}(t)$, and $\ddot{u}_{g_V}(t)$, respectively, of each ground-motion recording at the site. Here, ω is the *angular frequency* defined as $2\pi/f$.

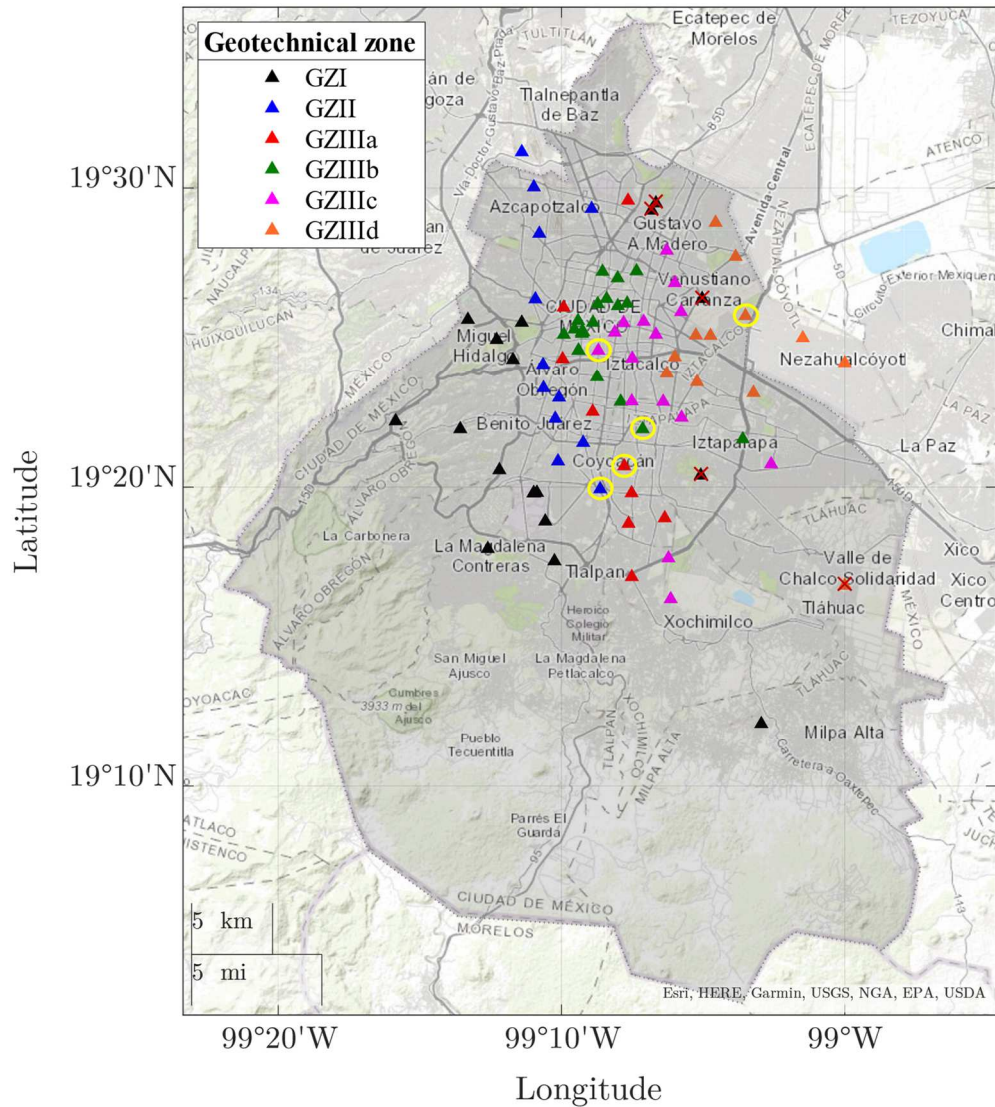


Figure 3.2 Map of Mexico City (shaded in gray) showing the location of the free-field ground-motion recording stations (triangles). Data from crossed-out stations was disregarded for the development of the strong-motion duration GMPEs. From north to south these are ESTS, CT64, CP28, CE18, and TH35. Stations marked with yellow circles are related to the examples shown in Table 3.1 and Figure 3.6. These are Station DX37 located in GZII, and stations IB22, SP51, BA49, and AE02 located in GZIIIa, GZIIIb, GZIIIc, and GZIIId, respectively

Note that, from a given $\ddot{u}_g(t)$, $F(\omega)$ can be computed as follows¹⁴:

$$F(\omega) = \sqrt{\left[\int_0^{t_f} \ddot{u}_g(t) \sin(\omega t) dt \right]^2 + \left[\int_0^{t_f} \ddot{u}_g(t) \cos(\omega t) dt \right]^2} \quad (3.5)$$

Equation (3.4) is based on the root mean square (RMS) formulation¹¹⁸ and it can be seen as a variation of the standard horizontal-to-vertical ratio as presented by Delgado et al.¹¹⁹

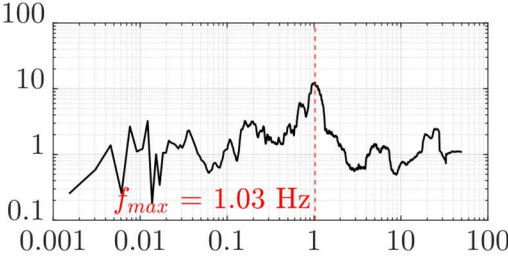
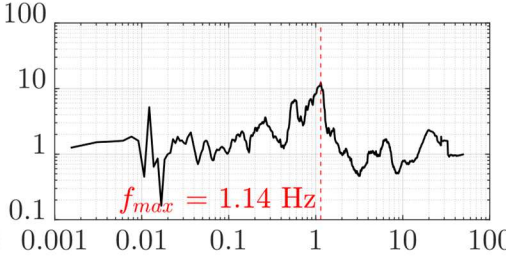
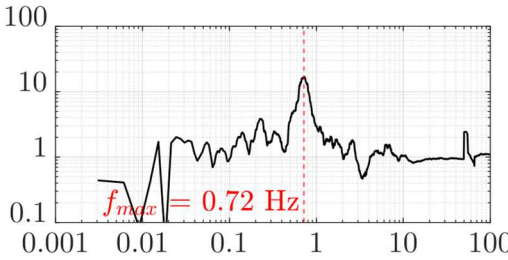
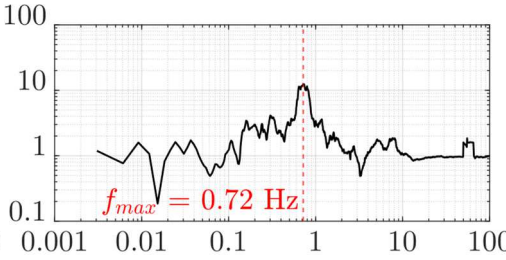
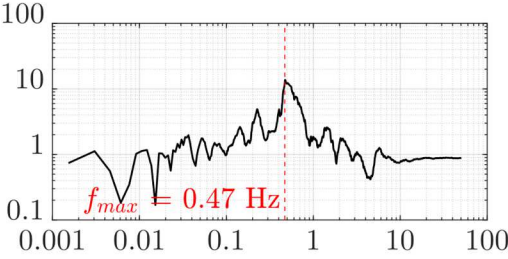
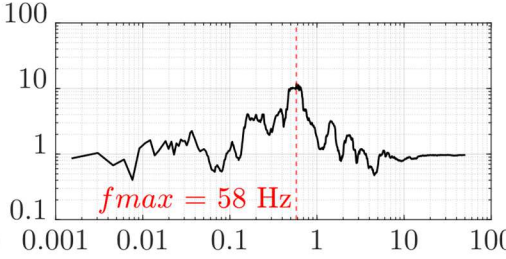
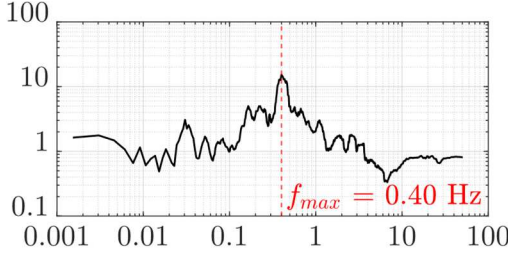
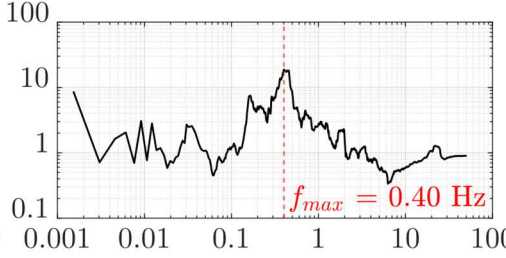
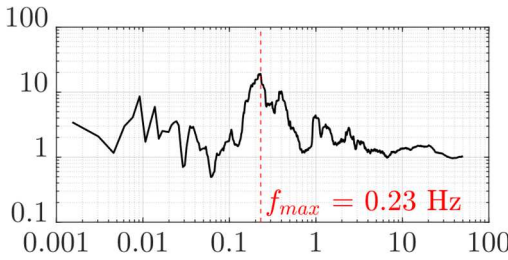
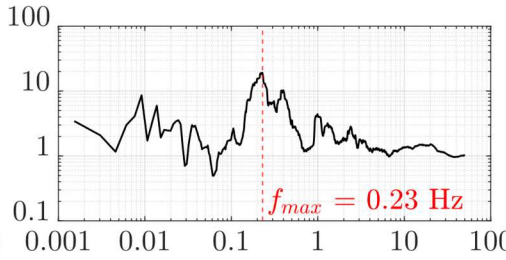
Based on Eq. (3.2), Table 3.1 shows the estimation of T_s from a set of ground motions recorded at five stations during the March 20, 2012 earthquake that occurred in Ometepec, Guerrero, and had $M_w = 7.4$. Each recording station is located in a different geotechnical zone. Specifically, station DX37 is located in GZII, and stations IB22, SP51, BA49, and AE02 in GZIIIa, GZIIIb, GZIIIc, and GZIIId, respectively. The sites are marked with yellow circles in Figure 3.2.

From the calculations, T_s vary from 0.4 s to 1.0 s for sites that are located in GZII and from 1.0 s to 1.5 s, 1.5 s to 2.5 s and 2.5 s to 3.5 s for sites that are located in GZIIIa, GZIIIb, and GZIIIc, respectively. The estimates of T_s were up to approximately 6.0 s for sites located in GZIIId. Specifically, the estimates of T_s from ground motions recorded at stations AE02, AR14, NZ20, NZ31, PD42, and ZARZ exhibited values of 5.5 s \pm 10%.

Overall, the estimates of T_s remained similar per site. Only values of T_s for some stations located in GZIIId exhibited a slight and constant decrease over the years. For instance, the estimates of T_s decreased from 4.2 s in 1995 to 3.4 s in 2018 for the site where station AR14 is located. This change in the estimates of T_s is attributed to the effects of the regional subsidence affecting the lake zone, which has been documented in the research works of Ovando-Shelley¹²⁰ and Avilés and Pérez-Rocha.¹²¹

It should be mentioned that many of the estimates of T_s obtained from ground motions recorded at station TH35 exceeded 6.0 s. This station is located at a site over the deepest clay deposits (with thicknesses greater than 130 m) in the Tláhuac lakebed area, which is settled where the ancient Chalco and Xochimilco lakes met. Then, by complex amplification patterns, the ground motions in this area behave very differently from other sites in Mexico City.¹¹⁶ Due to this atypical behavior, data from station TH35 was not considered for the development of the strong-motion duration GMPEs. The geographical localization of station TH35 is indicated in Figure 3.2.

Table 3.1 Estimation of T_s from a set of ground motions recorded at five stations located in different geotechnical zones

Station code	$F_1(\omega)/F_V(\omega)$	$F_2(\omega)/F_V(\omega)$	T_s
DX37			0.9 s
IB22			1.4 s
SP51			1.9 s
BA49			2.5 s
AE02			4.5 s

In general, all the estimates of T_s obtained using Eq. (3.4) are in good agreement with those reported in various specialized studies on the subject in which T_s was measured employing different techniques, such as ambient vibration tests or using FAS from ground-motion records.^{120,122–126}

3.2.3 Source-to-site Distance

Both R_{hypo} and R_{rup} were chosen to characterize the decrease in ground motion as it propagates away from the earthquake source. The estimation of R_{hypo} is quite obvious, so it needs no description, However, estimating finite-source distances, such as R_{rup} , is a task far from trivial as it requires knowledge of the shape, size, orientation, and location of the fault plane within the Earth. Gupta¹²⁷ proposed a quite practical method, which was used in this study to estimate R_{rup} , based on idealizing the fault plane as a rectangular shape with length L and width W . Relying on this idealization and knowing the orientation of the fault plane with respect to the site of interest, a global coordinate system (u, v, w) having the epicenter as the origin and a local coordinate system (ζ, η) with origin at the upper left corner of the fault plane is defined. Then, any point j in the fault plane with local coordinates (ζ_j, η_j) can be defined by global coordinates (u_j, v_j, w_j) as follows:

$$u_j = (\zeta_j - \zeta_0) \sin(\theta) + (\eta_j - \eta_0) \cos(\varphi) \cos(\theta) \quad (3.6a)$$

$$v_j = (\zeta_j - \zeta_0) \cos(\theta) - (\eta_j - \eta_0) \cos(\varphi) \sin(\theta) \quad (3.6b)$$

$$w_j = H_h + (\eta_j - \eta_0) \sin(\varphi) \quad (3.6c)$$

where (ζ_0, η_0) are the local coordinates of the hypocenter, θ is the azimuthal direction of the horizontal in the fault plane, and φ is the inclination of the fault plane relative to the horizontal. The angles θ and φ are known as fault strike and dip, respectively, and are measured in degrees. Figure 3.3 shows a schematic of the global and local coordinate systems as defined above. As per Figure 3.3, the global coordinates of the site of interest are $(R_{epi} \sin \psi, R_{epi} \cos \psi, -H_s)$, where H_s is the altitude of the site and ψ is the direction from the fault plane to the site measured in degrees clockwise from the north. The distance r_j between the site of interest and the point j on the fault plane can be computed easily using the Pythagorean theorem. Thus, R_{rup} can be obtained by finding the minimum of the distances r_j for a closely spaced grid of points covering the entire rectangular fault.

The interplate earthquakes and their corresponding source parameters selected for the development of the strong-motion duration GMPEs are presented

in Appendix C. Note that all the parameters necessary to compute R_{rup} were unavailable in the reviewed literature for earthquakes with $M_w < 7.2$. Nonetheless, typical rupture dimensions of these earthquakes are several orders of magnitude smaller than the distance to Mexico City, allowing R_{hypo} to be used instead of R_{rup} .

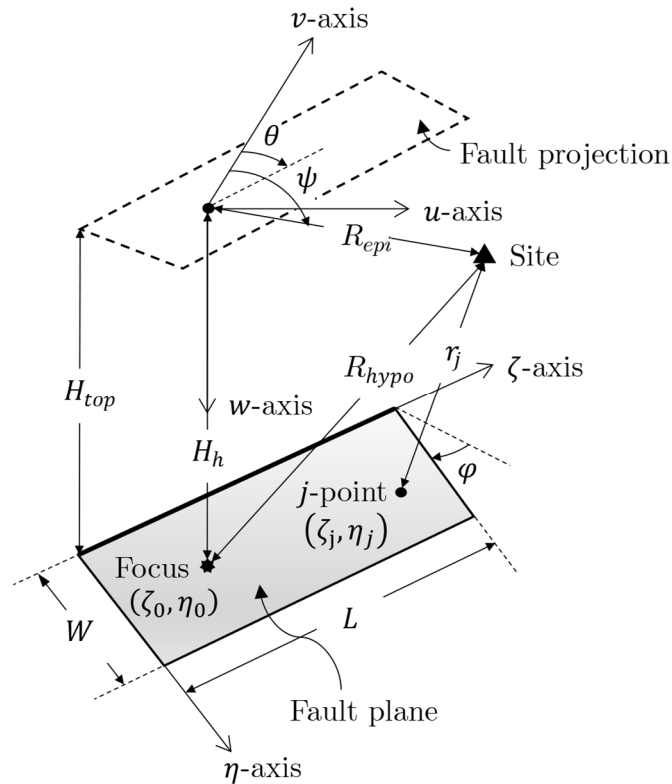


Figure 3.3 Schematic of the global and local coordinate systems used to compute R_{hypo} and R_{rup}

3.3 Estimation of Strong-motion Duration

Each of the definitions given in Section 2.2 was thoroughly analyzed in this study to determine which one was the best to measure the strong-motion duration in sites located in Mexico City. A careful exploration (almost accelerogram by accelerogram) was necessary to fully understand the behavior of the strong-motion duration in a region located several hundred kilometers from the earthquake sources of interplate earthquakes. It should be mentioned that the amplitudes of the vertical component of ground motions caused by such distant earthquakes are so small that they are not relevant for structural design in Mexico City. Therefore, the author focused on studying the strong-motion duration only from the horizontal components of the ground motion.

For the development of GMPEs, the use of both D_B and D_U was discarded because establishing the value of a_0 , either absolute or relative, was very difficult to determine. For instance, according to the literature review given in Section 2.2, the value of a_0 has been taken within the interval from $0.03g$ to $0.20g$. But notice that, even taking $a_0 = 0.03g$, almost all the values of D_B and D_U obtained from accelerograms recorded at GZI were equal to zero because the maximum PGA recorded in that zone was equal to approximately 33 cm/s^2 . Such a value of PGA corresponds to an accelerogram recorded at station CU01 during the September 19, 1985 earthquake, which occurred at $R_{hypo} = 379 \text{ km}$. Using the mentioned accelerogram, Figure 3.4 shows the measurement of the absolute D_B considering $a_0 = 0.03g$. The estimated value of the absolute D_B was equal to 4.85 s . Thus, should a_0 be taken equal to $0.01g$, $0.005g$, or $0.001g$? Most of these values represent acceleration amplitudes that are below human perception.

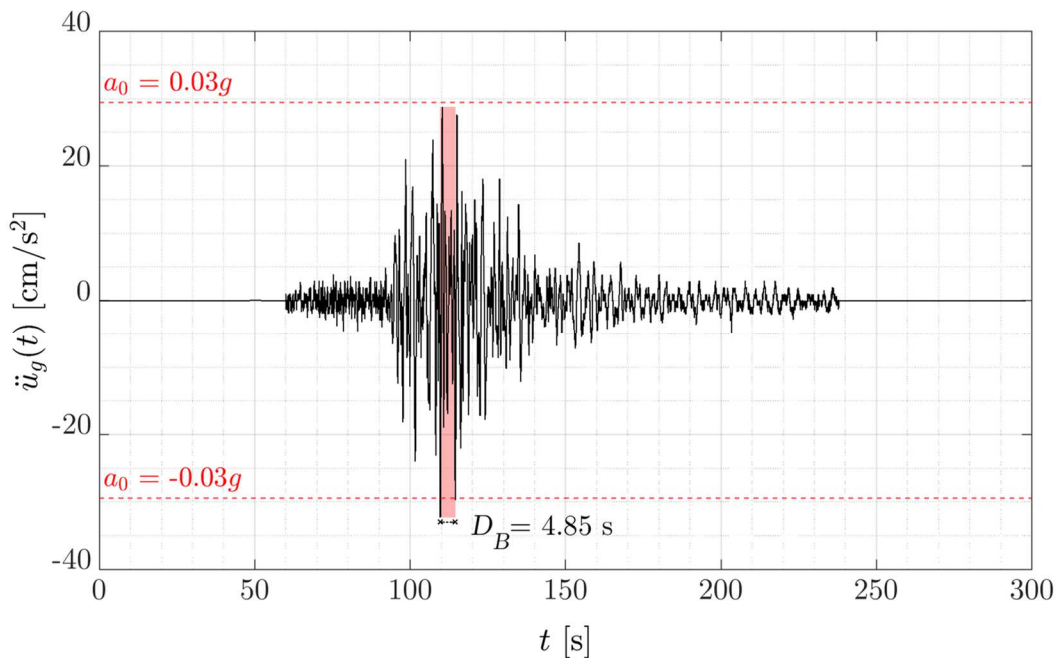


Figure 3.4 Estimation of the absolute D_B from an accelerogram recorded at station CU01 during the September 19, 1985 earthquake, with $M_w = 8.0$

For accelerograms recorded at sites located in GZII or GZIII, the use of D_B or D_U is unproblematic, but it is preferable to establish the same criteria to measure the strong-motion duration in all sites to make objective comparisons.

Thus, for the development of the GMPEs, the author preferred D_{Sr} , with $a_1 = 0.05$ and $a_2 = 0.95$. Although the estimation of D_{Sr} could be seen as an automatic process, attention was drawn to the influence exerted by trigger thresholds and memory availability of recording devices used in the accelerograph networks operated by the CIRES and II-UNAM.^{67,115} In this regard, some of the recording devices used in the early years had very high trigger acceleration thresholds and almost null pre- and post-event memory availabilities (varying from approximately 0 s to 8 s), leading to a significant loss of the first and last motions of the ground, which are very valuable for the estimation of D_{Sr} . For this reason, all ground-motion recordings from earthquakes that occurred before 1985 had to be discarded because of their incompleteness. Moreover, the few ground-motion recordings of the earthquakes that occurred in that year from sites located outside GZI also had to be discarded.

Most of the recording devices installed currently have sufficient memory availabilities, which leads to little or insignificant loss of information. Nevertheless, this large capacity entails that, in many cases, a considerable part of the beginning and end of a recording is not an intrinsic part of the ground motion caused by an earthquake. This may present no problem for estimating other ground-motion parameters, such as those used for response spectra, but it does when it comes to estimating the strong-motion duration. From the inspection of the accelerograms, it was observed that regardless of how weak the acceleration values are in the post-event trail, their contribution to the estimates of D_{Sr} could be considerable. For instance, following Figure 3.5, compare the estimated values of D_{Sr} from two accelerograms recorded at stations CUP1 and CUP4 during the September 14, 1995 earthquake that occurred in Guerrero at $R_{hypo} = 339$ km and had $M_w = 7.4$. Although the stations are located at almost the same geographical coordinates, station CUP1 recorded 97.50 s of ground motion, whereas station CUP4 recorded 492.57 s. While $D_{Sr} = 46.68$ s was obtained from the accelerogram recorded at station CUP1, $D_{Sr} = 93.80$ s was obtained from the accelerogram recorded at station CUP4. The second value of D_{Sr} is not credible for a site located in GZI, from an earthquake of such characteristics.

To overcome the problems described above it was decided to disregard the initial and final part of the accelerograms whose amplitudes were not representative of the ground motion for the estimation of D_{Sr} . The portion of the accelerograms to be considered was set between the first and last excursion of a specified acceleration threshold, a_0 , equal to 2 cm/s^2 . By applying the above standardization, more consistent values of D_{Sr} were obtained. For instance, for the case displayed in

Figure 3.5, values of D_{Sr} equal to 41.32 s and 37.18 s were estimated when considering such criterion.

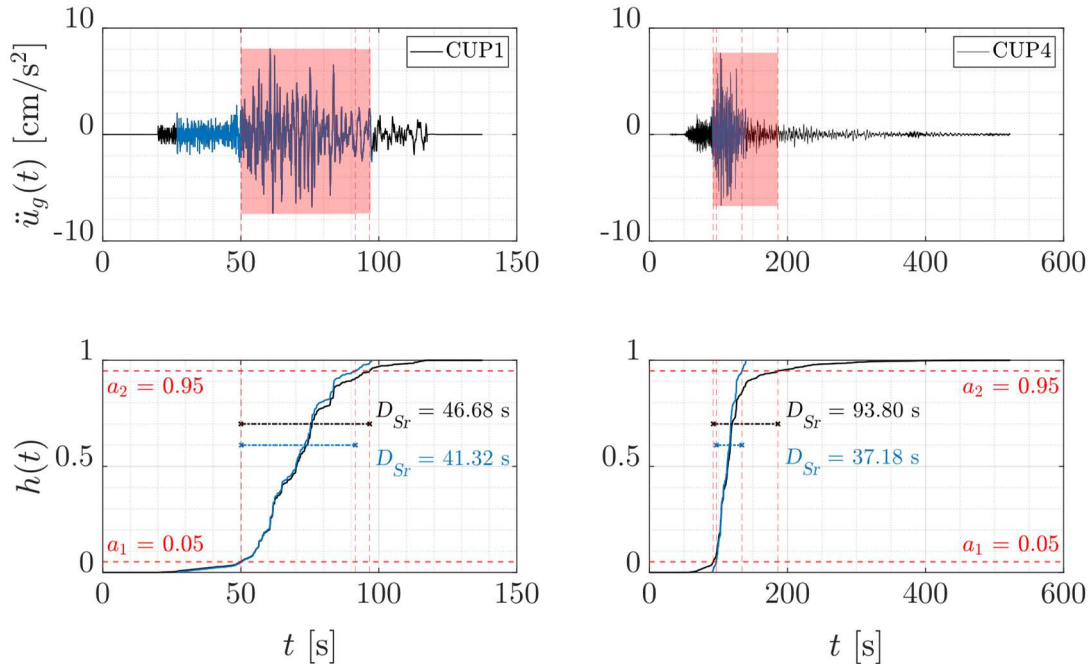


Figure 3.5 Estimation of D_{Sr} from two accelerograms recorded at stations CUP1 and CUP4 during the September 14, 1995 earthquake, with $M_w = 7.4$. The black lines stand for the computation of D_{Sr} using the raw accelerograms, whereas the blue lines stand for its computation using the portion of the accelerograms bounded by $a_0 = 2 \text{ cm/s}^2$

The selection of the value of a_0 was nonarbitrary. Various possibilities were analyzed. If a value of a_0 smaller than 2 cm/s^2 had been taken, many accelerograms would have to be discarded because some of the recording devices had trigger acceleration thresholds greater than 2 cm/s^2 . For instance, all the accelerograms recorded at GZII or GZIII during the September 19, 1985 earthquake were part of these. Although at first glance such accelerograms appeared to be complete (with values of $t_f \leq 315 \text{ s}$), they had to be discarded since they were recorded with devices having a trigger threshold of 4 cm/s^2 and almost null pre- and post-event memory availabilities (ranging from 0 s to 15 s). For instance, station SCT1, which was located in GZIIIb at a site with T_s of approximately 2 s, recorded 183.51 s of the ground motion. From the horizontal accelerograms of such ground-motion recording, values of D_{Sr} equal to 39 s and 71 s were computed. Such values are unrepresentative of the real strong-motion duration felt at that site during the earthquake.

Taking a value of a_0 greater than 2 cm/s^2 was also inexpedient. From an intensive exploration of “ideal” accelerograms of ground motions recorded in GZIIIb, values of D_{Sr} considering $a_0 = 4 \text{ cm/s}^2$ were up to 1.6 times smaller than those considering $a_0 = 2 \text{ cm/s}^2$ for accelerograms with values of PGA greater than approximately 15 cm/s^2 . Moreover, for accelerograms with smaller values of PGA , the differences became greater than 20 times. Similar results were observed for ground motions recorded at other geotechnical zones. For instance, for the case displayed in Figure 3.5, values of D_{Sr} equal to 27.06 s and 27.07 s were estimated from accelerograms recorded at stations CUP1 and CUP4, respectively, when taking $a_0 = 4 \text{ cm/s}^2$. These values extremely underestimate the expected strong-motion duration at the sites of interest.

Moreover, the value of a_0 was set equal to 2 cm/s^2 based on the serviceability criteria for human perception of vibrations, e.g., those provided by the 2014 Architectural Institute of Japan Recommendations for a 30% of probability of perception.¹²⁸ Furthermore, the selected value of a_0 is half the minimum limit defined for human perception criteria of other standards, such as ISO 10137:2007.¹²⁹ Thus, the information loss by the use of this threshold is expected to be negligible for structural engineering purposes.

It is worth mentioning that, noticing issues similar to those described above, Guerrero⁴⁷ and Reinoso and Ordaz⁴⁸ also trimmed the accelerograms at a fixed acceleration threshold for the estimation of D_{Sr} . Guerrero⁴⁷ used an acceleration threshold equal to 1 cm/s^2 , 2 cm/s^2 , and 4 cm/s^2 for accelerograms recorded at GZI, GZII, and GZIII, respectively. Similarly, Reinoso and Ordaz⁴⁸ set the fixed acceleration threshold equal to 4 cm/s^2 for those accelerograms recorded at GZII or GZIII, but for those from ground motions recorded at GZI non-acceleration threshold was used. Again, the author considers that it is preferable to establish the same criteria to estimate the strong-motion duration in all sites to make objective comparisons.

Figure 3.6 shows a collection of six accelerograms recorded at different sites of Mexico City during the March 20, 2012 earthquake. For the selected sites R_{hypo} varies approximately from 330 km to 340 km. As can be seen from Figure 3.6, there is a wide variation in the estimates of D_{Sr} in sites located within a 5-km radius. For instance, the estimated value of D_{Sr} from the accelerogram recorded at station AE02 (located in GZIIIId) is 2.7 times that from station CUP5 (located in GZI). Note that the accelerograms shown in Figure 3.6 are bounded by $a_0 = 2 \text{ cm/s}^2$.

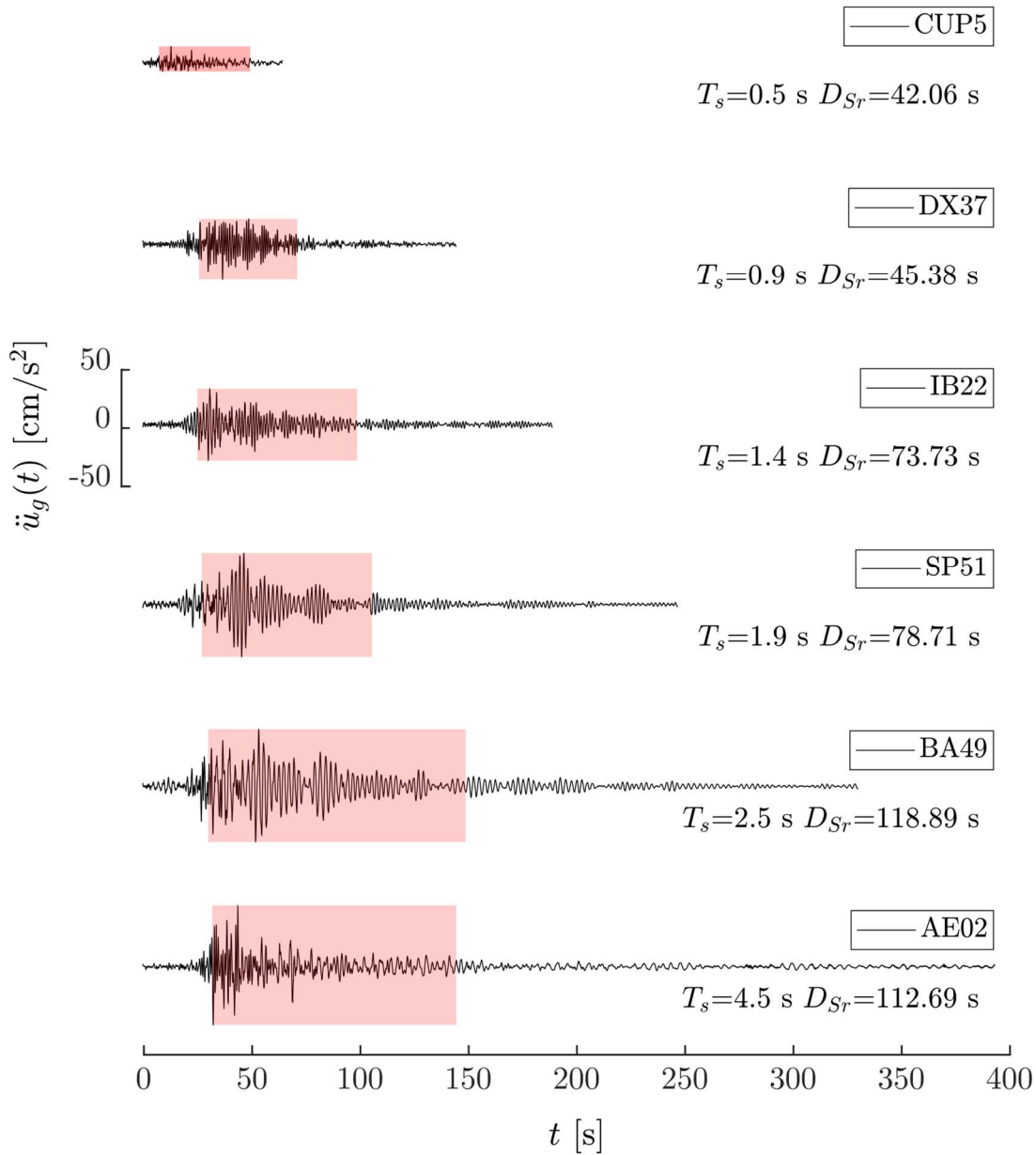


Figure 3.6 Collection of six accelerograms recorded at different sites in Mexico City during the March 20, 2012 earthquake, which had $M_w = 7.4$. The accelerograms are bounded by $a_0 = 2 \text{ cm/s}^2$. Shaded areas stand for the strong-motion duration lapse of each accelerogram

As noticed from Figure 3.6, accelerograms recorded in Mexico City are characterized by *extended codas*, which are defined as a succession of roughly harmonic beats of slowly decaying amplitude,¹³⁰ and they are generally attributed to the resonance of the local sedimentary layers that characterize Mexico City.¹³¹

Trimming the accelerograms with the criteria described above negligibly modifies the estimated values of D_{Sr} . In general, for ground motions with high values of PGA (e.g., greater than 15 cm/s^2 , which are the ones that could cause some damage in Mexico City), the difference between considering such threshold value or not is less than 5 s. For instance, Figure 3.7 shows the estimation of D_{Sr} from an accelerogram recorded at station BA49 during the March 20, 2012 earthquake that occurred in Ometepec, Guerrero, and had $M_w = 7.4$. The estimated values of D_{Sr} considering the raw accelerogram and the portion of it bounded by $a_0 = 2 \text{ cm/s}^2$ only differ by 2.5 s.

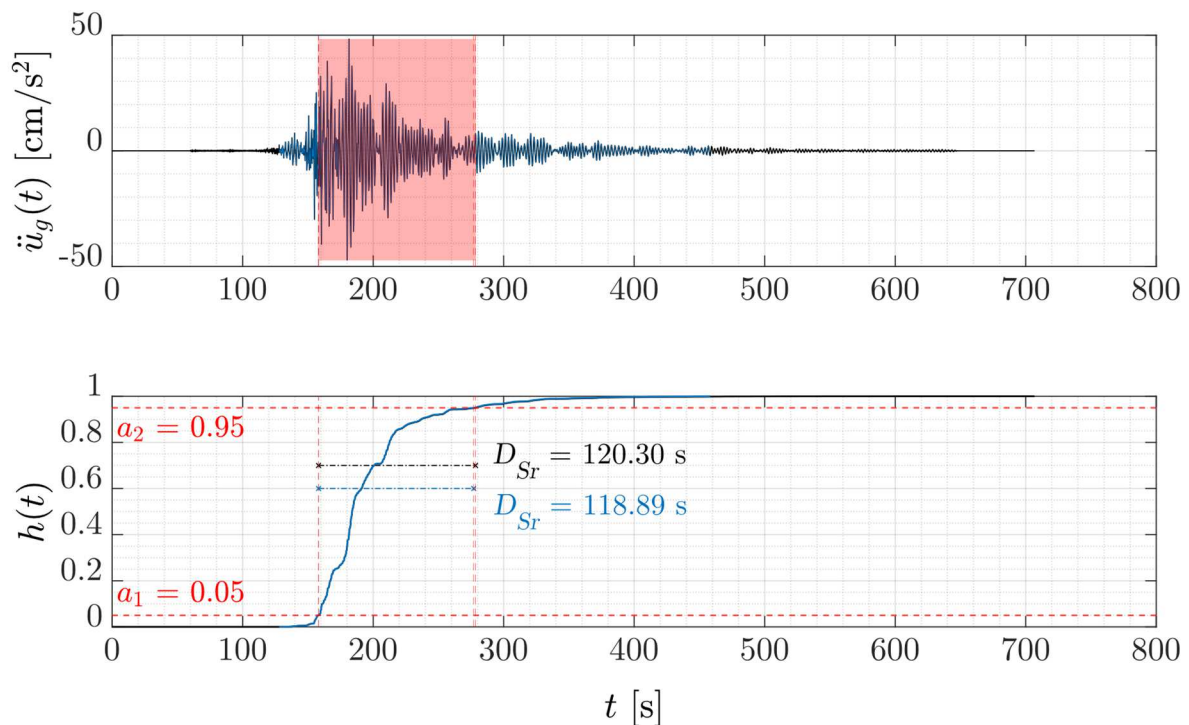


Figure 3.7 Estimation of D_{Sr} from an accelerogram recorded at station BA49 during the March 20, 2012 earthquake, with $M_w = 7.4$

3.3.1 Observed Trends Between Strong-motion Duration and Different Seismological Parameters

The observed trends between D_{Sr} and either M_w , R_{hypo} , R_{rup} , and T_s are briefly discussed next.

The ground-motion duration in a given site is expected to increase as the earthquake magnitude increases because, as it is well known, the size of an

earthquake is strongly dependent on the dimension of its fault plane, thus, the time needed to break large faults is longer.¹¹¹ This hypothesis is corroborated in Figure 3.8, which shows the distribution of D_{Sr} in M_w , grouped by earthquake event, where a positive dependence between both variables is noticed.

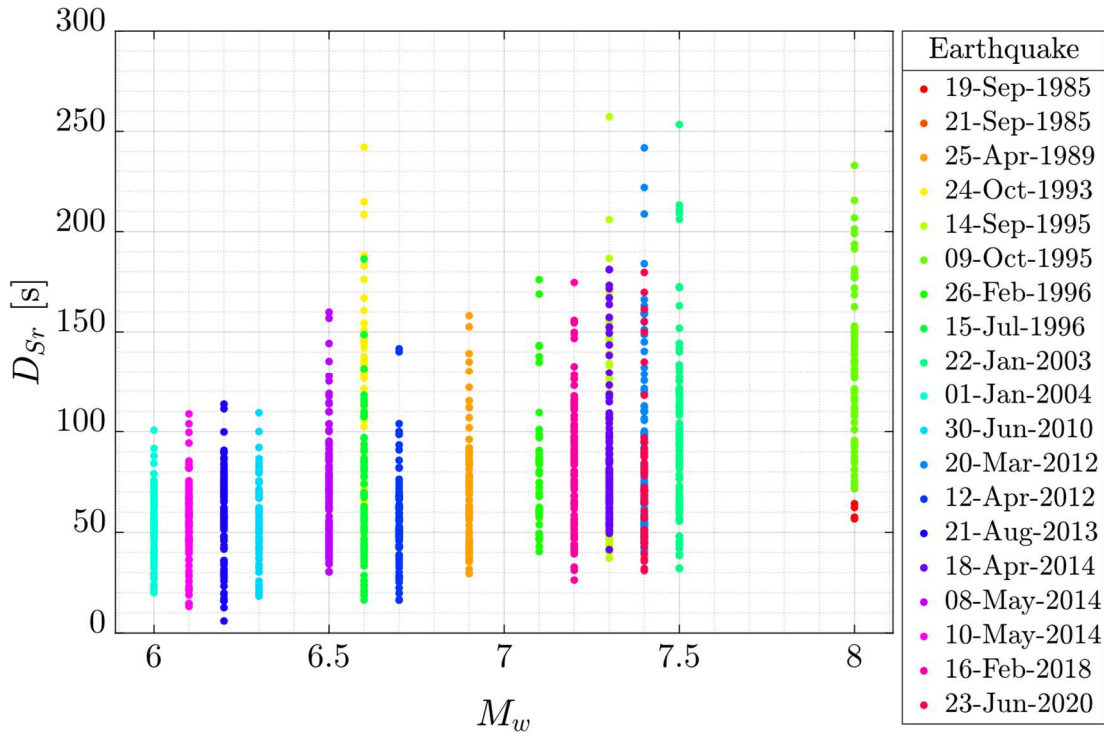


Figure 3.8 Distribution of D_{Sr} in M_w , grouped by earthquake event

On the other hand, D_{Sr} is expected to decrease with either R_{hypo} or R_{rup} . This is attributed to the effects of *attenuation*, which is the decrease in seismic wave amplitude with propagation, caused by intrinsic absorption and/or scattering.¹³² For example, the time elapsed between the first and last excursions of a specified value of a_0 will be shortened as either R_{hypo} or R_{rup} increases (even if a_0 is almost zero, as for ideal accelerograms). It is important to mention that the strong-motion duration measured at a given site should by no means be confused with the time it takes for seismic waves to arrive from a given earthquake source to the site. Clearly, the farther the site, the longer it will take for the waves to arrive. In this matter, the seismic waves reach Mexico City extremely attenuated (due to its great distance to the MAT) but, due to local site condition effects, they undergo considerable amplification.

Figures 3.9 and 3.10 show the distribution of D_{Sr} in R_{hyppo} and R_{rup} , respectively, grouped by earthquake event. A positive correlation between D_{Sr} and either R_{hyppo} or R_{rup} is observed when all the observations are considered as a single set. However, it should be noted from Figure 3.11, which shows the distribution of the two definitions of R in M_w , grouped by earthquake event, that observations for large R_{hyppo} or R_{rup} correspond to major earthquakes. This is the reason why a positive correlation is perceived in Figures 3.9 and 3.10 considering the data as a single set. Now, there is a lack of ground-motion recordings from large earthquakes occurring in seismic gaps located at R_{rup} from approximately 350 km to 400 km. Large events likely to occur at this range are expected to produce long-lasting ground motions. This is insofar as the attenuation effects would be expected to be less noticeable than those for distant earthquakes. Moreover, there are no ground-motion recordings of small earthquakes occurring at large R from Mexico City because, due to attenuation effects, these are unperceived. For such ground motions, the strong-motion duration is zero. Hence, imagining an “ideal” strong-motion database, a negative association can be visualized between D_{Sr} and either R_{hyppo} or R_{rup} .

Moreover, the positive correlation between D_{Sr} and either R_{hyppo} or R_{rup} observed from the scatter plots shown in Figures 3.9 and 3.10 is because these include data from sites with different local site conditions. As mentioned above, although the seismic waves of earthquakes occurring at the MAT arrive very attenuated to Mexico City, the peculiar (and intricate) local site conditions of said geographical region cause the waves to be greatly amplified. Then, D_{Sr} is expected to increase as T_s increases. Thus, the negative correlation between D_{Sr} and either R_{hyppo} and R_{rup} can be observed by grouping the data by earthquake event and sites with similar local site conditions.

To exemplify what was mentioned in the previous paragraph, Figure 3.12 shows the distribution of D_{Sr} in R_{rup} , grouped by geotechnical zone, for data from the earthquakes that occurred on July 15, 1996, June 30, 2010, and April 18, 2018. As noticed in Figure 3.12, a positive correlation between D_{Sr} and R_{rup} is observed when all the observations from the earthquakes that occurred on July 15, 1996 and April 18, 2018 are considered as a single set. But looking more closely, a negative correlation between D_{Sr} and R_{rup} is perceived for data belonging to the same geotechnical zone. The distribution of D_{Sr} in R_{rup} of the data from the June 30, 2010 earthquake shows that such parameters are negatively correlated.

The hypothesis that D_{Sr} decreases as T_s increases can be corroborated from Figure 3.13, which plots the distribution of D_{Sr} in T_s , grouped by earthquake event.

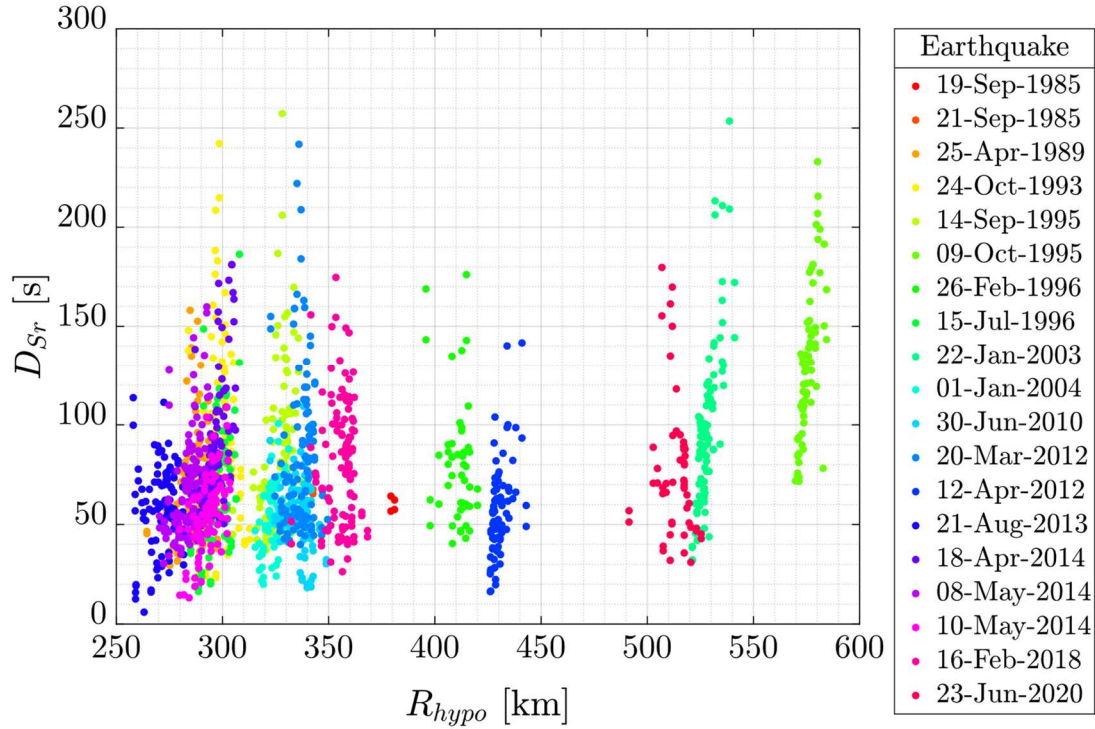


Figure 3.9 Distribution of D_{Sr} in R_{hypo} grouped by earthquake event

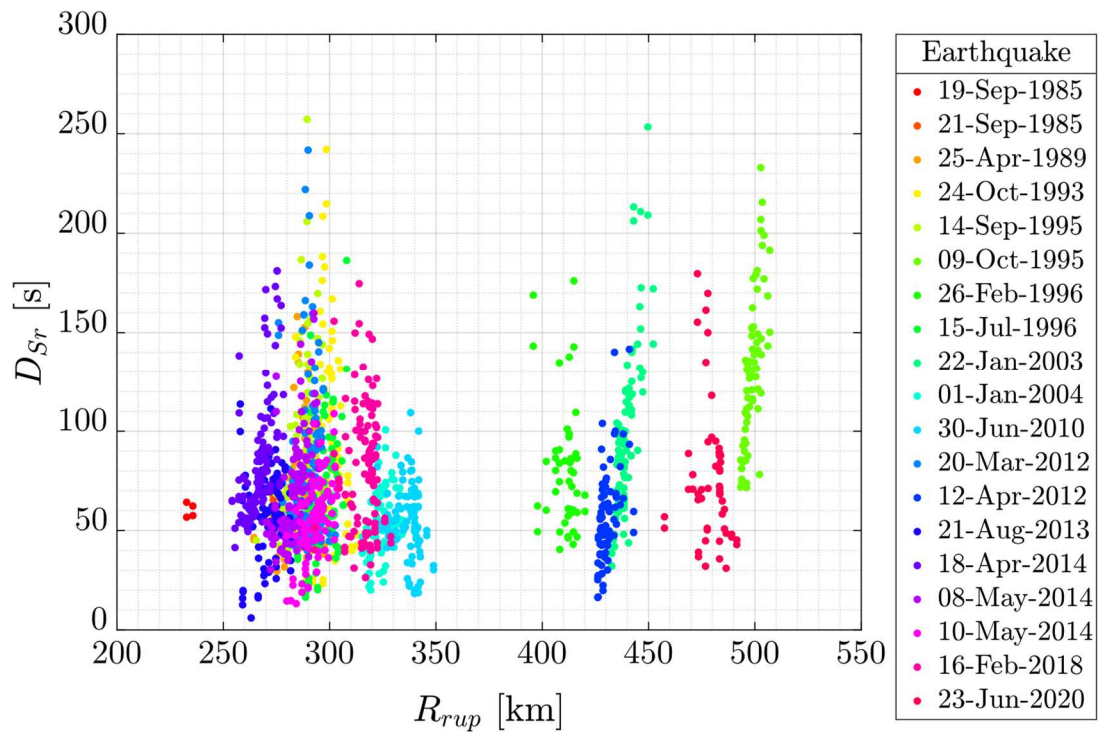


Figure 3.10 Distribution of D_{Sr} in R_{rup} grouped by earthquake event

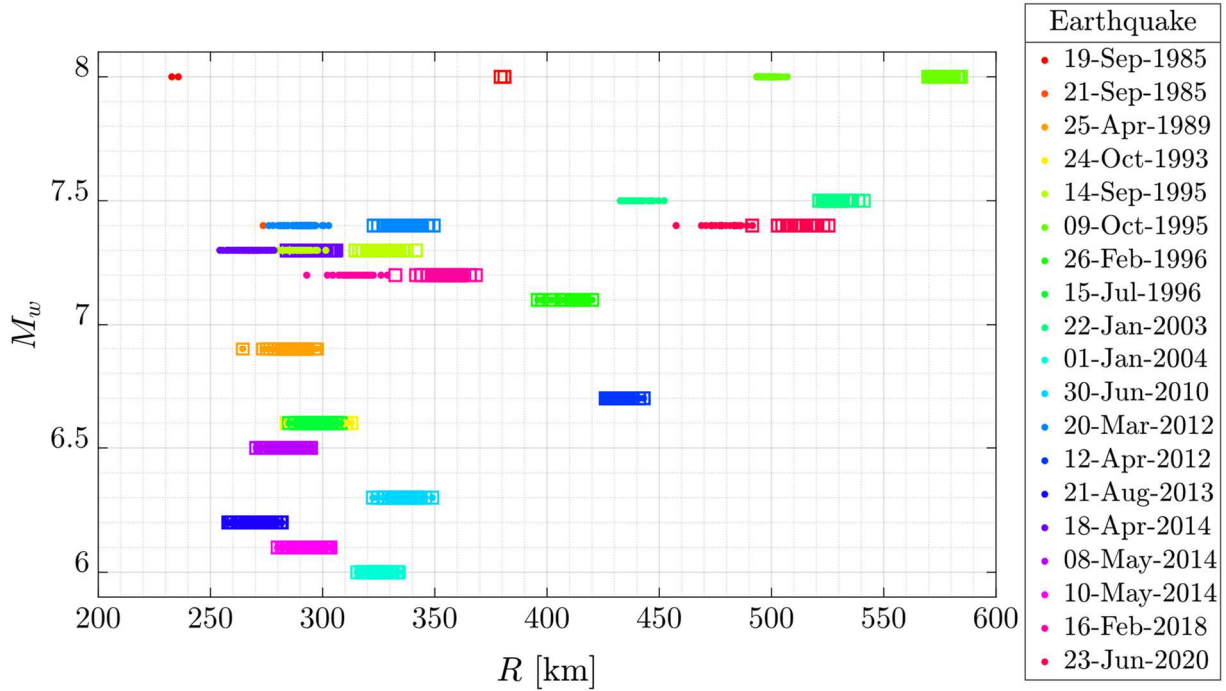


Figure 3.11 Distribution of R_{hypo} and R_{rup} in M_w , grouped by earthquake event. The measures for R_{hypo} are denoted by a dot and the measures for R_{rup} by a square

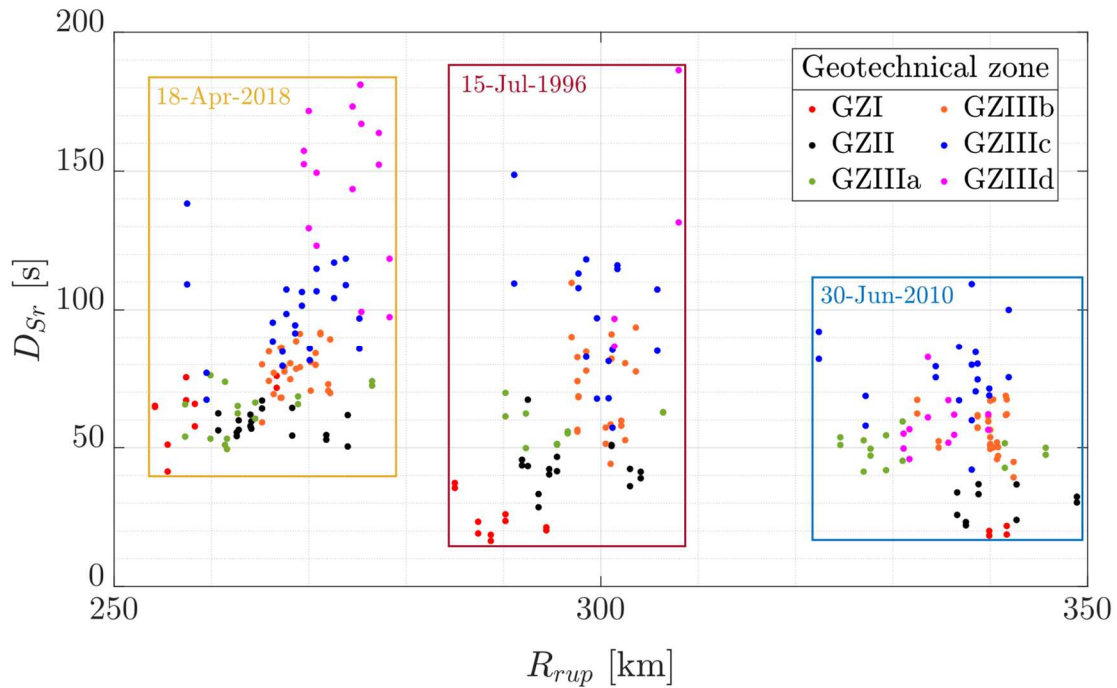


Figure 3.12 Distribution of D_{Sr} in R_{rup} , grouped by geotechnical zone, for data from the earthquakes that occurred on July 15, 1996 (yellow box), April 18, 2018 (burgundy box), and June 30, 2010 (blue box)

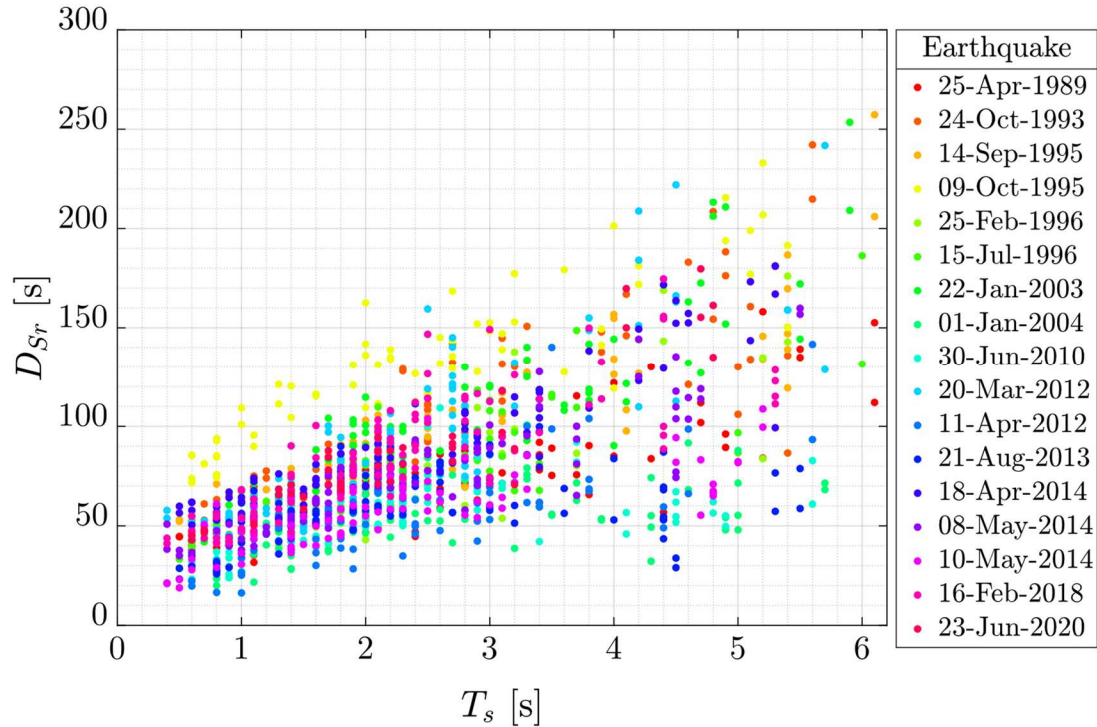


Figure 3.13 Distribution of D_{Sr} in T_s , grouped by earthquake event

3.3.2 Predictive Equations for Strong-motion Duration

Predictive equations for the strong-motion duration were developed for sites located in GZI and for sites located in GZII or GZIII. The regression analyses were performed based on the LME model given in Eq. (3.1), considering the natural logarithm of D_{Sr} as Y and M_w , T_s , and either R_{hypo} or R_{rup} as the set of X_1, \dots, X_p for the definition of \mathbf{X} , and by grouping the data by earthquake event. Specifically, 141 accelerograms were used for the development of the GMPEs for GZI and 1374 for the development of the GMPEs for GZII and GZIII. All accelerograms have $PGA \geq 3$ cm/s². The number of ground-motion recordings per earthquake considered is summarized in Appendix D. Note that all the ground-motion recordings had two horizontal accelerograms, except those from stations MT50 and PA34 obtained during the October 09, 1995 earthquake, from station CUP5 obtained during the August 21, 2013 earthquake, and from stations CUP5 and TP13 obtained during the May 10, 2014 earthquake.

Several functional forms were evaluated for the selection of the best suitable GMPEs. Random effects \mathbf{b}_i for all model coefficients and a full variance-covariance matrix $\sigma_{\mathbf{b}}^2$ using the Cholesky parameterization were first considered. From this preliminary inspection, it was observed from the estimated $\sigma_{\mathbf{b}}^2$ that \mathbf{b}_i seemed to be

weakly correlated and that only the one associated with the intercept was significant. Note that a model coefficient could be treated as a fixed effect if its corresponding variance estimate in σ_b^2 is near zero. Hence, regression analyses were carried out considering only the intercept, α_0 , as random and the design matrix of random effects \mathbf{Z}_i as a vector of ones.

The selected functional form for sites located in GZI is:

$$\ln(D_{S_r})_{ik} = \alpha_0 + (\alpha_1 + \alpha_2 M_{w_i}) \ln(R)_{ik} + b_{0_i} + e_{ik} \quad (3.7)$$

where $\ln(D_{S_r})_{ik}$ and $\ln(R)_{ik}$ are the natural logarithms of D_{S_r} and R , respectively, of the k th accelerogram recorded during the i th earthquake event, and M_{w_i} is the moment magnitude of the i th earthquake event. From the assumptions for the LME models given in Section 3.1, the terms b_{0_i} and e_{ik} have the prior distributions $b_{0_i} \sim \mathcal{N}(0, \sigma_b^2)$ and $e_{ik} \sim \mathcal{N}(0, \sigma_w^2)$, respectively.

The selected functional form for sites located in GZII or GZIII is:

$$\ln(D_S)_{ik} = \alpha_0 + \alpha_1 \ln(T_s)_{ik} + (\alpha_2 + \alpha_3 M_{w_i}) \ln(R)_{ik} + b_{0_i} + e_{ik} \quad (3.8)$$

where $\ln(T_s)_{ik}$ is the natural logarithm of T_s of the k th accelerogram recorded during the i th earthquake event.

Tables 3.2 and 3.3 summarize the estimates of α_0 , α_1 , α_2 , and α_3 obtained from the regression analysis for Eqs. (3.7) and (3.8), respectively. The results given in the columns titled GMPE A and GMPE C correspond to those considering R_{hypo} as the measure defining R , whereas the results shown in the columns titled GMPE B and GMPE D correspond to those considering R_{rup} . In Table 3.2 and 3.3 the estimates of α_0 , α_1 , α_2 , and α_3 are shown together with their corresponding standard error (SE) and p -value for a t -test. Note that the t -test is any statistical hypothesis in which the test statistic follows a Student's t -distribution under the null hypothesis. The Student's t distribution is commonly applied to the testing of one-sided hypotheses related to normally distributed data, and its density function can be found in Forbes et al.¹³³ In this study, the probability of rejecting the null hypothesis, given that it was assumed to be true, i.e., the significance level, was set at 0.05. Recall that the p -value is the probability of obtaining test results as extreme, or more extreme than, the results observed, under the assumption that the null hypothesis is true. The standard deviation of the normally distributed variables b_{0_i} and e_{ik} , i.e., σ_b^2 and σ_w^2 , respectively, together with their 95% confidence intervals

obtained from the regression analysis for Eqs. (3.7) and (3.8) are summarized in Table 3.4.

Table 3.2 Estimates of the elements of α for the strong-motion duration GMPEs developed for sites located in GZI. Results shown in columns titled GMPE A correspond to those considering R_{hypo} as the measure defining the R , whereas the results shown in the columns titled GMPE B correspond to those considering R_{rup}

Parameter	GMPE A			GMPE B		
	Estimate	SE	p -value	Estimate	SE	p -value
α_1	7.3586	1.6371	1.4903e-05	5.7300	1.4467	1.2080e-04
α_2	-1.6875	-4.2949	3.3313e-05	-1.2673	0.3125	8.4666e-05
α_3	0.1486	7.3278	1.9777e-11	0.1279	0.0171	9.2850e-12

Table 3.3 Estimates of the elements of α for the strong-motion duration GMPEs developed for sites located in GZII or GZIII. Results shown in columns titled GMPE C correspond to those considering R_{hypo} as the measure defining R , whereas the results shown in the columns titled GMPE D correspond to those considering R_{rup}

Parameter	GMPE C			GMPE D		
	Estimate	SE	p -value	Estimate	SE	p -value
α_1	5.5590	0.8544	1.0853e-10	5.4515	0.8080	2.2463e-11
α_2	0.5241	0.0088	0	0.5242	0.0089	0
α_3	-0.7859	0.2019	1.0447e-04	-0.7393	0.1787	3.7223e-05
α_4	0.0735	0.0108	1.3463e-11	0.0692	0.0094	2.8256e-13

Table 3.4 Estimates of σ_b and σ_w and their corresponding 95% confidence intervals (lower, upper)

GMPE	σ_b	σ_w
GMPE A	0.1821 (0.1214, 0.2731)	0.1790 (0.1578, 0.2031)
GMPE B	0.1993 (0.1344, 0.2955)	0.1786 (0.1574, 0.2026)
GMPE C	0.1094 (0.0771, 0.1552)	0.1858 (0.17882, 0.1930)
GMPE B	0.1090 (0.0769, 0.1547)	0.1863 (0.1793, 0.1935)

The variance, V , and covariance, C , for the GMPEs given in Eqs. (3.7) and (3.8) can be computed as follows¹³⁴:

$$V[\ln(D_{Sr})_{ik}] = \sigma_b^2 + \sigma_w^2 \quad (3.9a)$$

$$C[[\ln(D_{Sr})_{ik}, \ln(D_{Sr})_{i'k}]] = 0 \quad i \neq i' \quad (3.9b)$$

$$C[[\ln(D_{Sr})_{ik}, \ln(D_{Sr})_{ik'}]] = \sigma_b^2 \quad k \neq k' \quad (3.9c)$$

From Table 3.4, V is equal to 0.0652, 0.0716, 0.0465, and 0.0466 for GMPEs A, B, C, and D, respectively. Note that the first covariance statement given in Eq. (3.9b) indicates that earthquake events are independent of each other, whereas the second covariance statement given in Eq. (3.9c) indicates that σ_b^2 is the covariance for any two repeated measures within the same earthquake event. Expressing Eq. (3.9c) as a correlation yields the so-called *inter-class correlation*, ρ , which is defined as^{92,134}:

$$\rho = \frac{\sigma_b^2}{\sigma_b^2 + \sigma_w^2} \quad (3.10)$$

In this case, the intraclass correlation ρ represents the degree of association of the strong-motion data within earthquake events. In other words, two observations from the same earthquake are statistically associated with the correlation coefficient ρ . For instance, based on the results given in Table 3.4, values of ρ equal to 0.5547 and 0.5084 were obtained for GMPEs A and B, respectively, whereas values of ρ equal to 0.2574 and 0.2552 were obtained for the GMPEs C and D, respectively.

It should be mentioned that σ_b^2 and σ_w^2 are commonly referred to as the between-events variability and within-event variability, respectively.^{135,136} From the results given in Table 3.4, the major source of variation for GMPEs A and B can be attributed to the between-events variability. By contrast, the within-event variability is the major source of variation for GMPEs C and D.

Following Eq. (3.2), the density function of the natural logarithm of D_{Sr} is¹³⁷:

$$f_{\ln(D_{Sr})}[\ln(d)] = \frac{1}{\sigma\sqrt{2\pi}} \exp \left\{ -\frac{1}{2} \left[\frac{\ln(d) - \mu}{\sigma} \right]^2 \right\} \quad (3.11)$$

where the parameters μ and σ are the mean and standard deviation of the natural logarithm of D_{Sr} , respectively. The first can be computed from the estimated $\mathbf{X}\boldsymbol{\alpha}$ used to develop the GMPEs, and the second as the squared root of V . For instance, using GMPE C and considering three specific values of M_w , Figure 3.14 shows the distribution of μ and $\mu \pm \sigma$ of the natural logarithm of D_{Sr} in R_{hypp} and T_s . The

data considered in the regression analysis and that match the selected M_w values are superimposed in Figure 3.14. As can be appreciated from Figure 3.14, the behavior perceived in the empirical data and discussed in Subsection 3.3.1 is satisfactorily reflected in the GMPEs proposed in this study.

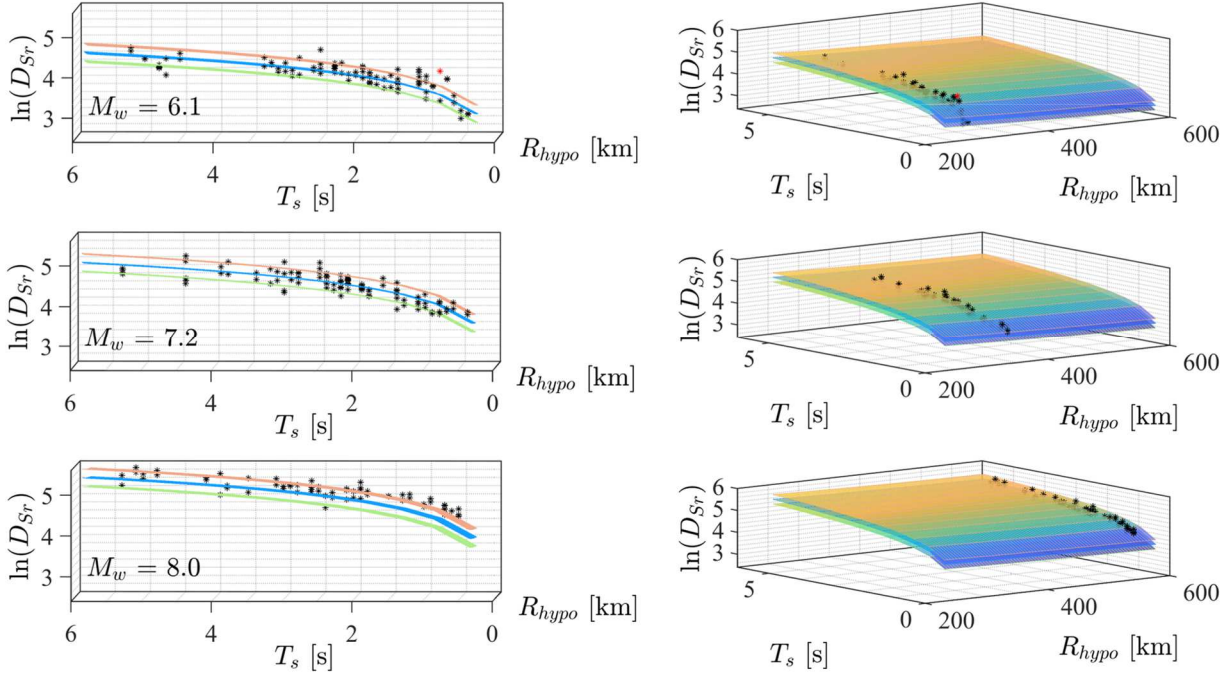


Figure 3.14 Distribution of μ and $\mu \pm \sigma$ of the natural logarithm of D_{S_r} , with respect to R_{hypo} and T_s , computed using GMPE C for three values of M_w . A 3D view of the plots is shown on the right, whereas their lateral view is shown on the left. Scatter plots of the data considered in the regression analysis that match the selected values of M_w are superimposed. Data points marked in red are outliers

3.3.2.1 Residual Analysis

The sources of variation \mathbf{e} and \mathbf{b} in LME models can generate three types of residuals, namely, *conditional residuals*, *marginal residuals*, and *best linear unbiased predictors* (BLUP).^{138,139} Based on the compact form of Eq. (3.1), the vector of conditional residuals, $\hat{\mathbf{e}}$, that predict the vector \mathbf{e} can be defined as:

$$\hat{\mathbf{e}} = \mathbf{y} - \mathbf{X}\hat{\boldsymbol{\alpha}} - \mathbf{Z}\hat{\mathbf{b}} \quad (3.12)$$

where $\hat{\boldsymbol{\alpha}}$ and $\hat{\mathbf{b}}$ are the estimators of $\boldsymbol{\alpha}$ and \mathbf{b} , respectively. Note that the BLUPs, $\mathbf{Z}\hat{\mathbf{b}}$, predict \mathbf{Zb} . The vector of marginal residuals, $\hat{\boldsymbol{\xi}}$, that predict the vector of marginal errors $\boldsymbol{\xi}$, can be defined as:

$$\hat{\boldsymbol{\xi}} = \mathbf{y} - \mathbf{X}\hat{\boldsymbol{\alpha}} \quad (3.13)$$

Thus, Figure 3.15 shows the distribution of the estimated BLUPs for GMPEs A and C. From Figure 3.15, no outlying earthquakes can be appreciated. Similar results as those given in Figure 3.15 were observed for GMPEs B and D.

Based on Eqs. (3.12) and (3.13) residual analyses were carried out to check the validity of LME model assumptions. For instance, for GMPE A, Figure 3.16 shows a scatter plot of the standardized $\hat{\mathbf{e}}$ versus fitted conditional values of the natural logarithm of D_{Sr} , $\hat{\mathbf{y}}$, and a frequency histogram and box plots of $\hat{\mathbf{e}}$. The standardized $\hat{\mathbf{e}}$ can be computed by dividing $\hat{\mathbf{e}}$ by the estimated σ_w and $\hat{\mathbf{y}} = \mathbf{X}\hat{\boldsymbol{\alpha}} + \mathbf{Z}\hat{\mathbf{b}}$. Notice that a *frequency histogram* is a bar plot for numeric data that groups data into bins of equal width. Each bin is plotted as a bar whose height corresponds to how many data points are in that bin. A *box plot* provides some statistics for a sample of data. It contains the following features⁴²: (a) The lines at the bottom and top of the box are the first and third quartiles, respectively, of the sample; the distance between these sections is the interquartile range. (b) The line in the center of the box is the sample median. (c) The dashed lines extending above and below the box, colloquially known as *whiskers*, go from the end of the interquartile range to the farther observation within a distance of 1.5 times the interquartile range. Observations beyond the whisker lengths are commonly referred to as *outliers*.

No obvious pattern can be observed from the inspection of the dispersion of the standardized $\hat{\mathbf{e}}$ in $\hat{\mathbf{y}}$ given in Figure 3.16. Thus, it can be said that \mathbf{e} is homoscedastic and that the components of \mathbf{e} are uncorrelated. The frequency histogram of $\hat{\mathbf{e}}$ corroborates that \mathbf{e} is well-represented by a normal distribution. The box plots indicate that the proposed GMPE has successfully accounted for earthquake event effects as they are centered in zero.

Scatter plots of $\hat{\boldsymbol{\xi}}$ versus M_w and R_{hypo} are also shown in Figure 3.16. The random behavior around the zero-axis observed in these plots supports the linearity of the natural logarithm of D_{Sr} with respect to M_w and R_{hypo} . Similar results as those given in Figure 3.16 were observed when performing residual analyses for GMPEs B, C, and D. For instance, graphical diagnostics are shown in Figure 3.17 for GMPE C.

It should be mentioned that preliminary residual analyses were conducted to identify the presence of outliers as part of the GMPEs fitting process. Initially, GMPEs A and B were fitted considering the entire data set of 141 observations, but it was noticed that four data points appeared to be outliers. These outliers were discarded for the final regression analyses. Similarly, 36 and 37 outliers were

discarded in the regression analysis for GMPEs C and D, respectively. Thus, the results presented in Tables 3.2, 3.3, and 3.4 and Figures 3.15, 3.16, and 3.17 are those of a refit of the models excluding such outliers. In Figure 3.14 the outliers are marked in red.

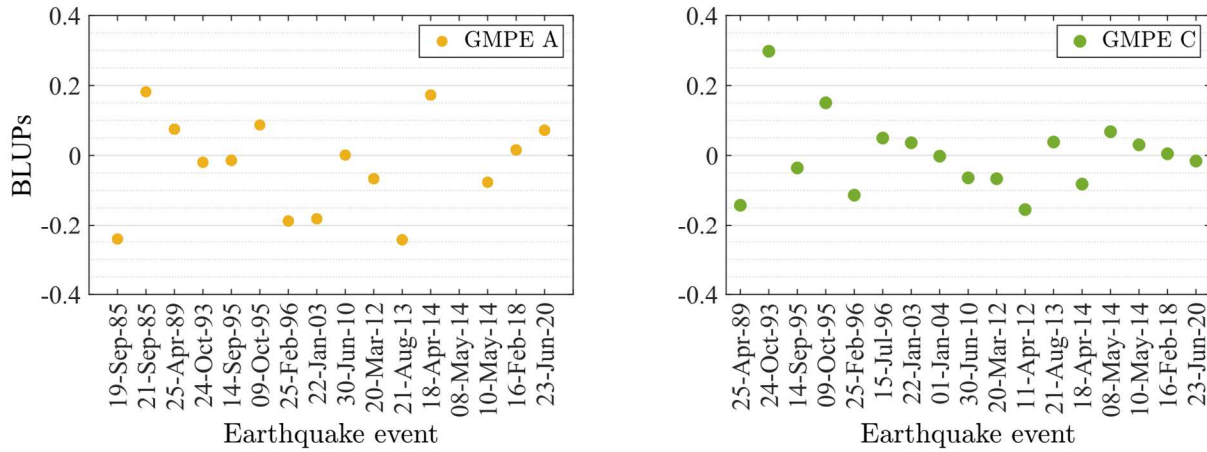


Figure 3.15 Estimated BLUPs for GMPEs A and C, respectively

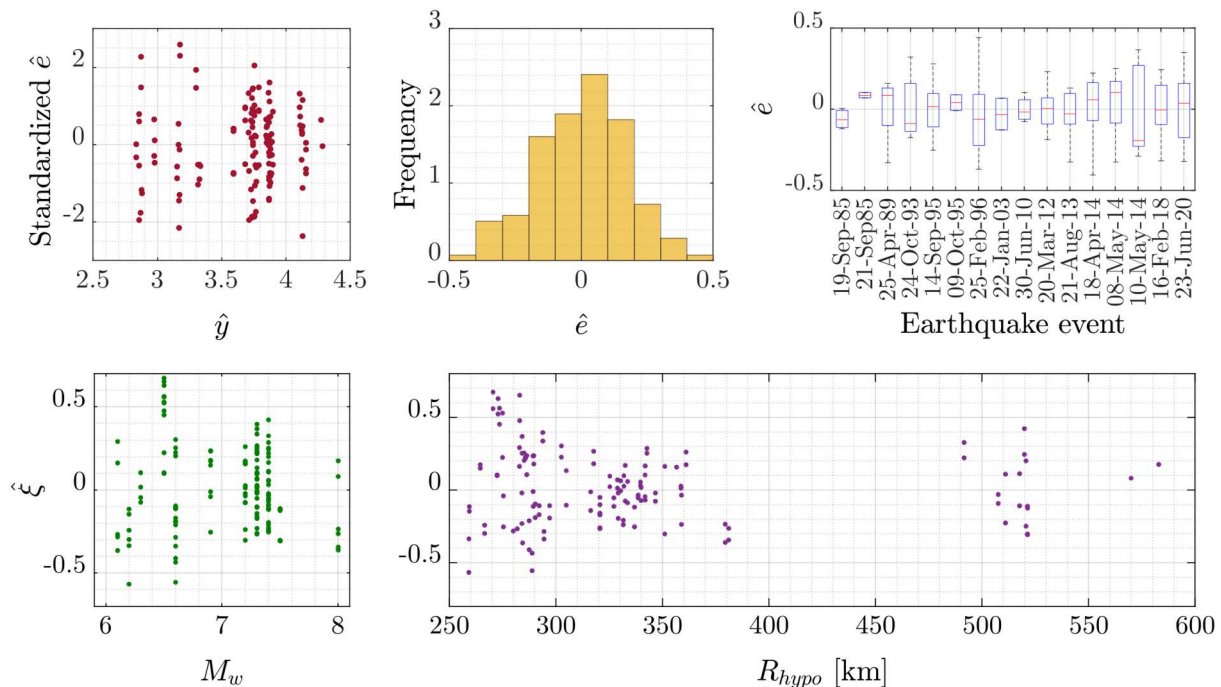


Figure 3.16 Residual analyses for GMPE A. At the top there are illustrated a scatter plot of the standardized $\hat{\epsilon}$ versus \hat{y} , a frequency histogram of $\hat{\epsilon}$, and box plots of $\hat{\epsilon}$ grouped by earthquake event. At the bottom there are illustrated scatter plots of $\hat{\xi}$ versus M_w and R_{hypo} , respectively

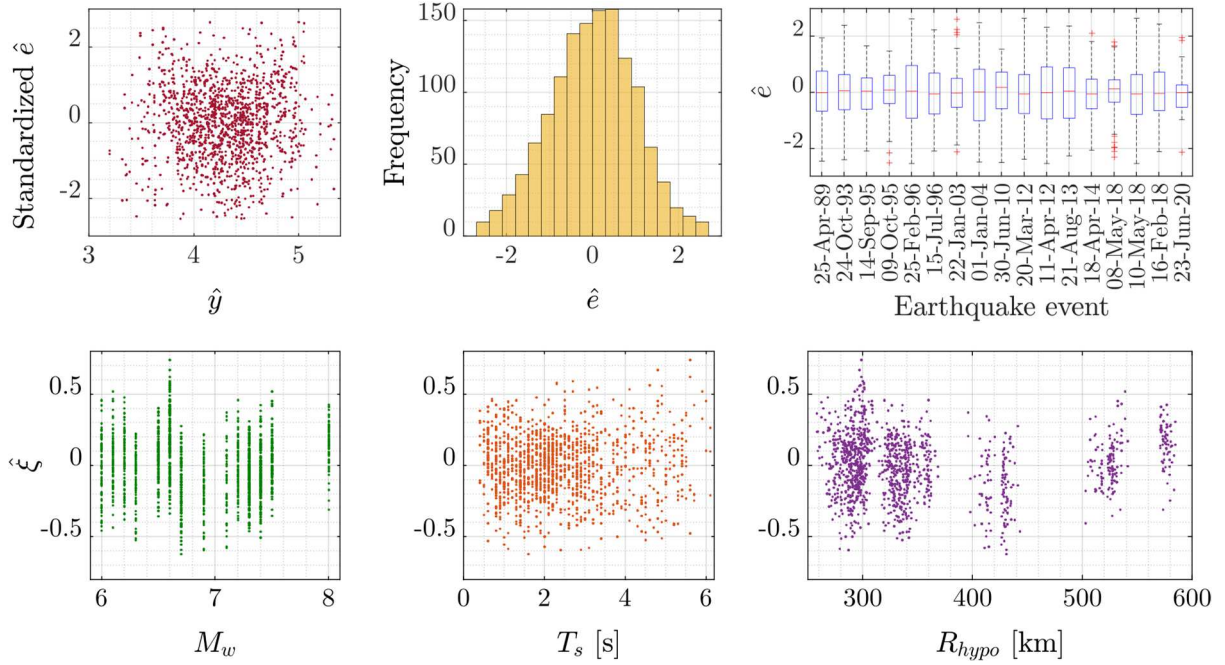


Figure 3.17 Residual analyses for GMPE C. At the top there are illustrated a scatter plot of the standardized $\hat{\epsilon}$ versus \hat{y} , a frequency histogram of $\hat{\epsilon}$, and box plots of $\hat{\epsilon}$ grouped by earthquake event. At the bottom there are illustrated scatter plots of $\hat{\xi}$ versus M_w , R_{hypo} , and T_s , respectively

3.4 Discussion

Four GMPEs were presented in this chapter. They allow estimating the strong-motion duration in sites located in Mexico City. The moment magnitude M_w , either R_{hypo} or R_{rup} , and T_s were the elements of \mathbf{X} selected to develop the GMPEs. A great effort was made in obtaining reliable data for its measurement. For instance, the moment and focal-mechanism data of the selected interplate earthquakes taken from the U.S. Geological Survey (USGS) National Earthquake Information Center (NEIC) catalog,¹⁰⁸ and reported in Appendix C, used to compute R_{rup} were generated using a kinematic finite fault inversion approach based on the method of Ji et al.,¹⁴⁰ which adequately considers the uncertainties related to the complex geometry of the faults.¹⁴¹

The strong-motion duration was measured from the orthogonal horizontal accelerograms of ground-motion recordings following the definition of D_{Sr} given in Eq. (2.8) and considering $a_1 = 0.05$ and $a_2 = 0.95$. The total durations t_f of the accelerograms used to compute D_{Sr} were considered equal to the portion of the accelerograms bounded by $a_0 = 2 \text{ cm/s}^2$. This was done to avoid overestimating the

strong-motion duration due to the influence of the accelerations registered in the initial and final parts of the accelerograms that (in most cases) are no intrinsic part of the ground motions. Disregarding the initial fraction of an accelerogram, which corresponds to the time elapsed between the P- and S-wave arrivals, insignificantly affect the estimated values of D_{Sr} . For instance, for all the accelerograms considered in the regression analyses, differences up to 5 s were observed. On the other hand, with the proposed value of $a_0 = 2 \text{ cm/s}^2$, the extended codas characterizing the ground motion in Mexico City are preserved.

Setting the acceleration threshold $a_0 = 2 \text{ cm/s}^2$ excludes accelerograms with very weak amplitudes. In particular, accelerograms with $PGA < 3 \text{ cm/s}^2$ were disregarded for the development of the strong-motion duration GMPEs. Nevertheless, ground motions associated with such values of PGA are unlikely to cause any harm to the civil engineering structures located in Mexico City.

It must be noted that, although noise may negligibly affect the estimates of any definition of the strong-motion duration, the accelerograms were filtered by rigor. The recommendations given in the works of Carreño et al.¹⁴² and Boore¹⁴³ were attained for this purpose. In particular, each accelerogram was filtered as follows:

1. First, a baseline correction of the signal was carried out.
2. Then, a 4th order Butterworth (bandpass) filter was applied. The high-pass cutoff frequency, f_c , was selected based on a visual examination of where the long-period portion of the FAS of the accelerogram deviates from the tendency of decay in the proportion of the frequency squared (considering 0.15 Hz as the maximum possible value for f_c). Also, the velocity and displacement time histories were inspected to detect unphysical tendencies. The low-pass cutoff frequency was set at 30 Hz. Before the application of the bandpass filter, a pad of zeros equal to $1.5n_b/f_c$, where n_b is the order of the Butterworth filter, was added to the signal. Half of this pad was added at the beginning and the other half at the end of the accelerogram.

The values of f_c and the low-pass cutoff frequency (equal to 30 Hz) employed when processing the accelerograms ensure that the filter will not have a significant effect on the computation of response-spectral ordinates for values of T_e varying from 0.05 s to 5 s (which will be used in Chapter 5). As an instance, Abrahamson and Silva¹⁴⁴ recommended using only values of response-spectral ordinates for the

interval where f is greater than 1.25 times f_c and less than $1/1.25$ times the low-pass cutoff frequency.

It should be mentioned that the estimates of T_s were computed from the unfiltered accelerograms. Particularly, only spectral smoothing was applied before the calculation of the spectral horizontal-to-vertical ratios $F_1(\omega)/F_V(\omega)$ and $F_2(\omega)/F_V(\omega)$.

The selection of the optimal strong-motion duration GMPEs was determined by: (i) likelihood ratio tests, such as the Akaike information criterion¹⁴⁵ (AIC) and Bayesian information criterion¹⁴⁶ (BIC), which are penalized likelihood criteria that allow determining the quality of a model among a finite set of models, (ii) ensuring that all fixed-effects coefficients and variance components were statistically significant, and (iii) guaranteeing that the behavior observed in the empirical data was well-represented by the fitted GMPEs. Thus, the GMPEs given in Eqs. (3.7) and (3.8) reached the best statistics. Note that the GMPEs given in Subsection 3.3.2 for sites located in GZI are slightly different than those given in the work of López-Castaneda and Reinoso.⁵¹ Either GMPE fits the data well, but the ones presented in this study have lower values of V . Moreover, GMPE B has a simpler functional form, which facilitates its application in practice.

Regardless of the functional form analyzed and as discussed in Subsection 3.3.2, the trends observed in the empirical strong-motion data were maintained. That is, a positive association of D_{Sr} in both M_w and T_s and a negative association between D_{Sr} and either R_{hypo} or R_{rup} were observed. Analogous trends are reported in research works focused on developing GMPEs for other definitions of the strong-motion duration (see Section 2.3) or energy-related ground-motion parameters such as I_A .^{147–149}

In the work of López-Castaneda and Reinoso¹⁵⁰ regression analyses were also performed grouping the data both by earthquake event and geotechnical zone, as a strategy to evaluate the possible influence that the local site conditions of Mexico City could have in the estimation of D_{Sr} . It was concluded that the dependence of D_{Sr} on geotechnical and topographic conditions is significant. Such kinds of GMPEs could be improved as more detailed micro zoning of Mexico City becomes available. The above leads to the conclusion that GMPEs must be updated every so often. The more (reliable) data is used for their development, the better the estimates of the expected ground motion at Mexico City. The latter encourages the constant improvement of the accelerograph networks operating not only throughout Mexico City but in several parts of the world subjected to seismic hazards.

[This page intentionally left blank]

CHAPTER 4

Strong-motion Duration Hazard

4.1 Introduction

The earthquake-resistant design seeks to produce structures that can withstand a certain ground motion without excessive damage. The ground-motion level y (for a specific Y) characterizing such ground motion is usually determined with the aid of an SHA. It may be conducted deterministically or probabilistically.

A *deterministic seismic hazard analysis* (DSHA) aims to estimate the ground motion expected at a site of interest from a particular earthquake scenario. The scenario consists of the postulated occurrence of an earthquake of a specified size occurring at a specified location, typically an active fault.⁴ For instance, the scenario earthquake can be either the *maximum probable earthquake* (MPE) or the *maximum credible earthquake* (MCE). The first is defined as the maximum historical event and the second is the maximum earthquake that appears capable of occurring under the known tectonic framework.¹⁵¹ Statistical models, like the GMPEs given in Chapter 3, are generally used for the estimation of the parameters characterizing the expected ground motion at the site caused by the scenario earthquake.

When performing a DSHA, not just one but several scenario earthquakes are commonly evaluated to select the one that will possibly produce the strongest ground motion at a site. The chosen one is called the *controlling earthquake* (or *design earthquake*). For instance, consider two earthquake scenarios that might affect the site where station CU01 was located. The first scenario consists in taking as the MPE the September 19, 1985 earthquake and the second in specifying as the MCE one earthquake with $M_w = 7.5$ occurring at $R_{hypo} = 250$ km. Using GMPE A, the MPE will generate a mean value of $D_{Sr} = 84$ s, and the MCE a value of $D_{Sr} = 69$ s. The former is recognized as the controlling earthquake, and it will be used to characterize the ground motion at the site of interest.

Although a DSHA provides an easy-to-follow and transparent method for estimating the expected level of ground motion at a site,⁸ it provides no information on the likelihood of occurrence of the scenario earthquake or the level of ground motion that might be expected during a finite time period.⁹ Moreover, the effects of any uncertainties involved in the modeling of the timing, location, size, and resulting

level of shaking of future earthquakes are not explicitly considered in it.^{4,152} A PSHA is a recognized technique, originally developed by Professors Luis Esteva Maraboto and Carl A Cornell,¹⁵³ capable of addressing the issues identified above because it considers the broad set of earthquakes that can occur on each fault or source zone that might affect a site of interest to calculate not merely the expected levels of ground motion at the site, but their exceedance probabilities.⁹

At its core, a PSHA uses the law of total probability to estimate the probability that Y takes a value greater than y as follows:

$$P(Y > y) = \int P(Y > y|x_1, \dots, x_p) f_{X_1, \dots, X_p}(x_1, \dots, x_p) dx_1 \cdots dx_p \quad (4.1)$$

where $P(Y > y|x_1, \dots, x_p)$ denotes the complementary distribution function of Y conditional on a set of explanatory variables X_1, \dots, X_p , which are defined by the joint density function $f_{X_1 \dots X_p}$. For instance, taking only M_w and R_{hyppo} as the explanatory variables X , and assuming that they are independent and had marginal distribution functions f_{M_w} and $f_{R_{hyppo}}$, respectively, the probability of exceeding y can be computed as follows:

$$P(Y > y) = \iint P(Y > y|m, r) f_{M_w}(m) f_{R_{hyppo}}(r) dm dr \quad (4.2)$$

where $P(Y > y|m, r)$ is the complementary distribution function of Y conditional on M_w and R_{hyppo} . Then, considering the contribution of N_S earthquake sources that can affect a site of interest, the mean annual rate of exceedance of y can be computed as:

$$\lambda_y = \sum_{i=1}^{N_S} \lambda_{m_{0_i}} \iint P(Y > y|m, r) f_{M_{w_i}}(m) f_{R_{hyppo_i}}(r) dm dr \quad (4.3)$$

where, for each $i = 1, \dots, N_S$ earthquake source, $\lambda_{m_{0_i}}$ is the mean annual rate at which an earthquake with a magnitude equal to m_0 will be exceeded. Notice that a *hazard curve* gives the estimated λ_y for a finite set of ground-motion levels y .

Assuming that the occurrence of earthquakes follows a *Poisson process*, i.e., that the events of a sequence occur with no “memory” of time, location, or size of preceding events, their interarrival times are exponentially distributed, and the overall rate of the process is stationary,⁹ it can be said that the occurrence of ground motions also follows a Poisson process.¹⁵⁴ Thereby, the probability that Y takes a value greater than y (at least once) in T can be written as follows:

$$P(Y > y) = 1 - \exp(-\lambda_y T) \quad (4.4)$$

Notice that, in the context of SRAs, T is usually chosen to represent the design or economic life of a structure and is called *exposure time*. Also, for earthquake engineering applications it is quite convenient to estimate T_r , which can be defined from Eq. (4.4) as:

$$T_r = \frac{1}{1 - \exp(-\lambda_y)} \quad (4.5)$$

where the denominator equals the probability that there is at least one event within one unit time interval T , i.e., within one year. Note that T_r is almost equal to the mean inter-arrival time, \bar{T} , defined as the inverse of λ_y , when they are greater than 10.¹⁵⁵ In Appendix E there are summarized typical values of exceedance probabilities of ground-motion levels y and associated values of T_r for seismic hazard analysis.

Thus, the probabilistic evaluation of the strong-motion duration hazard for sites located in Mexico City was performed considering D_{Sr} as Y . The identification and evaluation of all the interplate earthquake sources capable of inducing ground motions of engineering significance in sites located in the geographic region of interest are described first in Section 4.2. Then, the PSHAs results are summarized in Section 4.3. They were obtained using two of the GMPEs developed in Chapter 3, which allow to determine the complementary distribution function of D_{Sr} conditional on M_w and R_{hypo} necessary to solve Eq. (4.3). A brief discussion of the results is given in Section 4.4.

4.2 Identification and Characterization of Earthquake Sources

The identification of the geometries of earthquake sources depends on the tectonic processes involved in their formulation. For instance, earthquakes induced by volcanic activity or originating at small fault planes can be associated with *point sources*. On the other hand, well-defined fault planes in which earthquakes occur at many different (shallow) locations can be modeled as *areal sources*. The regions where earthquake focal mechanisms are not well defined can be modeled as *volumetric sources*.⁴

Identifying earthquakes of similar nature requires extensive knowledge of the tectonic and geologic structures that characterize the region of interest. Thus, this study relies in the work of Ramírez-Herrera and Urrutia-Fucugauchi.⁹⁷ They conducted a concrete and comprehensible analysis, employing topographic,

morphologic, geologic, and bathymetric maps, as well as field studies, to describe the morphology of the southern coast of Mexico. Also, the research works of Ordaz and Reyes¹⁵⁶ and Zúñiga et al.,¹¹⁰ who defined an earthquake source zonation for Mexico, were consulted. Thus, based on these research works, four source zones are proposed in this study. They encompass interplate earthquakes with $M_w \geq 6.0$ that occurred between 1900 and 2021 in the Mexican subduction zone (see Appendix B). The four source zones are depicted in Figure 4.1 and, as noticed, can be defined as areal sources.

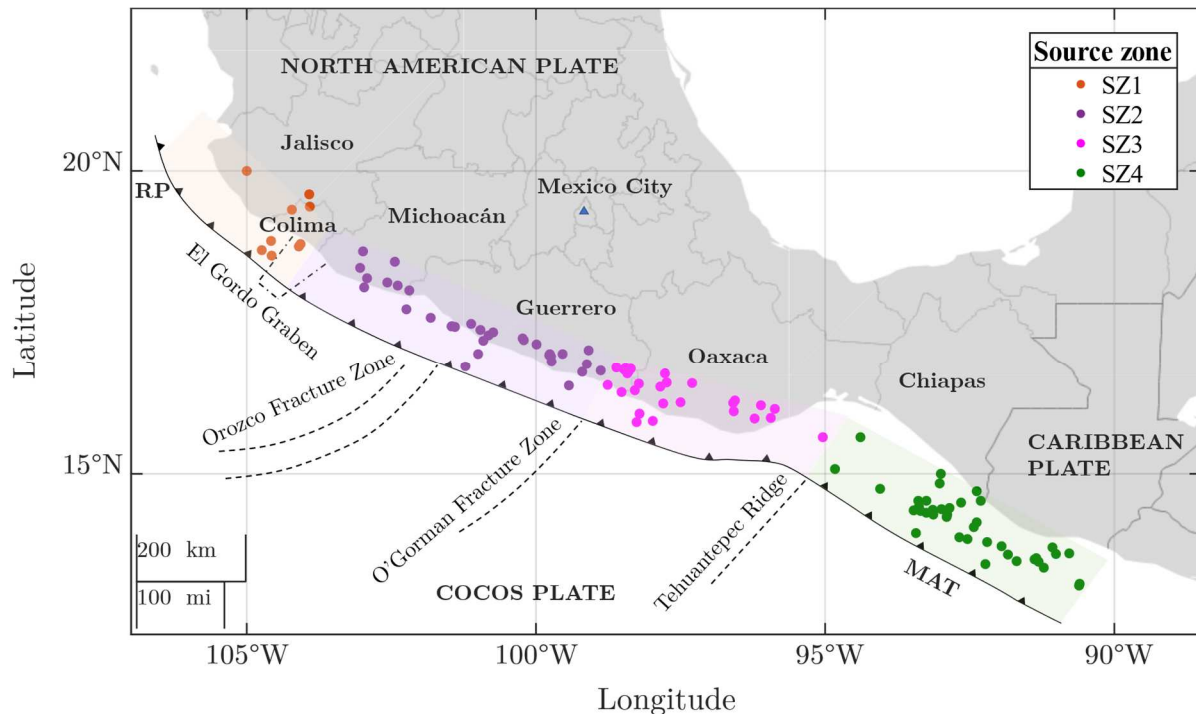


Figure 4.1 Map depicting the four source zones identified in this study for interplate earthquakes occurring along the MAT. The abbreviation RP means Rivera Plate. The epicenters of earthquakes that occurred between 1900 and 2021 and were considered to estimate the seismicity of each source zone are marked with circles. The blue triangle stands for an observational site located in Mexico City with geographic coordinates 19.35°N, 99.15°W

As per Figure 4.1, the first source zone, named SZ1, comprises the coupled interface of the Rivera and North American plates. It extends along the coast of Jalisco to the coast of Colima. Specifically, its boundary (to the southeast) is defined by the presence of the El Gordo Graben. The second source zone, named SZ2, corresponds to the coupled interface of the Cocos and North American plates that

extends from the southern part of the coast of Colima to the coast of Michoacán. The third source zone, named SZ3, also corresponds to the coupled interface of the Cocos and North American plates but covers the southern part of the coast of Michoacán and most of the coast of Oaxaca. The upper boundary of SZ3 is defined based on a change in seismicity near the O’Gorman Fracture Zone, whereas its lower boundary corresponds to the region where the Tehuantepec Ridge intersects the MAT. The fourth source zone, named SZ4, mainly comprises the coupled interface of the Cocos and Caribbean plates. It covers the southern part of the coast of Oaxaca and the coast of Chiapas. Its lower boundary corresponds to a region where the geometry of the subduction changes from a shallow to a steep dipping angle.

Note that SZ2 could be split into two source zones delimited by the Orozco Fracture Zone, but it was wanted to match, somehow, the zonation proposed by both Ordaz and Reyes¹⁵⁶ and Zúñiga et al.¹¹⁰ Also, it must be pointed out that the lower boundary of SZ4 was set close to the geographical demarcation between Guatemala and El Salvador because, although the earthquakes occurring at this region certainly implicate null danger at Mexico City, its consideration is important to calculate more accurately the seismicity in the said source zone.

The quantitative description of the time, size, and spatial distribution of earthquake occurrences is defined next under the assumption that each source zone describes a domain within which earthquakes (i) are equally likely in space, (ii) conform to a single magnitude distribution, (iii) have the same maximum magnitude, m_u , and (iv) are independent of each other.⁹

4.2.1 Earthquake Occurrence Models and Magnitude Distribution

In this study, the temporal occurrence of earthquakes is described by the Poisson distribution, which provides a simple framework for evaluating probabilities of events that follow a Poisson process. Keep in mind that the probability function of a Poisson-distributed random variable N , denoting the number of events n occurring in a fixed time interval T , is given by¹⁵⁷:

$$p_N(n) = P(N = n) = \frac{\mu^n \exp(-\mu)}{n!} \quad (4.6)$$

where $n!$ is the factorial of the non-negative integer n , and the parameter $\mu > 0$ is equal to both the mean and variance of the Poisson distribution. Equation (4.6) can also be written as:

$$P(N = n) = \frac{(\lambda t)^n \exp(-\lambda T)}{n!} \quad (4.7)$$

where λ is the mean rate of occurrence of the events. Given that, the probability of occurrence of at least one event in the time interval T of interest can be computed as:

$$P(N \geq 1) = 1 - \exp(-\lambda T) \quad (4.8)$$

On this basis, one can compute the probability that a certain earthquake magnitude m will be exceeded (at least once) in a predefined time interval T as follows:

$$P(M_w > m) = 1 - \exp(-\lambda_m T) \quad (4.9)$$

where λ_m is the mean rate of occurrence of earthquakes which magnitude is greater than m .

Gutenberg and Richter¹⁵⁸ first described the underlying pattern of earthquake magnitudes and their occurrence. They proposed the following empirical relation to estimate λ_m ^{159,160}:

$$\log_{10} \lambda_m = a + bm \quad (4.10)$$

where, for a given source zone, coefficient a indicates the rate of seismic activity, and coefficient b describes the ratio between the number of small and large earthquakes.⁹ In seismology, Eq. (4.10) is known as the *Gutenberg-Richter law*.

The standard Gutenberg-Richter law given in Eq. (4.10) is equivalent to the power-law distribution of earthquake energies or moments,¹⁶¹ and can also be expressed in exponential form as follows:

$$\lambda_m = 10^{a-bm} = \exp(\alpha - \beta m) \quad (4.11)$$

where $\alpha = a \ln(10)$ and $\beta = b \ln(10)$. In Eq. (4.11) 10^a gives the mean yearly number of earthquakes with magnitude higher than zero per unit of time.

The exponential form of the Gutenberg-Richter law given in Eq. (4.11) covers an infinite range of magnitudes, which is not necessarily favorable as much higher magnitude values can be estimated than those that would possibly be generated in the source zone of interest. On the other hand, and for engineering purposes, it is common to disregard those earthquakes that are unlikely to cause significant damage at the site of interest. For these reasons, it is quite convenient to set both an upper and lower limit of magnitude in the earthquake occurrence model.

Setting a lower-bound m_0 for earthquake magnitudes leads to a “shifted” form of the exponential Gutenberg-Richter law given in Eq. (4.11) as follows:

$$\lambda_m = \lambda_{m_0} \exp[-\beta(m - m_0)] \quad m_0 \leq m \quad (4.12)$$

Note that, as introduced in Section 4.1, λ_{m_0} is the mean annual rate of exceedance of the lower-bound m_0 and can be estimated from Eq. (4.11). Based on Eq. (4.12), f_{M_w} can be written as:

$$f_{M_w}(m) = \beta \exp[-\beta(m - m_0)] \quad m_0 \leq m \quad (4.13)$$

Then, introducing m_u , Eq. (4.12) becomes^{162,163}:

$$\lambda_m = \lambda_{m_0} \frac{\exp[-\beta(m - m_0)] - \exp[-\beta(m_u - m_0)]}{1 - \exp[-\beta(m_u - m_0)]} \quad m_0 \leq m \leq m_u \quad (4.14)$$

Given the “shifted and truncated” form of the exponential Gutenberg-Richter law in Eq. (4.14), f_{M_w} can be expressed as follows:

$$f_{M_w}(m) = \frac{\beta \exp[-\beta(m - m_0)]}{1 - \exp[-\beta(m_u - m_0)]} \quad m_0 \leq m \leq m_u \quad (4.15)$$

The estimation of the seismic activity parameters β and λ_{m_0} , as well as the determination of the magnitude thresholds m_0 and m_u , necessary to compute the corresponding exceedance rate λ_m of each source zone is developed next.

4.2.1.1 Estimation of Seismic Activity Parameters

Various mathematical approaches are available in the literature for estimating β (or b) and λ_{m_0} from historical data.^{164,165} For instance, assuming that the magnitude data are random samples from a population obeying the standard Gutenberg-Richter law given in Eq. (4.10) and using the MLE method, Aki¹⁶⁶ gave the following estimator of b :

$$\hat{b} = \frac{\log_{10} e}{\bar{m} - m_0} \quad (4.16)$$

where \bar{m} and m_0 are the arithmetic mean and minimum earthquake magnitudes in a given sample (catalog), respectively, and e is a mathematical constant known as Euler’s number and is approximately equal to 2.7183. Be informed that Utsu¹⁶⁷ was the first to propose the estimator given in Eq. (4.16) but he used the method of

moments to obtain the solution. Note that the Aki-Utsu estimator of b given in Eq. (4.16) is equivalent to:

$$\hat{\beta} = \frac{1}{\bar{m} - m_0} \quad (4.17)$$

Even today, the Aki-Utsu estimator of β given in Eq. (4.17) is preferred. Nevertheless, a complete earthquake catalog, starting from the specified level of completeness m_0 , is needed to apply it. The latter can be quite challenging because observation periods for large earthquakes are usually longer than those for small, or even moderate, earthquakes. For instance, the catalog compiled for this study (see Appendix B) is complete for $M_w = 7.0$ since 1900, $M_w = 6.5$ since 1950, and $M_w = 6.0$ since 1976. Figure 4.2 shows scatter plots of the earthquake occurrences over time for each source zone.

Then, various authors have proposed estimators for both β (or b) and λ_{m_0} considering unequal observation time periods T with different m_0 .^{168–170} The approach proposed by Kijko and Smit¹⁶⁹ was used in this study.

Let's consider that an incomplete earthquake catalog, with N_T earthquakes, is divided into $j = 1, \dots, N_C$ sub-catalogs, each with N_{E_j} earthquakes. Each sub-catalog j is complete for time periods T_j and earthquakes with magnitude m greater than or equal to m_{0_j} . Then, the estimator of β proposed by Kijko and Smit¹⁶⁹ is:

$$\hat{\beta} = \frac{N_T}{\sum_{j=1}^{N_C} S_j} \quad (4.18)$$

where S_j is computed as follows:

$$S_j = \sum_{k=1}^{N_{E_j}} (m_{k,j} - m_{0_j}) \quad (4.19)$$

If β is known, the estimator of $\lambda_{m_{0_1}}$ proposed by Kijko and Smit¹⁶⁹ is:

$$\lambda_{m_{0_1}} = \frac{N_T}{\sum_{j=1}^{N_C} T_j \exp(\hat{\beta} \Delta_j)} \quad (4.20)$$

where Δ_j is equal to $m_{0_j} - m_{0_1}$. Note that, for a complete catalog with observation period T , the estimator of β given in Eq. (4.18) reduces to the Aki-Utsu estimator

of β given in Eq. (4.17). Moreover, the maximum likelihood estimator of λ_{m_0} given in Eq. (4.20) takes the well-known form N_T/T .

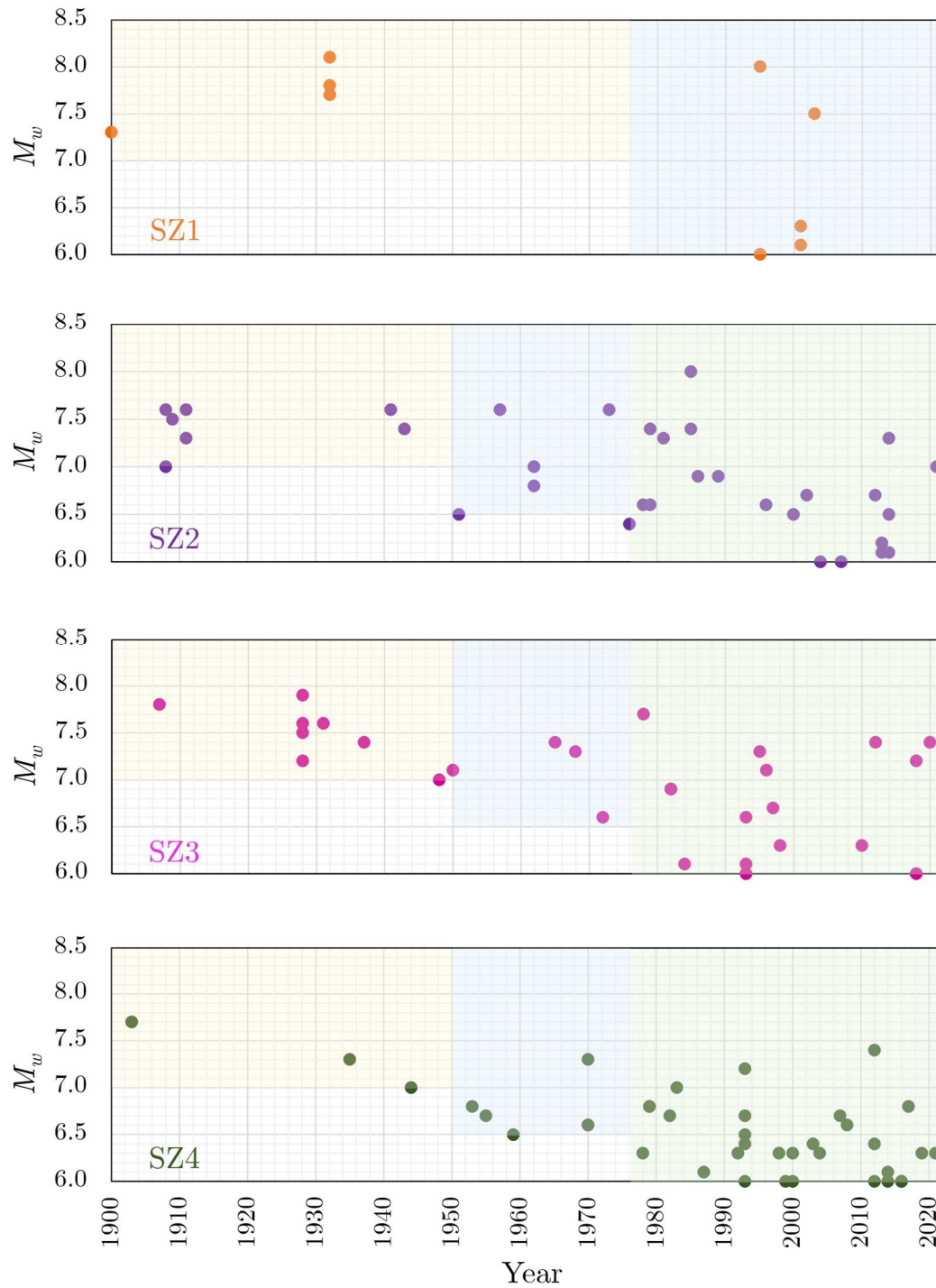


Figure 4.2 Scatter plots of earthquake occurrences over time. For each source zone, the shaded areas represent the grouping of earthquakes into sub-catalogs

Some of the nomenclature used above was borrowed from the work of Ordaz and Giraldo.¹⁷⁰ They also propose estimators of β and λ_{m_0} but, contrary to the estimators proposed by Kijko and Smit, which maximize the marginal likelihoods of the parameters, they gave estimators that maximize their joint likelihood. Vermeulen and Kijko¹⁷¹ demonstrated that the estimators of Ordaz and Giraldo¹⁷⁰ are merely a special case of the joint maximum likelihood expression given by Kijko and Sellevoll.¹⁷²

Based on the sub-catalogs shown in Figure 4.2, the estimates of β and $\lambda_{m_{o_1}}$ were obtained using Eqs. (4.18) and (4.20), respectively. Table 4.1 summarizes some statistics used in the estimation process and Table 4.2 reports the results. For each source zone, Figure 4.3 shows a curve of magnitudes ranging from m_0 to m_u versus their correspondent exceedance rate λ_m . The curves were developed using Eq. (4.14) and the estimates of β and $\lambda_{m_{o_1}}$ reported in Table 4.2. The magnitude thresholds m_0 and m_u used are also reported in Table 4.2. The lower-bound m_0 was set equal to 6.0 for all source zones. Such value is the smallest earthquake magnitude that is thought to be capable of damaging structures located in Mexico City. Therefore, λ_{m_0} equals $\lambda_{m_{o_1}}$ for each source zone. The upper-bound m_u was specified as $m_{max} + 0.2$, where m_{max} is the magnitude of the MPE known from each source zone. From Table 4.2 and Figure 4.3, one can tell that the seismic activity rate corresponding to m_o is much lower for SZ1 than for the other three source zones, which have a similar activity rate.

Table 4.1 Statistics used to estimate the β -values and seismicity rates λ_{m_0}

Source zone	Sub-catalog	Initial year	m_0	N_E
SZ1	1	1976	6.0	5
	2	1900	7.0	4
SZ2	1	1976	6.0	21
	2	1950	6.5	5
	3	1900	7.0	7
SZ3	1	1900	6.0	16
	2	1950	6.5	4
	3	1976	7.0	8
SZ4	1	1900	6.0	30
	2	1950	6.5	6
	3	1976	7.0	3

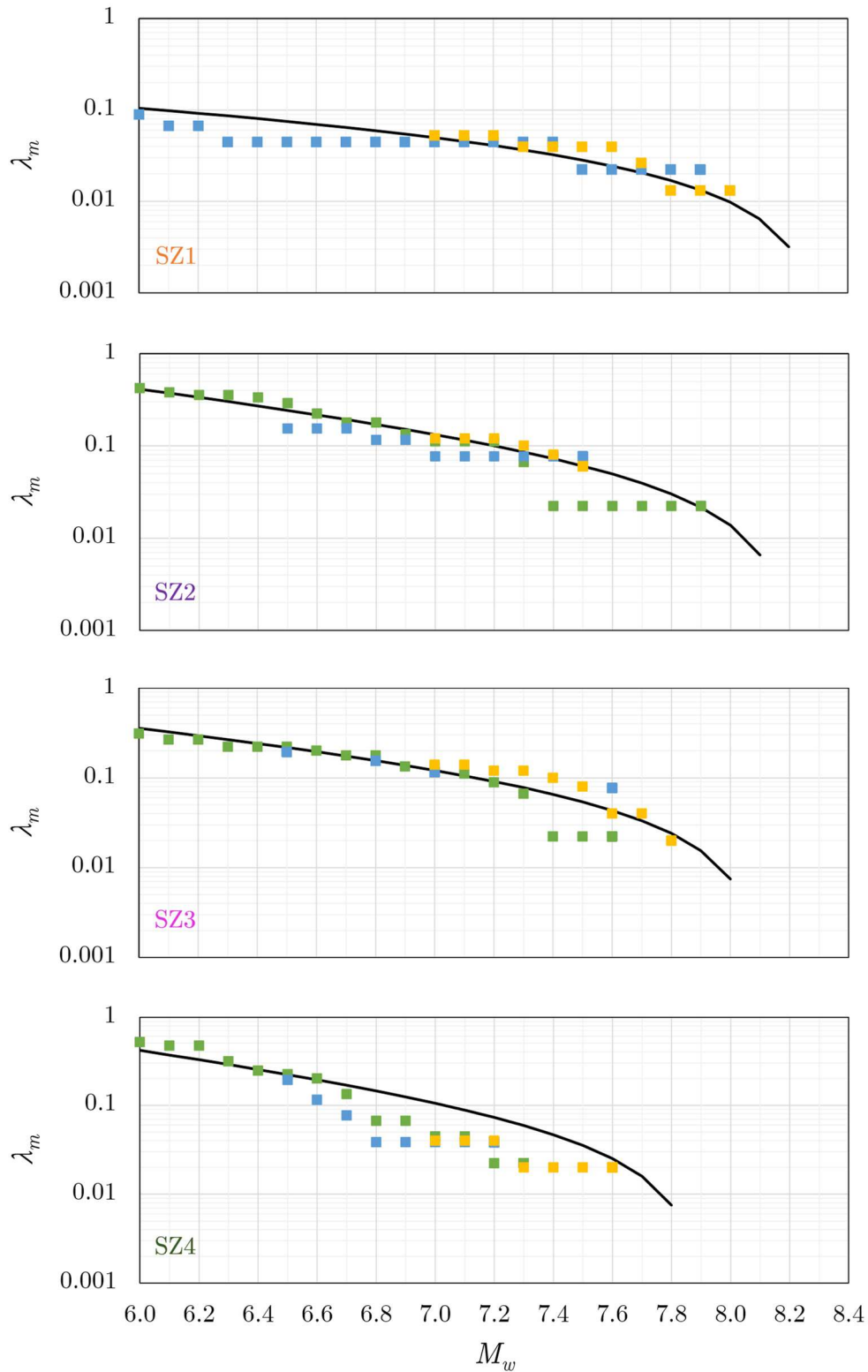


Figure 4.3 Annual exceedance rates of magnitude λ_m computed from the “shifted and truncated” form of the exponential Gutenberg-Richter law and data given in Table 4.2

Table 4.2 Estimates of the β -values and seismicity rates λ_{m_0} , and magnitude thresholds m_0 and m_u

Source zone	β	λ_{m_0} [1/year]	m_0	m_u
SZ1	0.3030	0.1041	6.0	8.3
SZ2	0.8571	0.4119	6.0	8.2
SZ3	0.7273	0.3559	6.0	8.1
SZ4	1.0130	0.4139	6.0	7.9

4.2.2 Source-to-site Distribution

The geometry of a source zone is commonly used to define the probability distribution of R .^{4,9} For instance, the distance between a point source and a site of interest can be seen as a constant, r , thus the probability that $R = r$ is one and the probability of $R \neq r$ is zero. On the other hand, when the depth of a fault plane is small, a planar source can be modeled as a linear source. Assuming that earthquakes are uniformly distributed over the fault length L , f_R can be computed as follows:

$$f_R(r) = \frac{r}{L\sqrt{r^2 - r_0^2}} \quad (4.21)$$

where r_0 is the closest distance to the fault plane. A schematic of the geometries described above is shown in Figure 4.4. On the other hand, for a source zone with complicated geometry, the probability distribution of R is commonly evaluated by numerical methods.^{4,173}

In this study, instead of defining the probability distribution of R by analytical or numerical methods, the statistical inference was used. This decision was made to reduce uncertainties related to modeling complex fault planes that are (for the author) imperfectly understood. Bear in mind that *statistical inference* is the process of using data analysis to infer properties of an underlying distribution of probability.¹⁷⁴ Therefore, for each source zone, the distances from an observation site located in Mexico City to the earthquake hypocenters were computed. Note that such point-source distance measure is indeed R_{hypo} . The observational site was set at the geographic coordinates 19.35°N, 99.15°W, with $H_s = 2240$ m. Figure 4.1 shows the location of the site on a map of Mexico. Table 4.3 summarizes the minimum and maximum values of R_{hypo} computed for each source zone. The closest R_{hypo} corresponds to the July 28, 1957 earthquake, with $M_w = 7.6$, that occurred in SZ2,

whereas the farthest corresponds to the November 20, 2004 earthquake, with $M_w = 6.3$, that occurred in SZ4.

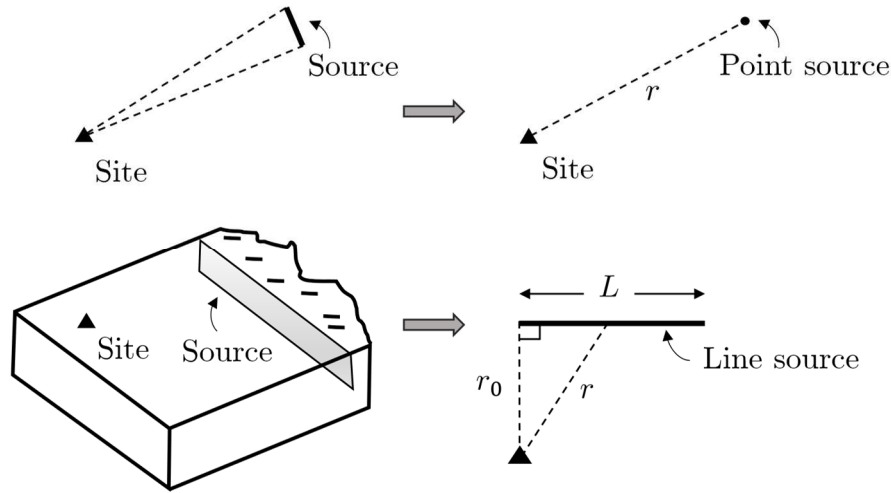


Figure 4.4 Schematic of the variations of R for a short fault that can be modeled as a point source and shallow fault modeled as a linear source

Table 4.3 Minimum and maximum values of R_{hypo} , i.e., r_{min} and r_{max} , respectively, observed for each source zone

R_{hypo}	SZ1	SZ2	SZ3	SZ4
r_{min} [km]	500	258	293	654
r_{max} [km]	617	426	603	1144

Various probability distributions were evaluated to determine which one best describes the set of R_{hypo} observations corresponding to each source zone. The gamma, generalized extreme value (GEV), lognormal, and normal distributions gave the best fits to the data. The one-sample Kolmogorov-Smirnov (KS) test was used to evaluate how well each probability distribution fits each set of point-source distances. Concretely, the one-sample KS test is a nonparametric test of the null hypothesis that the data comes from a population with a specific distribution function.¹⁷⁵ In this study, the significance level was set at 0.05. For each source zone, Table 4.4 summarizes the p -values of the hypothesis tests performed. Small p -values cast doubt on the validity of the null hypothesis. As per Table 4.4, the GEV distribution gave the best p -values for SZ2, SZ3, and SZ4. The p -values for SZ1 resulted when the January 22, 2003 earthquake was included as part of such source

zone. The mentioned earthquake had $M_w = 7.5$ and originated in the El Gordo Graben, i.e., near the juncture of the North American, Rivera, and Cocos plates. Without this observation, the estimated p -value for the GEV distribution was 0.8774. Based on the results given in Table 4.4, it appears that the GEV distribution describes well the set of point-source distance observations.

Table 4.4 Probability of observing a test statistic at least as extreme as the observed value under the null hypothesis that the point-source distances came from a population with a specific distribution function

Distribution	p -value			
	SZ1	SZ2	SZ3	SZ4
Gamma	0.7595	0.4013	0.5360	0.5735
GEV	0.7126	0.8337	0.7954	0.5945
Lognormal	0.8150	0.4696	0.6287	0.5125
Normal	0.7705	0.3428	0.4468	0.5888

Other goodness-of-fit tests were also carried out to determine if indeed the GEV distribution could represent R_{hypo} . For instance, graphical diagnostics are shown in Figure 4.5. These include probability plots, density histograms, and plots of density functions. Briefly, a *probability plot* is a graphical technique for assessing whether or not a sample of data follows a given probability distribution. The sample is plotted against a theoretical distribution in such a way that the points should form approximately a straight line. Departures from this straight line indicate departures from the specified distribution. Similar to a frequency histogram, a *density histogram* is a type of bar plot for numeric data that groups data into bins of equal width, but each bin is plotted as a bar whose height equals the proportion of data points that are in that bin divided by the length of the bin. Thus, the vertical axis of a density histogram shows units that make the total area of all the bars add to one.⁴² As seen from Figure 4.5, the GEV distribution (depicted with blue solid lines) appropriately estimates the probability of occurrence of the different possible outcomes of R_{hypo} .

The density function of R_{hypo} described by the GEV distribution, with location parameter μ , scale parameter σ , and shape parameter κ , can be denoted as follows:

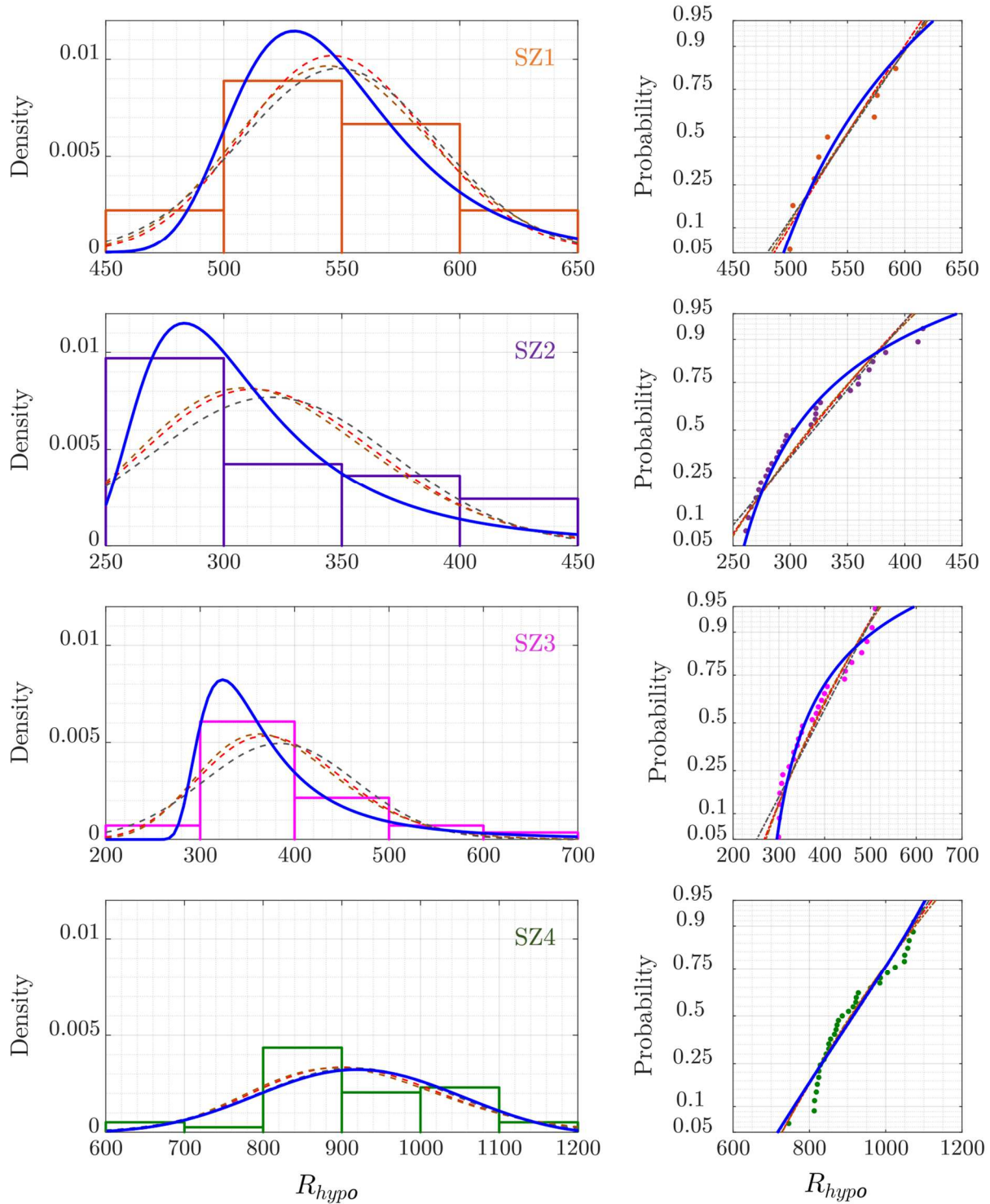


Figure 4.5 Graphical tests of goodness-of-fit used to determine the probability distribution of R_{hypo} . Density histograms of the data together with plots of density functions of samples coming from various probability distributions are shown on the left. Respective cumulative probability plots are shown on the right. The GEV distribution is shown in blue solid lines

$$f_{R_{hyppo}}(r) = \begin{cases} \frac{1}{\sigma} \exp[\exp(-s) - (s)] & \kappa = 0 \\ \frac{1}{\sigma} (1 + \kappa s)^{-(1+\frac{1}{\kappa})} \exp \left[-(1 + \kappa s)^{-\frac{1}{\kappa}} \right] & \kappa = 0 \text{ and } \kappa s > -1 \\ 0 & \text{otherwise} \end{cases} \quad (4.22)$$

where $s = (r - \mu)/\sigma$ is a standardized variable. In Eq. (4.22) μ and κ can be any real number, whereas $\sigma > 0$. The estimates of the GEV distribution parameters obtained for each source zone are presented in Table 4.5.

Table 4.5 Estimates of the GEV distribution parameters μ , σ , and κ , and distance thresholds r_1 and r_2 corresponding to the levels at which $F_{R_{hyppo}}$ equals 0.05 and 0.95, respectively

Source zone	μ	σ	κ	r_1 [km]	r_2 [km]
SZ1	529.7866	32.2100	-0.0021	494	625
SZ2	291.1710	33.1641	0.2836	260	446
SZ3	337.9961	47.5251	0.3709	295	595
SZ4	875.6903	119.3602	-0.3163	719	1106

4.3 Strong-motion Duration Hazard Curves

Equation (4.3) was used to estimate the mean annual rate of exceedance of a given level d of D_{Sr} . It was evaluated numerically by converting the integrals into discrete summations as follows^{4,152}:

$$\lambda_d = \sum_{i=1}^{N_S} \sum_{j=1}^{N_M} \sum_{k=1}^{N_R} \lambda_{m_{0i}} P(D_{Sr} > d | m_j, r_k) P(M_w = m_j) P(R_{hyppo} = r_k) \quad (4.23)$$

where λ_d is the exceedance rate of d , N_M is the total number of elements in a finite set of earthquake magnitudes bounded by the thresholds m_0 and m_u , and N_R is the total number of elements in a finite set of source-to-site distances bounded by the thresholds r_1 and r_2 , which are defined as the levels at which $F_{R_{hyppo}}$ equals 0.05 and 0.95, respectively. The values of λ_{m_0} , m_0 , and m_u are reported in Table 4.2 and the values of r_1 and r_2 are reported in Table 4.5. Notice that the latter were obtained using Eq. (4.22).

In Eq. (4.23), the probability that D_{Sr} exceeds d given m_j and r_k , can be computed as follows:

$$P[\ln(D_{Sr}) > \ln(d) | m_j, r_k] = 1 - F_{\ln(D_{Sr})}[\ln(d)] \quad (4.24)$$

where $F_{\ln(D_{Sr})}$ is the distribution function of the natural logarithm of D_{Sr} . It can be defined as the integral of $f_{\ln(D_{Sr})}$, which mathematical expression is given in Eq. (3.11). As M_w and R_{hypo} were considered as the explanatory variables X , the distribution parameters μ and σ of the density function $f_{\ln(D_{Sr})}$ corresponding to the GMPEs A and C were used for consistency —see Eqs. (3.7) and (3.8), respectively—. The first GMPE allows to estimate λ_d for sites located in GZI and the second for sites located in GZII or GZIII.

Figure 4.6 shows the strong-motion duration hazard curve for sites located in GZI, considering the contribution of all seismic sources of interplate earthquakes that occur at the MAT. As per Figure 4.6, SZ2 produces the greatest contribution to the estimates of λ_d . While SZ1 produces the smaller estimates of λ_d among other source zones for $d < 30$ s, SZ4 produces the smaller λ_d for $d > 30$ s. The estimates of λ_d for $d < 10$ s range from approximately 0.3206 to 0.3732 for SZ2, SZ3, and SZ4.

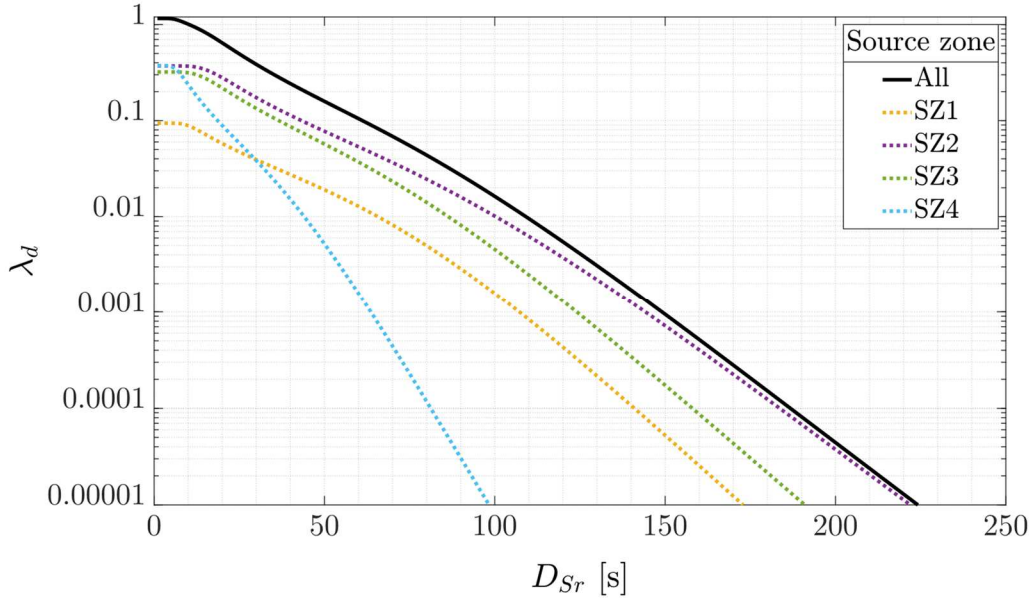


Figure 4.6 Hazard curves of D_{Sr} for sites located in GZI. The dashed lines stand for the contribution of the individual source zones identified for interplate earthquakes occurring at the MAT and the solid black line stands for the summation of all contributions

Similarly, Figure 4.7 shows the strong-motion duration hazard curves for sites with values of T_s ranging from 1 s to 5 s, in steps of 1 s, considering the contribution of all seismic sources of interplate earthquakes that occur at the MAT. For sites with such values of T_s , Figure 4.7 shows that the expected value of D_{Sr} approximates 115 s, 165 s, 205 s, 240 s, and 270 s, respectively, considering that $T_r = 250$ years.

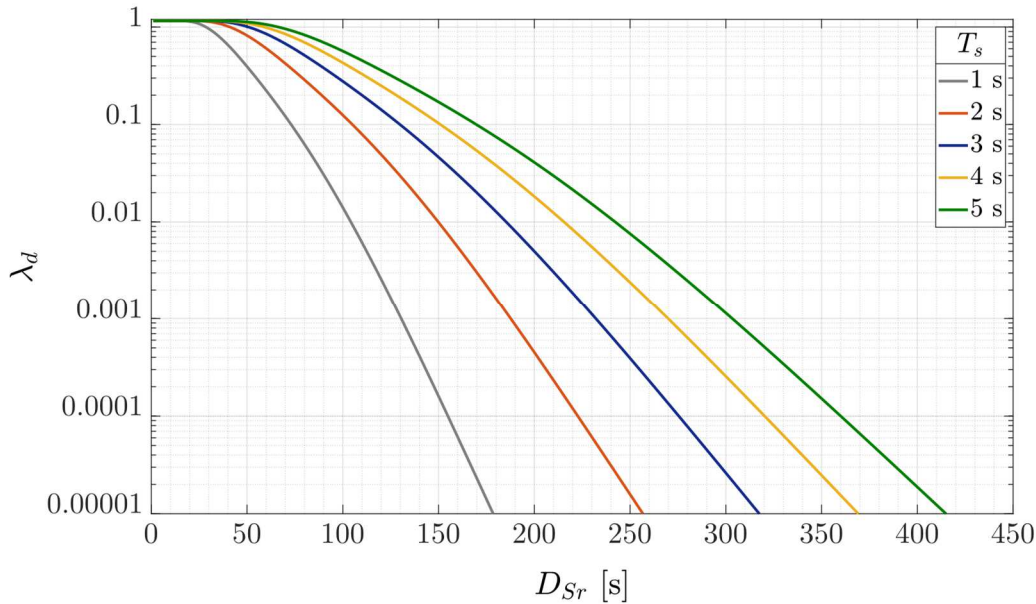


Figure 4.7 Hazard curves of D_{Sr} for sites located in Mexico City that have values of T_s that vary from 1 s to 5 s in steps of 1 s

Following Eq. (4.4), the probability that D_{Sr} takes a value greater than d at least once in T in sites located in GZI and either GZII or GZIII can be then estimated. For instance, for $T = 50$ years, $D_{Sr} = 200$ s has an exceedance probability equal to zero for a site located in GZI and equal to 2.23% for a site with $T_s = 2$ s. The expected exceedance probabilities increase abruptly for sites with $T_s \geq 3$ s, yielding values almost equal to 100%.

For sites located in GZI, Figure 4.8 shows plots of the expected value of D_{Sr} with an exceedance probability of 2%, 5%, 10%, and 20% over various exposure times T . Note that such probabilities of exceedance in $T = 50$ years correspond to values of T_r equal to 2475 years, 975 years, 475 years, and 224 years, respectively. Likewise, Figure 4.9 shows plots of the expected value of D_{Sr} with an exceedance

probability of 10% over various exposure times T , for sites located in Mexico City that had values of T_s ranging from 1 s to 5 s, in steps of 1 s.

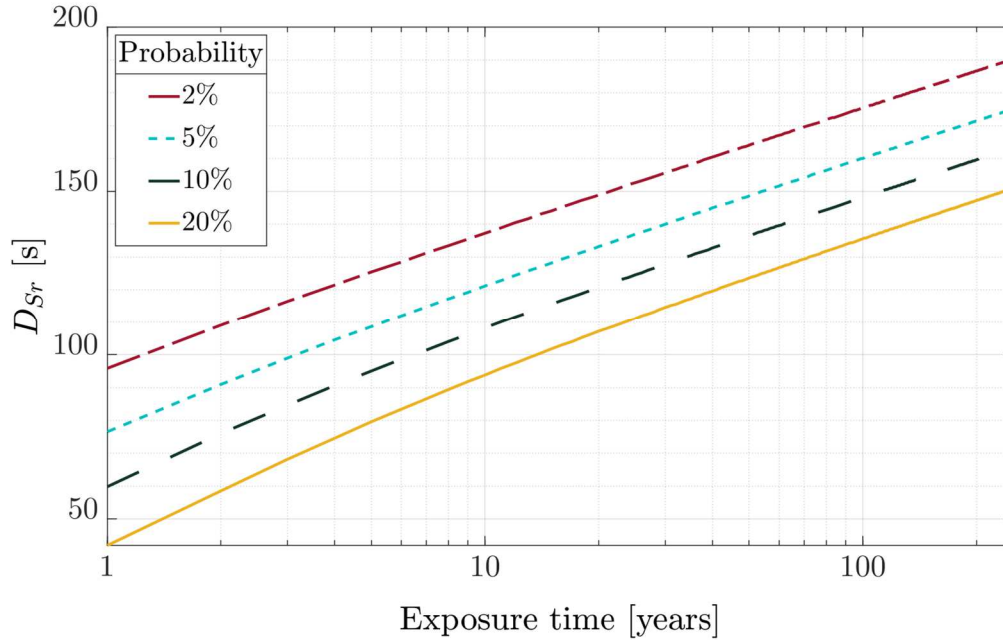


Figure 4.8 Expected D_{Sr} with an exceedance probability of 2%, 5%, 10%, and 20% over various exposure times for sites located in GZI

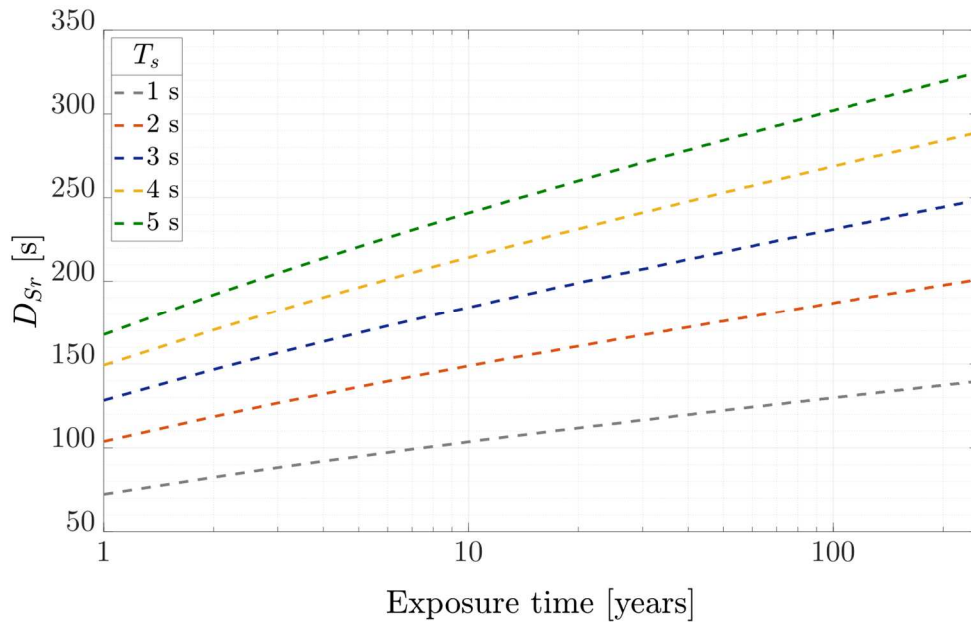


Figure 4.9 Expected D_{Sr} with an exceedance probability of 10% over various exposure times for sites with T_s varying from 1 s to 5 s, in steps of 1 s

4.3.1 Disaggregation of Strong-motion Hazard

Before concluding this chapter, it should be noted that some researchers have argued that in a PSHA the concept of design earthquake is lost.^{8,152} This may be true because a single influential earthquake cannot be simply linked with the results of a PSHA. Nevertheless, it is possible to identify the dominant contributor to the earthquake hazard through a process called *disaggregation* (also known as *deaggregation*) and this can serve as a convenient design earthquake. As the name implies, the disaggregation of the earthquake hazard allows identifying the combination of values of M_w and R_{hypo} that contributes the most to the probability of exceeding a given y , which is commonly associated with a predefined T_r .

For the case in hand, the conditional probability distribution of M_w and R_{hypo} given that D_{Sr} exceeds d at a site of interest can be computed as follows:

$$P(M_w = m_j, R_{hypo} = r_k | D_{Sr} > d) = \frac{P(M_w = m_j)P(R_{hypo} = r_k) \sum_{i=1}^{N_S} \lambda_{m_{0_i}} P(D_{Sr} > d | m_j, r_k)}{\lambda_d} \quad (4.25)$$

As noted, Eq. (4.25) considers the contribution of N_S earthquake sources that can affect a site of interest. If disaggregating the strong-motion hazard from the i th earthquake source is of interest, the M_w and R_{hypo} contributions to hazard from such earthquake source only have to be normalized by the rate of exceedance of d from the earthquake source i , λ_{d_i} . Note that $\lambda_d = \sum_{i=1}^{N_S} \lambda_{d_i}$.

Figure 4.10 shows the joint mass function of M_w and R_{hypo} conditional on exceeding 125 s, which is associated with a value of $T_r = 250$ years (see Figure 4.6) at a site located in GZI. From the results given in Figure 4.10, an earthquake with $M_w = 8.15$ occurred at $R_{hypo} = 278$ km is the most likely to cause the exceedance of the specified d .

Similarly, $M_w = 8.15$ and R_{hypo} equal to approximately 280 km contribute the most to the probability that D_{Sr} exceeds values of d associated with $T_r = 250$ years at sites located in GZII or GZIII. But also, the influence of an earthquake with $M_w = 8.05$ at R_{hypo} equal to approximately 300 km becomes more noticeable. As an instance, Figure 4.11 shows the joint mass function of M_w and R_{hypo} conditional on exceeding 237 s at a site with $T_s = 4.0$ s.

For any site, the largest contributions to the probability of exceedance of the specified d associated with $T_r = 250$ years occur at SZ2 and SZ3.

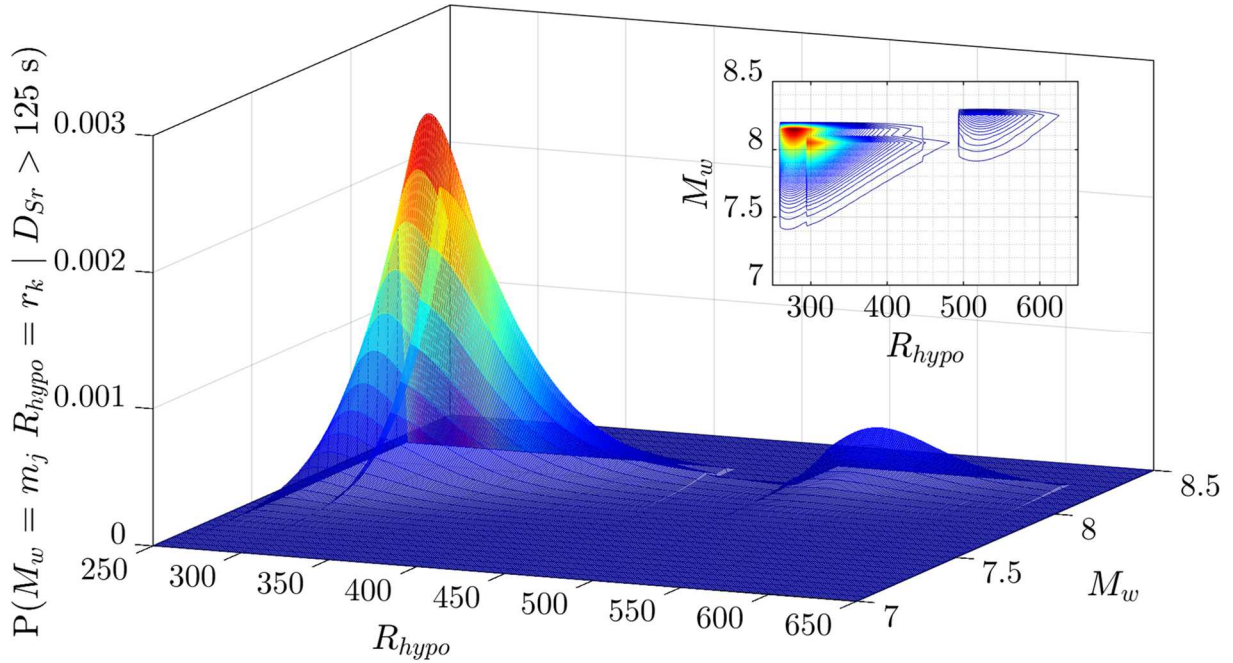


Figure 4.10 Joint mass distribution of M_w and R_{hypo} conditional on exceeding $D_{Sr} = 125$ s ($T_r = 250$ years) at a site located in GZI. A contour plot of the density is also displayed the figure

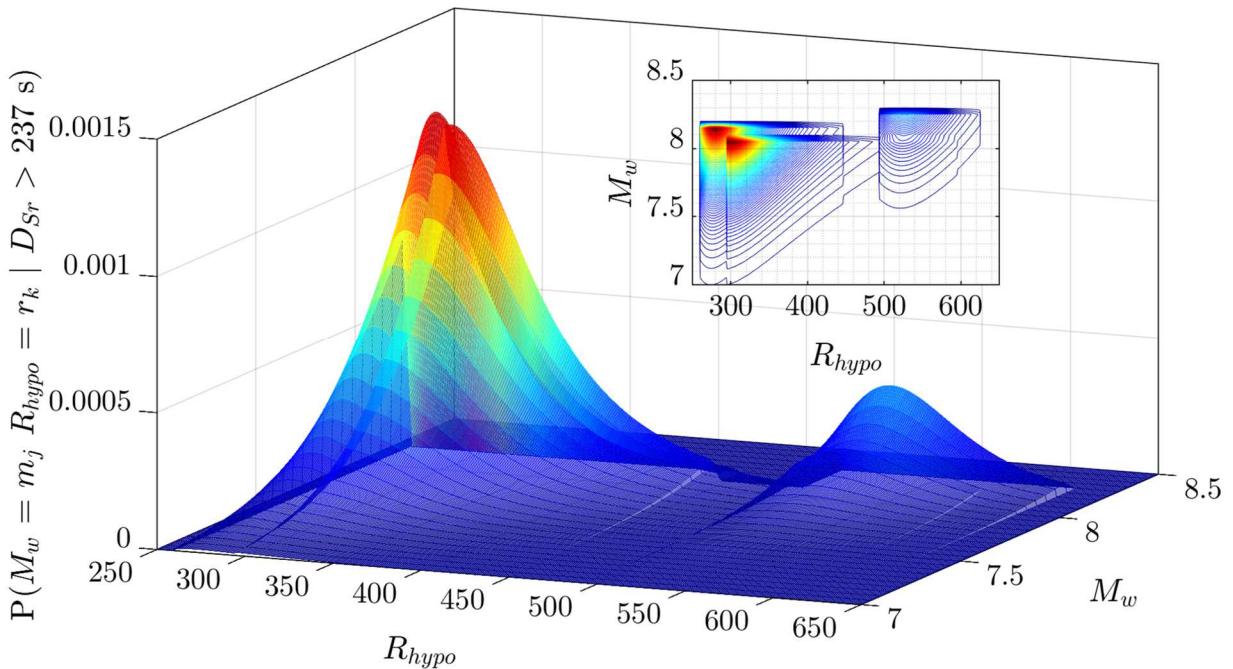


Figure 4.11 Joint mass distribution of M_w and R_{hypo} conditional on exceeding $D_{Sr} = 237$ s ($T_r = 250$ years) in a site with $T_s = 4.0$ s. A contour plot of the density is also displayed in the figure

4.4 Discussion

Strong-motion duration hazard curves for sites located in Mexico City were presented in this chapter. The specification of these curves required the identification and evaluation of the interplate earthquake sources capable of producing significant ground motions in the geographical region of interest. For the identification of the earthquake sources, the author relied on the research works of Ramírez-Herrera and Urrutia-Fucugauchi,⁹⁷ Ordaz and Reyes¹⁵⁶ and Zúñiga et al.¹¹⁰ Specifically, four source zones were proposed. They were defined as areal sources that encompass interplate earthquakes with $M_w \geq 6.0$ that occurred between 1900 and 2021 in the Mexican subduction zone. The evaluation of the source zones consisted in characterizing probabilistically the time, space, and size distribution of the earthquakes occurring at each one. This was done under the common assumption that earthquakes are random in time and follow a Poisson process.

The probability distribution of earthquake sizes and corresponding information on rates of occurrence was carried out based on the “shifted and truncated” Gutenberg-Richter law given in Eq. (4.14). As noticed in Appendix B, the earthquake catalog compiled for this study is complete for $M_w = 7.0$ since 1900, $M_w = 6.5$ since 1950, and $M_w = 6.0$ since 1976. In particular, the approach proposed by Kijko and Smit¹⁶⁹ was used for the estimation of the parameters β and λ_0 of the “shifted and truncated” Gutenberg-Richter law because it allows considering unequal observation time periods T with different m_0 .

It is worth mentioning that most of the PSHAs carried out for sites located not only in Mexico City but in other states of Mexico are commonly carried out considering the estimates of λ_m proposed by Ordaz and Reyes.¹⁵⁶ They proposed a similar zonation to the one proposed in this study (see Figure 4.1) but for small and moderate interplate earthquakes, i.e., with magnitudes smaller than 7.0, that occurred in the Mexican territory. As in this study, they employed Eq. (4.14) to estimate λ_m for each of these source zones. In contrast, they proposed 14 areal source zones along the MAT associated with major interplate earthquakes that were identified as characteristic earthquakes. Note that a *characteristic earthquake* is an earthquake that breaks the same fault segment with a similar magnitude during repeated seismic cycles.¹⁷⁶ For these source zones, Ordaz and Reyes¹⁵⁶ computed λ_m assuming that the earthquake magnitude follows a normal distribution, with parameters $\mu = 7.5$ and $\sigma = 0.3$. Then, beyond the differences in the estimation process of λ_m , the results reported by Ordaz and Reyes¹⁵⁶ and the ones obtained in this study are similar. For instance, Figure 4.12 shows a comparison between the mean annual exceedance rate of earthquakes with magnitudes ranging from 7.0 to

8.2, computed from both the data provided by Ordaz and Reyes¹⁵⁶ and this study. In Figure 4.12 the subscript T was added to the variable λ_m because the results include the contribution of all the N_S earthquake sources, i.e., 14 in the work of Ordaz and Reyes and four in this study. As can be seen, the initial segment of the curves (say up to $M_w = 7.6$) is practically the same. Likewise, the end segment of the curves drops at the same point. The estimated values of λ_m computed from the data of this study are higher for earthquakes with M_w greater than approximately 7.6, in comparison with those from the Ordaz and Reyes¹⁵⁶ data. This increment is attributed to the number of large earthquakes that have occurred in the last two decades. Thus, the results given in Subsection 4.2.1 can be seen as a readjustment of the information given in the work of Ordaz and Reyes.¹⁵⁶

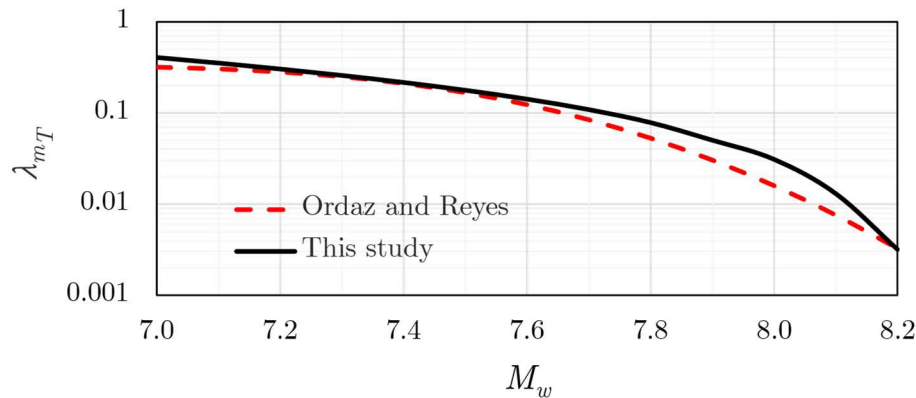


Figure 4.12 Comparison between the rate of exceedance of magnitude computed from the Ordaz and Reyes¹⁵⁶ data (dashed red line) and the one developed in this study (solid black line). The curves consider the contribution of all source zones, i.e., four in the present study and 14 in the work of Ordaz and Reyes.¹⁵⁶

It should also be mentioned that Zúñiga et al.¹¹⁰ recently defined the seismicity of distinct source zones located in the Mexican territory. They used the Aki-Utsu estimator of b given in Eq. (4.16). Although their work was developed flawlessly, the reported estimates were disregarded in the present study because they were developed using the surface wave magnitude, M_s , instead of M_w . As it is known, estimates of the Gutenberg and Richter parameters cannot be used interchangeably when the measures used to size the earthquakes are not calibrated to be identical.¹⁷⁷ The latter represents no problem if only moderate or large earthquakes were used, as estimates of M_s and M_w are similar for such earthquakes. However, in the work of Zúñiga et al.¹¹⁰ earthquakes as small as approximately 3.0 in magnitude were considered. The main reason they used M_s was that most of the

agencies that provide earthquake catalogs generally give values of such magnitude scale for historical earthquakes.

Concerning the characterization of the spatial distribution of earthquakes, in this work, it was proposed (in an unprecedented way) to define the probability distribution of R_{hyppo} using statistical inference. The author believes that the parameter uncertainties are significantly reduced this way in comparison with classic analytical methods (just as those briefly described in Subsection 4.2.2). Relying on goodness-of-fit tests, such as the one-sample KS test, it was determined that the GEV distribution could adequately represent R_{hyppo} . This probability distribution gave the best estimates of p -values not only for the proposed source zones (see Table 4.4 and Figure 4.5) but for other source zone proposals that were evaluated in preliminary PSHAs carried out by the author.

It is necessary to mention that, although the use of R_{rup} (or any other finite-source distance measure) is highly recommended when developing GMPEs (especially when considering strong-motion data from moderate and major earthquakes),¹⁰ the source parameters necessary for its estimation were unavailable for many historical earthquakes. The foregoing prevented determining the probability distribution of R_{rup} using statistical inference. Nevertheless, from a practical engineering perspective, the author considers the definition of R_{hyppo} is more user-friendly than that of R_{rup} .

Based on the strong-motion duration hazard curves given in Section 4.3 it can be said that the values of the ground-motion duration recommended in the NTC-2020²⁷ to select or (generate synthetic) accelerograms are considerably underestimated. Specifically, the NTC-2020²⁷ defines that the “free-field ground-motion duration” had to be equal to $80 + 20(T_s - 0.5)$. It is not specified but T_s should be equal to 0.5 for any site located in GZI when using such expression. The cited mathematical expression was developed considering that the ground-motion duration at sites located in GZI equals 80 s. Such value was determined using an unspecified GMPE and considering a scenario earthquake with $M_w = 7.8$ occurred at $R_{hyppo} = 265$ km. The latter was defined from the disaggregation of the earthquake hazard (the author assumes that for PGA) associated with $T_r = 250$ years. Then, among others, the following key-point observations stand out:

1. Using GMPE A and considering the same scenario earthquake as in the NTC-2020²⁷ for interplate earthquakes, the expected value of D_{Sr} for a site located in GZI is equal to 85 s. At a first glance, such value could be quite similar to the 80 s given in the NTC-2020²⁷ for sites located in GZI. However, this standard

does not define the strong-motion duration. As mentioned in the NTC-2020²⁷ it defines the “input ground-motion duration”, which the author interprets as the total duration of the ground motion. Therefore, a value of 80 s not only underestimates the expected strong-motion duration at sites located in GZI but the total duration of the ground motions.

2. If the value of the strong-motion duration was determined under the same criteria as the design spectrum, i.e., for $T_r = 250$ years, the expected value of D_{S_r} approximates 125 s at sites located in GZI (see Figure 4.6). Following this approach, the value reported in the NTC-2020²⁷ is underestimating the expected value of the strong-motion duration by 34% (assuming that the value of 80 s given in the NTC-2020²⁷ represents the strong-motion duration for sites located in GZI). Similarly, the underestimation would vary from 22% in sites with $T_s = 1$ s to 37% at sites with $T_s = 5$ s.
3. As per Figures 4.6 and 4.7, the increase in the strong-motion hazard as T_s increases is nonlinear, thus the mathematical expression given in the NTC-2020²⁷ could be causing bias in the estimates of the ground-motion duration.

[This page intentionally left blank]

CHAPTER 5

Multivariate Probabilistic Seismic Hazard Analysis

5.1 Introduction

As per Chapter 4, a conventional PSHA allows estimating the probability that a specific Y takes a value greater than y at least once in T . Nevertheless, the knowledge of the joint exceedance probability of various ground-motion levels y_1, \dots, y_q , each associated with one different ground-motion parameter of the set Y_1, \dots, Y_q , could improve the accuracy in the prediction of the seismic response of soils and structures.¹⁷⁸ Practical engineering applications include: (a) the evaluation of the seismic response of non-single-mode-dominated structures, (b) the evaluation of amplification functions of non-linear soil deposits, (c) the evaluation of the response of earth slopes, (d) the assessment of soil liquefaction potential, and (e) the generation of synthetic accelerograms.

Hence, assuming that the occurrence of earthquakes follows a Poisson process, the probability that Y_1, \dots, Y_q take values greater than y_1, \dots, y_q at least once in T can be defined as:

$$P(Y_1 > y_1, \dots, Y_q > y_q) = 1 - \exp(-\lambda_{y_1, \dots, y_q} T) \quad (5.1)$$

where $\lambda_{y_1, \dots, y_q}$ is the joint mean annual rate of exceedance of y_1, \dots, y_q . Considering the contribution of N_S earthquake sources and taking only M_w and R_{hypo} as the explanatory variables, $\lambda_{y_1, \dots, y_q}$ can be computed as follows:

$$\lambda_{y_1, \dots, y_q} = \sum_{i=1}^{N_S} \lambda_{m_{0_i}} \iint P(Y_1 > y_1, \dots, Y_q > y_q | m, r) f_{M_{w_i}}(m) f_{R_{hypo_i}}(r) dm dr \quad (5.2)$$

where, for each $i = 1, \dots, N_S$ earthquake source, $\lambda_{m_{0_i}}$ is the mean annual rate at which an earthquake with a magnitude equal to m_{0_i} will be exceeded and $P(Y_1 > y_1, \dots, Y_j > y_j | m, r)$ is the complementary joint distribution function of Y_1, \dots, Y_q conditional on M_w and R_{hypo} .

It is common for the multivariate normal distribution to be used by researchers for the determination of the joint probability distribution of Y_1, \dots, Y_q . Recall that, in probability theory and statistics, the multivariate normal distribution is a generalization of the (univariate) normal distribution.⁹³ For instance, let Y_1 and Y_2 be the random variables, their joint (binormal) density function is the function f_{Y_1, Y_2} defined by⁴²:

$$f_{Y_1, Y_2}(y_1, y_2) = \frac{1}{2\pi\sigma_1\sigma_2\sqrt{1-\rho^2}} \exp \left\{ -\frac{1}{2(1-\rho^2)} \left[\left(\frac{y_1 - \mu_1}{\sigma_1} \right)^2 + \left(\frac{y_2 - \mu_2}{\sigma_2} \right)^2 - 2\rho \left(\frac{y_1 - \mu_1}{\sigma_1} \right) \left(\frac{y_2 - \mu_2}{\sigma_2} \right) \right] \right\} \quad (5.3)$$

where $\mu_1, \mu_2, \sigma_1, \sigma_2$, and ρ are real numbers, with $\sigma_1, \sigma_2 > 0$ and $-1 \leq \rho \leq 1$. Note that $Y_1 \sim \mathcal{N}(\mu_1, \sigma_1^2)$ and $Y_2 \sim \mathcal{N}(\mu_2, \sigma_2^2)$.

Generalizing, the multivariate normal distribution of a $q \times 1$ random vector $\mathbf{Y} = Y_1, \dots, Y_q$ is denoted as $\mathcal{N}(\boldsymbol{\mu}, \boldsymbol{\Sigma})$, where $\boldsymbol{\mu} = \mu_1, \dots, \mu_q$ is a $q \times 1$ mean vector and $\boldsymbol{\Sigma}$ is a $q \times q$ variance-covariance matrix.⁹³ Clearly, in the bivariate case:

$$\boldsymbol{\mu} = \begin{pmatrix} \mu_1 \\ \mu_2 \end{pmatrix} \quad (5.4a)$$

$$\boldsymbol{\Sigma} = \begin{pmatrix} \sigma_1^2 & \rho\sigma_1\sigma_2 \\ \rho\sigma_1\sigma_2 & \sigma_2^2 \end{pmatrix} \quad (5.4b)$$

Be aware that the density function given in Eq. (5.3) stands when the bivariate normal distribution is said to be nondegenerate when $\boldsymbol{\Sigma}$ is positive definite. Note that, in linear algebra, a *positive definite matrix* is a symmetric matrix where each of its eigenvalues is positive, and a square matrix that is non-invertible is called *degenerate* (or singular).¹⁷⁹

The ease of using the multivariable normal distribution in a PSHA arises that one can get the values of the elements of $\boldsymbol{\mu}$ and $\boldsymbol{\Sigma}$ directly from GMPEs if an LME model is used for their development —please refer to Eq. (3.2)—. To proceed in this way, a literature review of GMPEs applicable to Mexico City for ground-motion parameters other than the strong-motion duration was carried out. In this search, the author became aware of their scarcity.^{180–185} For instance, the only GMPEs reported recently that allow estimating peak time-domain parameters and amplitudes of a response spectrum at various values of T_e were proposed by Reyes et al.¹⁸³ and Jaimes et al.^{184,185} In particular, Reyes et al.¹⁸³ developed a GMPE using ground motions caused by interplate earthquakes occurred from 1965 to 1995

and that had M_w ranging from 6.1 to 8.1. The ground motions were recorded at the main UNAM campus (where the stations whose code begins with the letters CU are located, see Appendix D). The geometric mean of PGA , as well as of the acceleration response-spectral ordinates for values of T_e varying from 0.1 s to 6.0 s, in steps of 0.1 s, computed from the horizontal accelerograms of ground-motion recordings were considered. For instance, Reyes et al.¹⁸³ report the following $\mathcal{g}(\mathbf{X}, \hat{\boldsymbol{\alpha}})$ for PGA :

$$\ln(\widehat{PGA}) = 5.5474 + 1.4024(M_w - 6) - 0.0130(M_w - 6)^2 - 0.5000 \ln(R) - 0.0058R \quad (5.5)$$

For the acceleration response-spectral ordinates, Reyes et al.¹⁸³ carried out a regression analysis for each specified value of T_e . The regression analyses were performed maintaining the same form of $\mathcal{g}(\mathbf{X}, \boldsymbol{\alpha})$, thereby 61 groups of estimates of the terms of $\boldsymbol{\alpha}$ were given. Likewise, Reyes et al.¹⁸³ presented results from regression analyses performed using data from the horizontal components of the ground-motion recordings separately. For their part, Jaimes et al.^{184,185} developed site-specific GMPEs for PGA , PGV , and acceleration response-spectral ordinates for a set of values of T_e , but from shallow-crustal and intraslab earthquakes, which are out of the focus of this dissertation.

Before proceeding it should be mentioned that Reyes et al.¹⁸³ and Jaimes et al.^{184,185} developed their GMPEs using Bayesian linear regression. As the name implies, a *Bayesian linear regression* is an approach to linear regression in which the statistical analysis is undertaken within the context of Bayesian inference. As the mixed-effects model approach, the Bayesian approach is based on a hierarchical statistical model but, in the latter, the values for all parameters must be specified.⁹²

As the reader can presume, the lack of GMPEs for other ground-motion parameters than the strong-motion duration and for sites other than the main UNAM campus prevented the author to carry out (in their fullness) multivariate PSHAs. Although it is possible to develop some GMPEs to achieve such an aim, these are out of the scope of this dissertation. Nevertheless, to exemplify a multivariate PSHA, Section 5.3 presents a study case conducted for sites located in GZI, where the main UNAM campus is located. The attention was focused on modeling the dependence between D_{Sr} and both PGA and acceleration response-spectral ordinates for specific values of T_e . Furthermore, thinking about the importance that other ground-motion parameters could have in earthquake engineering applications, the dependence between D_{Sr} and a selection of five ground-motion parameters is measured with detail in a prior section (i.e., in Section 5.2). The findings are discussed in Section 5.4.

5.2 Measuring Dependence Between Strong-motion Duration and □ther Ground-Motion Parameters

Several formulations can be found in the statistical literature to synthesize the dependence between two random variables, Y_1 and Y_2 , through the determination of a scalar value associated with them. In this regard, no quantity has been more characteristic in research work than ρ . As introduced in Section 2.4, ρ measures the linear dependence that exists between Y_1 and Y_2 and is called the Pearson correlation coefficient. Its sample definition was given in Eq. (2.16).

In addition to ρ , a *measure of association* can be used to quantify the way Y_1 and Y_2 are linked together. By far, the most widely known measures of association are Spearman's correlation coefficient on ranks (best known as Spearman's rho) and Kendall's concordance coefficient (best known as Kendall's tau).^{186,187}

A *rank correlation coefficient* measures the dependence between the rankings of Y_1 and Y_2 , where a ranking is the assignment of the ordering labels to the observations of Y_1 and Y_2 . Thus, Spearman's rho is defined as the Pearson correlation coefficient between the ranked Y_1 and Y_2 . This leads to the following definition for its sample version¹⁸⁸:

$$\widehat{\rho}_S = 1 \frac{\sum_{j=1}^n [\text{rank}(y_{1j}) - \overline{\text{rank}(Y_1)}] [\text{rank}(y_{2j}) - \overline{\text{rank}(Y_2)}]}{\sqrt{\sum_{j=1}^n [\text{rank}(y_{1j}) - \overline{\text{rank}(Y_1)}]^2 \sum_{j=1}^n [\text{rank}(y_{2j}) - \overline{\text{rank}(Y_2)}]^2}} \quad (5.6)$$

where $\text{rank}(y_{1j})$ and $\text{rank}(y_{2j})$ respectively stand for the ranks of the j th observation of Y_1 and Y_2 , and the sample means $\overline{\text{rank}(Y_1)}$ and $\overline{\text{rank}(Y_2)}$ are equal to $\frac{n+1}{2}$.

Let (y_{1p}, y_{2p}) and (y_{1q}, y_{2q}) denote an independent pair of observations from the vector (Y_1, Y_2) of continuous random variables. They are concordant if $y_{1p} < y_{1q}$ and $y_{2p} < y_{2q}$ or if $y_{1p} > y_{1q}$ and $y_{2p} > y_{2q}$. On the contrary, (y_{1p}, y_{2p}) and (y_{1q}, y_{2q}) are discordant if $y_{1p} < y_{1q}$ and $y_{2p} > y_{2q}$ or if $y_{1p} > y_{1q}$ and $y_{2p} < y_{2q}$.¹⁸⁷ Additionally, the pair of observations $\{(y_{1p}, y_{2p}), (y_{1q}, y_{2q})\}$ is said to be *tied* if $y_{1p} = y_{2p}$ or $y_{1q} = y_{2q}$, i.e., a tied pair is neither concordant nor discordant. Then, in the case of no ties, Eq. (5.6) may be more conveniently expressed in the following form¹⁸⁹:

$$\widehat{\rho}_S = \frac{12}{n(n^2 - 1)} \sum_{j=1}^n \left[\text{rank}(y_{1j}) - \frac{1}{2}(n+1) \right] \left[\text{rank}(y_{2j}) - \frac{1}{2}(n+1) \right] \quad (5.7)$$

In terms of concordance, the sample version of Kendall's tau is defined as^{187,188}:

$$\widehat{\tau}_K = \frac{N_{conc} - N_{disc}}{\binom{n}{2}} \quad (5.8)$$

where N_{conc} and N_{disc} are the number of concordant and discordant pairs, respectively, in the random sample $\{(y_{1_1}, y_{2_1}), \dots, (y_{1_n}, y_{2_n})\}$ from the vector (Y_1, Y_2) . Note that there are $\binom{n}{2}$ distinct pairs (y_{1_p}, y_{2_p}) and (y_{1_q}, y_{2_q}) of observations in $\{(y_{1_1}, y_{2_1}), \dots, (y_{1_n}, y_{2_n})\}$.

By the very definition, both ρ_S and τ_K are rank correlation coefficients.¹⁸⁹ They have the following properties⁸⁶:

- i) Their estimates take values from -1 to 1. Then, Y_1 and Y_2 are positively associated if the estimate of either ρ_S or τ_K is greater than zero, and negatively associated if it is smaller than zero.
- ii) If Y_1 and Y_2 are independent, their estimates take values equal to zero.
- iii) If $\mathcal{g}(Y_1)$ and $\mathcal{g}(Y_2)$ are strictly increasing functions, the estimate of either ρ_S or τ_K between Y_1 and Y_2 is equal to that between $\mathcal{g}(Y_1)$ and $\mathcal{g}(Y_2)$.

The Pearson correlation coefficient ρ shares with ρ_S and τ_K the first two properties.⁸⁶ Other correlation coefficients can be found in the statistical literature to measure the dependence between random variables. Nevertheless, this dissertation extends to the use of ρ , ρ_S , and τ_K .

Thus, the dependence between D_{Sr} and PGA , PGV , and the *peak ground displacement*, PGD , was measured. Note that PGD is defined as the maximum ground displacement that occurred at a site of interest during an earthquake. The observations of PGV and PGD were measured from time histories obtained by direct integration of accelerograms over t .

The dependence between D_{Sr} and acceleration response-spectral ordinates was also measured. The response-spectral ordinates were specified from response spectra that were developed considering that the SDOF systems had $\zeta_e = 5\%$ and values of T_e varying from 0.1 s to 5 s, in steps of 0.1 s, and using the Newmark

method. In this respect, a computational algorithm can be found in Chopra's world-renowned book.¹⁹⁰ The author wants to emphasize that the computed response spectra are defined by the *absolute acceleration*, which is the maximum acceleration of the seismic mass in an inertial reference frame.⁴⁵ To follow with the nomenclature used in related literature, the acceleration response-spectral ordinates are denoted as $S_a(T_e)$.

Moreover, the author considered it interesting to measure the dependence between D_{S_r} and the total ground-motion duration. The parameter t_f was used for this purpose. To be consistent with the criteria established in Section 3.3 for the measurement of D_{S_r} from accelerograms recorded in Mexico City, t_f was defined as the time elapsed between the first and last excursion of $a_0 = 2 \text{ cm/s}^2$.

Thereby, for sites located in GZI, the estimates of ρ , ρ_S , and τ_K between D_{S_r} and t_f , PGA , PGV , PGD , and $S_a(T_e)$, with values of T_e up to 5 s, were obtained using Eqs. (2.16), (5.6), and (5.8), respectively. Each vector of observations consisted of 141 elements. The observations were obtained from the same strong-motion database used to develop the GMPEs for D_{S_r} (see Subsection 3.3.2 and Appendix D). The results for the first four pairs of ground-motion parameters are summarized in Table 5.1 and for the last pair in Figure 5.1.

The results given in Table 5.1 imply that D_{S_r} increases as t_f , PGA , PGV , and PGD increase. This relationship can be corroborated by scatterplots of the strong-motion data presented in Table 5.1. Similarly, the results given in Figure 5.1 indicate a high positive dependence between D_{S_r} and $S_a(T_e)$. In this instance, Figure 5.2 shows scatterplots of the observed values of D_{S_r} and $S_a(T_e)$ for four specific values of T_e . Note that four data points stand out in the upper right quadrant of the scatterplots shown in Table 5.1. These are related to the ground motions caused by the September 19, 1985 earthquake, which lead to the higher values of PGA , PGV , and PGD from the entire database.

Following the third property of the measures of association (defined on page 91), the estimates of either ρ_S or τ_K between D_{S_r} and any other ground-motion parameter are equal to the estimates obtained from their natural logarithms. The latter cannot be true for the estimates of ρ , which dissatisfies such property. For instance, the estimates of ρ between the natural logarithm of D_{S_r} and the natural logarithms of t_f , PGA , PGV , and PGD for sites located in GZI are 0.9393, 0.6601, 0.6949, and 0.6986, respectively. These are greater values than the ones displayed in Table 5.1. The estimates of ρ between the natural logarithm of D_{S_r} and $S_a(T_e)$ for sites located in GZI are summarized in Figure 5.1.

Table 5.1 Estimates of ρ , ρ_S , and τ_K between D_{Sr} and t_f , PGA , PGV , and PGD considering data from sites located in GZI

Pair of ground-motion parameters	Correlation coefficient estimate	Graphical diagnostic
D_{Sr} and t_f	$\hat{\rho} = 0.8700$ $\widehat{\rho}_S = 0.8808$ $\widehat{\tau}_K = 0.7275$	
D_{Sr} and PGA	$\hat{\rho} = 0.5678$ $\widehat{\rho}_S = 0.5937$ $\widehat{\tau}_K = 0.4288$	
D_{Sr} and PGV	$\hat{\rho} = 0.4798$ $\widehat{\rho}_S = 0.5101$ $\widehat{\tau}_K = 0.3521$	
D_{Sr} and PGD	$\hat{\rho} = 0.4053$ $\widehat{\rho}_S = 0.5037$ $\widehat{\tau}_K = 0.3439$	

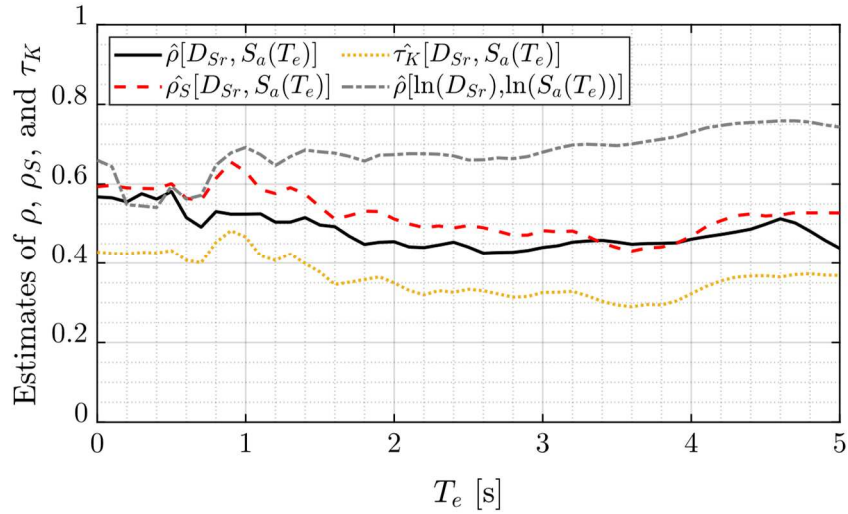


Figure 5.1 Estimates of ρ (solid black line), ρ_S (dashed red line), and τ_K (dotted yellow line) between D_{Sr} and $S_a(T_e)$ considering data from sites located in GZI. The dash-dotted gray line stands for the estimates of ρ between the natural logarithms of D_{Sr} and $S_a(T_e)$

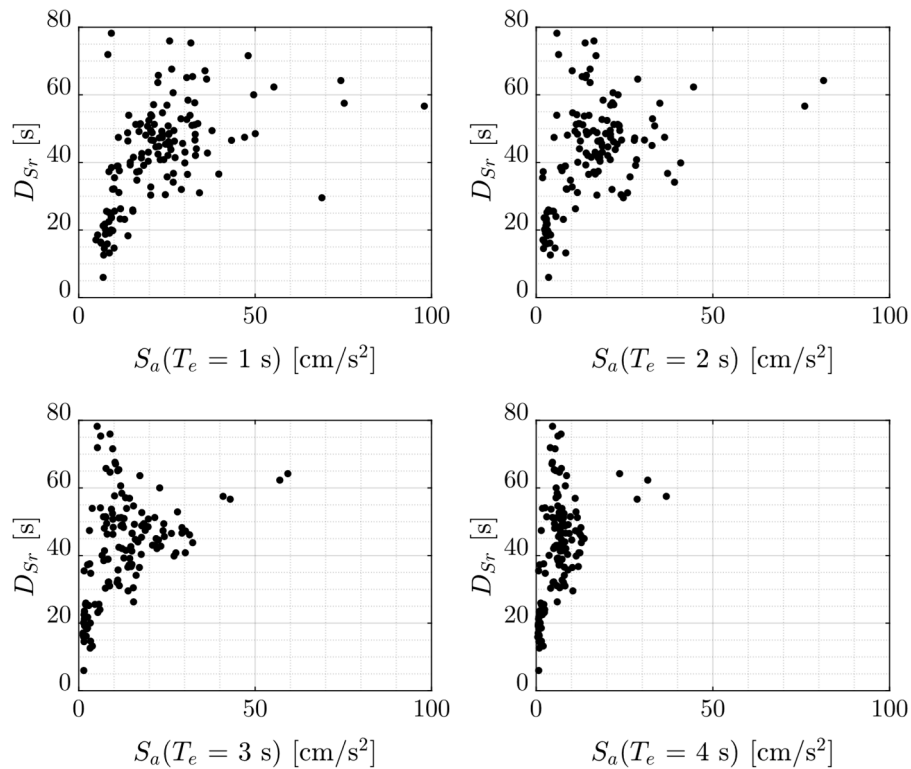


Figure 5.2 Scatter plots between the observations of D_{Sr} and $S_a(T_e)$, with values of T_e equal to 1.0 s, 2.0 s, 3.0 s, and 4.0 s, respectively, considering data from sites located in GZI

The estimates of ρ , ρ_S , and τ_K between D_{Sr} and t_f , PGA , PGV , PGD , and $S_a(T_e)$ for sites located outside GZI were obtained by grouping the observations per geotechnical zone (see Figure 3.2). The observations were obtained from the same strong-motion database used to develop the GMPEs for D_{Sr} (see Appendix D). Table 5.2 and Figure 5.3 summarize the results for the first four and last pair of ground-motion parameters, respectively. It could be said from Table 5.2 and Figure 5.3 that the estimates of ρ , ρ_S , and τ_K between the analyzed pairs of ground-motion parameters are quite similar among GZII, GZIIIa, GZIIIb, and GZIIIc. However, they differ from the estimates obtained considering observations from sites located in GZI or GZIId, which overall displayed greater values of correlation.

Table 5.2 Estimates of ρ , ρ_S , and τ_K between D_{Sr} and t_f , PGA , PGV , and PGD considering data from sites located in GZII or GZIII

Geotechnical zone	Pair of ground-motion parameters			
	D_{Sr} and t_f	D_{Sr} and PGA	D_{Sr} and PGV	D_{Sr} and PGD
GZII	$\hat{\rho} = 0.6286$	$\hat{\rho} = 0.1240$	$\hat{\rho} = 0.1987$	$\hat{\rho} = 0.3264$
	$\hat{\rho}_S = 0.6959$	$\hat{\rho}_S = 0.2811$	$\hat{\rho}_S = 0.4089$	$\hat{\rho}_S = 0.5088$
	$\hat{\tau}_K = 0.5342$	$\hat{\tau}_K = 0.2148$	$\hat{\tau}_K = 0.2659$	$\hat{\tau}_K = 0.3366$
GZIIIa	$\hat{\rho} = 0.5694$	$\hat{\rho} = 0.1530$	$\hat{\rho} = 0.1890$	$\hat{\rho} = 0.2752$
	$\hat{\rho}_S = 0.6203$	$\hat{\rho}_S = 0.3156$	$\hat{\rho}_S = 0.3418$	$\hat{\rho}_S = 0.3977$
	$\hat{\tau}_K = 0.4503$	$\hat{\tau}_K = 0.2016$	$\hat{\tau}_K = 0.2173$	$\hat{\tau}_K = 0.2622$
GZIIIb	$\hat{\rho} = 0.6777$	$\hat{\rho} = 0.2031$	$\hat{\rho} = 0.2408$	$\hat{\rho} = 0.3052$
	$\hat{\rho}_S = 0.7322$	$\hat{\rho}_S = 0.3798$	$\hat{\rho}_S = 0.4209$	$\hat{\rho}_S = 0.4893$
	$\hat{\tau}_K = 0.5477$	$\hat{\tau}_K = 0.2301$	$\hat{\tau}_K = 0.2640$	$\hat{\tau}_K = 0.3180$
GZIIIc	$\hat{\rho} = 0.6654$	$\hat{\rho} = 0.1339$	$\hat{\rho} = 0.1991$	$\hat{\rho} = 0.2741$
	$\hat{\rho}_S = 0.6900$	$\hat{\rho}_S = 0.2831$	$\hat{\rho}_S = 0.3262$	$\hat{\rho}_S = 0.3852$
	$\hat{\tau}_K = 0.5030$	$\hat{\tau}_K = 0.1573$	$\hat{\tau}_K = 0.1916$	$\hat{\tau}_K = 0.2419$
GZIId	$\hat{\rho} = 0.8404$	$\hat{\rho} = 0.4322$	$\hat{\rho} = 0.5331$	$\hat{\rho} = 0.5824$
	$\hat{\rho}_S = 0.8432$	$\hat{\rho}_S = 0.5242$	$\hat{\rho}_S = 0.5978$	$\hat{\rho}_S = 0.6711$
	$\hat{\tau}_K = 0.6708$	$\hat{\tau}_K = 0.3499$	$\hat{\tau}_K = 0.4204$	$\hat{\tau}_K = 0.4852$

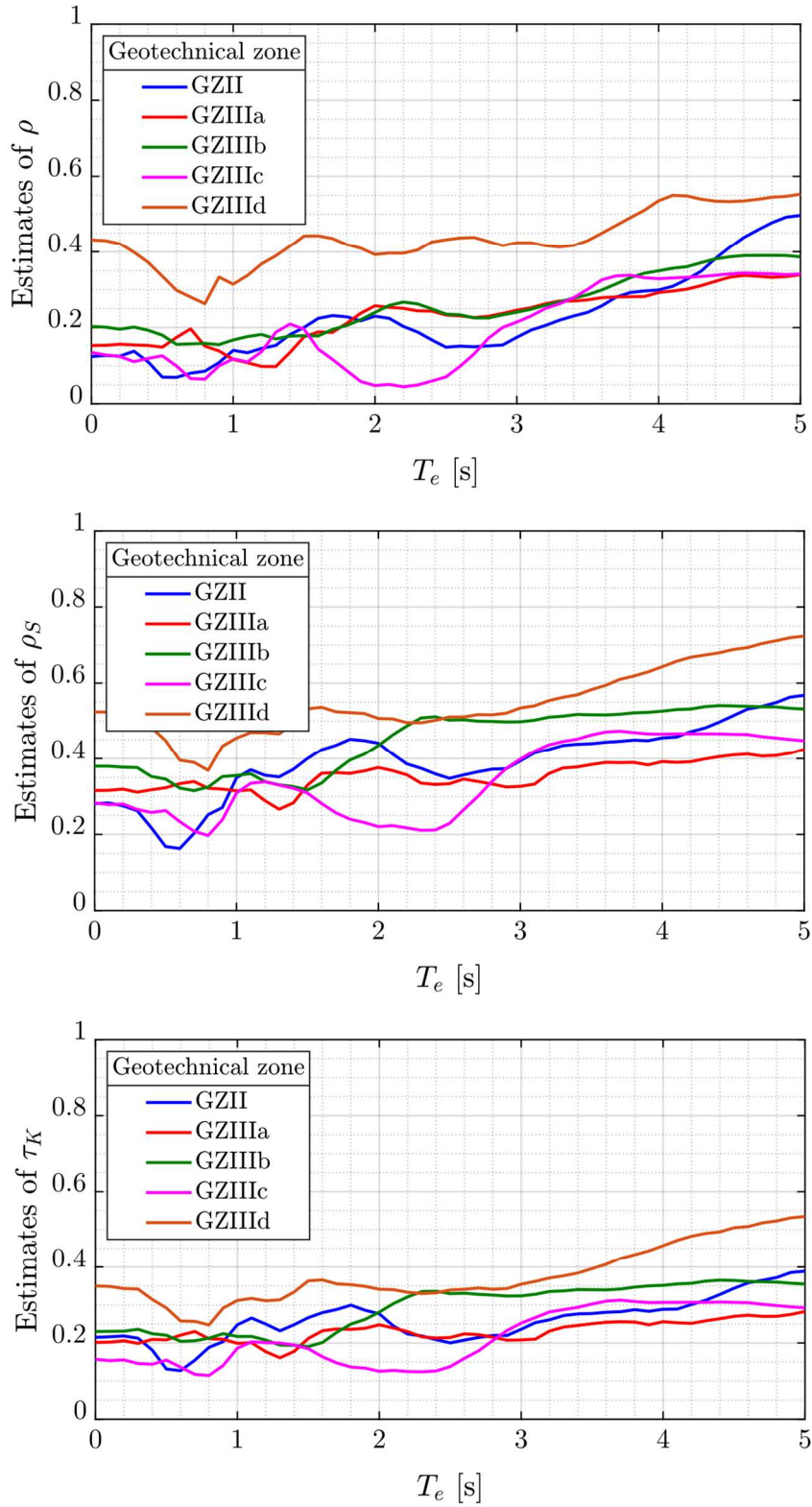


Figure 5.3 Estimates of ρ , ρ_S , and τ_K (from top to bottom) between D_{Sr} and $S_a(T_e)$ considering data from sites located in GZII or GZIII

As can be appreciated from Figure 5.3, the trends among the estimates of ρ , ρ_S , and τ_K between D_{Sr} and $S_a(T_e)$ are similar per geotechnical zone and, also, among themselves.

5.3 Multivariate Probabilistic Seismic Hazard Analyses for Sites Located in the Hill Zone of Mexico City

This section presents multivariate seismic hazard analyses that include the contribution of D_{Sr} and either PGA or $S_a(T_e)$. The study case is staged for sites located in GZI.

The determination of a GMPE that allows estimating the mentioned amplitude-based ground-motion parameters is presented first in Subsection 5.3.1. The multivariate PSHAs are then performed in Subsection 5.3.2.

5.3.1 Predictive Equation for Peak Ground Acceleration and Acceleration Response-spectral Ordinates

A GMPE for the natural logarithm of PGA and $S_a(T_e)$, with T_e varying from 0.1 s to 5 s, in steps of 0.1 s, was developed for sites located in GZI. For PGA and each $S_a(T_e)$, a regression analysis was performed based on the LME model given in Eq. (3.1), considering M_w and R_{hypo} for the definition of \mathbf{X} , and grouping the data by earthquake event. The selected functional form is the following:

$$\ln(PGA)_{ik} \text{ or } \ln[S_a(T_e)]_{ik} = \alpha_0 + (\alpha_1 + \alpha_2 M_{w_i}) \ln(R_{hypo})_{ik} + b_{0_i} + e_{ik} \quad (5.9)$$

where $\ln(PGA)_{ik}$, $\ln[S_a(T_e)]_{ik}$, and $\ln(R_{hypo})_{ik}$ are the natural logarithms of PGA , $S_a(T_e)$ and R_{hypo} of the k th accelerogram recorded during the i th earthquake event, respectively, and M_{w_i} is the moment magnitude of the i th earthquake event. Recall that the terms b_{0_i} and e_{ik} have the prior distributions $b_{0_i} \sim \mathcal{N}(0, \sigma_b^2)$ and $e_{ik} \sim \mathcal{N}(0, \sigma_w^2)$, respectively. The estimates of α_0 , α_1 , α_2 , σ_b^2 , and σ_w^2 obtained from the regression analysis are summarized in Appendix G.

Figure 5.4 shows the distribution of μ and $\mu \pm \sigma$ of the natural logarithms of PGA and $S_a(T_e)$, for five specific values of T_e , in R_{hypo} and M_w . As explained in Subsection 3.3.2 for D_{Sr} , μ and σ are the mean and standard deviation of the natural logarithm of either PGA or $S_a(T_e)$, respectively. The strong-motion data considered in the regression analyses are superimposed in Figure 5.4. Notice that the values of

PGA and $S_a(T_e)$ used to develop the GMPE were obtained from the acceleration response spectra depicted in Appendix F.

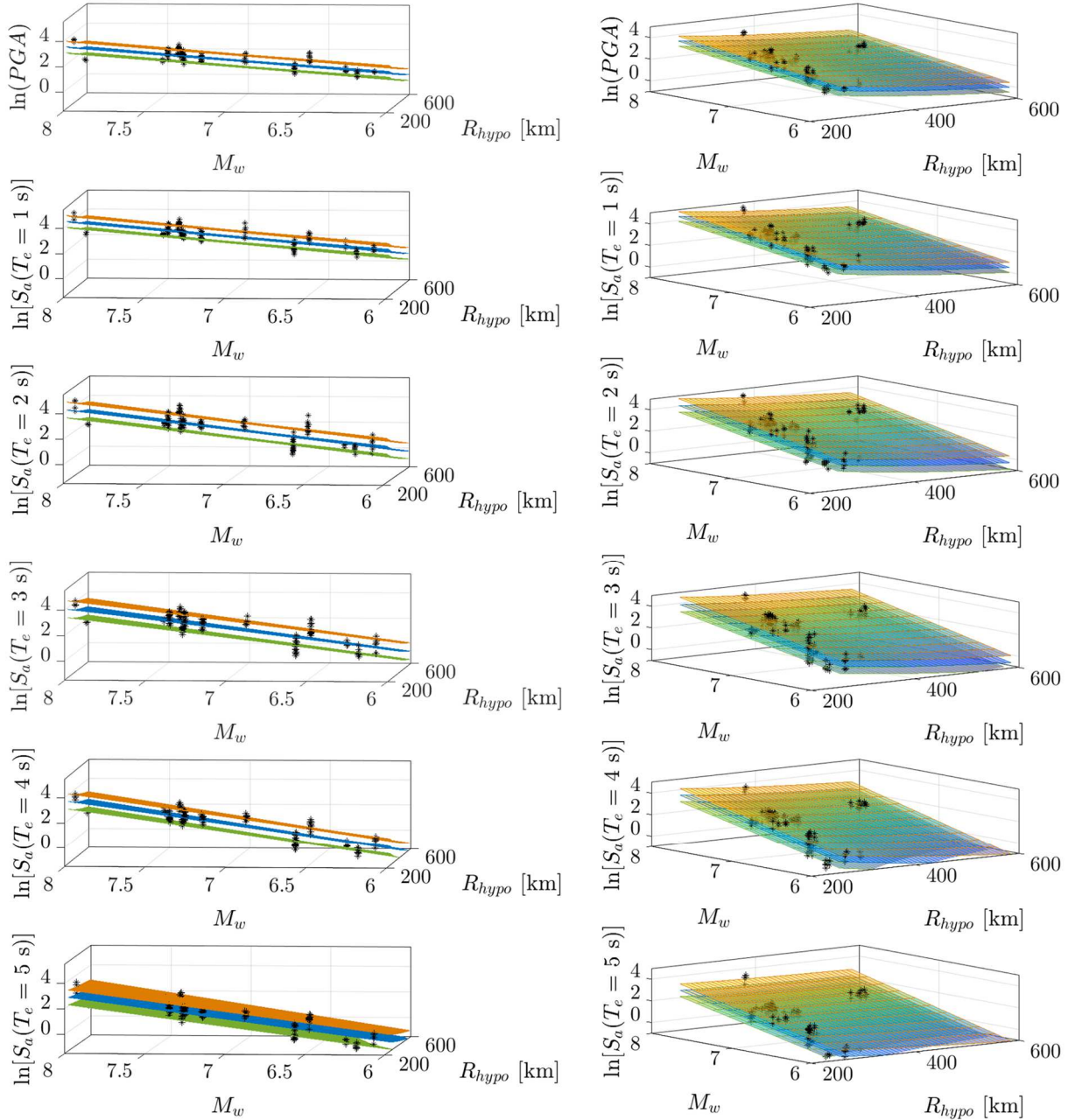


Figure 5.4 Distribution of μ and $\mu \pm \sigma$ of the natural logarithm of PGA and $S_a(T_e)$, with values of T_e varying from 1.0 s to 5.0 s, in steps of 1.0 s, with respect to R_{hypo} and M_w . A 3D view of the plots is shown on the right, whereas their lateral view is shown on the left. Scatter plots of the strong-motion data considered in the regression are superimposed

As noticed by the reader, the functional form given in Eq. (5.9) is the same as that for the natural logarithm of D_{Sr} given in Eq. (3.7). Either for PGA or $S_a(T_e)$, all model coefficients and variance components were statistically significant. That is, their corresponding p -values were smaller than 0.05 and their 95% confidence intervals contain no zeros. Only the estimates of α_0 for $S_a(T_e)$ with values of T_e equal to 4.8 s, 4.9 s, and 5.0 s showed no statistical significance. However, for such values of T_e , no regression analyses were performed considering other functional forms than the one given in Eq (5.9) for simplicity and because of the satisfactory representation of the strong-motion data by the fitted GMPE. The latter can be visually corroborated by Figure 5.4.

The LME model assumptions (such as homoscedasticity, normality, and linearity of effects) were verified from residual analyses and no outliers were discarded during the regression analyses to develop the GMPE for PGA and $S_a(T_e)$.

5.3.2 Multivariate Seismic Hazard Curves

Before further evaluation, as well as for comparison purposes, Figures 5.5 and 5.6 show the (marginal) hazard curves for PGA and $S_a(T_e)$, for values of T_e ranging from 1 s to 5 s, in steps of 1 s, respectively. These were obtained using the procedure described in detail in Section 4.3 to develop the hazard curves for D_{Sr} , but considering the GMPE for PGA and $S_a(T_e)$ developed in Subsection 5.3.1.

Concerning the multivariate PSHAs, Eq. (5.2) was used to estimate the joint mean annual rate of exceedance of a given level d of D_{Sr} and a given level a of either PGA and $S_a(T_e)$. It was evaluated numerically by converting the integrals into discrete summations. For instance, considering the ground-motion parameters D_{Sr} and PGA , the joint mean annual rate of exceedance of d and a , denoted as $\lambda_{d,a}$, can be estimated as follows:

$$\lambda_{d,a} = \sum_{i=1}^{N_S} \sum_{j=1}^{N_M} \sum_{k=1}^{N_R} \lambda_{m_{0i}} P(D_{Sr} > d, PGA > a | m_j, r_k) P(M_w = m_j) P(R_{hyppo} = r_k) \quad (5.10)$$

As for Eq. (4.23), N_M is the total number of elements in a finite set of earthquake magnitudes bounded by the thresholds m_0 and m_u , and N_R is the total number of elements in a finite set of source-to-site distances bounded by the thresholds r_1 and r_2 , which were defined as the levels at which $F_{R_{hyppo}}$ equals 0.05 and 0.95, respectively. For each $i = 1, \dots, N_S$ earthquake source, the values of λ_{m_0} , m_0 , and m_u are reported in Table 4.2 and the values of r_1 and r_2 are reported in Table 4.5.

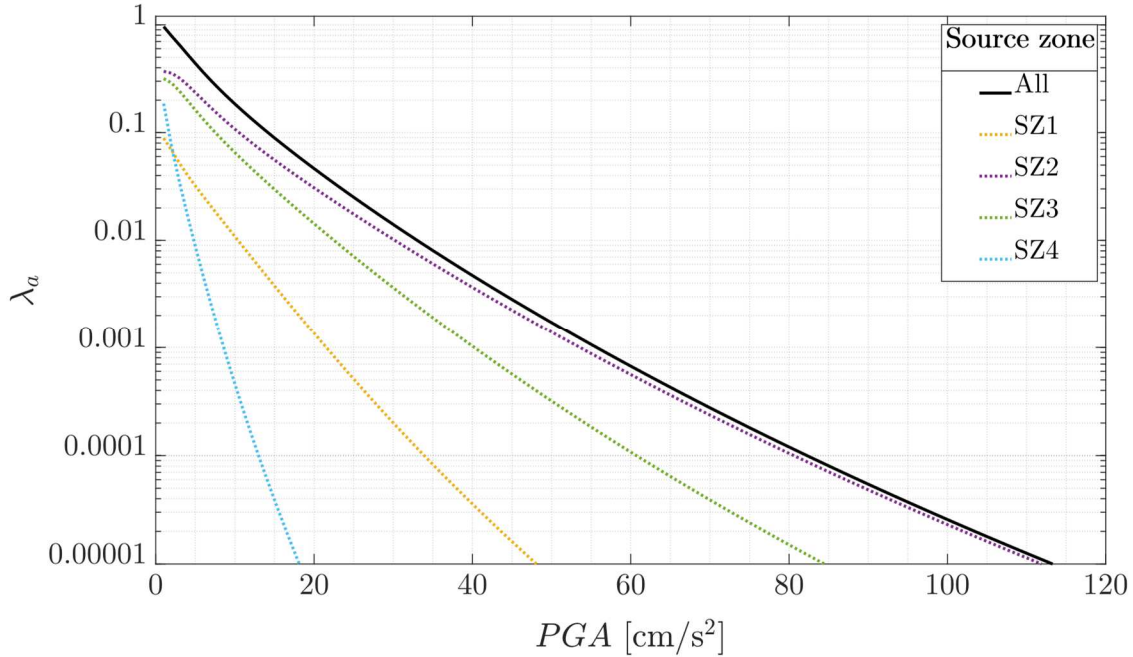


Figure 5.5 Hazard curves of PGA for sites located in GZI. The dashed lines stand for the contribution of the individual source zones identified for interplate earthquakes occurring at the MAT and the solid black line stands for the summation of all contributions

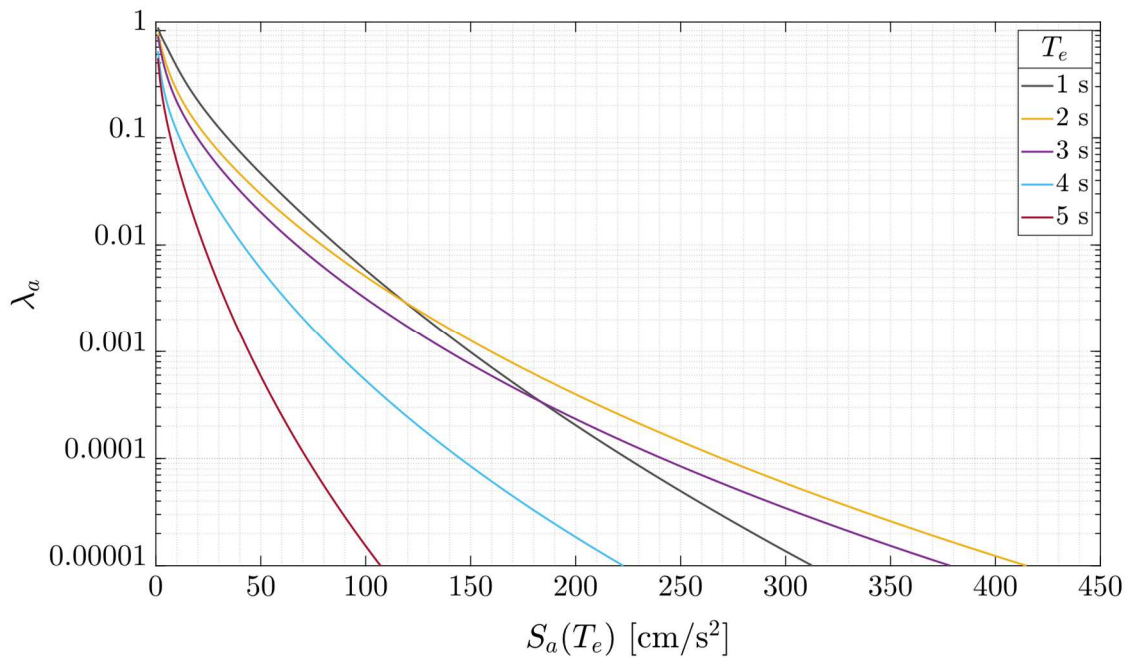


Figure 5.6 Hazard curves of $S_a(T_e)$, with values of T_e varying from 1 s to 5 s, in steps of 1 s, for sites located in GZI

In Eq. (5.10), the joint probability that D_{Sr} and PGA exceed d and a , respectively, given m_j and r_k , can be computed as follows:

$$P[\ln(D_{Sr}) > \ln(d), \ln(PGA) > \ln(a) | m_j, r_k] = 1 - F_{\ln(D_{Sr}), \ln(PGA)}[\ln(d), \ln(a)] \quad (5.11)$$

where $F_{\ln(D_{Sr}), \ln(PGA)}$ is the joint distribution function of the natural logarithms of D_{Sr} and PGA . It can be defined as the integral of their joint density function, which mathematical expression can be formulated based on Eq. (5.3). In this case, μ_1 and σ_1 are the mean and standard deviation of the natural logarithm of D_{Sr} , respectively, and μ_2 and σ_2 are the mean and standard deviation of the natural logarithm of PGA , respectively. They can be obtained from GMPE A given in Subsection 3.3.2 and the GMPE for PGA developed in Subsection 5.3.1. The estimate of ρ between the natural logarithms of D_{Sr} and PGA is already reported in Section 5.2.

Similarly, the joint mean annual rate of exceedance of d and a given level a of $S_a(T_e)$ can be estimated using Eqs. (5.10) and (5.11) but substituting $S_a(T_e)$ instead of PGA .

Figure 5.7 shows the multivariate hazard curve that considers the contribution of D_{Sr} and PGA for sites located in GZI. For its part, Figure 5.8 shows contour plots of the multivariate seismic hazard curves that consider the contribution of D_{Sr} and either PGA or $S_a(T_e)$, with values of T_e varying from 1 s to 5 s, in steps of 1 s. Note that, for better visualization, Figure 5.8 includes only the isolines for values of $\lambda_{d,a}$ equal to 1, 0.1, 0.01, 0.001, 0.0001, and 0.00001.

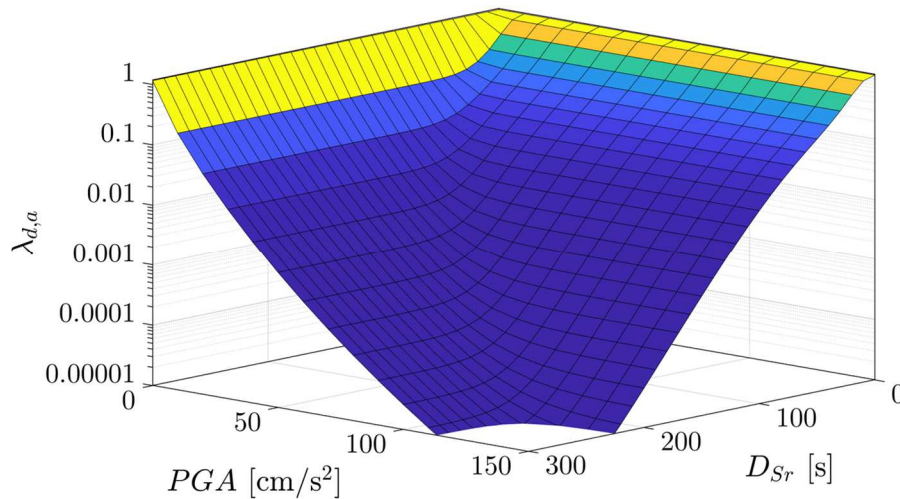


Figure 5.7 Joint annual rate of exceedance of D_{Sr} and PGA for sites located in GZI

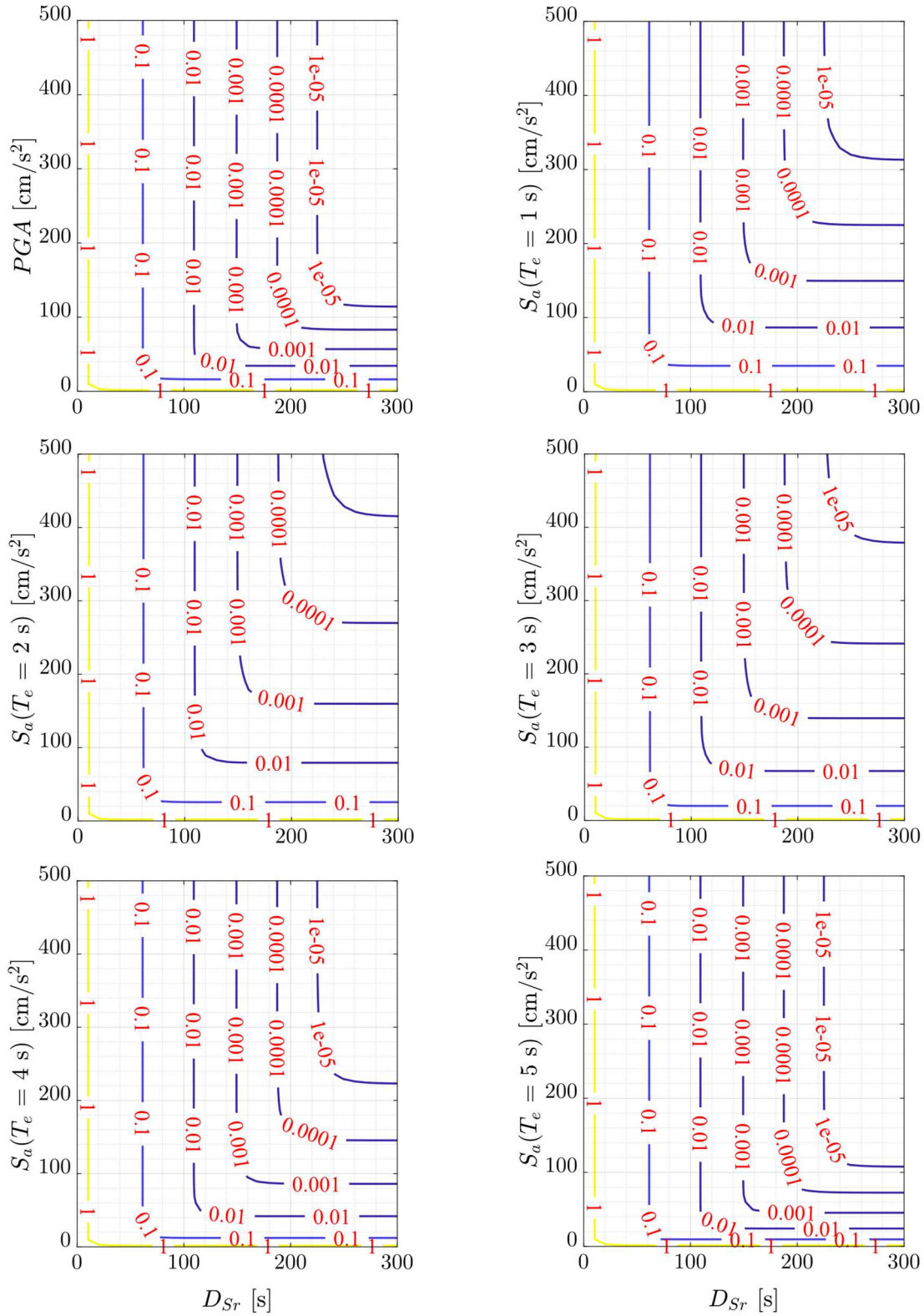


Figure 5.8 Contour plots of the joint annual rate of exceedance of D_{Sr} and either PGA or $S_a(T_e)$ for values of T_e varying from 1 s to 5 s, in steps of 1 s, for sites located in GZI

5.4 Discussion

In this chapter, the author first explains the method used to analyze the joint seismic hazard of a set of ground-motion parameters. The basic premise of the method is the application of the multivariate normal distribution for the definition of the mathematical function that gives the probabilities of occurrence of different possible outcomes of more than two ground-motion parameters, which are taken as random variables. The use of such probability distribution is permitted under the assumption that ground-motion parameters are marginally normally distributed. If ground-motion parameters have a normal distribution, the development of GMPEs for their estimation can be done using LME models (see Section 3.1). Then, the values of the elements of $\boldsymbol{\mu}$ and $\boldsymbol{\Sigma}$, which are parameters of the multivariate normal distribution, can be readily obtained from the GMPEs.

One should mention that Bazzurro and Cornell¹⁷⁸ were the first to illustrate the implementation of the multivariate extension of the normal distribution in PSHAs. They presented an example of how to estimate the joint mean annual rate of exceedance of acceleration response-spectral amplitudes at two values of T_e . Beyond this study, less than a handful of research works have addressed multivariate PSHAs. The above could be due to the lack of GMPEs regionally applicable.

The last statement undoubtedly applies to Mexico City. As stated in Section 5.1, the most recent stage in the development of GMPEs is quite limited there. In particular, the vast majority (of the few) GMPEs found in the literature have been developed for the site where the main UNAM campus is located. Scholars of the development of design ground motions have made a common practice the use of such GMPEs and empirical transfer functions to obtain response spectra at other sites located in Mexico City.^{85,191–193} The determination of transfer functions can be done using different techniques, a detailed description of them is beyond the scope of this thesis, but they can be consulted in the cited references. From this perspective, and for the development of PSHAs, an issue that remains to be solved is if there are no distortions in the values of the elements of $\boldsymbol{\mu}$ and $\boldsymbol{\Sigma}$ of the multivariate normal distribution of the ground-motion parameters. This is due to the application of transfer functions to estimate ground-motion values at other zones than GZI.

On the subject of the development of GMPEs, it would be highly desirable to have consistency in the way that the ground-motion parameters are obtained from the horizontal accelerograms of ground-motion recordings. As mentioned in Section 2.3, the most popular practice in recent years has become the use of the geometric mean of the observations obtained from each pair of horizontal accelerograms. As

discussed by Bommer et al.,⁵³ the geometric mean component was originally introduced as a surrogate for a random component of the ground motion. Nevertheless, it can be argued by the author that individual observations represent the randomness of the ground motion in its purest way. That is, there is no better measurement of a ground-motion parameter than the one obtained directly from a real accelerogram.

To perform multivariate PSHAs, expressly for the measurement of the dependence between ground-motion parameters, it must be ensured that the observations are obtained systematically. As a vague example, imagine trying to get estimates of ρ between one ground-motion parameter whose observations were obtained individually from each arbitrary component of ground-motion recordings and another ground-motion parameter whose observations are based on the geometric mean of the horizontal components. Such a calculation would be nonvalid because a noncompatible criterion would be employed.

The author considers that nowadays there are robust strong-motion databases (at least to Mexico City) with which to develop GMPEs. They must be developed meticulously. For instance, in addition to the GMPEs for D_{Sr} (advanced in Chapter 3), the author proposed in Section 5.2.1 a GMPE for PGA and $S_a(T_e)$ for sites located in GZI to fulfill the purpose of this dissertation about the multivariate PSHAs. For simplicity, the selected functional form of the GMPE for PGA and $S_a(T_e)$ was the same as that for D_{Sr} . The estimates of the elements of α , σ_b , and σ_w obtained from the regression analysis were statistically significant, except for values of T_e equal to 4.8 s, 4.9 s, and 5.0 s. Nevertheless, for structural engineering purposes, such values of T_e are related to unconventional structures (e.g., long-span bridges or supertall buildings). Thus, if necessary, a refit of the strong-motion data is recommended, considering distinct functional forms. Aside, the proposed GMPE fits the observed values of PGA and $S_a(T_e)$ satisfactorily (see Figure 5.4).

It is worth mentioning that, to validate the GMPE for PGA and $S_a(T_e)$ proposed in this dissertation, the estimates of such amplitude-based ground motion parameters were compared with those obtained using the GMPE reported in the research work of Reyes et al.,¹⁸³ giving satisfactory results. Moreover, the probabilistic evaluation of PGA and $S_a(T_e)$ led to a UHS for $T_r = 250$ years that is pretty similar to the one given in the NTC-2020²⁷ for sites located in GZI. Both UHSs are shown in Figure 5.9. The differences between these UHSs are mainly because they were developed under different considerations regarding the identification and probabilistic characterization of earthquake sources and, as

mentioned in previous paragraphs, in the way the ground-motion parameters were obtained from the horizontal accelerograms of ground-motion recordings.

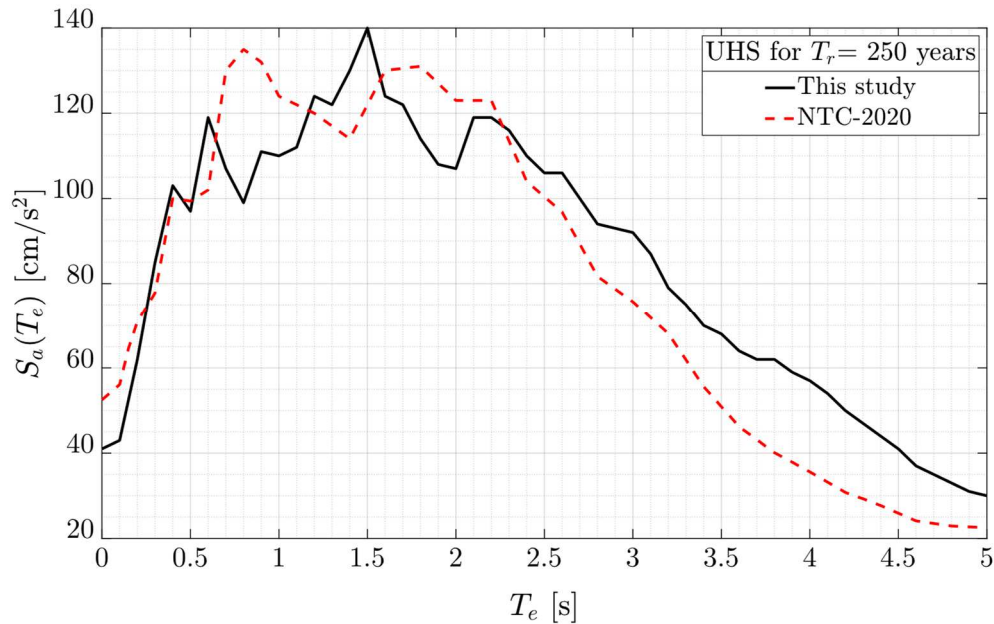


Figure 5.9 Comparison between the UHS for sites located in GZI developed in this study (solid black line) and the one given in the NTC-2020²⁷ (dashed red line)

The contour plots of the joint annual rate of exceedance of D_{S_r} and either PGA or $S_a(T_e)$ (see Figure 5.8) suggest that, to consider the joint effects of such ground-motion parameters in structural design, the values defining the vertex of the isolines associated to the value of T_r of interest must be selected.

Finally, the author wants to mention that the statistical dependence between D_{S_r} and PGA , PGV , PGD , $S_a(T_e)$, and t_f using ρ_S and τ_K for all sites was measured in Section 5.2. Such estimates would facilitate the performance of multivariate PSHAs considering other joint probability distributions different from the multivariate normal distribution. As an instance, they are customarily when modeling the dependence structure of random variables using *copulas*, which are functions that describe the nonlinear dependence between random variables in isolation from their marginal probability distributions.¹⁸⁷ They can be useful for structural reliability applications where non-Gaussian random variables with significant uncertainty are involved. In the case of D_{S_r} , PGA , and $S_a(T_e)$, there was no evidence to reject the null hypothesis that they are normally distributed random variables (relying on the one-sample KS test and other goodness-of-fit tests results)

allowing multivariate PSHAs to be performed using a multivariate normal distribution.

CHAPTER 6

Strong-motion Duration and Structural Performance

6.1 Introduction

For geotechnical and building code purposes, Mexico City has been divided into three zones, namely, GZI, GZII, and GZIII (see Subsection 3.2.2). A drastic amplification of the seismic waves in GZIII with respect to GZI is well documented. For instance, ground motions at GZIII are amplified 8 to 50 times with respect to the site where station CUP5 is located; the frequency at which the maximum amplification occurs varies from site to site and lies between 0.2 Hz and 0.7 Hz.¹⁹⁴ Even ground motions at GZI (where station CUP5 is located) present an amplification as large as 10 in the frequency range of 0.2 Hz to 0.7 Hz in comparison with ground motions at sites outside Mexico City that are located at similar source-to-site distances than station CUP5.^{104,117} Given this, a net amplification of 500 has been reached at some sites located in GZIII. The latter is the largest documented anywhere in the world and has been the cause of damage to structures located in Mexico City during earthquakes.¹⁹⁵

There is extensive research on the influence of amplitude-based ground-motion parameters (such as *PGA* and acceleration-response spectral ordinates) and the frequency content on the seismic response of structures located in Mexico City. Being the opposite for the strong-motion duration (as noted in Appendix A). Thus, investigations should be performed on the capacity of site-specific strong-motion duration to have an effect on the structural response, as well as on the way it is related with other ground-motion parameters.

The following sections present the main results of a series of studies that provide a useful starting point to begin the investigations. In particular, Section 6.3 illustrates the effects of the strong-motion duration as recorded in four different sites in Mexico City on the response of an equivalent SDOF system, which is first formally defined in Section 6.2. Fragility functions for this structure, that consider damage states related to the occupational, life safety, and collapse performance levels, are then presented in Section 6.4. This section extends to SRAs for the collapse performance level. A brief discussion of the results is given in Section 6.5.

6.2 Equivalent Single Degree of Freedom System Modeling

The structural system analyzed is based on an example presented in the book published by Goel and Chao.¹⁹⁶ It consists of a four-story one-bay steel moment frame designed by the plastic method. The gravity loads acting on the steel frame, structural profiles, and dimensions of the steel frame are presented in Figure 6.1.

A classical modal analysis of a two-dimensional finite element model (FEM) of the steel frame was used to find the periods at which the steel frame naturally resonates. It was determined that the first mode, which is triangular-shaped, controls the response of the steel frame. A natural period T_e equal to 1.2 s and mass participation of 0.82 were associated with the first mode. The seismic capacity of the steel frame was determined using an *incremental nonlinear static analysis* (NSA). Note that an incremental NSA, commonly called *pushover analysis*, is used to capture the initial yielding and gradual progressive plastic behavior of elements and the overall response of a given structure under seismic excitations. In particular, a nonlinear FEM of the structure is subjected to monotonically increasing lateral forces with a specified invariant height-wise distribution pattern until either a predetermined target displacement is met or the model collapses (i.e., it becomes unstable).¹⁹⁰ In this case, a load distribution pattern concordant to the first vibration mode of the steel frame was considered. The collapse mechanism developed by the steel frame is depicted in Figure 6.1.

A *pushover curve*, which plots the *base shear*, V_b , versus the *roof displacement*, u_e , for the steel frame was determined from the incremental NSA. It is presented in Figure 6.2. Note that whereas V_b is the horizontal shearing force at the base of a structure,¹⁶ u_e is the result of the lateral forces acting along the height of the structure.⁵ It can be said from the pushover curve given in Figure 6.2 that the yielding of the steel frame begins when the force reaches 379 kN, i.e., when the deformation reaches 17.7 cm. The yield strength and deformation are denoted as F_y and u_y , respectively. As per Figure 6.2, the maximum deformation, u_u , takes place at 58.6 cm and is associated with a maximum force, F_u , equal to 490 kN. The *ductility ratio* of the system, $\mu_e = u_u/u_y$, is approximately 3.3. Notice that *ductility* is a property of a structure that allows it to continue to have significant strength after it has yielded or begun to fail.

An equivalent SDOF system of the steel frame was defined to perform a massive number of IDAs at an affordable computational cost. Its lateral stiffness, k_e , was determined from the linear interval in the pushover curve for the steel frame shown in Figure 6.2 and its mass, m_e , was computed so that the period of the

equivalent SDOF system matched that of the first mode of the steel frame. Here, ζ_e was assumed as 5%. The selected constitutive model of the equivalent SDOF system considers an elastic-plastic behavior with hardening. Figure 6.3 depicts schemes for the equivalent SDOF system and its constitutive model. In Figure 6.3, $c_e = 2\zeta_e m_e \sqrt{\frac{k_e}{m_e}}$ is the viscous damping coefficient, $u_t = u_g + u_e$ is the total displacement of the equivalent SDOF system, and α_e is a fraction of k_e determined from the values of F_u and u_u (see Figure 6.2). The latter is needed for the definition of the secondary stiffness of the constitutive model.

The capacity curve of the equivalent SDOF system is shown in Figure 6.2 together with the pushover curve of the steel frame. As noticed in Figure 6.3, the area under the capacity curve of the equivalent SDOF is smaller than the area under the pushover curve for the steel frame. Expressly, there is a difference of less than 5%. This difference is not expected to cause biases in the IDAs results. As demonstrated by De Luca et al.,¹⁹⁷ maintaining the values of k_e and u_u when employing an equivalent bi-linear SDOF system with hardening for IDAs ensures negligible errors in the structural response despite small differences in the area beneath both curves.

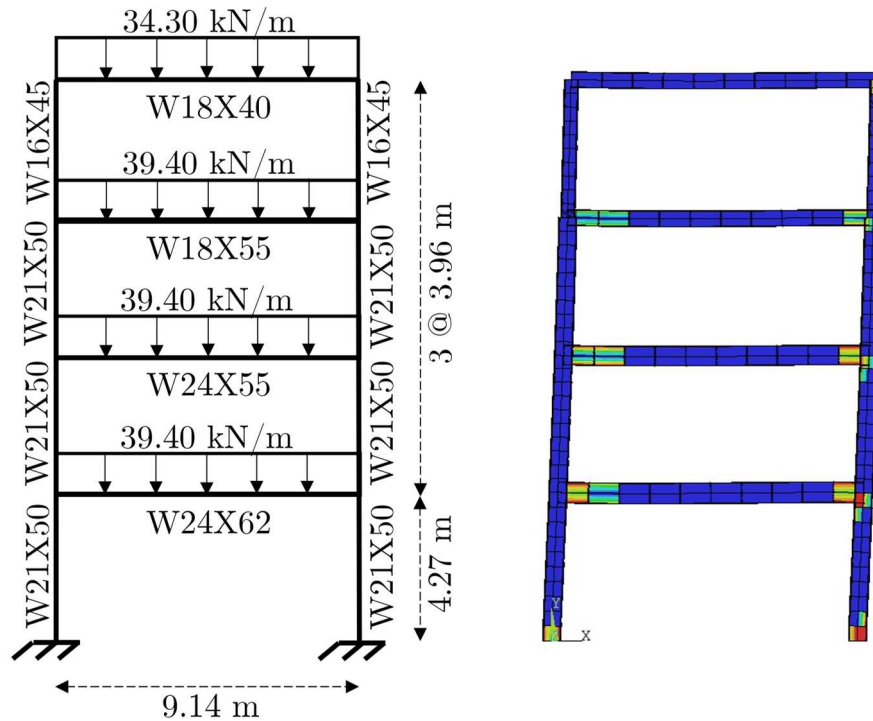


Figure 6.1 At the left is shown a schematic of the moment-resisting steel frame model and at the right is shown the collapse mechanism developed by the steel frame when subjected to a pushover analysis considering a first-mode distribution pattern

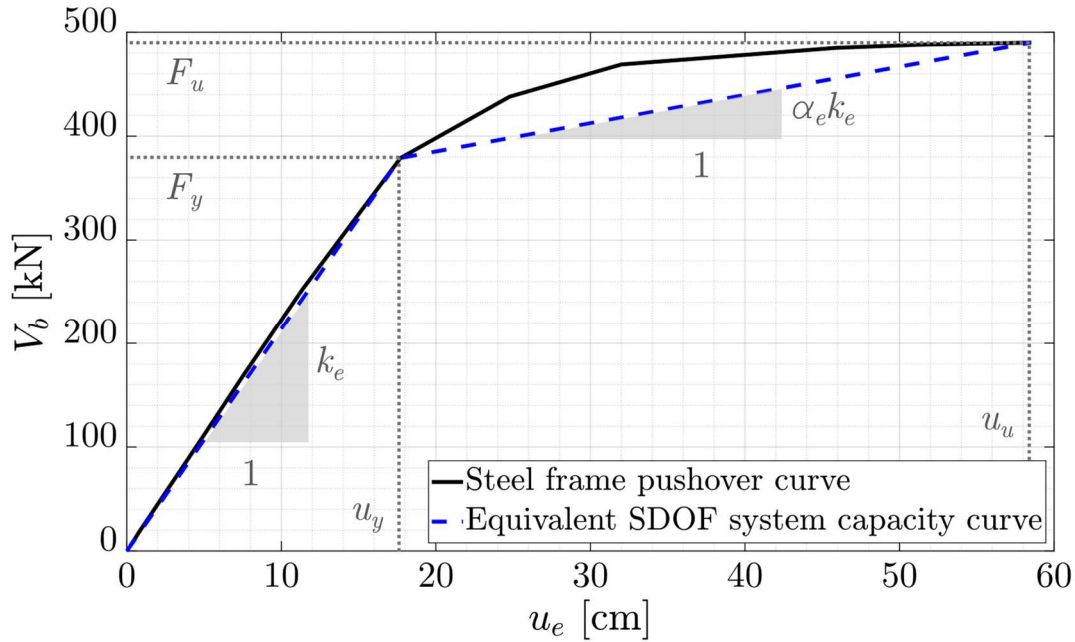


Figure 6.2 Pushover curve for the steel frame and capacity curve of the equivalent SDOF system

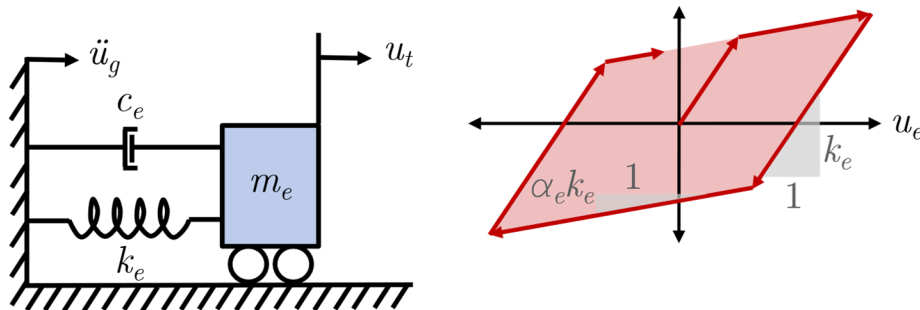


Figure 6.3 Schematics of the equivalent SDOF system and constitutive model considered for its development

6.3 Effects of Strong-motion Duration as Recorded in Mexico City on Structural Response

Accelerograms recorded at stations CUP5, UC44, BO39, and AU11 during the earthquakes that occurred on January 22, 2003, March 20, 2013, April 18, 2014, and June 18, 2020 were used to evaluate the effects of the strong-motion duration on the response of the equivalent SDOF system defined in Section 6.1. In chronological order, the earthquakes will be referred to as E1, E2, E3, and E4, respectively. A map of Central Mexico showing the epicenters of the four interplate earthquakes is

presented in Figure 6.4. Also, a map of Mexico City showing the location of the four stations is presented in Figure 6.4. According to the c the sites where stations CUP5, UC44, BO39, and AU11 are located exhibit values of T_s equal to 0.5 s, 1.3 s, 2.5 s, and 4.0 s, respectively. Station CUP5 is located at the central campus of UNAM in GZI. The other three stations are located in GZIII.

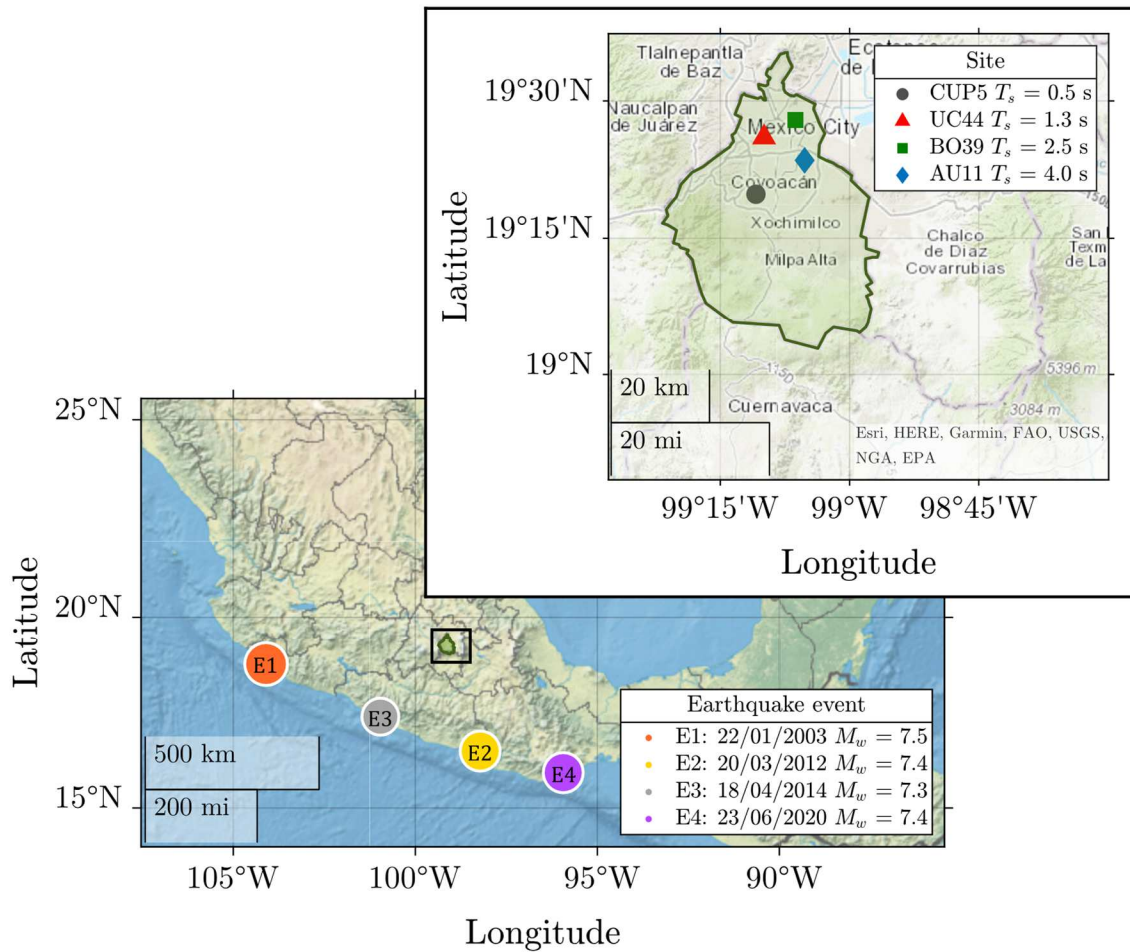


Figure 6.4 Map of Central Mexico showing the epicenters of the earthquakes that occurred on January 22, 2003, March 20, 2013, April 18, 2014, and June 18, 2020, in the Mexican subduction zone. Listed in chronological order, the first earthquake had $M_w = 7.5$, the second and fourth earthquakes had $M_w = 7.4$, and the third earthquake had $M_w = 7.3$. The map overlay shows the territorial delimitation of Mexico City and the geographical location of the stations CUP5, UC44, BO39, and AU11. The sites where these stations are located exhibit values of T_s equal to 0.5 s, 1.3 s, 2.5 s, and 4.0 s, respectively, in accordance with the NTC-2020²⁷

The portion of the accelerograms bounded by $a_0 = 2 \text{ cm/s}^2$ that was recorded in stations CUP5, UC44, BO39, and AU11 during the aforementioned earthquakes are presented in Figure 6.5. As stated in Section 3.3, accelerograms must be bounded by $a_0 = 2 \text{ cm/s}^2$ for objective comparisons of the measured values of t_f and D_{Sr} . As per Figure 6.5, there is a wide variation between the values of t_f from accelerograms recorded in sites located within a radius of approximately 8 km. While station CUP5 recorded accelerograms with $t_f > 80 \text{ s}$ and $D_{Sr} > 41 \text{ s}$, stations UC44, BO39, and AU11 recorded accelerograms with values of t_f greater than 120 s, 205 s, and 320 s, as well as values of D_{Sr} greater than 49 s, 88 s, and 153 s, respectively. The latter indicates the positive correlation between T_s and both t_f and D_{Sr} .

As mentioned in Sections 1.1 and 2.2, the first and last amplitudes of accelerograms generally are so small that they are of little significance for earthquake engineering purposes.¹⁷ For this reason, the strong-motion duration has been adopted to account for the portion of an accelerogram to be considered in the evaluation of the seismic response of structures using NDAs. Indeed, the response of the equivalent SDOF system was evaluated through NDAs using both the accelerograms bounded by $a_0 = 2 \text{ cm/s}^2$ and the time windows in which their amplitudes may be considered strong based on the definition of D_{Sr} given in Eq. (2.8) and considering $a_1 = 0.05$, $a_2 = 0.95$, and t_f equal to the time elapsed between the portion of the accelerograms that encompasses the first and last excursion of $a_0 = 2 \text{ cm/s}^2$. Such time windows are shaded in Figure 6.5. The *peak displacement*, u_{max} , and *maximum hysteretic energy*, $E_{h_{max}}$, were selected to evaluate the response of the equivalent SDOF system. The former is defined as the maximum absolute displacement exhorted in the equivalent SDOF system by an accelerogram and can be directly identified from a displacement time history, $u_e(t)$, which is an output of an NDA. The second is the energy dissipated in the inelastic behavior of the equivalent SDOF system and is equal to the area within the hysteresis loop resulting from each NDA. Note that a hysteresis loop is presented as a plot of the isolated forces on the spring of the equivalent SDOF system, F_k , versus the deformations u_e (see Figure 6.3).¹⁹⁰

The displacement histories $u(t)$ of the equivalent SDOF system obtained from the NDAs are given in Figure 6.5. As noted in Figure 6.5, the displacement histories $u(t)$ produced by the time window defined by D_{Sr} look exactly like those produced by the accelerograms bounded by $a_0 = 2 \text{ cm/s}^2$. Hence, the values of u_{max} are practically the same. As per Figure 6.5, the maximum difference between values of u_{max} is observed for the accelerogram recorded at station UC44 during the March 20, 2013 earthquake. This difference is equal to 0.69 cm and, to the mild opinion of

the author, is inconsequential from a structural engineering perspective for the structure under analysis.

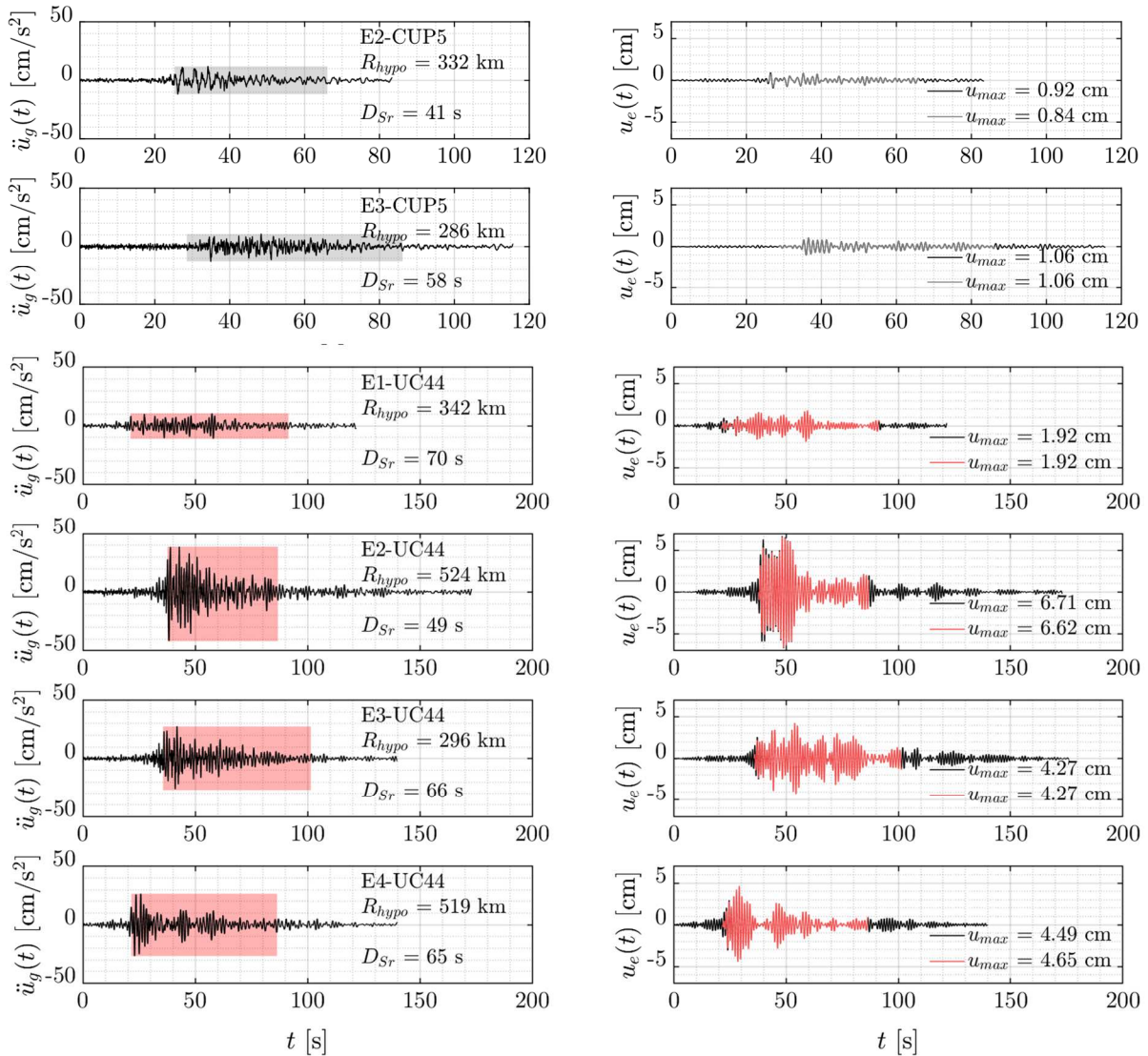


Figure 6.5 On the left, there are shown accelerograms (bounded by $a_0 = 2 \text{ cm/s}^2$) recorded in stations CUP5, UC44, BO39, and AU11 during four earthquakes that occurred in the Mexican subduction zone (see Figure 6.4). The shaded areas represent the time windows in which the ground motions may be considered strong according to the definition of D_{Sr} . On the right, there are shown the displacement histories $u_e(t)$ of the equivalent SDOF system when subjected to the accelerograms shown on the left side. The structural displacement measured considering the accelerograms (bounded by $a_0 = 2 \text{ cm/s}^2$) is depicted by the black lines and the structural displacement measured considering only the strong phase of the ground motions is depicted by the colored lines

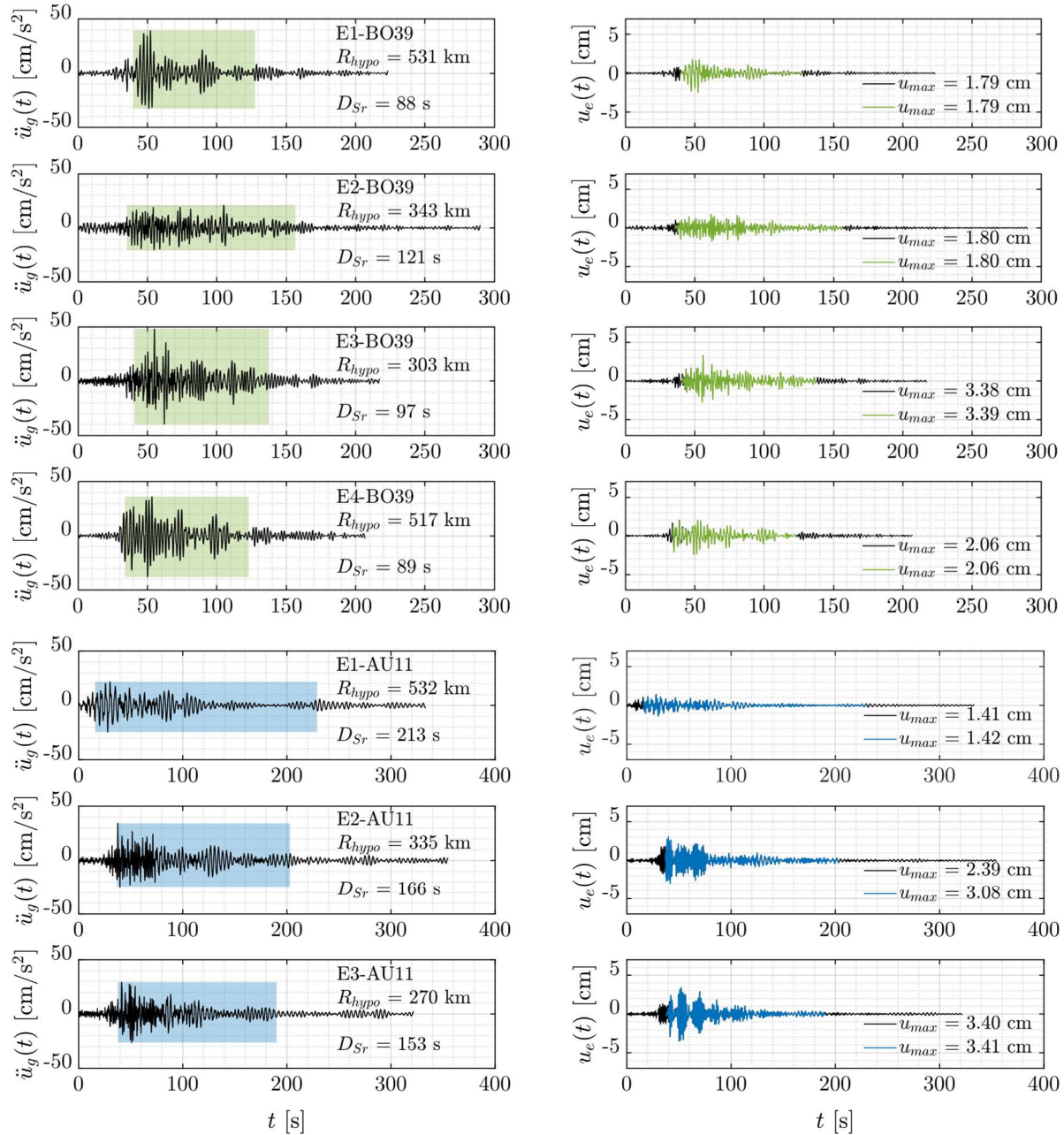


Figure 6.5 On the left, there are shown accelerograms (bounded by $a_0 = 2 \text{ cm/s}^2$) recorded in stations CUP5, UC44, BO39, and AU11 during four earthquakes that occurred in the Mexican subduction zone (see Figure 6.4). The shaded areas represent the time windows in which the ground motions may be considered strong according to the definition of D_{Sr} . On the right, there are shown the displacement histories $u_e(t)$ of the equivalent SDOF system when subjected to the accelerograms shown on the left side. The structural displacement measured considering the accelerograms (bounded by $a_0 = 2 \text{ cm/s}^2$) is depicted by the black lines and the structural displacement measured considering only the strong phase of the ground motions is depicted by the colored lines

As can be noticed from Figure 6.5, the equivalent SDOF system never undergoes its plastic behavior when subjected to the accelerograms. This implies line-like hysteresis loops, i.e., values of hysteretic energy, $E_{h_{max}}$, equal to zero.

It is worth mentioning that the energy input to the equivalent SDOF system considering both an accelerogram bounded by $a_0 = 2 \text{ cm/s}^2$ and the time window in which its amplitudes may be considered as strong based on the definition of D_{Sr} is just about the same. For instance, Figure 6.6 depicts the *input energy*, E_i , as a function of t and normalized with respect to m_e , imparted to the equivalent SDOF system when subjected to the accelerograms recorded at station UC44 during E2 and E4 (see Figure 6.5). Notice that $E_i(t)$ can be defined as follows¹⁹⁸:

$$E_i(t) = \int m_e \ddot{u}_t(t) \dot{u}_g(t) dt \quad (6.1)$$

where $\ddot{u}_t(t) = \ddot{u}_e(t) + \ddot{u}_g(t)$ is the absolute acceleration, with $\ddot{u}_e(t)$ being the relative acceleration of the equivalent SDOF system as function of t .

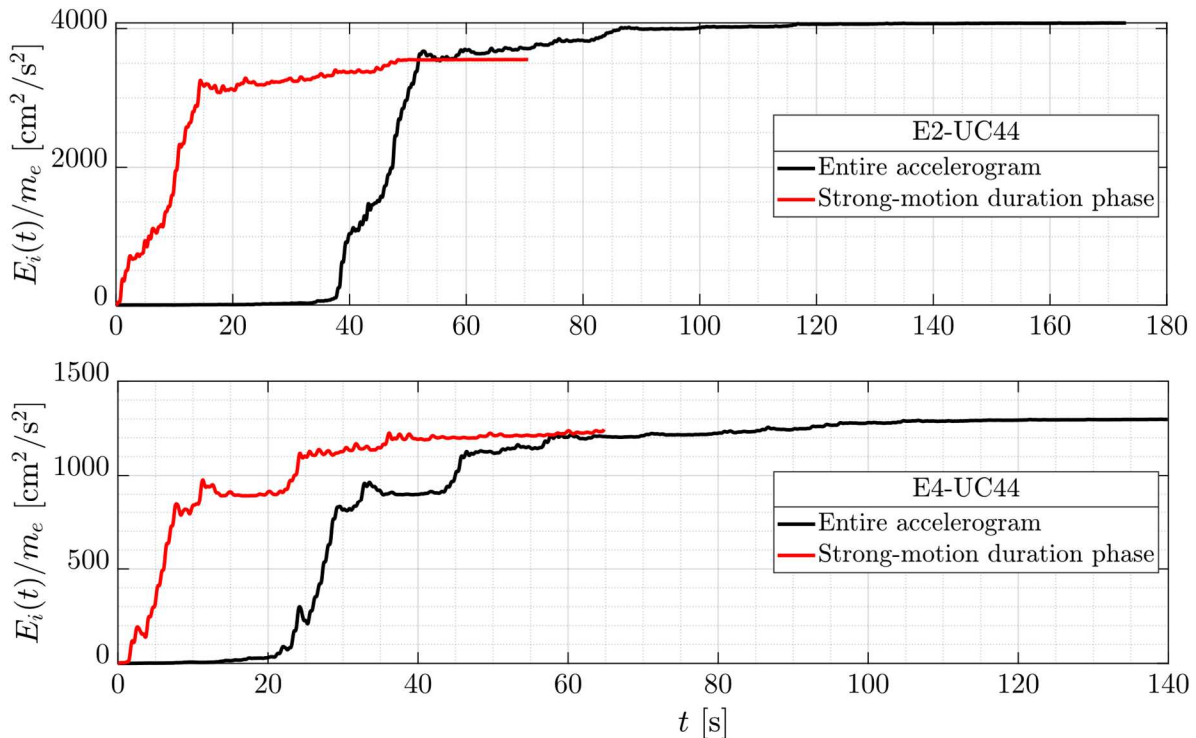


Figure 6.6 Input energy imparted to the equivalent SDOF system when subjected to accelerograms recorded at station UC44 during E2 and E4. The black line represents the energy disclosed by the accelerograms (bounded by $a_0 = 2 \text{ cm/s}^2$), whereas the red line represents the energy disclosed by the strong phase of the ground motions

As per Figure 6.6, the value of E_i disclosed by the accelerograms (bounded by $a_0 = 2 \text{ cm/s}^2$) recorded during E2 and E4 to the equivalent SDOF system was approximately 15% and 4% greater, respectively, than that disclosed when considering only the time windows in which the ground motions may be considered strong according to the definition of D_{Sr} . Such percentages were smaller when examining the input energy imparted by accelerograms with greater values of PGA .

6.4 Relating Strong-motion Duration and Structural Damage

Nowadays, relationships between the severity of ground motions and structural damage are commonly given in the form of fragility functions, which define the conditional probability of exceeding various damage states given postulated ground-motion levels y . Expressly, the first term of the integral given in Eq. (1.1) provides the generic definition of a fragility function.

As explained in Section 1.1, developing a fragility function commonly involves an IDA, which requires the use of either real or synthetic accelerograms. As discussed in Section 2.5, due to the lack of real site-specific accelerograms, it has been common practice to use accelerograms recorded worldwide to perform IDAs. In a certain way, any problem is dismissed as the acceleration response spectra of the accelerograms are scaled based on site-specific target spectra, which can be obtained, e.g., from either predetermined design spectra or GMPEs for PGA and response-spectral ordinates. The foregoing does not cover that the (strong-motion) duration of such accelerograms is representative of the one observed at the site where a structure of interest is (or will be) located. Furthermore, there is a tendency to evaluate the effect of the strong-motion duration on the structural response by categorically classifying accelerograms as “short” or “long” according to different duration intervals (which are based on different subjective opinions) or depending on the tectonic environment that caused the recorded ground motions (e.g., those accelerograms associated to interplate earthquakes are cataloged as long, while those associated to shallow-crustal are cataloged as short).

Such as the use of a target response spectrum to define the amplitude and frequency content of ground motions at a specific site, one may directly utilize GMPEs (just as those given in Subsection 3.3.2) to define the strong-motion duration of ground motions located at the site of interest. By doing so, the two problems identified above can be easily avoided.

Thus, this section presents the development of fragility functions that allow evaluating the influence of the strong-motion duration on the performance of the

equivalent SDOF system defined in Section 6.2. Particularly, the results of the IDAs needed to develop the fragility functions are first presented in Subsection 6.4.1 and the fragility functions are then given in Subsection 6.4.2.

6.4.1 Incremental Dynamic Analyses

Incremental dynamic analyses were used to evaluate the seismic response of the equivalent SDOF system, which was assumed to be situated at three different sites in Mexico City. The sites are located where stations UC44, BO39, and AU11 are situated (see Figure 6.1). Site-specific accelerograms were needed to conduct IDAs. Instead of selecting accelerograms recorded at each of the three sites, mutually independent accelerograms were simulated by employing the well-known SIMQKE-I software. For each site, the target response spectrum was taken as the UHS given in the NTC-2020.²⁷ Figure 6.7 shows the site-specific target spectrum considered in for the generation of the synthetic accelerograms.

Deterministic seismic hazard analyses that considered the MCE as one earthquake with $M_w = 7.5$ occurring at $R_{hypo} = 250$ km were conducted to characterize the strong-motion duration at each site of interest. The estimates of μ of the natural logarithm of D_{Sr} obtained using GMPE C are shown in Table 6.1. Recall that the values of μ can be computed from the estimated $\mathbf{X}\boldsymbol{\alpha}$ used to develop GMPE C—see Eq. (3.8)—and $\sigma = 0.2156$.

If the natural logarithm of D_{rS} is assumed to be normally distributed, then it can be said that D_{Sr} is lognormally distributed. Therefore, the density function of D_{Sr} can be defined as¹⁹⁹:

$$f_{D_{Sr}}(d) = \frac{1}{d\sigma\sqrt{2\pi}} \exp \left\{ -\frac{1}{2} \left[\frac{\ln(d) - \mu}{\sigma} \right]^2 \right\} \quad (6.2)$$

Based on Eq. (3.11), one can estimate the mean and standard deviation of D_{Sr} , denoted as $\mu_{D_{Sr}}$ and $\sigma_{D_{Sr}}$, respectively, as follows:

$$\mu_{D_{Sr}} = \exp \left(\mu + \frac{V}{2} \right) \quad (6.3a)$$

$$\sigma_{D_{Sr}} = \sqrt{\exp(2\mu + V)[\exp(V) - 1]} \quad (6.3b)$$

The estimates of $\mu_{D_{Sr}}$ and $\sigma_{D_{Sr}}$ obtained for each site where the equivalent SDOF system is hypothetically located are also reported in Table 6.1.

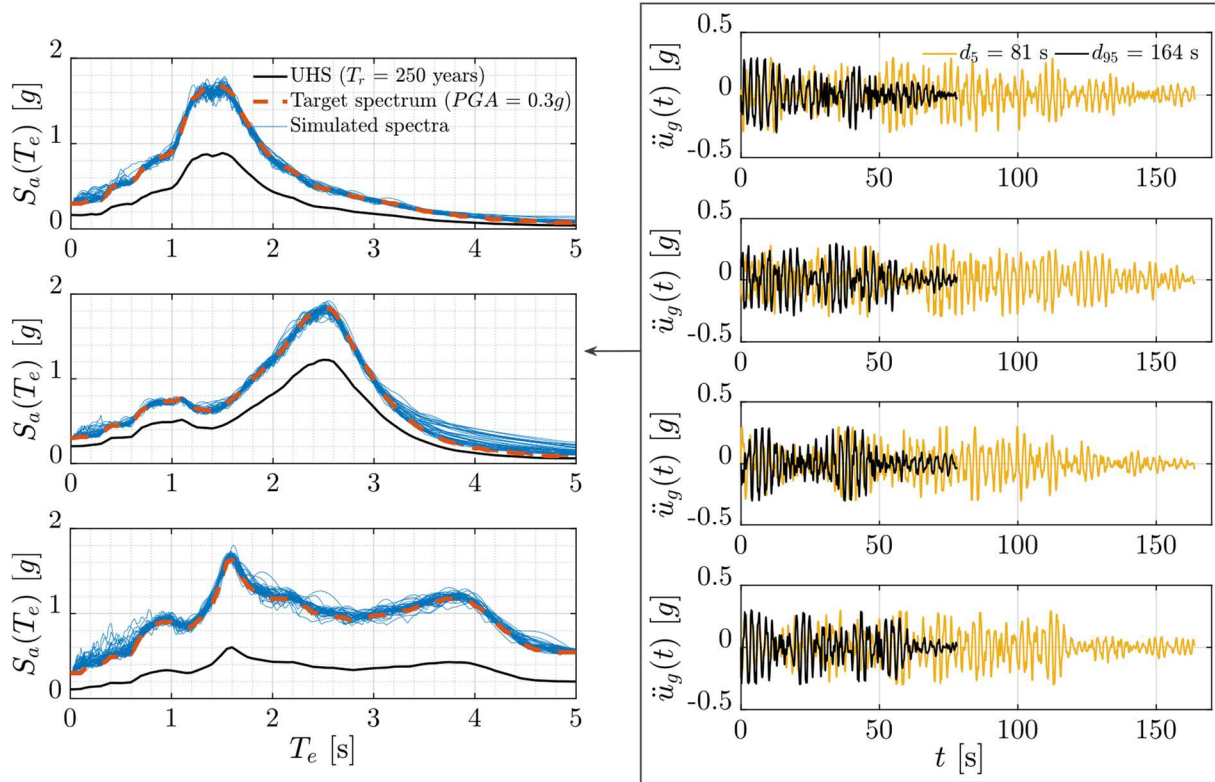


Figure 6.7 On the left, there are shown the design spectra given in the NTC-2020²⁷ (UHSs for $T_r = 250$ years) for the sites where stations UC44, BO39, and AU11 are located. The response spectra of three aleatory groups (one per site) of 40 synthetic accelerograms each (with $PGA = 0.3g$) overlap the design spectra. On the right, there are shown a sample of eight synthetic accelerograms with $PGA = 0.3g$ from two aleatory groups generated for the site where station BO39 is located. Each sample consists of four synthetic accelerograms with equal duration

Table 6.1 Estimates of μ of the natural logarithm of D_{Sr} , $\mu_{D_{Sr}}$, and $\sigma_{D_{Sr}}$ obtained from a DSHA that considers a scenario earthquake with $M_w = 7.5$ occurred at $R_{hypo} = 250$ km from three sites with T_s equal to 1.3 s, 2.5 s, and 4.0 s. The last two columns summarize the values placed at the 5th and 95th percentile for $F_{D_{Sr}}$

T_s	μ	$\mu_{D_{Sr}}$	$\sigma_{D_{Sr}}$	d_5	d_{95}
1.3 s	4.4024	18 s	65 s	57 s	116 s
2.5 s	4.7451	26 s	92 s	81 s	164 s
4.0 s	4.9915	151 s	33 s	103 s	210 s

Then, two sets of synthetic accelerograms were generated per site, each with a duration equal to the values placed at the 5th and 95th percentile, respectively, for the probability distribution of D_{Sr} , $F_{D_{Sr}}$, which can be defined as the integral of Eq. (6.2). Note that, for $F_{D_{Sr}}$, the i th percentile, with i varying from 1 to 100, is defined to be the smallest number D_{Sr_i} satisfying $\frac{i}{100} \leq F_{D_{Sr}}(d_i)$. Thus, per site, Table 6.1 summarizes the values of d_5 and d_{95} .⁴²

Notice that the use of GMPE C (or of any other strong-motion duration GMPE given in Subsection 6.3.2) means the simulation of the time windows in which the ground motions may be considered as strong according to the definition of D_{Sr} , with $a_1 = 0.05$ and $a_2 = 0.95$. Therefore, it was necessary to establish amplitude envelopes using the intervals over which accelerograms recorded at each site may be considered as strong. The selected accelerograms were from ground motions caused by interplate earthquakes with similar characteristics as the MCE, e.g., those presented in Figure 6.5.

Every set of synthetic accelerograms consisted of seven groups of forty accelerograms each. Every group was associated with one discrete value of PGA , which varies from $0.1g$ to $0.4g$, in increments of $0.05g$. As an instance, Figure 6.7 shows samples of four synthetic accelerograms (with $PGA = 0.3g$) from two aleatory groups generated for the site where station BO39 is located. Notice that Figure 6.7 also includes the response spectra from three aleatory groups of synthetic accelerograms (one per site) having that $PGA = 0.3g$.

Figure 6.8 shows the IDAs results in form of box plots. As noticed in Figure 6.8, the structural response of the equivalent SDOF system was evaluated by means of u_{max} and $E_{h_{max}}$. It can be seen from Figure 6.8 that, for each site, the medians of both u_{max} and $E_{h_{max}}$ (visually represented by the horizontal line at the middle of each box) increase as PGA increases. In general, at each value of $PGA \geq 0.2g$, the medians of u_{max} and E_h associated with durations equal to d_5 are smaller than those associated to durations equal to d_{95} . For $PGA < 0.20g$, the medians of u_{max} and $E_{h_{max}}$ obtained from accelerograms with durations equal to $d_{0.05}$ are practically the same as those obtained from accelerograms with durations equal to d_{95} .

From Figure 6.8 it can also be noticed that, at values of $PGA \leq 0.25g$, the medians of both u_{max} and $E_{h_{max}}$ (from accelerograms with duration equal to either d_5 or d_{95}) for the site with $T_s = 1.3$ s are greater than the medians obtained for other sites. The above seems to be quite logical because the dominating frequency of the applied accelerograms is close to the natural frequency of the equivalent SDOF system, which generates increased amplitudes.

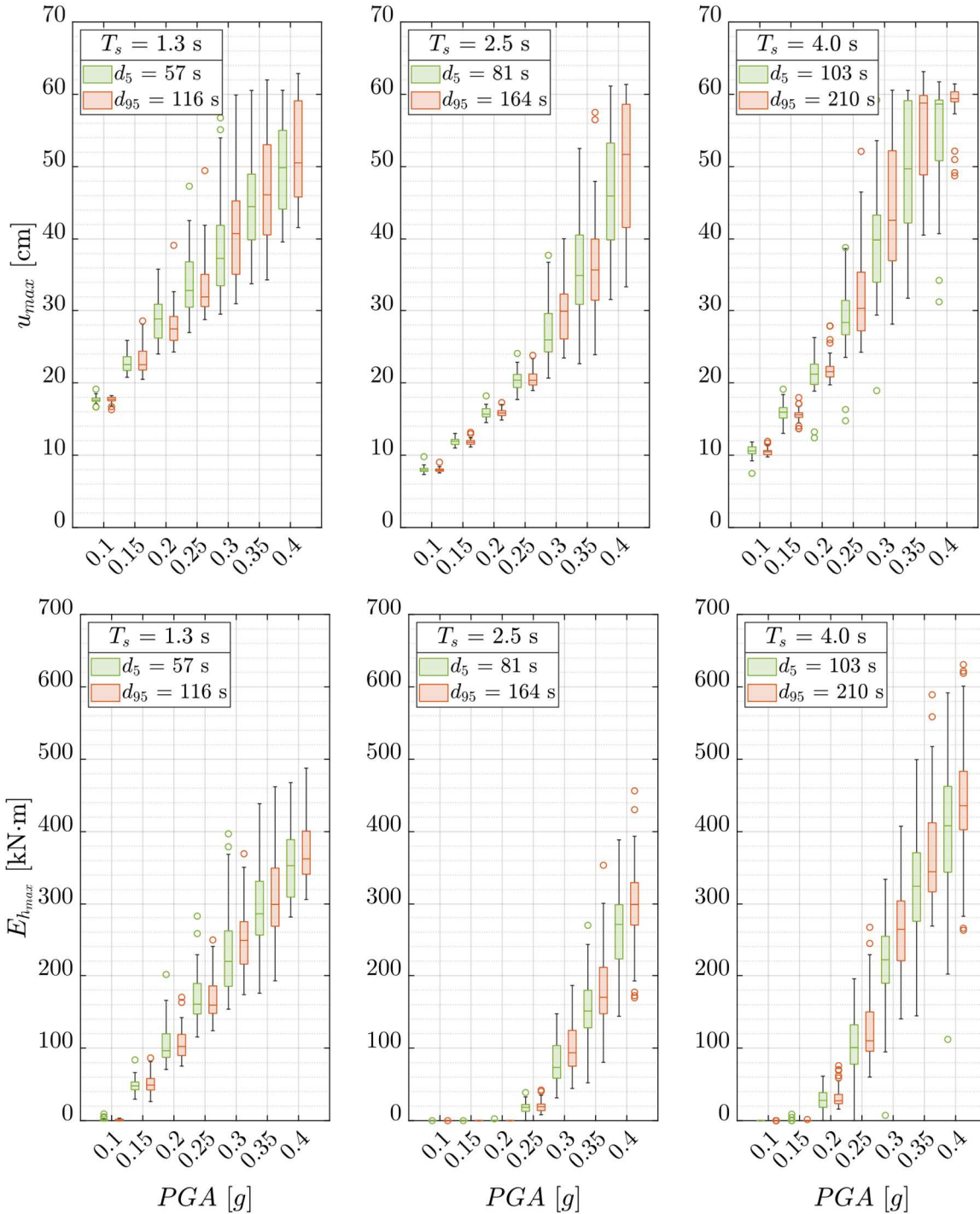


Figure 6.8 Incremental dynamic analysis results for the equivalent SDOF system, which was assumed to be located at three different sites in Mexico City. The results that considered synthetic accelerograms with a duration equal to d_5 are shown in green and those results that considered synthetic accelerograms with a duration equal to d_{95} are shown in orange. At the top are shown the results for u_{max} , while at the bottom for E_{hmax}

6.4.2 Fragility Functions

Based on the IDAs results, fragility functions that consider displacement- and energy-based damage states were developed to evaluate the effects of the strong-motion duration on the performance of the equivalent SDOF system, which was assumed to be situated at the sites where stations UC44, BO39, and AU11 are located.

Specifically, the fragility functions were developed considering damage states related to the operational, life safety, and collapse performance levels of the equivalent SDOF system. On one hand, the displacement-based damage states were defined as follows based on the recommendations given in the SEAOC²⁰⁰:

- (a) The damage state related to the operational performance level was set from a displacement threshold equal to $u_y = 17.7$ cm.
- (b) The damage state related to the life safety performance level was set from a displacement threshold equal to $u_y + 0.6u_p$, where $u_p = u_u - u_y$. Therefore, the damage state was assumed to be equal to 42.2 cm.
- (c) For the last performance level, which is associated with the collapse of the equivalent SDOF system, the damage state was set equal to $u_u = 58.6$ cm.

On the other hand, for the energy-based fragility functions, the response of the equivalent SDOF system was defined in terms of a damage index proposed by Díaz et al.² Such damage index, hereafter denoted as DI_{EC} , is determined using a linear relation between $E_{h_{max}}$ and the *maximum strain energy*, $E_{s_{max}}$, each normalized with respect to their correspondent energy capacity of the system (associated to the predetermined performance levels). Note that the strain energy, E_s , is related to the stiffness variation and the ductility of a structure.

Thus, DI_{EC} can be computed as follows:

$$DI_{EC} = \eta_E E_{s_{max}}^N + (1 - \eta_E) E_{h_{max}}^N \quad (6.4)$$

where $E_{s_{max}}^N$ and $E_{h_{max}}^N$ are the normalized-maximum strain and hysteretic energy, respectively. For this study, they were estimated as follows²:

$$E_{s_{max}}^N = \begin{cases} 0 & 0 \leq u \leq u_y \\ \frac{E_{s_{max}}}{E_s(u_d)} & u_y < u \leq u_u \end{cases} \quad (6.5a)$$

$$E_{h_{max}}^N = \begin{cases} 0 & 0 \leq u \leq u_y \\ \frac{E_{h_{max}}}{E_h(u_d)} & u_y < u \leq u_u \end{cases} \quad (6.5b)$$

where $E_s(u_d)$ and $E_h(u_d)$ are the strain and hysteretic energy, respectively, associated with a displacement u_d equal to $u_y + 0.6u_p$ for the life safety performance level or equal to u_u for the collapse performance level. Note that, by definition, the values of DI_{EC} are zero for $u_e < u_y$. Therefore, fragility functions associated with the operational performance level were omitted. The parameter η_E is defined ahead in the text.

It is worth emphasizing that Díaz et al.² considered $u_d = u_u$. Although in this study such value was considered for analyzing the collapse performance level of the structure, $u_d = u_y + 0.6u_p$ was established to have a comparable index to evaluate the life safety performance level. Note that $E_s(u_d)$ and $E_h(u_d)$ can be obtained from the capacity curve of the equivalent SDOF system. For instance, Figure 6.9 depicts the computation of $E_s(u_d)$ and $E_h(u_d)$ for $u_d = u_u$.

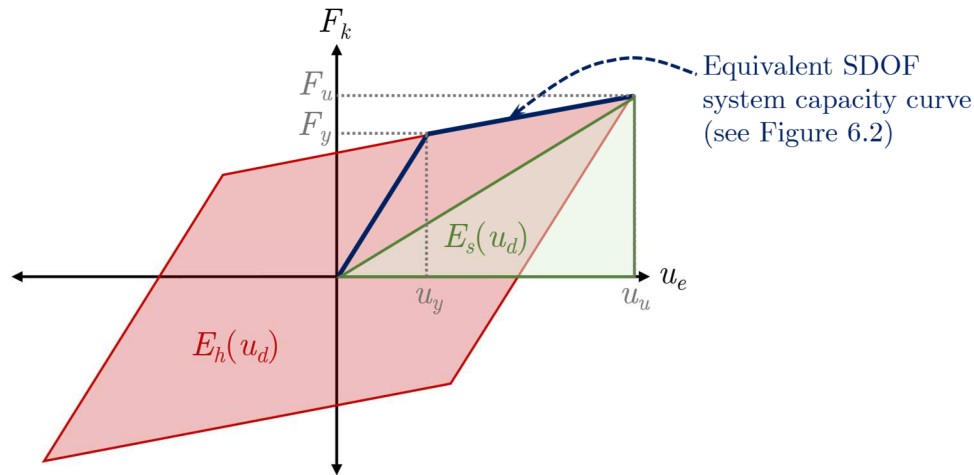


Figure 6.9 Schematic for the determination of $E_s(u_d)$ and $E_h(u_d)$ for $u_d = u_u$ using the capacity curve of the equivalent SDOF system

In Eq. (6.4), η_E is a proportionality factor that describes how much $E_s(u_e)_N$ contributes to the structural damage. On the other hand, $1 - \eta_E$ describes how much the energy dissipated through hysteresis contributes to the structural damage. According to Díaz et al.,² values of η_E ranging from 0.6 to 0.7 have been determined

for steel structures. Here, $\eta_E = 0.68$ was considered for the development of the fragility functions for the equivalent SDOF system.

In this manner, for the development of the energy-based fragility functions, the damage state is set equal to one for the evaluation of the life safety and collapse performance levels of the equivalent SDOF system. Following Eq. (1.1), each fragility function was defined using the form of the lognormal distribution, with parameters μ and σ , as follows:

$$P(\text{structural response} > \text{damage state} | PGA = a) = \Phi \left[\frac{\ln(a) - \mu}{\sigma} \right] \quad (6.6)$$

where $P(\text{structural response} > \text{damage state} | PGA = a)$ is the probability that the structural response, measured as either u_{max} or DI_{EC} , exceeds a damage state given that PGA takes a value equal to a and Φ represents the distribution function of the standard normal distribution.¹³⁷ Note that, for better reading, the left side of Eq. (6.3) will be denoted as $P_{F|a}$ hereafter.

As noticed, the right side of Eq. (6.6) stands for the distribution function of a lognormal distribution. Such probability distribution was considered to fit the data to the effects of a continuous function. Specifically, for each site and set of synthetic accelerograms of equal duration, the data fitting was performed as follows:

1. The probability of exceeding each damage state at each value of PGA was determined using the lognormal distribution.
2. For each damage state, the parameters μ and σ were estimated from linear regression knowing that Eq. (6.6) comprises a linear combination of such parameters as follows:

$$\Phi^{-1}(P_{F|a}) = \frac{1}{\sigma} \ln(a) - \frac{\mu}{\sigma} \quad (6.7)$$

The estimates of μ and σ that describe the displacement- and energy-based fragility functions are summarized in Tables 6.2 and 6.3, respectively.

Based on Eq. (6.6), Figures 6.10 and 6.11 show the site-specific fragility curves developed for the selected performance levels of the equivalent SDOF system. Note that a *fragility curve* is a graphical tool for presenting the probability of exceeding a specific damage state as a function of a ground-motion parameter.⁶

Table 6.2 Estimates of μ and σ for the displacement-based fragility functions developed for the operational, life safety, and collapse performance levels of the equivalent SDOF system located in sites with T_s of 1.3 s, 2.5 s, and 4.0 s

T_s	D_{Sr}	Operational		Life safety		Collapse	
		$\hat{\mu}$	$\hat{\sigma}$	$\hat{\mu}$	$\hat{\sigma}$	$\hat{\mu}$	$\hat{\sigma}$
1.3 s	$d_5 = 57$ s	-2.3560	0.1459	-1.1152	0.1602	-0.6077	0.2504
	$d_{95} = 116$ s	-2.3254	0.1498	-1.1625	0.1620	-0.6613	0.2600
2.5 s	$d_5 = 81$ s	-1.5147	0.0735	-0.9583	0.0865	-0.7956	0.0955
	$d_{95} = 164$ s	-1.5025	0.0717	-0.9842	0.0968	-0.8293	0.0901
4.0 s	$d_5 = 103$ s	-1.7330	0.0890	-1.1370	0.1279	-0.8304	0.1892
	$d_{95} = 210$ s	-1.7904	0.0973	-1.2253	0.0934	-0.9512	0.1356

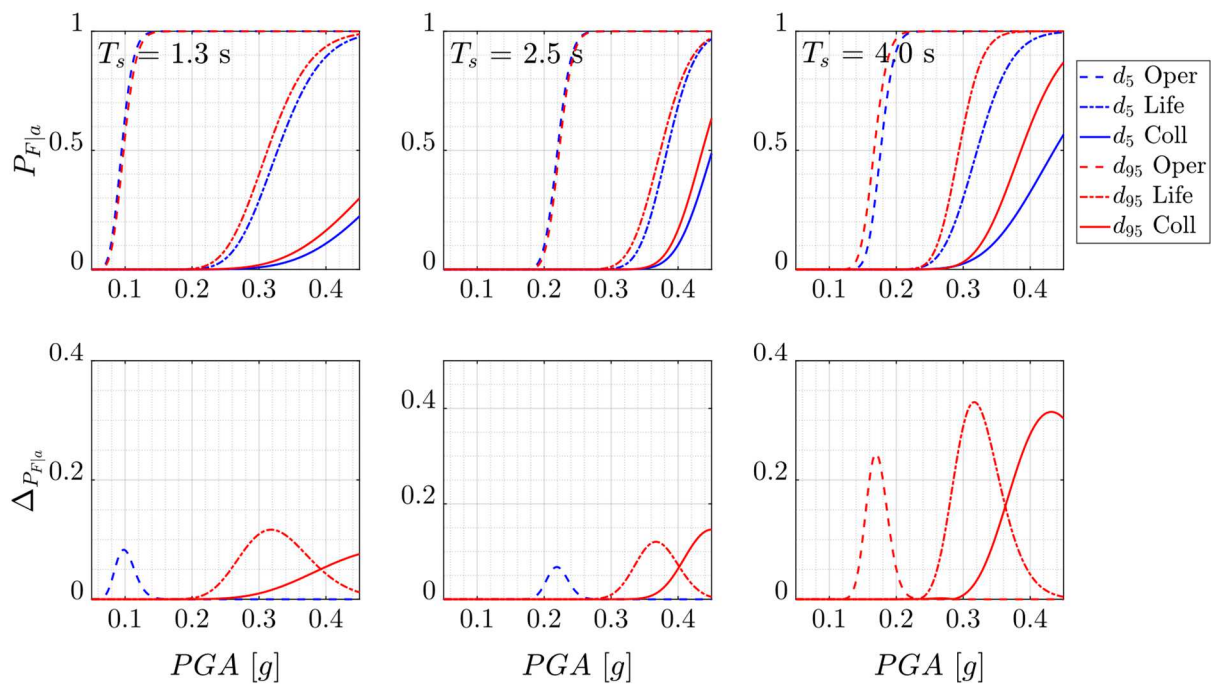


Figure 6.10 At the top are shown the displacement-based fragility curves developed for the operational (dashed lines), life safety (long-short lines), and collapse (solid lines) performance levels of the equivalent SDOF system located in sites with T_s of 1.3 s, 2.5 s, and 4.0 s when subjected to sets of synthetic accelerograms with duration equal to d_5 (blue lines) and d_{95} (red lines). At the bottom are shown the differences in fragility $\Delta P_{F|a}$ between the results obtained from synthetic accelerograms with a duration equal to d_5 and those from synthetic accelerograms with a duration equal to d_{95}

Table 6.3 Estimates of μ and σ for the energy-based fragility functions developed for the life safety and collapse performance levels of the equivalent SDOF system located in sites with T_s of 1.3 s, 2.5 s, and 4.0 s

T_s	D_{Sr}	Life safety		Collapse	
		$\hat{\mu}$	$\hat{\sigma}$	$\hat{\mu}$	$\hat{\sigma}$
1.3 s	$d_5 = 57$ s	-1.0805	0.1408	-0.3399	0.3093
	$d_{95} = 116$ s	-1.1227	0.1306	-0.4706	0.2756
2.5 s	$d_5 = 81$ s	-0.9238	0.0875	-0.7452	0.0921
	$d_{95} = 164$ s	-0.9536	0.0797	-0.7816	0.0905
4.0 s	$d_5 = 103$ s	-1.1140	0.1388	-0.7687	0.1837
	$d_{95} = 210$ s	-1.1939	0.0807	-0.9029	0.0957

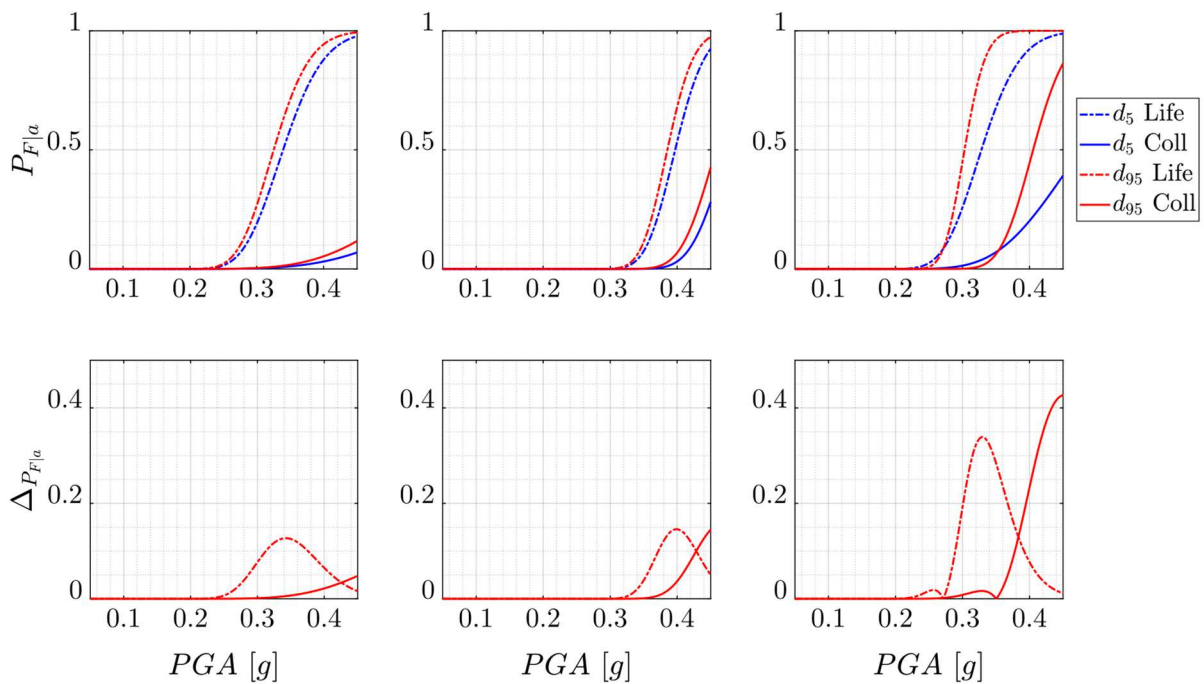


Figure 6.11 At the top are shown the energy-based fragility curves developed for life safety (long-short lines) and collapse (solid lines) performance levels of the equivalent SDOF system located in sites with T_s of 1.3 s, 2.5 s, and 4.0 s when subjected to sets of synthetic accelerograms with duration equal to d_5 (blue lines) and d_{95} (red lines). At the bottom are shown the differences in fragility $\Delta P_{F|a}$ between the results obtained from synthetic accelerograms with a duration equal to d_5 and those from synthetic accelerograms with a duration equal to d_{95}

Following the procedure provided by Martín del Campo et al.,²⁰¹ the absolute differences in the probability of failure, $\Delta_{P_{F|a}}$, between the results from synthetic accelerograms with a duration equal to $d_{\bar{5}}$ and those from synthetic accelerograms with a duration equal to $d_{9\bar{5}}$ were computed (per site and performance level). They are also depicted in Figures 6.10 and 6.11.

As per Figures 6.10 and 6.11, the synthetic accelerograms with longer duration led to higher values of $P_{F|a}$. Only negligible differences are seen for the displacement-based operational performance level for the sites with T_s equal to 1.3 s and 2.5 s. The higher differences in fragility $\Delta_{P_{F|a}}$ were observed for the site $T_s = 4.0$ s (which exceeded 40%).

6.4.3 Translating Seismic Hazard into Risk

The fragility functions $P_{F|a}$ developed in Subsection 6.4.2 allow estimating the probability of exceeding specific damage states given that PGA takes a value equal to a . By integrating the product of such functions and the derivative of the function characterizing the annual rate of exceedance of a given value a of PGA , i.e., λ_a , one can estimate the annual probability of exceedance of such damage states, P_F .

Based on Eq. (6.6), Eq. (1.1) can be rewritten as follows:

$$P_F = \int P_{F|a} \left| \frac{d\lambda_a}{da} \right| da \quad (6.8)$$

Equivalently, P_F can be estimated as follows⁷:

$$P_F = \int \lambda_a \left| \frac{dP_{F|a}}{da} \right| da \quad (6.9)$$

Note that the right part of the integral given in Eq. (6.9) stands for the capacity distribution of the structure of interest. Commonly, the estimates of P_F are so small that they could be seen as annual rates of collapse exceedance, λ_F .

The definition of λ_a requires a GMPE for PGA (in this case for sites located in GZII or GZIII, where the equivalent SDOF system is assumed to be located). Nevertheless, as reported in Section 5.1, there is a lack of GMPEs for sites other than the main UNAM campus. Therefore, to carry out SRAs, a GMPE for the natural logarithm of PGA was developed for sites located in GZII or GZIII. For this purpose, a regression analysis was performed based on the LME model given in Eq. (3.1), considering M_w , R_{hypo} , and T_s for the definition of \mathbf{X} , and grouping the data

by earthquake event. For convenience, the functional form given in Eq. (3.8) was taken. Expressly, the selected functional form is the following:

$$\ln(PGA)_{ik} = \alpha_0 + \alpha_1 \ln(T_s)_{ik} + (\alpha_2 + \alpha_3 M_{w_i}) \ln(R_{hypo})_{ik} + b_{0_i} + e_{ik} \quad (6.10)$$

where $\ln(PGA)_{ik}$, $\ln(T_s)_{ik}$, and $\ln(R_{hypo})_{ik}$ are the natural logarithms of PGA , T_s , and R_{hypo} of the k th accelerogram recorded during the i th earthquake event, respectively, and M_{w_i} is the moment magnitude of the i th earthquake event. Recall that the terms b_{0_i} and e_{ik} have the prior distributions $b_{0_i} \sim \mathcal{N}(0, \sigma_b^2)$ and $e_{ik} \sim \mathcal{N}(0, \sigma_w^2)$, respectively.

For the development of the GMPE for PGA , 92 accelerograms were incorporated to the strong-motion database, in addition to the 1374 accelerograms used for the development of the GMPEs for D_{Sr} (for sites located in GZII or GZIII). The incorporated accelerograms were recorded at some of the stations given in Appendix D (even from the stations situated in GZII or GZIIIb reported in Table D.2, which were discarded for the generation of the GMPEs for D_{Sr}). All accelerograms have $PGA \geq 3$ cm/s².

The estimates of α_0 , α_1 , α_2 , α_3 , σ_b^2 , and σ_w^2 obtained from the regression analysis are summarized in Table 6.4. It should be mentioned that all model coefficients and variance components reported in Table 6.4 were statistically significant. That is, their corresponding p -values were smaller than 0.05 and their 95% confidence intervals contain no zeros. Also, the LME model assumptions were verified from residual analyses. No outliers were discarded during the regression analysis carried out to develop the GMPE given in Eq. (6.10).

Table 6.4 Estimates of the elements of α , σ_b , and σ_w for the GMPE for PGA developed for sites located in GZII or GZIII

$\widehat{\alpha}_0$	$\widehat{\alpha}_1$	$\widehat{\alpha}_2$	$\widehat{\alpha}_3$	σ_b	σ_w
16.7297	0.2187	-3.9733	0.221	0.4179	0.3156

Using Eq. (6.10) and the information given in Chapter 4 for the probabilistic characterization of M_w and R_{hypo} , Eq. (4.3) was applied to estimate λ_a for sites with T_s equal to 1.3 s, 2.5 s, and 4.0 s. The corresponding hazard curves of PGA are shown in Figure 6.12.

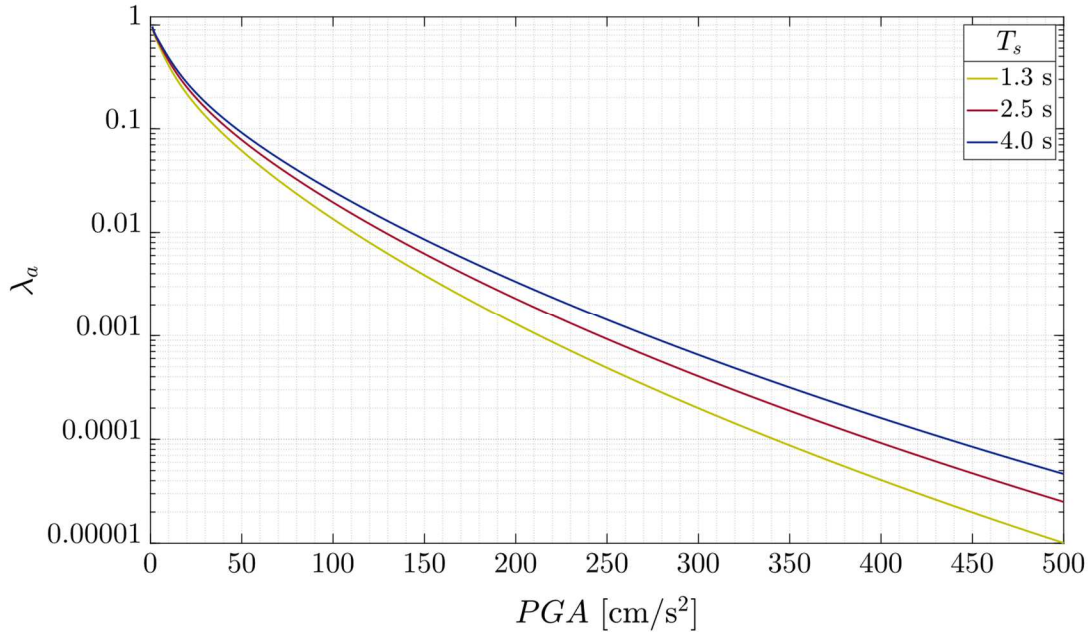


Figure 6.12 Hazard curves of PGA for sites with T_s equal to 1.3 s, 2.5 s, and 4.0 s

Subsequently, using the hazard curves of PGA , as well as the fragility functions developed in Subsection 6.4.2, Eq. (6.9) was evaluated numerically converting the integrals into discrete summations to estimate the annual probabilities of failure P_F for the damage states related to the collapse performance level (as defined in Subsection 6.4.2) of the equivalent SDOF system, which is assumed to be located in sites with T_s of 1.3 s, 2.5 s, and 4.0 s. Note that, as per Figures 6.10 and 6.11, the higher values of $\Delta_{P_F|a}$ are seen for the collapse performance level. That is the reason why the author focused the attention on conducting SRAs for said performance level. The results are reported in Table 6.5.

Despite the small amounts, considerable differences are observed between the estimated values of P_F associated with synthetic accelerograms with a duration equal to d_5 and those with a duration equal to d_{95} . For instance, depending on the site, the values of P_F correspondent to a duration equal to d_{95} can be at least 20% and up to nearly 60% greater than those from synthetic accelerograms with a duration equal to d_5 . The greatest differences are seen for the sites with T_s equal to 1.3 s and 4.0 s. These results might owe to the fact that the response spectra of these sites have higher amplitudes near $T_e = 1.2$ s, which is the natural period of the equivalent SDOF system (contrary to the site with $T_s = 2.5$ s, whose response spectra have peaks far enough from $T_e = 1.2$ s).

Table 6.5 Annual probabilities of exceeding displacement- and energy-based damage states related to the collapse performance level of the equivalent SDOF system, which is assumed to be located at sites with T_s of 1.3 s, 2.5 s, and 4.0 s

T_s	D_{Sr}	Displacement-based collapse performance level	Energy-based collapse performance level
1.3 s	$d_5 = 57$ s	2.0134e-05	7.1164e-06
	$d_{95} = 116$ s	2.9304e-05	1.1171e-05
2.5 s	$d_5 = 81$ s	5.9471e-05	4.4090e-05
	$d_{95} = 164$ s	7.0883e-05	5.4166e-05
4.0 s	$d_5 = 103$ s	1.7394e-04	1.2434e-04
	$d_{95} = 210$ s	2.6076e-04	1.8469e-04

6.5 Discussion

This chapter presented three examinations that allow evaluating the influence of site-specific strong-motion duration on structural performance. In particular, an equivalent SDOF system, with $T_e = 1.2$ s, was analyzed. It was supposed to be situated in four different sites in Mexico City. The sites are where stations CUP5, UC44, BO39, and AU11 are located. Following the NTC-2020,²⁷ they had values of T_s equal to 0.5 s, 1.3 s, 2.5 s, and 4.0 s.

The first examination (given in Section 6.3) consisted in evaluating the response of the equivalent SDOF system when subjected to accelerograms recorded at each site during four major interplate earthquakes that occurred in the Mexican subduction zone. The results revealed that having longer ground motions does not necessarily translate into a higher structural response. This will depend on the dynamic characteristics of the structure. For instance, the effects of resonance were exposed in the results given in Figure 6.5. As noticed, the higher values of u_{max} were produced by the accelerograms recorded at UC44.

The second examination (given in Section 6.4) consisted in developing displacement- and energy-based fragility functions for which IDAs were carried out. Instead of using real accelerograms to perform the IDAs, synthetic site-specific accelerograms were generated. Specifically, the time windows denoting the part in which ground motions may be considered as strong were simulated (following the criteria proposed in Chapter 3 to compute D_{Sr}). Precisely, two sets of accelerograms were computed per site, one having a duration equal to $d_{0.05}$ and another equal to

$d_{0.95}$ (see Table 6.1). The IDAs results indicated that, at each site, the medians of u_{max} and $E_{h_{max}}$ increase as PGA increases. Similar, at each site, the medians of both u_{max} and $E_{h_{max}}$ increase as D_{Sr} increases for $PGA \geq 0.2g$, however, this is unlikely for smaller values of PGA . Based upon the conclusions of various researchers (as those cited in Appendix A), the latter tendency was anticipated for $E_{h_{max}}$, but not for u_{max} . Under post-result reasoning, it was concluded that, for $PGA \geq 0.2g$, the positive correlation between D_{Sr} and u_{max} owes to the fact that once the equivalent SDOF system starts to show inelastic behavior, the more it continues deforming, the more likely for residual displacement to show greater values. On the other hand, for smaller values of PGA (e.g., of $0.1g$), negligible differences were observed between the medians of either u_{max} or E_H computed using the accelerograms (bounded by $a_0 = 2 \text{ cm/s}^2$) and those computed using the portion representing the strong-motion duration. The latter is attributed to the fact that at such levels of PGA the equivalent SDOF system still maintains a linear-elastic behavior.

Figure 6.8 showed that some observations at large values of PGA had lesser values of $E_{h_{max}}$ with reference to others at lower values of PGA . This is attributed to how the amplitudes are distributed along the accelerograms. That is, if the record displays the occurrence of large amplitudes of acceleration at an early time step, it is more likely for the equivalent SDOF system to reach its ultimate displacement at this step, leaving it with no opportunity of dissipating energy via damage, i.e., hysteresis. To illustrate the latter, Figure 6.13 depicts the seismic response of the equivalent SDOF system when subjected to a sample of three synthetic accelerograms with $PGA = 0.4g$ and duration equal to 183 s, i.e., the value of $\mu_{D_{rs}} + \sigma_{D_{rs}}$ computed for the site with $T_s = 4.0$ s (see Table 6.1). Thus, a crucial factor in the proper generation of synthetic accelerograms is how the amplitudes are distributed along the signal. As mentioned before, the distribution of amplitudes from real site-specific accelerograms was used as a reference for the generation of the synthetic accelerograms used to perform the IDAs in Sections 6.4 and 6.5.

From the site-specific displacement- and energy-based fragility curves for the equivalent SDOF system presented in Figures 6.10 and 6.11, respectively, one can tell that longer ground motions cause an increase in the probability of exceeding damage states associated with life safety and collapse performance levels. Similar, but on a smaller scale, for the damage state related to the operational performance level. For instance, values of $\Delta_{P_{Fa}}$ of approximately 20% were observed when considering either u_{max} or DI_{EC} for life safety or collapse performance levels.

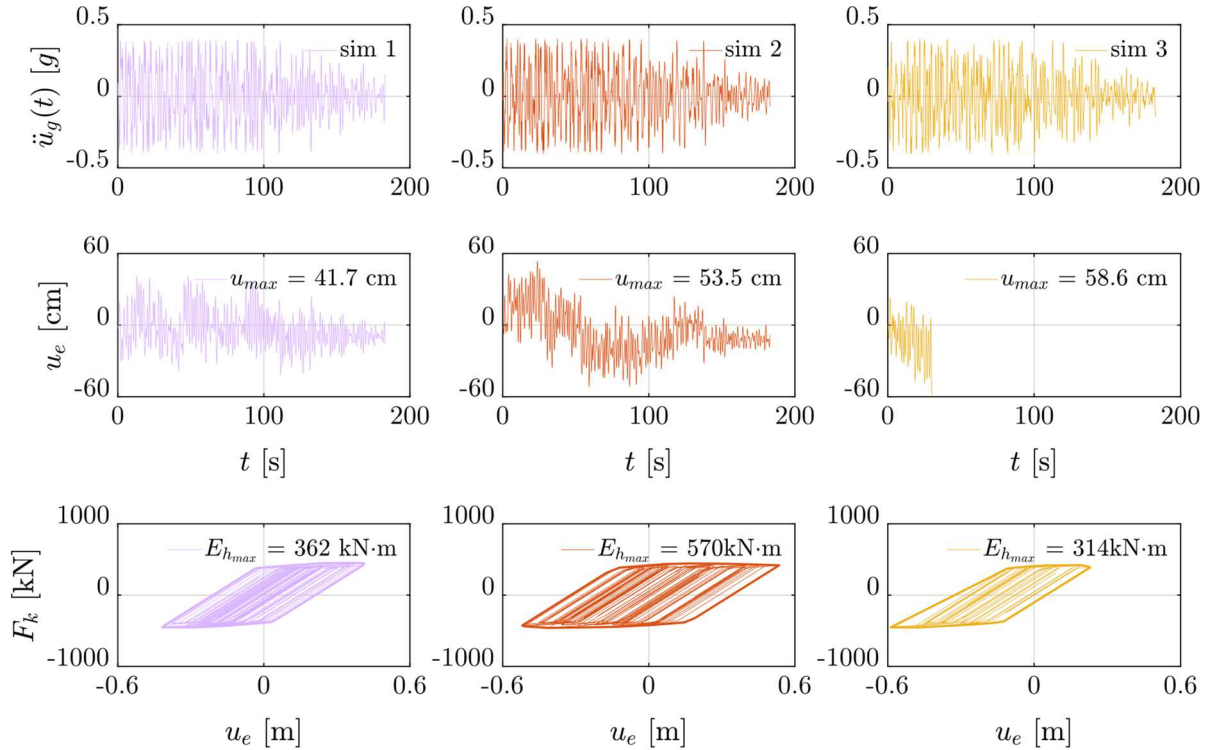


Figure 6.13 Results of three NDAs when subjecting the equivalent SDOF system to three synthetic accelerograms with $PGA = 0.4g$ and duration equal 183 s. The duration is equal to $\mu_{D_{rS}} + \sigma_{D_{rS}}$ and was computed for the site with $T_s = 4.0$ s (see Table 6.1). At the top are the synthetic accelerograms. In the middle are the displacement histories $u_e(t)$ of the equivalent SDOF system when subjected to such accelerograms. At the bottom are the hysteresis loops resulting from each NDA

The third and last examination consisted in performing SRAs. They were focused on evaluating the collapse performance level of the equivalent SDOF system. The results given in Table 6.5 indicate that ground motions with longer values of D_{Sr} translate to higher values of P_F for displacement- and energy-based damage states. Specifically, the highest values of P_F occur at sites whose acceleration-response spectrum leads the equivalent SDOF system to fall more notoriously into the inelastic state.

Both real and synthetic accelerograms used to perform the examinations carried out in Sections 6.3 and 6.4 showed that even ground motions caused by earthquakes from the same tectonic environment and, moreover, by the same earthquake could be classified as short- or long-lasting. For instance, the value of D_{Sr} caused by E2 increased from 41 s to 213 s (i.e., more than 5 times) from a site with $T_s = 0.5$ s to a site with $T_s = 4.0$ s, which are located within an 8 km radius.

This variation allows saying that those ground motions recorded in GZI are short-lasting and that those recorded in GZIII are long-lasting. Furthermore, in the context of synthetic accelerograms, those whose duration equals d_5 could be referred to as short-lasting and those whose duration equals d_{95} as long-lasting. That was the point the author wanted to highlight in Section 2.6, when mentioning that it is extremely subjective to categorically classify the accelerograms as short and long depending on if they are associated with subduction or shallow crustal earthquakes, respectively.

To conclude this chapter, it should be mentioned that Sections 6.4 and 6.5 share, but also complement, some of the results given in a manuscript under review by López-Castañeda et al.²⁰² The fragility functions presented in that study were also developed for the equivalent SDOF system defined in Section 6.2 but considering two earthquake scenarios to establish the durations of the sets of synthetic accelerograms to be used in the IDAs. The durations of the shortest accelerograms somehow are comparable to the ones of this study. Then, it is to be expected that the fragility functions would be quite similar. This occurred indeed, except for those related to the collapse performance level. The differences are because López-Castañeda et al.²⁰² use an extreme value distribution to compute the probability of exceeding each damage state at high values of PGA (say greater than $0.35g$). As stated in point one of page 123, in this study such probabilities were determined using the lognormal distribution, which gave the best results when performing one-sample KS tests. Thus, the author considers that to conduct any SRA of a real structure it is recommendable to perform the IDAs in sufficient intervals of PGA and carry out goodness-of-fit tests to determine which distribution fits the data better.

CHAPTER 7

Conclusions

7.1 Synthesis of Results

This dissertation presented a detailed investigation of the strong-motion duration associated with interplate earthquakes that occurred in the Mexican subduction zone and had a moment magnitude (denoted through the text as M_w) greater than or equal to 6. Mexico City was the geographical area of interest. The motivation of the investigation relies on evaluating the inclusion of the strong-motion duration as a main design parameter in earthquake engineering.

To fulfill the amendment of this dissertation it was necessary to: (1) compile a strong-motion database, (2) define the strong-motion duration, (3) develop GMPEs that allow its estimation, (4) generate site-specific hazard curves of said ground-motion parameter, and (5) evaluate its effects on structural performance. The hightails about these points will be made below.

7.1.1 Strong-motion Database Compilation

A robust strong-motion database was collected at the very beginning of this dissertation. The overall strong-motion database consisted of thousands of ground-motion recordings obtained from the accelerograph network catalogs provided by the CIRES and II-UNAM. A large fraction of the ground-motion recordings from the overall database was considered in this study (see Appendices C and D). In general, the selected recordings came from free-field stations and include two orthogonal horizontal accelerograms and one vertical. All the horizontal accelerograms have peak ground acceleration (denoted as PGA) greater than or equal to 3 cm/s^2 and were filtered following the recommendations given by Carreño et al.¹⁴² and Boore.¹⁴³

Depending on where the ground motions were recorded, they were classified into three groups, each encompassing sites located in Mexico City with similar geotechnical characteristics. The groups were defined following the NTC-2020²⁷ and are named the hill, transition, and lake zones (abbreviated through the text as GZI, GZII, and GZIII, respectively).

In addition to the strong-motion database, a catalog of interplate earthquakes that occurred along the Middle American Trench (abbreviated MAT) from 1900 to 2021 was compiled (see Appendix B). The earthquake catalog is complete for $M_w \geq 7.0$ since 1900, $M_w \geq 6.5$ since 1950, and $M_w \geq 6.0$ since 1976. The source data was obtained from the Global CMT Project,^{105,106} ISC,¹⁰⁷ and USGS-NEIC¹⁰⁸ catalogs. The works of Singh et al.¹⁰⁹ and Zúñiga et al.¹¹⁰ were also consulted.

7.1.2 Defining Strong-motion Duration

Among many definitions, the relative significant duration (denoted as D_{Sr}) was selected to measure the strong-motion duration. As stated in Section 2.2, D_{Sr} is the time required to accumulate between 5% and 95% of the total energy of an accelerogram. The energy was represented as a measure of the normalized Arias intensity (denoted as I_A). The formula for D_{Sr} was given in Eq. (2.8).

A parameter that intervenes in Eq. (2.8) is the total duration of an accelerogram (denoted as t_f). Undoubtedly, the value of t_f of an “ideal” accelerogram would be equal to the time elapsed between the arrival of the first seismic wave generating the ground motion to the departure of the last one. Nevertheless, the accelerograms provided by the CIRES and II-UNAM were recorded using devices with different acceleration trigger thresholds and pre- and post-event memory availabilities, causing inconsistency in the measurement of t_f . To avoid this problem, the total durations t_f were set equal to the portion of the accelerograms that encompasses the first and last excursion of a specified acceleration threshold (denoted as a_0) equal to 2 cm/s². Comparable values of t_f , and therefore of D_{Sr} , were obtained by applying the above standardization.

7.1.3 Development of Strong-motion Duration Predictive Equations

Once the strong-motion duration was defined and using the horizontal accelerograms of the ground-motion recordings, ground-motion predictive equations (abbreviated as GMPEs) were developed. They allow estimating the expected value of D_{Sr} given specified values of a set of seismological parameters. Specifically, four GMPEs were proposed: (i) two for sites located in GZI and (ii) another two for sites located in GZII or GZIII. The set of seismological parameters considered in the GMPEs for sites located in GZI was: (1) M_w and (2) the source-to-site distance, which was defined as either the hypocentral distance or closest distance to the rupture area (denoted as R_{hypo} and R_{rup} , respectively). In addition to these seismological parameters, the GMPEs for sites located in GZII or GZIII consider the dominant

period of the soil (denoted as T_s). The functional forms of the GMPEs were given in Eqs. (3.7) and (3.8).

Linear mixed-effects (abbreviated as LME) models were used to describe relationships between D_{Sr} and M_w , R_{hypo} , R_{rup} , and T_s in strong-motion data grouped per earthquake event. The importance of using LME models is that they provide an estimate of the variability resulting from strong-motion data from the same earthquake event, as well as an estimate of the variability resulting from differences in strong-motion data from different earthquake events. Note that the estimates of the components of the vector of fixed effects (denoted as α), which defines the functional form of the proposed GMPEs, will be practically the same as those obtained using a fixed-effects model (which assumes that observations are independent and identically distributed) if and only if the between-events variability is close to zero (which was not the case of the results obtained in this study). Thus, it is very important to consider correlations between strong-motion data from the same earthquake event. Neglecting this relation can lead to biased results.

The proposed strong-motion duration GMPEs satisfactorily fit the empirical observations. Although they were developed using a confinable and robust strong-motion database, the author encourages their refinement over the years. If that were the case, it is advisable to follow the criteria established in Sections 3.2 and 3.3 to define the selected seismological parameters and strong-motion duration, respectively. The latter includes, e.g., considering horizontal accelerograms with $PGA \geq 3 \text{ cm/s}^2$.

The strong-motion duration GMPEs enable an enriched characterization of the ground motion expected at a site of interest (located in Mexico City) for a given earthquake scenario. For engineering purposes, the estimated values of the strong-motion duration can be directly implemented in the generation of synthetic accelerograms. In this way, only the part of the ground motion that has sufficient strength to affect civil structures is contemplated. The latter leads to the advantage of reducing the computational cost to complete, e.g., nonlinear dynamic analyses (abbreviated as NDAs).

Bear in mind that the direct characterization of the strong-motion duration at a site through GMPEs (considering a specific or various scenario earthquakes) translates into a deterministic seismic hazard analysis (abbreviated as DSHA). To some extent, a DSHA provides a transparent method for defining seismic loading at the site. An example of this implementation was carried out in Section 6.3.

7.1.4 Generation of Strong-motion Duration Hazard Curves

The identification of all interplate earthquake sources capable of generating ground motions that can damage civil structures located in Mexico City, as well as the probabilistic characterization of the time, size, and spatial distribution of earthquakes occurring in the identified earthquake sources are mandatory to generate strong-motion duration hazard curves through a process named probabilistic seismic hazard analysis (abbreviated as PSHA). The more relevant aspects considered for their definition are listed below.

- The identification of the interplate earthquake sources consisted of defining their geometries. In this case, the Mexican subduction zone was divided into four areal sources (see Figure 4.1).
- The probabilistic characterization of the source zones was defined under the assumption that each one described a domain within which earthquakes: (i) were equally likely in space, (ii) conformed to a single magnitude distribution, (iii) had the same maximum magnitude (denoted as m_u), and (iv) were independent of each other.
- The “shifted and truncated” form of the exponential Gutenberg-Richter law — see Eq. (4.14)— was used to define the probability distribution of M_w at each source zone. The parameters that compose Eq. (4.14) are: (a) a lower-bound magnitude (denoted as m_0), (b) m_u , (c) the ratio between the number of small and large earthquakes occurring at each source zone (denoted as β), and (d) the mean annual rate of exceedance of m_0 (denoted as λ_{m_0}). The first parameter was set equal to 6. The second was defined as the magnitude of the MPE known from each source zone plus 0.2. The values of the remaining two parameters were determined using estimators that maximize their marginal likelihoods as proposed by Kijko and Smit.¹⁶⁹
- The source-to-site distance distribution of earthquakes occurring at each source zone was determined using statistical inference. Based on one-sample Kolmogorov-Smirnov (abbreviated as KS) tests, it was determined that the generalized extreme value (abbreviated as GEV) distribution properly fitted each set of source-to-site distances, which were measured as R_{hypo} .

Following these considerations, strong-motion duration hazard curves were developed (see Figures 4.6 to 4.9). They showed that, for a site located in GZI, a value of D_{Sr} equal to 125 s has a 2% probability of exceedance in a 5-year exposure period (denoted as T). Said value of D_{Sr} increases to, e.g., 132 s, 186 s, and 238 s

for sites with T_s equal to 1.3 s, 2.5 s, and 4.0 s, respectively. Comparing the mentioned values of D_{Sr} with the duration values proposed in the NTC-2020²⁷ for the selection of accelerograms to be used in nonlinear dynamic analyses (abbreviated as NDAs), it can be said that the duration values proposed in such standard are underestimated. In turn, such underestimation may cause an unfavorable rough calculation of the response of structures whose natural period (defined as T_e) is near the crests of the acceleration response spectra characterizing the sites where they are or will be located. The latter was demonstrated in Section 6.4.

Continuing with the PSHAs, bivariate hazard curves that consider the contribution of D_{Sr} and either PGA or acceleration-response spectral ordinates — denoted as $S_a(T_e)$ — for sites located in GZI were developed in an unprecedented way. The results suggest that, to consider the joint effects of such ground-motion parameters in structural design, the values of the vertex of the isolines associated with the value of T_r of interest (see Figure 5.8) must be selected.

7.1.5 Evaluating the Effects of Strong-motion Duration on Structural Performance

Examinations were carried out in this dissertation to evaluate the effects of the strong-motion duration on structural performance. They included assessing the response of an equivalent single degree of freedom (abbreviated as SDOF) system via NDAs, the generation of displacement- and energy-based fragility functions for such structure, and seismic risk analyses (abbreviated as SRAs) associated with structural collapse.

The equivalent SDOF system follows a four-story one-bay steel moment frame presented in the book published by Goel and Chao.¹⁹⁶ The selected constitutive model of the equivalent SDOF system considers an elastic-plastic behavior with hardening. The equivalent SDOF system had $T_e = 1.2$ s and a ductility ratio (denoted as μ_e) of 3.3. From the capacity curve of the equivalent SDOF system (see Figure 6.2) it was determined that its yielding begins when the deformation (denoted as u_y) reaches 17.7 cm and its maximum deformation (denoted as u_u) takes place at 58.6 cm.

When evaluating the response of the equivalent SDOF system employing real accelerograms, it was demonstrated that the response of the equivalent SDOF system —measured as the maximum roof displacement (denoted as u_{max})— is the same either if complete accelerograms (bounded by $a_0 = 2\text{cm/s}^2$) or the time window of them that encompasses the phase of the motion defined by D_{Sr} are used in the

NDA. Moreover, the input energy (denoted as E_i) is held without relevant losses. Therefore, the possibility of using such time windows instead of the whole accelerograms reduces the computational cost.

The fragility curves for the equivalent SDOF system showed the probability of exceeding displacement- and energy-based damage states related to the operational, life safety, and collapse performance levels (see Figures 6.10 and 6.11). They were developed using site-specific synthetic accelerograms whose durations were obtained from one of the GMPEs proposed in this dissertation. The results reveal that the strong-motion duration has a meaningful effect on the response of the equivalent SDOF system if it is located at a site whose dominant frequency matches its natural frequency. Such influence is also reflected in sites whose dominant period does not coincide with that of the equivalent SDOF system, only if the structure incurred in the plastic behavior—which commonly occurs at high values of PGA (say greater than $0.3g$, for the analyzed case)—. The fragility curves indicate that the strong-motion duration has a negligible influence on the probability of exceeding the damage state related to the operational performance level. On the other hand, the differences in the probability of failure (denoted as $\Delta_{P_{F|a}}$) increase when evaluating damage states related to the life safety and collapse performance levels of the equivalent SDOF system. The greater values of $\Delta_{P_{F|a}}$ were found for the collapse of the structure.

To go further, the impact of the strong-motion duration in the collapse risk assessment was evaluated. The results indicated that long-lasting ground motions could significantly increase the probability of failure (denoted as P_F) of a structure considering displacement- or energy-based damage measures. In particular, higher values of P_F are expected if the natural frequency of the structure approaches the dominant frequency of the site where it is located.

Overall, from the examinations performed in this study, it can be concluded that the strong-motion duration does not influence the response of ductile structures when they remain elastic or when they immediately collapse under the action of very-large amplitude seismic loadings. However, the strong-motion duration does have a notorious influence on the response of ductile structures when they engage in inelastic behavior. In other words, the strong-motion duration becomes noticeable when design earthquakes are taken into account. Therefore, the author recommends that said parameter (which, it is worth recalling, is one of the main parameters characterizing ground motions) should be properly included in the new versions of earthquake engineering regulations (specifically, in the NTC-2020²⁷), following the design criteria already established in them.

7.2 The Challenges Ahead

The rapid increase in the number of large-scale civil structures in Mexico City, such as high-rise buildings and skyscrapers, which have values of T_e of 1 s to 10 s (or even longer), led the author to attend to the characterization of ground motions caused by interplate earthquakes. As mentioned in Subsection 3.2.1, these earthquakes have larger energy content at lower frequencies, which can generate resonance conditions and, consequently, severe structural damage. Nevertheless, moderate-to-large intraslab earthquakes are also of interest as they can produce ground motions that can prompt structural damage to low-rise buildings, medium-span bridges, and other structures with $T_e \leq 1$ s. Like many worldwide urbanized areas, Mexico City has a higher density of these structures. For instance, the worst example of destruction caused by ground motions that occurred in Mexico City (in the last decades and after the great earthquake of September 19, 1985) is related to the earthquake that occurred on September 19, 2017, in Morelos. Thus, analogously to the characterization of the strong-motion duration associated with interplate earthquakes, it is imperative to develop GMPEs and site-specific hazard curves of this ground-motion parameter associated with intraslab earthquakes. The latter must be done by maintaining the criteria established in Chapter 3 to measure the strong-motion duration and selected seismological parameters.

The effects of the strong-motion duration on the seismic response of structures with different mechanical properties should be evaluated. As per Chapter 6, this dissertation offered a series of examples that, to some extent, allow some decisions about incorporating the strong-motion duration as a design parameter in earthquake engineering. These include the proper estimation of the expected value of D_{Sr} at sites whose dominant period could coincide with that of a structure of interest.

As López-Castañeda et al.²⁰² commented in a recent work, it is crucial to gain knowledge of the performance of structures. The knowledge must be linked to realistic ground motions affecting the site(s) of interest. Preferably, said ground motions should be directly related (via PSHAs) to specific values of T_r . For design purposes, no UHSs are reported in the literature for sites located in Mexico City other than those given in the NTC-2020.²⁷ Said UHSs are associated with $T_r = 250$ years. The absence of UHSs for different values of T_r —moreover, of UHSs associated with reference values of exceedance probabilities of ground-motion levels y (see Appendix E)—prevents the correct assessment of structural performance. For instance, UHSs associated with small values of T_r (e.g., 72 years) enable the practitioner to design a structure of interest with a guarantee that it will remain operable during serviceability earthquakes.^{8,203} Then, the hazard curves given in

Section 4.3 allow the practitioner to select accelerograms (or, in its lack, generate synthetic accelerograms) with durations associated with specific values of T_r . Further credence to the structural response obtained by NDAs will be gained using these tools (together with the design spectra given in the NTC-2020²⁷).

With the above, it will be possible to elucidate the similarities and differences of the strong-motion duration (as recorded in Mexico City) caused by distinct tectonic environments and its effects on the seismic response of structures.

Once the mentioned challenges are achieved, more suitable seismic loadings to be used for structural design can be defined in the upgrades of the NTC-2020,²⁷ specifically.

7.3 Peer Reviewed Publications

To conclude, the author wants to mention that she achieved publishing two peer-reviewed articles and one manuscript under review, each in a different journal. All journals are related to the earthquake engineering discipline and are ranked as Quartile 1 (Q1) and Quartile 2 (Q2) by Journal Citation Indicator (JCI) and Journal Impact Factor (JIF), respectively.²⁰⁴

The two published articles were co-authored by the author and her adviser, Dr. Eduardo Reinoso Angulo. The manuscript under review was co-authored by the named authors and Ph.D. candidate J. Osvaldo Martín del Campo Preciado. Their references (listed in chronological order) are:

1. López-Castañeda AS, Reinoso E. Strong-motion duration predictive models from subduction interface earthquakes recorded in the hill zone of the Valley of Mexico. *Soil Dyn Earthq Eng.* 2021;144. doi:10.1016/j.soildyn.2021.106676.
2. López-Castañeda AS, Reinoso E. Significant duration predictive models developed from strong-motion data of thrust-faulting earthquakes recorded in Mexico City. *Earthq Eng Struct Dyn.* 2022;51(1):129-152. doi:10.1002/eqe.3559.
3. López-Castañeda AS, Reinoso E., Martín del Campo, JO. Influence of site-specific strong-motion duration on structural performance. *Bull Earthq Eng.* doi:Under review

As declared in Subsection 1.3.3, this dissertation included data and results from the cited articles.

In light of Section 7.2, there are still problems to be solved related to the strong-motion duration as recorded in Mexico City. Thus, it is expected that the author continues with the investigation and prepares a couple of more manuscripts that will be submitted for possible peer review.

[This page intentionally left blank]

APPENDIX A

Studies on the Influence of Strong-motion Duration in Structural Response

Table A.1 summarizes the structural systems analyzed and the number of accelerograms used in 16 studies that evaluated the influence of the strong-motion duration on the structural response using NDAs. The studies were published in the literature between 2006 to 2021.

Table A.1 List of 16 studies carried out from 2006 to 2021 on the influence of the strong-motion duration in the structural response using NDAs

Author(s)	Structural system analyzed and number of accelerograms
1. Barbosa et al. ⁸⁸	Structural system(s): three-, nine-, and 20-story steel moment resisting frame buildings. Strong-motion data: 22 “long-duration” accelerograms from five worldwide subduction earthquakes with M_w ranging from 7.6 to 9.0. Also, 22 “short-duration” accelerograms from 20 shallow-crustal earthquakes with M_w ranging from 5.1 to 7.4. All “short-duration” accelerograms had $D_{Sr} < 25$ s. Here, D_{Sr} was computed considering $a_1 = 0.05$ and $a_2 = 0.75$, respectively. No information about local site conditions was provided. The accelerograms were obtained from worldwide databases, including the PEER NGA-West2 database. ⁵⁶
2. Belejo et al. ⁸⁹	Structural system(s): three-story plan asymmetric reinforced concrete building. Strong-motion data: 32 “long-duration” ground-motion recordings (each with two horizontal accelerograms) from eight earthquakes with M_w varying from 6.3 to 9.0. At least one accelerogram of each “long-duration” ground-motion recording had $D_{Sr} > 25$ s. Here, D_{Sr} was computed considering $a_1 = 0.05$ and $a_2 = 0.75$. Also, 32 “short-duration” ground-motion recordings (each with two horizontal accelerograms) from earthquakes with M_w ranging from 6.0 to 7.2. The accelerograms from each “short-duration” ground-motion recording were scaled to have similar acceleration response spectra as the accelerograms in a “long-duration” ground-

Table A.1 List of 16 studies carried out from 2006 to 2021 on the influence of the strong-motion duration in the structural response using NDAs

Author(s)	Structural system analyzed and number of accelerograms
2. Belejo et al. ⁸⁹ (cont.)	motion recording. The “short-duration” accelerograms had $D_{Sr} < 25$ s. No information about local site conditions was provided. The accelerograms were obtained from the PEER NGA-West2 database ⁵⁶ and from the databases provided by the Strong-Motion Virtual Data Center (VDC) operated by the Center for Engineering Strong Motion Data (CESMD) ²⁰⁵ and the Kyoshim network (K-NET) and Kiban Kyoshin network (KiK-net) operated by the National Research Institute for Earth Science and Disaster Resilience (NIED) from Japan. ²⁰⁶
3. Bommer et al. ²⁰⁷	Structural system(s): seven SDOF systems representing low-to-medium-rise masonry buildings encountered in Europe. Strong-motion data: no information was provided.
4. Bravo-Haro and Elghazouli ⁹⁰	Structural system(s): various steel moment frames modeled as degrading and non-degrading SDOF systems that accounted for gravity loads and P- Δ effects. Also, four steel moment frames modeled as two-dimensional MDOF systems. Strong-motion data: 17 “long-duration” accelerograms from six earthquakes with M_w varying from 7.2 to 9.0 and that occurred in different parts of the world. Such accelerograms had $D_{Sr} > 25$ s. Here, D_{Sr} was computed considering $a_1 = 0.05$ and $a_2 = 0.75$. The longest accelerogram had $D_{Sr} = 86$ s. Also, 77 “short-duration” accelerograms from shallow-crustal earthquakes with M_w between 4.11 and 7.62 were used. Such accelerograms had $D_{Sr} < 25$ s. Each “short-duration” accelerogram was spectrally equivalent to one “long-duration” accelerogram. No information about local site conditions was provided. The accelerograms were obtained from worldwide databases, including the PEER NGA-West2 database. ⁵⁶
5. Bravo-Haro et al. ⁸⁷	Structural system(s): various non-deteriorating and deteriorating SDOF systems controlled by gravity loads and P- Δ effects. Strong-motion data: same as Bravo-Haro and Elghazouli. ⁹⁰
6. Chandramohan et al. ⁸³	Structural system(s): five-story steel moment resisting frame and a reinforced concrete bridge pier. Strong-motion data: 73 “long-duration” ground-motion recordings (each with two horizontal

Table A.1 List of 16 studies carried out from 2006 to 2021 on the influence of the strong-motion duration in the structural response using NDAs

Author(s)	Structural system analyzed and number of accelerograms
6. Chandramohan et al. ⁸³ (cont.)	accelerograms) from 10 earthquakes with M_w from 7.2 to 9.0. All ground motions were recorded on rock or firm soils and had a geometric mean of PGA greater than or equal to $0.1g$ (or geometric mean of PGV greater than or equal to 10 cm/s). Also, 106 “short-duration” accelerograms were used. The accelerograms were obtained from worldwide databases, including the PEER NGA-West2 database. ⁵⁶
7. Chandramohan et al. ²⁰⁸	Structural system(s): a reinforced concrete bridge pier. Strong-motion data: 79 “long-duration” ground-motion recordings (each with two horizontal accelerograms) from six worldwide earthquakes. At least one accelerogram of each ground-motion record had $D_{Sr} > 45\text{ s}$. All accelerograms had a geometric mean of PGA greater or equal to $0.1g$ (or a geometric mean of PGV greater or equal to 10 cm/s). Also, “short-duration” ground-motion records were used. Each “short-duration” ground-motion record was spectrally equivalent to one “long-duration” record and had $D_{Sr} < 45\text{ s}$. The accelerograms were obtained from worldwide databases, including the PEER NGA-West2 database. ⁵⁶
8. Hancock and Bommer ²⁰⁹	Structural system(s): an eight-story reinforced concrete wall-frame building. Strong-motion data: 30 accelerograms (recorded at different soil profile sites) from earthquakes with M_w ranging from 5.7 to 7.9. No restrictions about the seismological characteristics of the earthquakes were considered. The accelerograms were scaled to the same target response spectrum, which was obtained from a GMPE for ground motions caused by strike-slip-fault earthquakes and recorded at soft sites considering a scenario earthquake with $M_w = 7$ and $R_{rup} = 5\text{ km}$. The accelerograms were obtained from worldwide databases, including the PEER NGA database. ⁵⁶
9. Iervolino et al. ²¹⁰	Structural system(s): various SDOF systems considering four oscillation periods, three hysteretic behaviors, and two target ductility levels. Strong-motion data: 60 accelerograms from earthquakes with M_w ranging from 6.4 to 6.7. The accelerograms were grouped according to their strong-motion duration. The groups were named “small duration”, “moderate duration”, and “large

Table A.1 List of 16 studies carried out from 2006 to 2021 on the influence of the strong-motion duration in the structural response using NDAs

Author(s)	Structural system analyzed and number of accelerograms
9. Iervolino et al. ²¹⁰ (cont.)	duration". The "large duration" group exhibited a median of $I_{C\&M}$ equal to 22.
10. Liapopoulou et al. ²¹¹	Structural system(s): various SDOF systems (with a trilinear backbone) with different structural properties. Strong-motion data: 101 "long-duration" accelerograms from seven earthquakes that occurred in different parts of the world. These accelerograms had $D_{Sr} > 25$ s. Here, D_{Sr} was computed considering $a_1 = 0.05$ and $a_2 = 0.75$. Also, 101 "short-duration" accelerograms from worldwide earthquakes with $D_{Sr} < 25$ s. Each "short-duration" accelerogram was spectrally equivalent to one "long-duration" accelerogram.
11. Molazadeh and Saffari ²¹²	Structural system(s): various SDOF systems. Strong-motion data: 47 accelerograms from earthquakes with $M_w \geq 6.5$. They had D_{Sr} varying from 4.2 s to 82.45 s. Here, D_{Sr} was computed considering $a_1 = 0.05$ and $a_2 = 0.95$. The accelerograms were classified as "short-duration" or "long-duration" accelerograms whether D_{Sr} was greater or smaller than 30 s, respectively. The accelerograms were scaled to the same target response spectrum, which was obtained from a GMPE given in the ASCE ²⁵ for a site located in California and classified as Class D. The accelerograms were obtained from the PEER NGA database. ⁵⁶
12. Raghunandan and Liel ²¹³	Structural system(s): 17 reinforced concrete frame buildings and various SDOF systems with different structural properties. Strong-motion data: 11 accelerograms from four subduction earthquakes and 57 accelerograms from nineteen shallow-crustal earthquakes. Here, M_w varies from 4.8 to 7.9. The accelerograms were recorded at sites with different soil profiles. Also, eight synthetic accelerograms were used. They were developed considering a subduction earthquake with $M_w = 9.2$ and occurred at R_{epi} equal to either 446.8 km or 481.3 km). The accelerograms were obtained from the PEER NGA-West2 database ⁵⁶ and CESMD VDC database. ²⁰⁶
13. Ruiz-García ⁸⁴	Structural system(s): Various SDOF and three MDOF systems. The MDOF systems consisted of a one-bay, two-bay generic frame model with three stories and two similar frame models having 18 stories.

Table A.1 List of 16 studies carried out from 2006 to 2021 on the influence of the strong-motion duration in the structural response using NDAs

Author(s)	Structural system analyzed and number of accelerograms
13. Ruiz-García ⁸⁴ (cont.)	Strong-motion data: 40 accelerograms (recorded at rock and stiff soil sites) associated with earthquakes with M_w varying from 6.5 to 8.0. The longest accelerogram had $D_{Sr} = 51.7$ s. Here, D_{Sr} was computed considering $a_1 = 0.05$ and $a_2 = 0.95$.
14. Vega and Montejo ²¹⁴	Structural system(s): a reinforced concrete bridge column and a reinforced concrete squat wall. Strong-motion data: 119 “long-duration” accelerograms from earthquakes occurred in different parts of the world. Each accelerogram had $D_{Sr} > 20$ s. Here, D_{Sr} was computed considering $a_1 = 0.05$ and $a_2 = 0.75$. The longest accelerogram had D_{Sr} equal to approximately 80 s. All accelerograms had a geometric mean of PGA greater than or equal to $0.1g$ (or a geometric mean of PGV greater than or equal to 10 cm/s). In addition, 10 “short-duration” sets of accelerograms were used. The accelerograms of each set were spectrally equivalent to one “long-duration” accelerogram.
15. Wang et al. ²¹⁵	Structural system(s): A high concrete-faced rockfill dam. Strong-motion data: 35 ground-motion recordings (each with two horizontal accelerograms) from 18 worldwide earthquakes with $M_w > 6.2$. The accelerograms were scaled and matched to a target response spectrum. The accelerograms had values of D_{Sr} ranging from 5.81 s to 36.32 s. Such values of D_{Sr} were computed considering $a_1 = 0.05$ and $a_2 = 0.95$. No specific information about local site conditions was provided. The accelerograms were obtained from the PEER NGA database. ⁵⁶
16. Xu et al. ²¹⁶	Structural system(s): a high concrete-faced rockfill dam. Strong-motion data: 40 ground-motion recordings (each with two horizontal accelerograms) from 19 worldwide earthquakes with M_w ranging from 6.22 to 7.62. The accelerograms had values of D_{Sr} ranging from 5.81 s to 39.51 s. Such values of D_{Sr} were computed considering $a_1 = 0.05$ and $a_2 = 0.95$. The accelerograms were obtained from the PEER NGA database. ⁵⁶

[This page intentionally left blank]

APPENDIX B

Earthquake Catalog

A list of interplate earthquakes that have occurred along the MAT from 1900 to 2021 is given in Table B.1. The catalog is complete for $M_w \geq 7.0$ since 1900, $M_w \geq 6.5$ since 1950, and $M_w \geq 6.0$ since 1976. The earthquakes are grouped in accordance with the source zonation given in Section 4.2. Their hypocenters were taken from the catalogs provided by the Global CMT Project,^{105,106} ISC,¹⁰⁷ and USGS-NEIC.¹⁰⁸ The works of Singh et al.¹⁰⁹ and Zúñiga et al.¹¹⁰ were also consulted. Recall that most of the consulted catalogs provide values of M_s instead of M_w for earthquakes that occurred before 1976. But, as estimates of M_s and M_w do not depart significantly from each other for moderate to large earthquakes,¹¹⁰ values of M_s were taken as the values of M_w for such historical earthquakes.

Table B.1 List of interplate earthquakes with $M_w \geq 6$ that occurred in the Mexican subduction zone from 1900 to 2021

Source Zone	Date	Latitude [°N]	Longitude [°W]	H_h [km]	M_w
SZ1	20-Jan-1900	20.00	105.00	0.0	7.3
	03-Jun-1932	19.62	103.92	35.0	8.1
	18-Jun-1932	19.42	103.91	15.0	7.8
	22-Jun-1932	19.37	104.22	25.0	7.7
	09-Oct-1995	18.86	104.58	16.0	8.0
	10-Oct-1995	18.81	104.07	20.0	6.0
	29-Apr-2001	18.71	104.74	15.0	6.1
	20-May-2001	18.62	104.57	15.0	6.3
	22-Jan-2003	18.77	104.10	24.0	7.5
SZ2	26-Mar-1908	16.70	99.20	33.0	7.6
	27-Mar-1908	17.00	101.00	0.0	7.0
	30-Jul-1909	16.47	99.43	20.0	7.5
	07-Jun-1911	18.52	102.44	30.0	7.6
	16-Dec-1911	17.16	99.99	30.0	7.3
	15-Apr-1941	18.69	102.99	30.0	7.6

Table B.1 List of interplate earthquakes with $M_w \geq 6$ that occurred in the Mexican subduction zone from 1900 to 2021

Source Zone	Date	Latitude [°N]	Longitude [°W]	H_h [km]	M_w
SZ2 (cont.)	22-Feb-1943	17.46	101.45	20.0	7.4
	28-Dec-1951	16.72	98.88	30.7	6.5
	28-Jul-1957	17.06	99.09	37.8	7.6
	19-May-1962	16.87	99.73	25.0	6.8
	11-May-1962	16.96	99.74	25.0	7.0
	30-Jan-1973	18.42	103.04	47.0	7.6
	07-Jun-1976	17.22	100.91	29.0	6.4
	19-Mar-1978	17.00	99.76	19.9	6.6
	16-Jan-1979	17.23	100.21	33.3	6.6
	14-Mar-1979	17.46	101.46	15.0	7.4
	25-Oct-1981	17.74	102.24	15.0	7.3
	19-Sep-1985	18.18	102.57	17.0	8.0
	21-Sep-1985	17.60	101.82	20.0	7.4
	30-Apr-1986	18.25	102.92	20.7	6.9
	25-Apr-1989	16.83	99.12	15.0	6.9
	15-Jul-1996	17.50	101.12	22.4	6.6
	09-Aug-2000	18.13	102.39	33.0	6.5
	18-Apr-2002	16.79	101.22	15.0	6.7
	01-Jan-2004	17.45	101.40	15.0	6.0
	13-Apr-2007	17.26	100.23	32.2	6.0
	11-Apr-2012	18.10	102.97	20.5	6.7
	22-Apr-2013	18.05	102.19	26.6	6.1
	21-Aug-2013	17.00	99.54	23.3	6.2
	18-Apr-2014	17.40	100.96	24.0	7.3
	08-May-2014	17.36	100.74	21.3	6.5
	10-May-2014	17.31	100.82	20.7	6.1
	07-Sep-2021	16.98	99.77	20.0	7.0
SZ3	15-Apr-1907	16.51	97.30	30.0	7.8
	22-Mar-1928	16.14	96.11	15.0	7.6
	17-Jun-1928	16.18	96.59	20.0	7.9
	04-Aug-1928	16.00	98.21	20.0	7.2
	09-Oct-1928	16.19	97.50	25.0	7.5

Table B.1 List of interplate earthquakes with $M_w \geq 6$ that occurred in the Mexican subduction zone from 1900 to 2021

Source Zone	Date	Latitude [°N]	Longitude [°W]	H_h [km]	M_w
SZ3 (cont.)	15-Jan-1931	16.04	96.58	35.0	7.6
	23-Dec-1937	16.75	98.36	25.0	7.4
	06-Jan-1948	16.74	98.48	35.0	7.0
	14-Dec-1950	16.74	98.48	35.0	7.1
	23-Aug-1965	16.08	95.87	25.0	7.4
	02-Aug-1968	16.52	97.74	25.0	7.3
	13-Nov-1972	15.61	95.04	15.0	6.6
	29-Nov-1978	16.22	96.56	16.1	7.7
	07-Jun-1982	16.39	98.29	28.0	6.9
	07-Jun-1982	16.36	98.52	25.9	6.9
	02-Jul-1984	16.76	98.45	32.5	6.1
	15-May-1993	16.67	98.42	19.7	6.0
	15-May-1993	16.70	98.40	20.8	6.1
	24-Oct-1993	16.77	98.61	21.8	6.6
	14-Sep-1995	16.48	98.76	15.9	7.3
	25-Feb-1996	15.88	97.98	15.0	7.1
	19-Jul-1997	15.86	98.26	15.0	6.7
	03-Feb-1998	15.92	96.22	24.0	6.3
	30-Jun-2010	16.67	97.77	17.8	6.3
	20-Mar-2012	16.50	98.22	20.0	7.4
16-Feb-2018	16.45	97.85	25.0	7.2	
17-Feb-2018	16.17	97.80	16.7	6.0	
23-Jun-2020	15.93	95.94	20.0	7.4	
SZ4	14-Jan-1903	15.00	93.00	33.0	7.7
	14-Dec-1935	14.71	92.38	35.0	7.3
	28-Jun-1944	14.32	92.89	25.0	7.0
	17-Nov-1953	13.49	92.23	25.0	6.8
	28-Aug-1955	13.67	90.78	44.8	6.7
	28-Apr-1959	14.55	92.31	25.0	6.5
	29-Apr-1970	14.43	92.85	35.0	6.6
	29-Apr-1970	14.52	92.65	35.0	7.3
30-Apr-1970	14.55	93.25	35.0	6.6	

Table B.1 List of interplate earthquakes with $M_w \geq 6$ that occurred in the Mexican subduction zone from 1900 to 2021

Source Zone	Date	Latitude [°N]	Longitude [°W]	H_h [km]	M_w
SZ4 (cont.)	30-Oct-1978	13.54	91.69	25.0	6.3
	17-Oct-1979	13.66	91.01	27.6	6.8
	27-Oct-1979	13.77	91.07	29.8	6.8
	06-Apr-1982	13.79	91.95	42.6	6.7
	02-Dec-1983	13.86	92.20	31.0	7.0
	12-Mar-1987	15.61	94.39	17.0	6.1
	30-May-1992	14.32	93.13	28.9	6.3
	03-Sep-1993	14.40	93.14	27.4	6.7
	10-Sep-1993	13.91	92.54	16.0	6.0
	10-Sep-1993	14.41	92.99	29.1	7.2
	19-Sep-1993	14.39	93.47	16.0	6.4
	30-Sep-1993	15.08	94.83	15.0	6.5
	10-May-1998	13.59	91.35	25.0	6.3
	08-May-1999	14.19	92.38	32.1	6.0
	12-Mar-2000	14.84	93.02	66.7	6.3
	04-Dec-2000	14.75	94.05	30.0	6.0
	21-Jan-2003	13.53	91.31	41.0	6.4
	20-Nov-2004	13.13	90.61	34.4	6.3
	13-Jun-2007	13.43	91.22	31.6	6.7
	16-Oct-2008	14.28	92.90	29.9	6.6
	01-May-2012	14.38	93.35	13.1	6.0
	07-Nov-2012	14.11	92.43	21.3	7.4
	11-Nov-2012	13.94	92.68	12.0	6.4
	02-Mar-2014	14.35	93.25	15.5	6.0
	07-Dec-2014	13.65	91.84	25.8	6.1
	25-Apr-2016	14.45	93.38	17.0	6.0
	27-Apr-2016	14.55	93.39	22.2	6.0
	22-Jun-2017	13.57	91.38	38.1	6.8
	20-Nov-2019	14.01	93.43	22.7	6.3
	12-May-2021	13.16	90.60	34.5	6.3

APPENDIX C

Earthquake Source Parameters

Table C.1 summarizes the interplate earthquakes that were selected for the development of the strong-motion duration GMPEs. Their corresponding source parameters are presented as well. In particular, the source parameters for earthquakes with $M_w > 7.2$ were taken from the Global CMT Project catalog^{105,106} and for earthquakes that occurred on October 9, 1995, March 20, 2012, August 21, 2013, February 16, 2018, and June 23, 2020 from the USGS-NEIC catalog.¹⁰⁸ The works of Mendoza and Hartzell,²¹⁷ Mendoza,²¹⁸ and Courboux²¹⁹ were consulted for the earthquakes that occurred on September 19 and 21, 1985 and January 22, 2003, respectively.

Table C.1 List of interplate earthquakes and corresponding finite-source rupture model parameters used for the development of the GMPEs

Date	M_w	θ [°]	φ [°]	ψ [°]	L [km]	W [km]	H_{top} [km]	ζ_0 [km]	η_0 [km]
19-Sep-85	8.0	300	14	61	180	139	6	125	42
21-Sep-85	7.4	300	14	100	90	90	12	55	34
25-Apr-89	6.9	276	10	66					
24-Oct-93	6.6	276	17	67					
14-Sep-95	7.3	289	11	75	75	55	11	37	27
09-Oct-95	8.0	309	14	92	300	30	5	113	25
25-Feb-96	7.1	280	16	74					
15-Jul-96	6.6	297	21	93					
22-Jan-03	7.5	304	16	111	105	164	1	53	82
01-Jan-04	6.0	299	13	92					
30-Jun-10	6.3	286	12	72					
20-Mar-12	7.4	296	13	95	85	84	7	43	57
11-Apr-12	6.7	282	25	77					
21-Aug-13	6.2	281	22	71					
18-Apr-14	7.3	303	18	98	114	75	9	57	48
08-May-14	6.5	289	22	80					

Table C.1 List of interplate earthquakes and corresponding finite-source rupture model parameters used for the development of the GMPEs

Date	M_w	θ [°]	φ [°]	ψ [°]	L [km]	W [km]	H_{top} [km]	ζ_0 [km]	η_0 [km]
10-May-14	6.1	285	22	77					
16-Feb-18	7.2	297	12	91	63	51	20	32	26
23-Jun-20	7.4	272	23	58	48	48	11	23	23

APPENDIX D

Accelerograph Network Catalog

Table D.1 lists the geographical coordinates of the free-field ground-motion recording stations considered to develop the strong-motion duration GMPEs. The disregarded stations are listed in Table D.2.

At the end of this appendix, Table D.3 summarizes the number of ground-motion recordings used to develop the strong-motion duration GMPEs. All the ground-motion recordings came from the stations cited in Table D.1 and had two horizontal accelerograms (with $PGA \geq 3 \text{ cm/s}^2$), except those from stations MT50 and PA34 obtained during the October 09, 1995 earthquake, from station CUP5 obtained during the August 21, 2013 earthquake, and from stations CUP5 and TP13 obtained during the May 10, 2014 earthquake. They only had one accelerogram.

Table D.1 List of free-field ground-motion recording stations considered for the development of the strong-motion duration GMPEs

Geotechnical zone	Station code	Station name	Lat. [°N]	Long. [°W]	H_s [m]
GZI	CENA	Cenapred	19.31	99.18	2270
	CHAS	Chapultepec Superficie	19.42	99.20	2245
	CS78	Colinas del Sur	19.37	99.23	2430
	CU01	II-UNAM Laboratorio de Instrumentación Sísmica	19.33	99.18	2240
	CUP1	II-UNAM Patio 1	19.33	99.18	2240
	CUP2	II-UNAM Patio 2	19.33	99.18	2240
	CUP4	II-UNAM Patio 4	19.33	99.18	2240
	CUP5	II-UNAM Patio 5	19.33	99.18	2240
	FJ74	Fundación Javier Barros Sierra	19.30	99.21	2240
	IM40	Instituto Mexicano del Petróleo	19.34	99.20	2240
	MT50	Mariscal Tito	19.43	99.19	2234
	PA34	San Pedro Atocpan	19.20	99.05	2240

Table D.1 List of free-field ground-motion recording stations considered for the development of the strong-motion duration GMPEs

Geotechnical zone	Station code	Station name	Lat. [°N]	Long. [°W]	H_s [m]
GZI (cont.)	TACY	Tacubaya	19.40	99.20	2240
	TE07	Tecamachalco	19.43	99.22	2290
	TP13	Tlalpan	19.29	99.17	2265
	UI21	Universidad Iberoamericana	19.37	99.26	2540
GZII	AO24	Alberca Olímpica	19.36	99.15	2235
	AU46	Angel Urraza	19.38	99.17	2233
	CO47	Coyoacán	19.37	99.17	2247
	COYS	Coyoacán Superficie	19.35	99.17	2250
	DR16	Deportivo Reynosa	19.50	99.18	2233
	DX37	Xotepingo	19.33	99.14	2240
	EO30	Esparza Oteo	19.39	99.18	2236
	ES57	Escandón	19.40	99.18	2242
	GR27	Granjas	19.47	99.18	2238
	IMPS	Instituto Mexicano del Petróleo Superficie	19.49	99.15	2230
	ME52	Mariano Escobedo	19.44	99.18	2238
	RIDA	UAM Azcapotzalco	19.52	99.19	2240
	GZIIIa	CH84	Culhuacán	19.33	99.13
DFRO		Roma Sur	19.41	99.17	2240
GC38		García Campillo	19.32	99.11	2233
IB22		Esc. Sec. Técnica No. 95	19.35	99.13	2234
JC54		Parque Jardines de Coyoacán	19.31	99.13	2237
LV17		Lindavista	19.49	99.13	2233
MI15		Miramontes	19.28	99.13	2237
SI53		San Simón	19.38	99.15	2235
UC44		Unidad Colonia IMSS	19.43	99.17	2234
GZIIIb		AL01	Alameda	19.44	99.15
	BL45	Balderas	19.43	99.15	2233
	CI05	Cibeles	19.42	99.17	2233
	CJ03	Centro Urbano Juárez	19.41	99.16	2233

Table D.1 List of free-field ground-motion recording stations considered for the development of the strong-motion duration GMPEs

Geotechnical zone	Station code	Station name	Lat. [°N]	Long. [°W]	H_s [m]	
GZIIIb (cont.)	CJ04	Multifamiliar Juárez II	19.41	99.16	2233	
	CO56	Esc. Sec. Técnica No. 18	19.42	99.16	2233	
	CTCL	Catedral Campo Libre	19.43	99.13	2240	
	GA62	Esc. Sec. Técnica No. 2	19.44	99.14	2232	
	JPSK	Jardín Pushkin	19.42	99.15	2240	
	LI58	Esc. Sec. Diurna No. 23	19.43	99.16	2233	
	PE10	Esc. Prim. Plutarco Elías Calles	19.38	99.13	2232	
	RIDI	UAM Iztapalapa	19.36	99.06	2235	
	RM48	Esc. Prim. Rodolfo Menéndez	19.44	99.13	2232	
	RMAS	Estación No. 10	19.42	99.15	2235	
	RMBS	Estación No. 11	19.42	99.15	2235	
	RMCS	Estación No. 12	19.42	99.15	2235	
	SCT2	SCT B-2	19.39	99.15	2240	
	SP51	Sector Popular	19.37	99.12	2234	
	TL08	Deportivo Antonio Caso	19.45	99.13	2232	
	TL55	Tlatelolco	19.45	99.14	2232	
	VG09	Valle Gómez	19.45	99.12	2233	
	GZIIIc	AP68	Apatlaco	19.38	99.11	2232
		BA49	Buenos Aires	19.41	99.15	2233
		BO39	Bondojito	19.47	99.10	2232
		CA59	Candelaria	19.43	99.12	2233
		CDAO	Central de Abastos Oficinas	19.37	99.10	2240
		CU80	Esc. Prim. Aurora López Velarde	19.29	99.10	2232
DM12		Deportivo Moctezuma	19.43	99.10	2232	
HJ72		Hospital Juárez	19.43	99.13	2232	
JA43		Jamaica	19.41	99.13	2234	
MY19		Meyehualco	19.35	99.04	2237	
RI76	República de Italia	19.45	99.10	2232		

Table D.1 List of free-field ground-motion recording stations considered for the development of the strong-motion duration GMPEs

Geotechnical zone	Station code	Station name	Lat. [°N]	Long. [°W]	H_s [m]
GZIIC (cont.)	UNKS	Estación No. 9, U. Kennedy	19.42	99.11	2235
	VM29	Villa del Mar	19.38	99.13	2234
	XO36	Xochimilco	19.27	99.10	2232
	XP06	Xochipilli	19.42	99.14	2232
GZIId	AE02	Aeropuerto	19.43	99.06	2232
	AR14	Aragón	19.48	99.08	2232
	AU11	Autódromo	19.39	99.09	2234
	CE23	Cetis	19.46	99.06	2233
	CE32	Cetis No. 57	19.39	99.05	2233
	HA41	Hangares	19.42	99.08	2233
	NZ20	Nezahualcóyotl A	19.40	99.00	2232
	NZ31	Nezahualcóyotl B	19.42	99.02	2234
	PD42	Palacio de los Deportes	19.41	99.10	2234
	TLAS	Estación No. 7, Tacotal	19.40	99.10	2235
	ZARS	Estación No. 8, Zaragoza	19.42	99.09	2235

Table D.2 List of free-field ground-motion recording stations disregarded for the development of the strong-motion duration GMPEs

Geotechnical zone	Station code	Station name	Lat. [°N]	Long. [°W]	H_s [m]
GZI	CE18	Escuela Ramón Espinoza Villanueva	19.34	99.08	2240
	CP28	Cerro del Peñón	19.44	99.08	2240
	CT64	Cerro del Tepeyac	19.49	99.11	2240
	ESTS	Estanzuela superficie	19.49	99.11	2245
GZII	SXVI	Sismex Viveros	19.36	99.17	2240
GZIIB	SCT1	SCT B-1	19.39	99.15	2240
	TLHD	Tláhuac Deportivo	19.29	99.04	2240
GZIId	TH35	Tláhuac	19.28	99.00	2238
	TLHB	Tláhuac Bombas	19.28	99.01	2240

Table D.3 Number of ground-motion recordings per earthquake and per geotechnical zone used for the development of the strong-motion duration GMPEs

Date	M_w	Geotechnical zone					
		GZI	GZII	GZIIIa	GZIIIb	GZIIIc	GZIId
19-Sep-85	8.0	2	-	-	-	-	-
21-Sep-85	7.4	1	-	-	-	-	-
25-Apr-89	6.9	4	7	7	12	9	5
24-Oct-93	6.6	4	6	4	9	11	7
14-Sep-95	7.3	10	10	4	12	8	6
09-Oct-95	8.0	2	8	2	10	10	4
25-Feb-96	7.1	-	-	3	11	9	2
15-Jul-96	6.6	5	8	5	11	8	2
22-Jan-03	7.5	3	5	6	13	12	7
01-Jan-04	6.0	-	4	8	13	10	8
30-Jun-10	6.3	2	5	7	14	10	6
20-Mar-12	7.4	8	9	8	13	11	6
11-Apr-12	6.7	-	5	7	13	12	4
21-Aug-13	6.2	4	7	7	12	12	8
18-Apr-14	7.3	5	9	8	14	12	8
08-May-14	6.5	6	9	8	15	11	8
10-May-14	6.1	4	8	8	12	9	6
16-Feb-18	7.2	7	9	5	16	12	7
23-Jun-20	7.4	6	3	4	7	4	3
Total		73	112	101	207	170	97

[This page intentionally left blank]

APPENDIX E

Exceedance Probabilities and Return Periods for Probabilistic Seismic Hazard Analyses

Table E.1 summarizes reference values of exceedance probabilities of ground-motion levels y and associated values of T_r .

Table E.1 Relationships among typical values of exceedance probabilities of ground-motion levels y and T_r

Probability of exceedance [%]	T [years]	T_r [years]
1	5	497
2	5	247
10	5	47
1	10	995
2	10	495
5	10	195
10	10	95
1	50	4,975
2	50	2,475
5	50	975
10	50	475
20	50	224
50	50	72
1	100	9,950
2	100	4,950
5	100	1,950
10	100	949
20	100	448
50	100	144

[This page intentionally left blank]

APPENDIX F

Acceleration Response Spectra Determined from Accelerograms Recorded in the Hill Zone of Mexico City

Figure F.1 depicts 141 acceleration response spectra determined from accelerograms recorded in GZI considering SDOF systems with $\zeta_e = 5\%$ and values of T_e varying from 0.1 s to 5 s, in steps of 0.1 s. They are defined by the absolute acceleration and grouped by earthquake event.

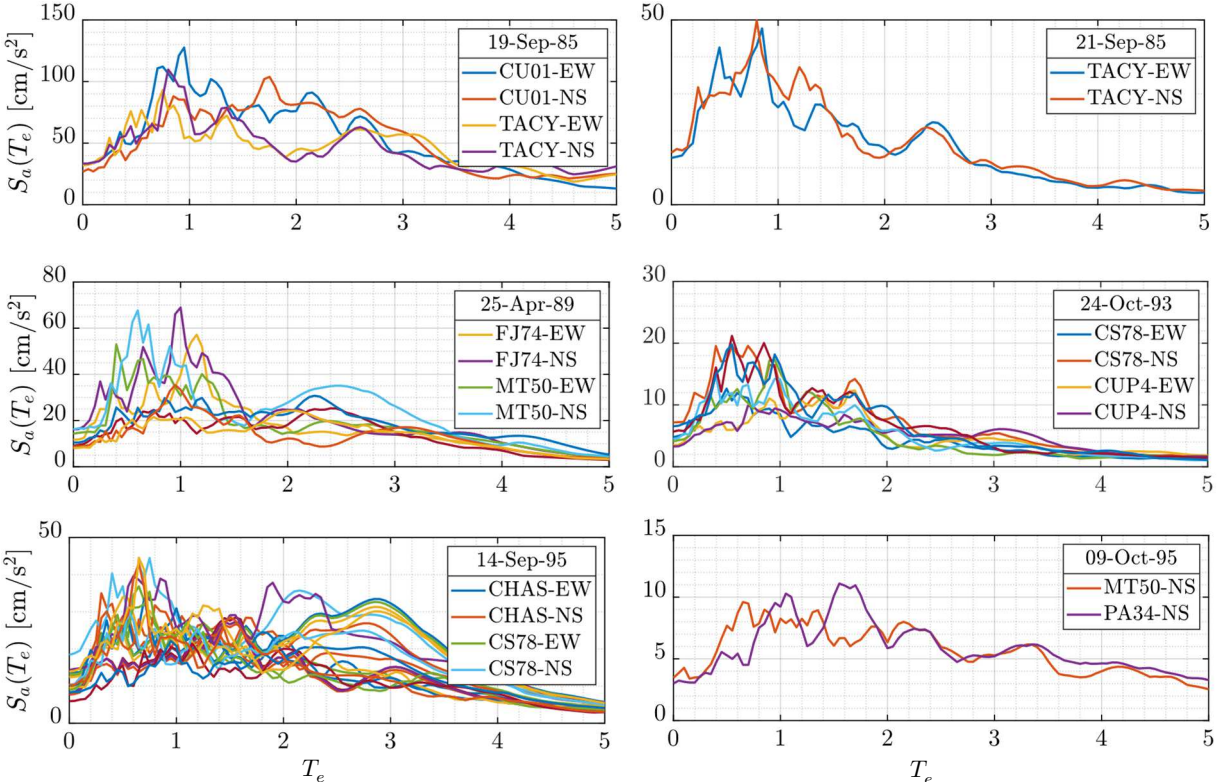


Figure F.1 Acceleration response spectra determined from accelerograms recorded in GZI. They are grouped by earthquake event. The legends show the code of stations where the accelerograms were recorded. To avoid saturation, only four acceleration response spectra are referenced

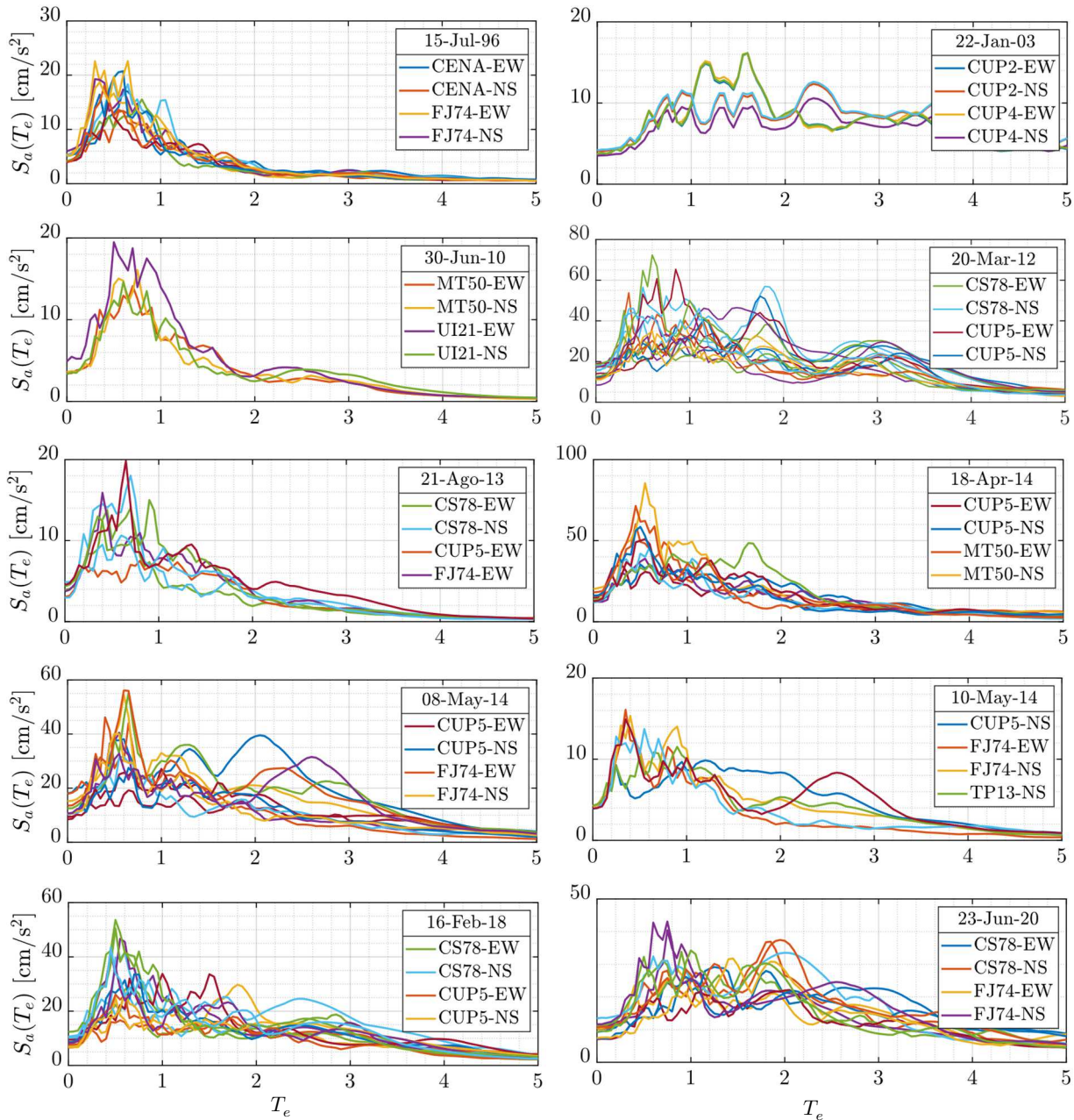


Figure F.1 Acceleration response spectra determined from accelerograms recorded in GZI. They are grouped by earthquake event. The legends show the code of stations where the accelerograms were recorded. To avoid saturation, only four acceleration response spectra are referenced

APPENDIX G

Predictive Equation for Peak Ground Acceleration and Acceleration Response-spectral Ordinates

A GMPE that allows estimating PGA and $S_a(T_e)$ for sites located in GZI was developed in Subsection 5.3.1. As already given in Eq. (5.9), its functional form is:

$$\ln(PGA)_{ik} \text{ or } \ln[S_a(T_e)]_{ik} = \alpha_0 + (\alpha_1 + \alpha_2 M_{w_i}) \ln(R_{hypo})_{ik} + b_{0_i} + e_{ik} \quad (5.9)$$

where $\ln(PGA)_{ik}$, $\ln[S_a(T_e)]_{ik}$, and $\ln(R_{hypo})_{ik}$ are the natural logarithms of PGA , $S_a(T_e)$, and R_{hypo} of the k th accelerogram recorded during the i th earthquake event, and M_{w_i} is the moment magnitude of the i th earthquake event. Recall that the terms b_{0_i} and e_{ik} have the prior distributions $b_{0_i} \sim \mathcal{N}(0, \sigma_b^2)$ and $e_{ik} \sim \mathcal{N}(0, \sigma_w^2)$, respectively.

The estimates of α_0 , α_1 , α_2 , σ_b^2 , and σ_w^2 obtained from the regression analysis are summarized in Table G.1.

Table G.1 Estimates of the elements of α , σ_b , and σ_w of the GMPE for PGA and $S_a(T_e)$ reported in Subsection 5.3.1

Ground-motion parameter	$\widehat{\alpha}_0$	$\widehat{\alpha}_1$	$\widehat{\alpha}_2$	$\widehat{\sigma}_b$	$\widehat{\sigma}_w$
PGA	11.1784	-2.7190	0.1636	0.3983	0.2225
$S_a(T_e = 0.1 \text{ s})$	12.0694	-2.8657	0.1646	0.3705	0.2142
$S_a(T_e = 0.2 \text{ s})$	16.3153	-3.5784	0.1689	0.3491	0.2185
$S_a(T_e = 0.3 \text{ s})$	16.9648	-3.5952	0.1620	0.3501	0.2877
$S_a(T_e = 0.4 \text{ s})$	17.5134	-3.6909	0.1660	0.3169	0.3290
$S_a(T_e = 0.5 \text{ s})$	11.4550	-2.3710	0.1289	0.4125	0.3288
$S_a(T_e = 0.6 \text{ s})$	13.8804	-2.9741	0.1566	0.3902	0.3604
$S_a(T_e = 0.7 \text{ s})$	12.0422	-2.5846	0.1460	0.4160	0.3056
$S_a(T_e = 0.8 \text{ s})$	8.4729	-1.9411	0.1407	0.4643	0.2617
$S_a(T_e = 0.9 \text{ s})$	11.8876	-2.7773	0.1759	0.4170	0.2637
$S_a(T_e = 1.0 \text{ s})$	12.9563	-3.0719	0.1903	0.3881	0.2517

Table G.1 Estimates of the elements of α , σ_b , and σ_w of the GMPE for *PGA* and $S_a(T_e)$ reported in Subsection 5.3.1

Ground-motion parameter	$\widehat{\alpha}_0$	$\widehat{\alpha}_1$	$\widehat{\alpha}_2$	$\widehat{\sigma}_b$	$\widehat{\sigma}_w$
$S_a(T_e = 1.1 \text{ s})$	13.5710	-3.3034	0.2064	0.3888	0.2566
$S_a(T_e = 1.2 \text{ s})$	14.9960	-3.6523	0.2206	0.4043	0.2673
$S_a(T_e = 1.3 \text{ s})$	15.0527	-3.7336	0.2294	0.4196	0.2362
$S_a(T_e = 1.4 \text{ s})$	15.9941	-4.0490	0.2499	0.4148	0.2389
$S_a(T_e = 1.5 \text{ s})$	17.2803	-4.4181	0.2696	0.4111	0.2439
$S_a(T_e = 1.6 \text{ s})$	14.9927	-3.9729	0.2615	0.4020	0.2549
$S_a(T_e = 1.7 \text{ s})$	13.9001	-3.7686	0.2585	0.4205	0.2769
$S_a(T_e = 1.8 \text{ s})$	12.7371	-3.5179	0.2495	0.4646	0.2926
$S_a(T_e = 1.9 \text{ s})$	11.8332	-3.3481	0.2454	0.5107	0.2945
$S_a(T_e = 2.0 \text{ s})$	11.8537	-3.3729	0.2469	0.5421	0.2980
$S_a(T_e = 2.1 \text{ s})$	12.6494	-3.6581	0.2675	0.5500	0.3024
$S_a(T_e = 2.2 \text{ s})$	12.6212	-3.6923	0.2723	0.5505	0.3103
$S_a(T_e = 2.3 \text{ s})$	11.9956	-3.5734	0.2699	0.5588	0.3185
$S_a(T_e = 2.4 \text{ s})$	11.0456	-3.3695	0.2635	0.5687	0.3219
$S_a(T_e = 2.5 \text{ s})$	10.0621	-3.1194	0.2514	0.5980	0.3312
$S_a(T_e = 2.6 \text{ s})$	10.2802	-3.1670	0.2524	0.6048	0.3313
$S_a(T_e = 2.7 \text{ s})$	9.9621	-3.0992	0.2497	0.6025	0.3304
$S_a(T_e = 2.8 \text{ s})$	9.5990	-3.0314	0.2478	0.5951	0.3298
$S_a(T_e = 2.9 \text{ s})$	10.0257	-3.1694	0.2563	0.5774	0.3309
$S_a(T_e = 3.0 \text{ s})$	10.3911	-3.2989	0.2650	0.5688	0.3252
$S_a(T_e = 3.1 \text{ s})$	10.2718	-3.3136	0.2689	0.5539	0.3094
$S_a(T_e = 3.2 \text{ s})$	9.6177	-3.2107	0.2690	0.5362	0.2936
$S_a(T_e = 3.3 \text{ s})$	9.1631	-3.1717	0.2730	0.5332	0.2837
$S_a(T_e = 3.4 \text{ s})$	8.9383	-3.1635	0.2755	0.5355	0.2752
$S_a(T_e = 3.5 \text{ s})$	9.2966	-3.2785	0.2808	0.5578	0.2688
$S_a(T_e = 3.6 \text{ s})$	9.4325	-3.3240	0.2818	0.5804	0.2677
$S_a(T_e = 3.7 \text{ s})$	10.0764	-3.5052	0.2901	0.5782	0.2667
$S_a(T_e = 3.8 \text{ s})$	10.7817	-3.7103	0.3004	0.5761	0.2660
$S_a(T_e = 3.9 \text{ s})$	10.9926	-3.8058	0.3075	0.5626	0.2643
$S_a(T_e = 4.0 \text{ s})$	10.9076	-3.8391	0.3132	0.5452	0.2544
$S_a(T_e = 4.1 \text{ s})$	10.6347	-3.8256	0.3167	0.5278	0.2523

Table G.1 Estimates of the elements of α , σ_b , and σ_w of the GMPE for PGA and $S_a(T_e)$ reported in Subsection 5.3.1

Ground-motion parameter	$\widehat{\alpha}_0$	$\widehat{\alpha}_1$	$\widehat{\alpha}_2$	$\widehat{\sigma}_b$	$\widehat{\sigma}_w$
$S_a(T_e = 4.2 \text{ s})$	10.0758	-3.7385	0.3166	0.5184	0.2533
$S_a(T_e = 4.3 \text{ s})$	9.8982	-3.7310	0.3184	0.5155	0.2455
$S_a(T_e = 4.4 \text{ s})$	9.7057	-3.7171	0.3197	0.5118	0.2352
$S_a(T_e = 4.5 \text{ s})$	9.5593	-3.7081	0.3206	0.5015	0.2324
$S_a(T_e = 4.6 \text{ s})$	8.9181	-3.5793	0.3165	0.4964	0.2368
$S_a(T_e = 4.7 \text{ s})$	8.1169	-3.4316	0.3137	0.5020	0.2448
$S_a(T_e = 4.8 \text{ s})$	7.1390	-3.2317	0.3079	0.5173	0.2470
$S_a(T_e = 4.9 \text{ s})$	6.1717	-3.0528	0.3050	0.5203	0.2461
$S_a(T_e = 5.0 \text{ s})$	5.2765	-2.8833	0.3019	0.5282	0.2414

[This page intentionally left blank]

References

1. Esteva L, Rosenblueth E. Espectros de temblores a distancias moderadas y grandes. *Boletín la Soc Mex Ing Sísmica*. 1964;2(1):1-18.
2. Díaz SA, Pujades LG, Barbat AH, Vargas-Alzate YF, Hidalgo-Leiva DA. Energy damage index based on capacity and response spectra. *Eng Struct*. 2017;152(1):424-436. doi:10.1016/j.engstruct.2017.09.019
3. Cosenza E, Manfredi G. The improvement of the seismic-resistant design for existing and new structures. In: Fajfar P, Krawinkler H, eds. *Proceedings of the International Workshop on Seismic Design Methodologies for the Next Generation of Codes*. 1st ed. Bled, Slovenia: Taylor & Francis; 1997:119-130. doi:10.1201/9780203740019-11
4. Kramer SL. *Geotechnical Earthquake Engineering*. (Hall WJ, ed.). Upper Saddle River, NJ; 1996.
5. Somerville PG, Moriwaki Y. Seismic hazard and risk assessment in engineering practice. In: Lee WHK, Kanamori H, Jennings PC, Kisslinger C, eds. *International Handbook of Earthquake and Engineering Seismology, Part B*. 1st ed. Academic Press; 2003:1065-1080.
6. Singhal A, Kiremidjian AS. Method for probabilistic evaluation of seismic structural damage. *J Struct Eng*. 1996;122:1459-1467.
7. McGuire RK. *Seismic Hazard and Risk Analysis*. Colorado: Earthquake Engineering Research Institute (EERI) Publication; 2004.
8. Sen TK. *Fundamentals of Seismic Loading on Structures*. Chichester, West Sussex: John Wiley & Sons, Ltd; 2009.
9. McGuire RK, Arabasz JW. An introduction to probabilistic seismic hazard analysis. In: Stanley HW, ed. *Geotechnical and Environmental Geophysics: Volume I, Review and Tutorial*. Tulsa, Oklahoma: Society of Exploration Geophysicists; 1990:333-353.
10. Campbell KW. Strong-motion attenuation relations. In: Lee WHK, Kanamori H, Jennings PC, Kisslinger C, eds. *International Handbook of Earthquake and Engineering Seismology, Part B*. 1st ed. Academic Press; 2003:1003-1012.
11. Reinoso E, Ordaz M, Guerrero R. Influence of strong ground motion duration in

- seismic design of structures. In: *Proceedings of the 12th World Conference on Earthquake Engineering*. Auckland; 2000.
12. Jennings PC. Ground motion parameters that influence structural damage. In: Scholl RE, King JL, eds. *Strong Ground Motion Simulation and Engineering Applications*. Berkeley, California: Earthquake Engineering Research Institute (EERI) Publication; 1985.
 13. Trifunac MD, Brady AG. A study on the duration of strong earthquake ground motion. *Bull Seismol Soc Am*. 1975;65(3):581-626. doi:10.1785/BSSA0650030581
 14. Naem F. Earthquake Excitation and Response of Buildings. In: Braun S, Ewins D, Rao SS, eds. *Encyclopedia of Vibration*. London: Academic Press; 2001:439-461. doi:10.1006/rwvb.2001.0067
 15. Pavel F, Lungu D. Frequency content indicators of strong ground motions. In: *Proceedings of the 15th World Conference on Earthquake Engineering*. Lisboa; 2012:10.
 16. Jennings PC. An Introduction to the Earthquake Response of Structures. In: Lee WHK, Kanamori H, Jennings PC, Kisslinger C, eds. *International Handbook of Earthquake and Engineering Seismology, Part B*. 1st ed. Academic Press; 2003:1097-1124.
 17. Salmon MW, Short SA, Kennedy RP. *Strong Motion Duration and Earthquake Magnitude Relationships*. Livermore, California; 1992.
 18. Moreno-Murillo JM. The 1985 Mexico earthquake,. *Geofísica Colomb*. 1995;3:5-19.
 19. Williams D. Mexico quake loss put at \$4 billion: Report by U.N. panel includes damages to economy. *Los Angeles Times*. <https://www.latimes.com/archives/la-xpm-1985-10-25-mn-14160-story.html>. Published 1985.
 20. Anderson JG, Bodin P, Brune JN, et al. Strong ground motion from the Michoacan, Mexico, earthquake. *Science (80-)*. 1986;233(4768):1043-1049. doi:10.1126/science.233.4768.1043
 21. Para recordar el sismo del 85. *El Universal*. <https://www.eluniversal.com.mx/articulo/cultura/letras/2015/08/27/palabras-e-imagenes-para-recordar-el-terremoto-del-85>. Published 2015.
 22. Douglas J. Ground motion prediction equations 1964-2016. <http://www.gmpe.org.uk>. Published 2017. Accessed August 8, 2018.
 23. Bommer JJ, Martínez-Pereira A. The effective duration of earthquake strong motion. *J Earthq Eng*. 1999;3(2):127-172. doi:10.1080/13632469909350343
 24. Vamvatsikos D, Cornell A. Incremental dynamic analysis. *Earthq Eng Struct Dyn*. 2002;31(3):491-514. doi:10.1002/eqe.141

25. American Society of Civil Engineers (ASCE). *Minimum Design Loads and Associated Criteria for Buildings and Other Structures (ASCE/SEI 7-16)*. Reston, Virginia; 2016.
26. European Committee for Standardization (CEN). *Eurocode 8: Design of Structures for Earthquake Resistance Part 1: General Rules, Seismic Actions and Rules for Buildings*. London; 2004.
27. Secretaría de Obras y Servicios de la Ciudad de México (SOS-CDMX). *Normas Técnicas Complementarias (NTC-2020)*. Mexico City; 2020.
28. Arias A. A measure of earthquake intensity. In: Hansen R, ed. *Seismic Design for Nuclear Power Plants*. Cambridge, Massachusetts: Mass. Inst. Tech. Press; 1970:438-483.
29. Snaebjornsson JT, Sigbjörnsson R. The duration characteristics of earthquake ground motions. In: *Proceedings of the 14th World Conference on Earthquake Engineering*. Beijing; 2008.
30. Ambraseys NN, Sarma SK. The response of earth dams to strong earthquakes. *Géotechnique*. 1967;17(3):181-283. doi:10.1680/geot.1967.17.3.181
31. Page RA, Boore DM, Joyner WB, Coulter HW. Ground motion values for use in the seismic design of the Trans-Alaska pipeline system. *US Geol Surv Circ*. 1972;672.
32. McGuire RK, Barnhard TP. The usefulness of ground motion duration in prediction of severity of seismic shaking. In: *Proceedings of the 2nd US International Conference on Earthquake Engineering*. Stanford; 1979:713-722.
33. Kawashima K, Aizawa K. Bracketed and normalized durations of earthquake ground acceleration. *Earthq Eng Struct Dyn*. 1989;18(7):1040-1051. doi:10.1002/eqe.4290180709
34. Bolt BA. Duration of strong ground motion. In: *Proceedings of the 5th World Conference on Earthquake Engineering*. Rome; 1973:1304-1313.
35. Zahara TF, Hall WJ. Earthquake energy absorption in SDOF structures. *J Struct Eng*. 1984;110(8):1957-1772. doi:10.1061/(ASCE)0733-9445(1984)110:8(1757)
36. Husid R. Características de terremotos. Análisis General. *Rev del IDIEM*. 1969;8(1):21-42.
37. Dobry R, Idriss IM, Ng E. Duration characteristics of horizontal components of strong-motion earthquake records. *Bull Seismol Soc Am*. 1978;68(5):1487-1520. doi:10.1785/BSSA0680051487
38. Somerville PG, Smith NF, Graves RW, Abrahamson NA. Modification of empirical strong ground motion attenuation relations to include the amplitude

- and duration effects of rupture directivity. *Seismol Res Lett.* 1997;68(1):199-222. doi:10.1785/gssrl.68.1.199
39. Taflampas IM, Spyarakos CC, Koutromanos IA. A new definition of strong motion duration and related parameters affecting the response of medium-long period structures. *Soil Dyn Earthq Eng.* 2009;29(752-763). doi:10.1016/j.soildyn.2008.08.005
 40. Rosenblueth E, Bustamante JI. Distribution of structural response to earthquakes. *J Eng Mech ASCE.* 1962;88(3):75-106. doi:10.1061/JMCEA3.0000300
 41. Bates DM, Watts. *Nonlinear Regression Analysis and Its Applications.*; 1988.
 42. Evans MJ, Rosenthal JS. *Probability and Statistics: The Science of Uncertainty.* 2nd ed. New York, New York: W. H. Freeman and Company; 2010.
 43. Kanamori H. The energy release in great earthquakes. *J Geophys Res.* 1977;82(20):2981-2987. doi:10.1029/JB082i020p02981
 44. Hanks TC, Kanamori H. A moment magnitude scale. *J Geophys Res.* 1979;84(B5):2348-2350. doi:10.1029/JB084iB05p02348
 45. Anderson JG. Strong-motion seismology. In: Lee WHK, Kanamori H, Jennings PC, Kisslinger C, eds. *International Handbook of Earthquake and Engineering Seismology, Part B.* 1st ed. Academic Press; 2003:937-965.
 46. Agresti A. *An Introduction to Categorical Data Analysis.* Hoboken, New Jersey: John Wiley & Sons, Inc.; 2007.
 47. Guerrero R. *Duración Del Movimiento Durante Sismos: Implicaciones En La Degradación Estructural.* Ciudad de México: Universidad Nacional Autónoma de México (UNAM); 1997.
 48. Reinoso E, Ordaz M. Duration of strong ground motion during Mexican earthquakes in terms of magnitude, distance to the rupture area and dominant site period. *Earthq Eng Struct Dyn.* 2001;30:365-673. doi:10.1002/eqe.28
 49. Pinheiro JC, Bates DM. *Mixed-Effects Models in S and S-Plus.* New York, New York: Springer-Verlag; 2000.
 50. Özbey C, Sari A, Lance M, Erdik M, Fahjan Y. An empirical attenuation relationship for Northwestern Turkey ground motion using a random effects approach. *Soil Dyn Earthq Eng.* 2004;24(2):115-125. doi:10.1016/j.soildyn.2003.10.005
 51. López-Castañeda AS, Reinoso E. Strong-motion duration predictive models from subduction interface earthquakes recorded in the hill zone of the Valley of Mexico. *Soil Dyn Earthq Eng.* 2021;144. doi:10.1016/j.soildyn.2021.106676

52. Kempton JJ, Stewart JP. Prediction equations for significant duration of earthquake ground motions considering site and near-source effects. *Earthq Spectra*. 2006;22(4):985-1013. doi:10.1193/1.2358175
53. Bommer JJ, Stafford PJ, Alarcón JE. Empirical equations for the prediction of the significant, bracketed, and uniform duration of earthquake ground motion. *Bull Seismol Soc Am*. 2009;99(6):3217-3233. doi:10.1785/0120080298
54. Lee J, Green RA. An empirical bracketed duration relation for stable continental regions of North America. *Earthquakes Struct*. 2012;3(1):1-15. doi:10.12989/eas.2012.3.1.001
55. Beyer K, Bommer JJ. Relationships between median values and between aleatory variabilities for different definitions of the horizontal component of motion. *Bull Seismol Soc Am*. 2006;96(4A):1512-1522. doi:10.1785/0120050210
56. Pacific Earthquake Engineering Research Center (PEER). PEER Strong Ground Motion Databases. <https://peer.berkeley.edu/peer-strong-ground-motion-databases>.
57. Ghanat S. *Duration Characteristics of the Mean Horizontal Component of Shallow Crustal Earthquake Records in Active Tectonic Regions*. Tempe: Arizona State University; 2011. <https://keep.lib.asu.edu/items/149831>.
58. Yaghmaei-Sabegh S, Shoghian Z, Sheik MN. A new model for the prediction of earthquake ground-motion duration in Iran. *Nat Hazards*. 2014;70:69-92. doi:10.1007/s11069-011-9990-6
59. Building Seismic Safety Council (BSSC). *NEHRP Recommended Provisions for Seismic Regulations for New Buildings and Other Structures (FEMA 450)*. Washington, D.C.; 2003.
60. Housing and Building National Research Center. Housing and Building National Research Center. <http://www.hbrc.edu.eg/>.
61. Lee J, Green RA. An empirical significant duration relationship for stable continental regions. *Bull Earthq Eng*. 2014;12(1):217-235. doi:10.1007/s10518-013-9570-0
62. Afshari K, Stewart JP. Physically parameterized prediction equations for significant duration in active crustal regions. *Earthq Spectra*. 2016;32(4):2057-2081. doi:10.1193/063015EQS106M
63. Du W, Wang G. Prediction equations for ground-motion significant durations using the NGA-West2 Database. *Bull Seismol Soc Am*. 2017;107(1):319-333. doi:10.1785/0120150352
64. Meimandi-Parizi A, Daryoushi M, Mahdavian A, Saffari H. Ground-motion

- models for the prediction of significant duration using strong-motion data from Iran. *Bull Seismol Soc Am.* 2020;110(1):319-330. doi:10.1785/0120190109
65. Boore DM. Orientation-independent, nongeometric-mean measures of seismic intensity from two horizontal components of motion. *Bull Seismol Soc Am.* 2010;100(4):1830-1835. doi:10.1785/0120090400
66. Jaimes MA, García-Soto AD. Ground-motion duration prediction model from recorded Mexican interplate and intermediate-depth intraslab earthquakes. *Bull Seismol Soc Am.* 2021;111(1):258-273. doi:10.1785/0120200196
67. Instituto de Ingeniería de la Universidad Nacional Autónoma de México (II-UNAM). Red acelerográfica del Instituto de Ingeniería (RAII-UNAM). <https://aplicaciones.iingen.unam.mx/AcelerogramasRSM/>. Published 2020. Accessed June 24, 2020.
68. Alcántara L, García S, Ovando-Shelley E, Macías-Castillo MA. Neural estimation of strong ground motion duration. *Geofísica Int.* 2014;53(3):221-239.
69. MathWorks. Neural Networks. What is a Neural Network? <https://www.mathworks.com/discovery/neural-network.html>. Published 2022.
70. Kotha SR, Bindi D, Cotton F. Site-corrected magnitude- and region-dependent correlations of horizontal peak spectral amplitudes. *Earthq Spectra.* 2017;33(4):1415-1432. doi:10.1193/091416eqs150m
71. Stafford PJ. Interfrequency correlations among Fourier spectral ordinates and implications for stochastic ground-motion simulation. *Bull Seismol Soc Am.* 2017;107(6):2774-2791. doi:10.1785/0120170081
72. Jaimes MA, Candia G. Interperiod correlation model for Mexican interface earthquakes. *Earthq Spectra.* 2019;35(3):1351-1365. doi:10.1193/080918EQS200M
73. Harati M, Mashayekhi M, Estekanchi HE. Correlation of ground-motion duration with its intensity metrics: A simulation based approach. *J Soft Comput Civ Eng.* 2020;4(3):17-39. doi:10.48550/arXiv.1905.02369
74. Jaimes MA, Candia G, López-Castañeda AS, Macedo J. Ground motion correlations from recorded Mexican intermediate-depth, intraslab earthquakes. *J Earthq Eng.* 2021. doi:10.1080/13632469.2021.2001393
75. Baker JW, Cornell CA. Correlation of response spectral values for multicomponent ground motions. *Bull Seismol Soc Am.* 2006;96(1):215-227. doi:10.1785/0120050060
76. Bradley BA. Correlation of significant duration with amplitude and cumulative intensity measures and its use in ground motion selection. *J Earthq Eng.* 2011;15:809-832. doi:10.1080/13632469.2011.557140

77. Baker JW, Bradley BA. Intensity measure correlations observed in the NGA West2 database, and dependence of correlations on rupture and site parameters. *Earthq Spectra*. 2017;33(1):145-156.
78. Seed HB, Idriss IM. Simplified procedure for evaluating soil liquefaction potential. *J Soil Mech Found Div*. 1971;97(9):1249-1273.
79. Rauch AF, Martin JR. EPOLLS model for predicting average displacements on lateral spreads. *J Geotech Geoenvironmental Eng*. 2000;126(4):361-371. doi:10.1061/(ASCE)1090-0241(2000)126:4(360)
80. Liu AH, Stewart JP, Abrahamson NA, Moriwaki Y. Equivalent number of uniform stress cycles for liquefaction analysis. *J Geotech Geoenvironmental Eng*. 2001;127(12):1017-1026. doi:10.1061/(ASCE)1090-0241(2001)127:12(1017)
81. Seed RB, Cetin KO, Moss RES, et al. Recent advances in soil liquefaction engineering and seismic site response evaluation. In: *Proceedings of the 4th International Conference on Recent Advances in Geotechnical Earthquake Engineering and Soil Dynamics*. San Diego; 2001:45.
82. Hancock J, Bommer JJ. A state-of-knowledge review of the influence of strong-motion duration on structural damage. *Earthq Spectra*. 2006;22(3):827-845. doi:10.1193/1.2220576
83. Chandramohan R, Baker JW, Deierlein GG. Quantifying the influence of ground-motion duration on structural collapse capacity using spectrally equivalent records. *Earthq Spectra*. 2016;32(2):927-950. doi:10.1193/122813eqs298mr2
84. Ruiz-García J. On the influence of strong-ground motion duration on residual displacement demands. *Earthquakes Struct*. 2010;1(4). doi:10.12989/eas.2010.1.4.327
85. Jaimes MA, Reinoso E, Ordaz M. Comparison of methods to predict response spectra at instrumented sites given the magnitude and distance of an earthquake. *J Earthq Eng*. 2006;10(6):887-902. doi:10.1080/13632460609350622
86. Lebrun R, Dutfoy A. An innovating analysis of the Nataf transformation from the copula viewpoint. *Probabilistic Eng Mech*. 2009;24:312-320. doi:10.1016/j.probengmech.2008.08.001
87. Bravo-Haro MA, Liapopoulou M, Elghazouli AY. Seismic collapse capacity assessment of SDOF systems incorporating duration and instability effects. *Bull Earthq Eng*. 2020;18:3025-3056. doi:10.1007/s10518-020-00829-9
88. Barbosa AR, Ribeiro FLA, Neves LC. Influence of earthquake ground-motion duration on damage estimation: application to steel moment resisting frames. *Earthq Eng Struct Dyn*. 2017;46:27-79. doi:10.1002/eqe.2769

89. Belejo A, Barbosa AR, Bento R. Influence of ground motion duration on damage index-based fragility assessment of a plan-asymmetric non-ductile reinforced concrete building. *Eng Struct.* 2017;151:682-703. doi:10.1016/j.engstruct.2017.08.042
90. Bravo-Haro MA, Elghazouli AY. Influence of earthquake duration on the response of steel moment frames. *Soil Dyn Earthq Eng.* 2018;115:634-651. doi:10.1016/j.soildyn.2018.08.027
91. Laird NM, Ware JH. Random-effects models for longitudinal data. *Biometrics.* 1982;38(4):963-974.
92. Demidenko E. *Mixed Models: Theory and Applications.* Hoboken, New Jersey: John Wiley & Sons, Inc.; 2004.
93. Forbes C, Evan M, Hastings N, Peacock B. Multivariate Normal (Multinormal) Distribution. In: *Statistical Distributions.* 4th ed. Hoboken, New Jersey: John Wiley & Sons, Inc.; 2011:137-138.
94. Kostoglodov V, Pacheco JF. Cien años de sismicidad en México. Instituto de Geofísica UNAM. <http://usuarios.geofisica.unam.mx/vladimir/sismos/100a%F1os.html> . Published 1999. Accessed November 18, 2021.
95. García-Palomo A, Macías JL, Tolson G, Valdez G, Mora JC. Volcanic stratigraphy and geological evolution of the Apan region, east-central sector of the Trans-Mexican Volcanic Belt. *Geofísica Int.* 2002;41(2):133-150.
96. Ferrari L, Orozco-Esquivel T, Manea V, Manea M. The dynamic history of the Trans-Mexican Volcanic Belt and the Mexico subduction zone. *Tectonophysics.* 2012;522-523:122-149. doi:10.1016/j.tecto.2011.09.018
97. Ramírez-Herrera MT, Urrutia-Fucugauchi J. Morphotectonic zones along the coast of the Pacific continental margin, southern Mexico. *Geomorphology.* 1999;28:237-250. doi:10.1016/S0169-555X(99)00016-1
98. Singh SK, Ordaz M, Pérez-Campos X, Iglesias A. Intraslab versus interplate earthquakes as recorded in Mexico City: Implications for seismic hazard. *Earthq Spectra.* 2015;31(2):795-812. doi:10.1193/110612EQS324M
99. Gardi A, Cocco M, Negredo AM, Sabadini R, Singh SK. Dynamic modelling of the subduction zone of central Mexico. *Geophys J Int.* 2000;143(3):809-820. doi:10.1046/j.1365-246X.2000.00291.x
100. García D, Singh SK, Herráiz M, Ordaz M, Pacheco JF. Inslab earthquakes of Central Mexico: peak ground-motion parameters and response spectra. *Bull Seismol Soc Am.* 2005;95(6):2272-2282. doi:10.1785/0120050072

101. Jaimes MA, Reinoso E. Comparación del comportamiento de edificios en el Valle de México ante sismos de subducción y de falla normal. *Rev Ing Sísmica*. 2006;75:1-22.
102. Iglesias A, Singh SK, Pacheco JF, Ordaz M. A source and wave propagation study of the Copalillo, Mexico, Earthquake of 21 July 2000 (Mw 5.69): Implications for seismic hazard in Mexico City from inslab earthquakes. *Bull Seismol Soc Am*. 2002;92(3):1060-1071. doi:10.1785/0120010144
103. Barbosa AR, Ribeiro FLA, Neves LC. Effects of ground-motion duration on the response of a 9-story steel frame building. In: *Proceedings of the 10th US National Conference on Earthquake Engineering*. Anchorage; 2014. doi:10.4231/D3ZK55N05
104. Montalvo-Arrieta JC, Reinoso E, Sánchez-Sesma FJ. Observations of strong motion at hill sites in Mexico City from recent earthquakes. *Geofísica Int*. 2003;42(2):205.
105. Dziewonski AM, Chou T-A, Woodhouse JH. Determination of earthquake source parameters from waveform data for studies of global and regional seismicity. *J Geophys Res*. 1981;86:2825-2852. doi:10.1029/JB086iB04p02825
106. Ekström G, Nettles M, Dziewonski AM. The global CMT project 2004-2010: Centroid-moment tensors for 13,017 earthquakes. *Phys Earth Planet Inter*. 2012;200-201:1-9. doi:doi:10.1016/j.pepi.2012.04.002
107. International Seismological Centre (ISC). On-Line Bulletin. <http://www.isc.ac.uk/>. Accessed November 23, 2021.
108. U.S. Geological Survey (USGS). Earthquake Hazards Program. <https://www.usgs.gov/natural-hazards/earthquake-hazards/earthquakes>. Accessed November 23, 2021.
109. Singh SK, Rodríguez M, Espindola JM. A catalog of shallow earthquakes of Mexico from 1900 to 1981. *Bull Seismol Soc Am*. 1984;74(1):267-279. doi:10.1785/BSSA0740010267
110. Zuñiga RF, Suárez G, Figueroa-Soto Á, Mendoza A. A first order seismotectonic regionalization of Mexico for seismic hazard and risk estimation. *J Seismol*. 2017;21:1295-1322. doi:10.1007/s10950-017-9666-0
111. Heaton TH, Tajima F, Mori AW. Estimating ground motions using recorded accelerograms. *Surv Geophys*. 1986;8:25-83. doi:10.1007/BF01904051
112. Reinoso E. Riesgo sísmico en la Ciudad de México. La Academia de Ingeniería México. http://www.ai.org.mx/ai/archivos/coloquios/2/Riesgo_sismico_de_la_Ciudad_de_Mexico.pdf. Published 2007. Accessed July 2, 2019.

113. Jaime-Paredes A. *Características Dinámicas de La Arcilla Del Valle de México*. Mexico City: Universidad Nacional Autónoma de México (UNAM); 1987.
114. Marsal RJ, Mazari M. *El Subsuelo de La Ciudad de México*. Ciudad de México: Instituto de Ingeniería UNAM; 1969.
115. Centro de Instrumentación y Registro Sísmico (CIRES). Red acelerográfica de la Ciudad de México (RACM). <http://www.cires.org.mx>. Published 2020. Accessed June 24, 2020.
116. Reinoso E, Ordaz M. Spectral ratios for Mexico City from free-field recordings. *Earthq Spectra*. 1999;15(2):273-295. doi:10.1193/1.1586041
117. Ordaz M, Singh SK. Source spectra and spectral attenuation of seismic waves from Mexican earthquakes, and evidence of amplification in the hill zone. *Bull Seismol Soc Am*. 1992;82(1):24-43.
118. Jones AR. *Probability, Statistics and Other Frightening Stuff, Volume II*. 1st ed. New York, New York: Routledge; 2019. doi:10.4324/9781315160061
119. Delgado J, López-Casado C, Giner J, Estévez A, Cuenca A, Molina S. Microtremors as a geophysical exploration tool: Applications and limitations. *Pure Appl Geophys*. 2000;157:1445-1462.
120. Ovando-Shelley E, Ossa A, Romo MP. The sinking of Mexico City: Its effects on soil properties and seismic response. *Soil Dyn Earthq Eng*. 2007;27:333-343. doi:10.1016/j.soildyn.2006.08.005
121. Avilés J, Pérez-Rocha LE. Regional subsidence of Mexico City and its effects on seismic response. *Soil Dyn Earthq Eng*. 2010;30:981-989. doi:10.1016/j.soildyn.2010.04.009
122. Arroyo D, Ordaz M, Ovando-Shelley E, et al. Evaluation of the change in dominant periods in the lake-bed zone of Mexico City produced by ground subsidence through the use of site amplification factors. *Soil Dyn Earthq Eng*. 2013;44:54-66. doi:10.1016/j.soildyn.2012.08.009
123. Jaramillo A, Cabrera M. Comparación de la estimación del periodo de suelo en diez sitios de la Ciudad de México mediante el uso de vibración ambiental y sismos de mediana magnitud. In: *Proceedings of the XXVI Reunión Nacional de Mecánica de Suelos e Ingeniería Geotécnica*. Cancún; 2012.
124. Lermo J, Chávez-García FJ. Site effect evaluation at Mexico City: dominant period and relative amplification from strong motion and microtremor records. *Soil Dyn Earthq Eng*. 1994;13(413):423.
125. Martínez-González JA, Lermo J, Vergara-Huerta F, Ramos-Pérez E. Avances en la zonificación sísmica de la Ciudad de México y zona de Chalco, Edo. de Mex.,

- propuesta de nuevo mapa de periodos dominantes para las NTC para diseño por sismo del reglamento del D.F. In: *Proceedings of the XX Congreso Nacional de Ingeniería Sísmica*. Acapulco; 2015.
126. Martínez-González JA, Lermo J, Ismael E, Angulo J. Efectos del hundimiento regional en los cambios de periodo dominante del suelo en la Cuenta de México: Propuesta de nuevos mapas para las Normas Técnicas Complementarias para Diseño por Sismo (NTCDS). In: *Proceedings of the XVIII Congreso Nacional de Ingeniería Sísmica*. Aguascalientes; 2011.
 127. Gupta ID. Defining source-to-site distances for evaluation of design earthquake ground motion. In: *Proceedings of the 13th Symposium on Earthquake Engineering*. Roorkee; 2006:295-306. doi:10.13140/RG.2.1.3881.2005
 128. Architectural Institute of Japan (AIJ). *Guidelines for the Evaluation of Habitability to Building Vibration (AIJES-V001-2004)*. Tokyo; 2014.
 129. International Organization for Standardization (ISO). *Bases for Design of Structures - Serviceability of Buildings and Walkways against Vibrations (ISO 10137:2007)*. Geneva; 2007.
 130. Shapiro NM, Olsen KB, Singh SK. On the duration of seismic motion incident onto the Valley of Mexico for subduction zone earthquakes. *Geophys J Int*. 2002;151:501-510. doi:10.1046/j.1365-246X.2002.01789.x
 131. Shapiro NM, Singh SK, Almora D, Ayala M. Evidence of dominance of higher-mode surface waves in the lake bed zone of the Valley of Mexico. *Geophys J Int*. 2001;147:517-527.
 132. Lay T. The Earth's Interior. In: Lee WHK, Kanamori H, Jennings P, Kisslinger C, eds. *International Handbook of Earthquake and Engineering Seismology, Part A*. 1st ed. Academic Press; 2002:829-860.
 133. Forbes C, Evan M, Hastings N, Peacock B. Student's t Distribution. In: *Statistical Distributions*. 4th ed. Hoboken, New Jersey: John Wiley & Sons, Inc.; 2011:183-186.
 134. Hedeker D, Gibbons RD. *Longitudinal Data Analysis*. Hoboken, New Jersey: John Wiley & Sons, Inc.; 2006.
 135. Strasser FO, Abrahamson NA, Bommer JJ. Sigma: Issues, Insights, and Challenges. *Seismol Res Lett*. 2009;80(1):40-56. doi:10.1785/gssrl.80.1.40
 136. Al Atik L, Abrahamson NA, Bommer JJ, Scherbaum F, Cotton F, Kuehn N. The variability of ground-motion prediction models and its components. *Seismol Res Lett*. 2010;81(5):794-801. doi:10.1785/gssrl.81.5.794
 137. Forbes C, Evan M, Hastings N, Peacock B. Normal (Gaussian) Distribution. In:

- Statistical Distributions*. 4th ed. Hoboken, New Jersey: John Wiley & Sons, Inc.; 2011:143-148.
138. Nobre JS, Singer J da M. Residual analysis for linear mixed models. *Biometrical J.* 2007;49(6):863-875. doi:10.1002/bimj.200610341
 139. Singer J da M, Nobre JS, Rocha F. Diagnostic and treatment for linear mixed models. In: *59th World Statistics Congress of the International Statistical Institute*. Hong Kong; 2013:5486-5491.
 140. Ji C, Wald DJ, Helmberger D V. Source description of the 1999 Hector Mine, California, Earthquake, part I: Wavelet domain inversion theory and resolution analysis. *Bull Seismol Soc Am.* 2002;92(4):1192-1207. doi:10.1785/0120000916
 141. Hayes GP. The finite, kinematic rupture properties of great-sized earthquakes since 1990. *Earth Planet Sci Lett.* 2017;468:94-100. doi:10.1016/j.epsl.2017.04.003
 142. Carreño E, Bravo B, Suárez A, Tordecillas JM. Registro y tratamiento de acelerogramas. *Física la Tierra.* 1999;11:81-111.
 143. Boore DM, Bommer JJ. Processing of strong-motion accelerograms: needs, options and consequences. *Soil Dyn Earthq Eng.* 2005;25(2):93-115. doi:10.1016/j.soildyn.2004.10.007
 144. Abrahamson NA, Silva WJ. Empirical response spectral attenuation relations for shallow crustal earthquakes. *Seismol Res Lett.* 1997;68(1):94-127.
 145. Sakamoto Y, Ishiguro M, Kitagawa G. *Akaike Information Criterion Statistics*. Dordrecht: Springer Netherlands; 1986.
 146. Schwarz G. Estimating the dimension of a model. *Ann Stat.* 1978;6(2):461-464.
 147. Travasarou T, Bray J, Abrahamson NA. Empirical attenuation relationship for Arias Intensity. *Earthq Eng Struct Dyn.* 2003;32:1133-1155. doi:10.1002/eqe.270
 148. Danciu L, Tselentis G-A. Engineering ground-motion parameters attenuation relationships for Greece. *Soil Dyn Earthq Eng.* 2007;97(1B):162-183. doi:10.1785/0120050087
 149. Stafford PJ, Berrill JB, Pettinga JR. New predictive equations for Arias intensity from crustal earthquakes in New Zealand. *J Seismol.* 2009;13:31-82. doi:10.1007/s10950-008-9114-2
 150. López-Castañeda AS, Reinoso E. Significant duration predictive models developed from strong-motion data of thrust-faulting earthquakes recorded in Mexico City. *Earthq Eng Struct Dyn.* 2022;51(1):129-152. doi:10.1002/eqe.3559
 151. Faccioli E, Pessina V. Use of engineering seismology tools in ground shaking scenarios. In: *International Handbook of Earthquake and Engineering Seismology*,

- Part B*. 1st ed. ; 2003:1031-1048.
152. Baker JW. Introduction to probabilistic seismic hazard analysis. [http://web.stanford.edu/~bakerjw/Publications/Baker_\(2013\)_Intro_to_PSH_A_v2.pdf](http://web.stanford.edu/~bakerjw/Publications/Baker_(2013)_Intro_to_PSH_A_v2.pdf). Published 2013. Accessed November 6, 2021.
 153. McGuire RK. Probabilistic seismic hazard analysis: Early history. *Earthq Eng Struct Dyn*. 2008;37:329-338.
 154. Abrahamson NA. State of the practice of seismic hazard evaluation. In: *ISRM International Symposium*. Melbourne, Australia; 2000.
 155. Wang C-H, Holmes JD. Exceedance rate, exceedance probability, and the duality of GEV and GDP for extreme hazard analysis. *Nat Hazards*. 2020;102:1305-1321. doi:10.1007/s11069-020-03968-z
 156. Ordaz M, Reyes C. Earthquake hazard in Mexico City: Observations versus computations. *Bull Seismol Soc Am*. 1999;89(5):1379-1383. doi:10.1785/BSSA0890051379
 157. Forbes C, Evan M, Hastings N, Peacock B. Poisson Distribution. In: *Statistical Distributions*. 4th ed. Hoboken, New Jersey: John Wiley & Sons, Inc.; 2011:152-156.
 158. Gutenberg B, Richter CF. Frequency of earthquakes in California. *Bull Seismol Soc Am*. 1944;34(4):185-188. doi:10.1785/BSSA0340040185
 159. Richter CF. *Elementary Seismology*. W. H. Freeman and Company; 1958.
 160. Epstein B, Lomnitz C. A model for the occurrence of large earthquakes. *Nature*. 1966;211:954-956.
 161. Utsu T. Statistical Features of Seismicity. In: Lee WHK, Kanamori H, Jennings P, Kisslinger C, eds. *International Handbook of Earthquake and Engineering Seismology, Part A*. 1st ed. Academic Press; 2003:719-732.
 162. Cornell CA, Vanmarcke EH. The major influences on seismic risk. In: *Proceedings of the 4th World Conference on Earthquake Engineering*. Santiago de Chile, Chile; 1969.
 163. Youngs RR, Coppersmith KJ. Implications of fault slip rates and earthquake recurrence models to probabilistic seismic hazard estimates. *Bull Seismol Soc Am*. 1985;75(4):939-964.
 164. Marzocchi W, Sandri L. A review and new insights on the estimation of the b-value and its uncertainty. *Ann Geophys*. 2003;46(6):1271-1282.
 165. López-Castañeda AS. *Assessment of the Effect of Parameter Uncertainty in Probabilistic Seismic Hazard Analysis*. Mexico City: Universidad Nacional

- Autónoma de México (UNAM); 2017.
https://ru.dgb.unam.mx/handle/DGB_UNAM/TES01000766810.
166. Aki K. Maximum likelihood estimate of b in the formula $\log N = a - bM$ and its confidence limits. *Bull Earthq Res Institute, Tokyo Univ.* 1965;43:237-239.
167. Utsu T. A method for determining the value of b in a formula $\log N = a - bM$ showing the magnitude-frequency relation for earthquakes. *Geophys Bull Hokkaido Univ.* 1965;13:99-103.
168. Weichert DH. Estimation of the earthquake recurrence parameters for unequal observation periods for different magnitudes. *Bull Seismol Soc Am.* 1980;70(4):1337-1346. doi:10.1785/BSSA0700041337
169. Kijko A, Smit A. Extension of the Aki-Utsu b -value estimator for incomplete catalogs. *Bull Seismol Soc Am.* 2012;102(3):1283-1287. doi:10.1785/0120110226
170. Ordaz M, Giraldo S. Joint maximum likelihood estimators for Gutenberg and Richter parameters λ_0 and β using subcatalogs. *Earthq Spectra.* 2018;34(1):301-312. doi:10.1193/092816EQS162M
171. Vermeulen PJ, Kijko A. Joint maximum likelihood estimators for Gutenberg-Richter parameters λ_0 and β using subcatalogs. *Earthq Spectra.* 2019;35(2):1053-1058. doi:10.1193/092816EQS162M
172. Kijko A, Sellevoll MA. Estimation of earthquake hazard parameters from incomplete data files. Part I. Utilization of extreme and complete catalogs with different threshold magnitudes. *Bull Seismol Soc Am.* 1989;79(3):645-654. doi:10.1785/BSSA0790030645
173. Der Kiureghian A, Ang AH-S. A fault-rupture model for seismic risk analysis. *Bull Seismol Soc Am.* 1977;67(4):1173-1194. doi:10.1785/BSSA0670041173
174. Gutiérrez H, de la Vara R. *Análisis y Diseño de Experimentos*. 2nd ed. McGraw-Hill/ Interamericana Editores, S.A. de C.V.; 2008.
175. Massey FJ. The Kolmogorov-Smirnov test for goodness of fit. *J Am Stat Assoc.* 1951;46(253):68-72. doi:10.2307/2280095
176. Singh SK, Rodríguez M, Esteva L. Statistics of small earthquakes and frequency of occurrence of large earthquakes along the Mexican subduction zone. *Bull Seismol Soc Am.* 1983;73(6):1779-1796.
177. Utsu T. Relationships between magnitude scales. In: Lee WHK, Kanamori H, Jennings PC, Kisslinger C, eds. *International Handbook of Earthquake and Engineering Seismology, Part A*. 1st ed. Academic Press; 2002:733-746.
178. Bazzurro P, Cornell CA. Vector-valued probabilistic seismic hazard analysis (VPHSA). In: *7th U.S. National Conference on Earthquake Engineering*. Boston,

- Massachusetts; 2002.
179. Grossman SI. *Álgebra Lineal*. 6th ed. Mexico City: McGraw-Hill/ Interamericana Editores, S.A. de C.V.; 2008.
 180. Singh SK, Mena E, Castro R, Carmona C. Empirical prediction of ground motion in Mexico City from coastal earthquakes. *Bull Seismol Soc Am*. 1987;77(5):1862-1867. doi:10.1785/BSSA0770051862
 181. Singh SK, Mena E, Castro R. Some aspects of the source characteristics and ground motion amplification in and near Mexico City from acceleration data of the September, 1985, Michoacan, Mexico, earthquakes. *Bull Seismol Soc Am*. 1988;78(2):451-477.
 182. Ordaz M, Singh SK, Arciniega A. Bayesian attenuation regressions: an application to Mexico City. *Geophys J Int*. 1994;117:335-334.
 183. Reyes C, Miranda E, Ordaz M, Meli R. Estimación de espectros de aceleraciones correspondientes a diferentes periodos de retornos para las distintas zonas sísmicas de la Ciudad de México. *Rev Ing Sísmica*. 2002;66:95-121.
 184. Jaimes MA, Lermo J, García-Soto AD. Ground-motion prediction model from local earthquakes of the Mexico basin at the hill zone of Mexico City. *Bull Seismol Soc Am*. 2016;106(6):2532-2544. doi:10.1785/0120150283
 185. Jaimes MA, Ramírez-Gaytán A, Reinoso E. Ground-motion prediction model from intermediate-depth intraslab earthquakes at the hill and lake-bed zones of Mexico City. *J Earthq Eng*. 2015;19(8):1260-1278. doi:10.1080/13632469.2015.1025926
 186. Drouet-Mari D, Kotz S. *Correlation and Dependence*. London: Imperial College Press; 2001.
 187. Nelsen RB. *An Introduction to Copulas*. 2nd ed. New York: Springer Science+Business Media, Inc.; 2006.
 188. Genest C, Favre A-C. Everything you always wanted to know about copula modeling but were afraid to ask. *J Hydrol Eng*. 2007;12(4):347-368. doi:10.1061/(ASCE)1084-0699(2007)12:4(347)
 189. McNeil AJ, Frey R, Embrechts P. *Quantitative Risk Management: Concepts, Techniques and Tools*. 2nd ed. Princeton: Princeton University Press; 2015.
 190. Chopra AK. Evaluación numérica de la respuesta dinámica. In: *Dinámica de Estructuras*. 4th ed. Ciudad de México: Pearson Educación; 2014:752.
 191. Gallego M. *Estimación de Riesgo Sísmico En La República de Colombia*. Mexico City: Universidad Nacional Autónoma de México (UNAM); 2000. <https://tesiunam.dgb.unam.mx/F/USEPGT216Y1TEAFMCN32ASRX2RX1SA>

- 4JYIPIICG92NN86P64SF-42780?func=full-set-set&set_number=289281&set_entry=000001&format=999.
192. Flores-Estrella H, Yussim S, Lomnitz C. Seismic response of the Mexico City basin: A review of twenty years of research. *Nat Hazards*. 2007;40:357-372. doi:10.1007/s11069-006-0034-6
 193. Perez A, Jaimes MA, Ordaz M. Spectral attenuation relations at soft sites based on existing attenuation relations for rock sites. *J Earthq Eng*. 2009;13(2):236-251. doi:10.1080/13632460802347430
 194. Singh SK, Quaas R, Ordaz M, et al. Is there a “hard” rock site in the Valley of Mexico? *Geophys Res Lett*. 1995;22(4):481-484. doi:10.1029/94GL03298
 195. Singh SK, Ordaz M. On the origin of long coda observed in the lake-bed strong-motion records of Mexico City. *Bull Seismol Soc Am*. 1993;83(3):1298-1306.
 196. Goel SC, Chao S-H. Plastic design versus elastic design. In: *Performance-Based Plastic Design*. International Code Council; 2008:7-16.
 197. De Luca F, Vamvatsikos D, Iervolino I. Near-optimal piecewise linear fits of static pushover capacity curves for equivalent SDOF systems*. *Earthq Eng Struct Dyn*. 2013;42(4):523-543. doi:10.1002/eqe.2225
 198. Uang C-M, Bertero V V. Evaluation of seismic energy in structures. *Earthq Eng Struct Dyn*. 1990;19(1):77-90. doi:10.1002/eqe.4290190108
 199. Forbes C, Evan M, Hastings N, Peacock B. Lognormal distribution. In: *Statistical Distributions*. 4th ed. Hoboken, New Jersey: John Wiley & Sons, Inc.; 2011:131-134.
 200. Structural Engineers Association of California (SEAOC). *Recommended Lateral Force Requirements and Commentary (SEAOC Blue Book)*. (Shea GH, ed.). Sacramento, California: Structural Engineers Association of California (SEAOC); 1999.
 201. Martín del Campo JO, Pozos-Estrada A, Pozos-Estrada O. Development of fragility curves of land-based wind turbines with tuned mass dampers under cyclone and seismic loading. *Wind energy*. 2021;24(7):737-753. doi:10.1002/we.2600
 202. López-Castañeda AS, Reinoso E, Martín del Campo JO. Influence of site-specific strong-motion duration on structural performance. *Bull Earthq Eng*. doi:Under review
 203. Applied Technology Council (ATC). *Seismic Evaluation and Retrofit of Concrete Buildings. Volume 1 (ATC-40)*. Redwood, California; 1996. <https://www.atcouncil.org/pdfs/atc40toc.pdf>.

204. Clarivate. Journal Citation Reports. <https://jcr.clarivate.com/jcr/home>. Accessed July 13, 2022.
205. Center for Engineering Strong Motion Data (CESMD). Strong-Motion Virtual Data Center (VDC). <https://www.strongmotioncenter.org/vdc/scripts/default.plx>.
206. National Research Institute for Earth Science and Disaster Resilience (NIED). Strong-motion Seismograph Networks (K-NET, KiK-net). <https://www.kyoshin.bosai.go.jp/>.
207. Bommer JJ, Magenes G, Hancock J, Penazzo P. The influence of strong-motion duration on the seismic response of masonry structures. *Bull Earthq Eng.* 2004;2(1):1-26. doi:10.1023/B:BEEE.0000038948.95616.bf
208. Chandramohan R, Baker JW, Deierlein GG. Influence of ground motion duration on the collapse of bridge structures. In: *Proceedings of the 7th National Seismic Conference on Bridges and Highways*. Oakland; 2013:12.
209. Hancock J, Bommer JJ. Using spectral matches records to explore the influence of strong-motion duration on inelastic structural response. *Soil Dyn Earthq Eng.* 2007;27(4):291-299. doi:10.1016/j.soildyn.2006.09.004
210. Iervolino I, Manfredi G, Cosenza E. Ground motion duration effects on nonlinear seismic response. *Earthq Eng Struct Dyn.* 2006;35(1):21-38. doi:10.1002/eqe.529
211. Liapopoulou M, Bravo-Haro MA, Elghazouli AY. The role of ground motion duration and pulse effects in the collapse of ductile systems. *Earthq Eng Struct Dyn.* 2020;49:1051-1071. doi:10.1002/eqe.3278
212. Molazadeh M, Saffari H. The effects of strong motion duration and pinching-degrading behavior on seismic response. *Soil Dyn Earthq Eng.* 2018;114:333-347. doi:10.1016/j.soildyn.2018.06.032
213. Raghunandan M, Liel AB. Effect of ground motion duration on earthquake-induced structural collapse. *Struct Saf.* 2013;41:119-133. doi:10.1016/j.strusafe.2012.12.002
214. Vega E de J, Montejo LA. Influence of ground motion duration on ductility demands of reinforced concrete structures. *Int J Adv Struct Eng.* 2019;11:503-517. doi:10.1007/s40091-019-00249-3
215. Wang X, Xue B, Xu B, Pang R. Role of strong motion duration on seismic responses of high concrete faced rockfill dams. *Structures.* 2021;32:1092-1102. doi:10.1016/j.istruc.2021.03.092
216. Xu B, Wang X, Pang R, Zhou Y. Influence of strong motion duration on the seismic performance of high CFRDs based on elastoplastic analysis. *Soil Dyn*

- Earthq Eng.* 2018;114:438-447. doi:10.1016/j.soildyn.2018.08.004
217. Mendoza C, Hartzell SH. Slip distribution of the 19 September 1985 Michoacan, Mexico, Earthquake: Near-source and teleseismic constraints. *Bull Seismol Soc Am.* 1989;79(3):655-669. doi:10.1029/93JB00021
218. Mendoza C. Coseismic slip of two large Mexican earthquakes from teleseismic body waveforms: Implications for asperity interaction in the Michoacan plate boundary segment. *J Geophys Res.* 1993;98(B5):8197-8210.
219. Courboux F, Singh SK, Pacheco JF, Ammon CJ. The 14 September 1995 (M = 7.3) Copala, Mexico, earthquake: A source study using teleseismic, regional, and local data. *Geophys Res Lett.* 1997;87(4):999-1010.